3D mapping of underground utility networks using ultra-wideband multi antenna array step frequency radar

Rakeeb Mohamed Jaufer

THESE DE DOCTORAT DE

NANTES UNIVERSITE

ECOLE DOCTORALE N° 601
Mathématiques et Sciences et Technologies de l'Information et de la Communication
Spécialité : *Electronic, signal processing and telecommunications*

Par

Rakeeb Mohamed Jaufer

3D mapping of underground utility networks using ultra-wideband multi antenna array step frequency radar

Thèse présentée et soutenue à Nantes, le « 31.08.2022 »
Unité de recherche : ENDSUM, Cerema

Rapporteurs avant soutenance :

Mohammed Serhir	Maitre de confèrences des université : Univ Paris-Saclay
EL Khamlichi Drissi Khalil	Professeur des Universités - HDR : Universités Clermont-Auvergne

Composition du Jury :

Président :	Thierry Château	Professeur des Universités - HDR Universités Clermont-Auvergne
Examinateurs :	Yide Wang	Professeur des Universités - HDR : Ecole Polytechnique de l'université de Nantes
	Albane Saintenoy	Maitre de confèrences des université - HDR : Université Paris-Saclay
	Mohammed Serhir	Maitre de confèrences des université : Univ Paris-Saclay
	Khalil EL K Drissi	Professeur des Universités - HDR : Universités Clermont-Auvergne
	Donatienne Leparoux	Directrice de Recherche - HDR : Université Gustave Eiffel
	David Guilbert	OPA - Rechercheur : Cerema Ouest
Dir. de thèse :	Amine Ihamouten	Researcher, Université Gustave Eiffel, Nantes Campus, France.

Invité(s)
Co-dir. de thèse : Xavier Derobert Senior Researcher, Université Gustave Eiffel, Nantes Campus, France.

Acknowledgement

To my beloved parents, wife, son, siblings, in laws, my relatives, my friends, my school teachers, and university professors. I owe it all to you.

First of all, I am indebted to my Thesis director, Dr. Amine Ihamouten and my co-director Dr. Xavier Derobert for their great support and invaluable advice throughout the course of my research. I extend my gratitude to Dr. Yann Goyat for his guidance and funding support.

I am grateful to Dr. Amine Ihamouten, my co-director Dr. Xavier Derobert and Dr. Yann Goyat for their insights and sharing their knowledge and experience in GPR, Signal Processing and Machine Learning. I also thanks, Prof. Jean Marie Billbout, a guide who encouraged my professional journey in France. Then, Dr. David Guildbert and Dr. Shreedar Todkar for their continuous support and assistance throughout my thesis. And thanking, Dr. Cedric Lebastard who was my supervisor of the masters intern, and he shared the principles and experience in GPR domain.

A very special gratitude goes out to all the members of 'Comite de Suivi de Thèse' for providing me their valuable feedback and suggestions to improve my work. A personal note of thanks to my dissertation rapporteurs for taking their valuable time in providing me a speedy response. I extend my gratitude towards the thesis committee members for their presence during the defense and their comments that helped me improve the final version of the manuscript.

And at last but by no means least, a special thanks to all my colleagues at Cerema, logiroad and UGE for directly or indirectly sharing their experience with me throughout the course of the thesis. This dissertation would not have been possible without their warm love, continued patience, and endless support.

Thanks one and all for your encouragement!

Contents

List of Figures

List of Tables

Chapter 1

Introduction

1.1 Abstract

The thesis study is part of a collaboration between Cerema, Logiroad, and the Université Gustave Eiffel. The research is fully funded by Logiroad. The goal of this thesis is to provide the signal processing steps required for automatic identification, localisation, and classification of underground utility networks. The acquisition of data is focused on Ultra-Wideband (UWB) multi-antenna array Step Frequency Radar (SFR). The system must be equipped with a linear antenna array that can cover the whole width of the road or survey channel at ideal high speed, making it suited for highways and local urban roads. As a result, it may make large-scale 3D mapping easier. The thesis was motivated as a response to recently implemented government regulations in keeping a geomatics database of underground utility networks and positioning standards as damage avoidance measures during excavations. For example, the precision of three-dimensional location of critical underground networks in Class A is 40 cm, as specified in the NF-S70-003-2 standard in France. Furthermore, the potential solution must be highly resilient in the highly dynamic, complex, unexpected, and dispersed subsurface environment indicated by the nature of this application. We have divided the overall goal of the research into three distinct subtasks, such as automatic pipe detection, and depth and diameter estimate, given that the localisation accuracy satisfies the Class A precision. Then, a multi-antenna array step frequency radar was built to provide the proof of concept. This might aid in the creation of customized, high-density, low-cost array SFR. As a result, all investigated signal processing methods are highly based on the physical and machine learning approaches such as Ray-based, SVM, SVR, ANN, KNN, CNN, Faster R-CNN, and YOLOv4, in conjunction with other physical GPR signal and image pre-processing techniques. In this context, all models were validated numerically and using partial experimental data.

1.2 Research overview

Utility survey, in general, refers to the locating, positioning, and identification of buried pipes, cables, and ducts, regardless of their sizes, depths, material types, or proximity to other utilities, through the use of a variety of techniques or technologies to effectively facilitate work planning, design, and excavation. The need for rigorous utility mapping developed as a result of catastrophic damage to the existing utility network while undertaking excavations around existing facilities [1, 2]. Traditional destructive testing techniques and physical manhole verification processes, which are costly and time-consuming, are frequently used in this context, and borehole tests cause damage to the examined structure. These drawbacks, however, can be addressed using Non-Destructive Testing (NDT) methodologies for evaluation. Traditional NDT methods such as acoustics, electromagnetic, or RFID technologies were used to find subsurface

pipes. However, because many operations are limited to metallic pipes, these approaches are neither cheap nor precise enough to meet expectations. Ground Penetrating Radar (GPR), on the other hand, is a non-destructive testing (NDT) technology based on electromagnetic pulses that is utilised in a range of civil engineering applications, including utility detection. GPR can detect both metallic and non-metallic objects. Among them, the usage of GPR in subsurface utility surveys has been steadily increasing. The recognized high level process phases to follow in utility finding are GPR data collection, pipe detection, physical and geometrical parameter estimate, and 2D/3D mapping. GPR data acquisition in the context of 3D mapping necessitates the use of an array system that permits simultaneous B-scan profiles for 3D mapping of utility networks over a large territory. In contrast, traditional single antenna impulse GPR requires a grid survey, which takes a long time to complete. In another hand, to resolve the technological limitations of traditional time-domain impulse GPR, researchers and commercial manufacturers created Stepped Frequency Radar (SFR), a form of GPR that operates in the frequency domain, allowing ultra-wide band applications. SFR is appealing because of its dynamic management of the impulse bandwidth (frequency points) and faster acquisition speed. Unlike typical impulse GPR, which functions in the time domain, SFR operates in the frequency domain. In this thesis, multi-antenna array SFR was considered as the potential data acquisition system. Further, the thesis work is mainly focused on the study of various signal processing algorithms for the automated detection and localisation of buried pipes. In addition, a proof of concept of a two antenna array prototype was constructed and field validated to demonstrate the principle of an array system.

In the context of automatic pipe detection, GPR does not give direct identification of the pipe, but rather a 2D B-scan that must be evaluated by an expert or an automatic detection model. The most crucial local feature for establishing the presence of pipes in the target material is the hyperbola signal on the B-scan. For small data sets, human interpretation the hyperbola location is utilised after GPR signal preprocessing, and it is typically insufficient. As a result, all GPR-based signal processing algorithms have been developed with the goal of identifying and characterizing such hyperbolic properties on the B-scan utilizing human interpretation. In the case of large-scale GPR based utility mapping, however, an automatic detection approach is necessary to decrease the number of time-consuming and expensive processing steps. As a result, in this research work, we studied Faster R-CNN and YOLOv4 based automatic pipe detection models with two different Annotation approaches, taking into account the large scale detection challenges and advantages of Faster R-CNN and YOLOv4. The algorithms were chosen due to their automatic feature extraction, inbuilt sliding window techniques, and ability to locate multiple hyperbolas in a single B-scan. The purpose of YOLOv4 is to enable real-time detection, which Faster R-CNN is can not accomplish. The detection model was studied hypothesis that, the target is assumed as single, in case of non-seperable high dense scenarios.

Furthermore, after automatic pipes detection, the depth and radius of the pipes must be estimated accurately in the subsequent stage of automated mapping. Based on a survey of the literature, this work investigated numerous physical and machine learning approaches to pipe localisation and classification, taking into consideration the benefits and limits of each strategy for the large GPR-based utility mapping application. The purpose of the models presented in this thesis is to assess the applicability of the Ray-based approach, multi-class SVM (Support Vector Machine) classification, SVR (Support Vector Regression), ANN (Artificial Neural Network), and DCNN (Deep Convolutional Neural Network) for the estimation of velocity (v), depth (r), and radius (r) of underground utility pipes. In particular, depth estimate at Class A precision. According to the study, the multilayer subsurface is approximated as a single homogeneous layer. Thus, the average of multilayer permittivity, is presumed to be a single layer configuration. In all proposed models and studies, necessary but minimal GPR signal pre-processing methods (time zero off set, Gain, Frequency filters etc. . .) has been adopted

as single global settings for large scale processing context. The subsurface conditions of a large area are widely heterogeneous. Therefore, dynamic signal processing is unfeasible and time-consuming for large scale mapping.

Overall, the thesis establishes the groundwork for a global framework to address all aspects of automatic 3D utility mapping challenges and proposes practical scientific solutions for acquisition and data processing using physical and machine learning approaches in a large GPR data context. The thesis report is organized into four chapters in this regard: Introduction, Automatic pipe detection, Parameter estimation, and Experimental validation and step frequency radar prototype development. Despite the fact that the global solution presented automated 3D mapping, each step was scientifically assessed as an independent scope, and the fully automated pipeline development was kept for future work. Because it needs more experimental validation and complicated engineering development to reach a fully functioning solution.

1.3 Problem statement

In the utility mapping context, as a result of catastrophic damage to the existing utility network when trying excavations around existing facilities, the necessity for detailed utility mapping arose. Excavation damage, particularly in metropolitan locations, necessitates a significant amount of time and resources for corrective maintenance. In France, the inaccuracy of the underground utility network asset details resulted in serious accidents roughly at scale of 50,000 to 100,000 per year including 4500 gas leaks [3] causing several damages and put human life at risk. It is the case worldwide. In addition to the excavation utility damage, according to the *Association Canalisateurs de France*, there are over 900,000 km of drinking water network in France, of which 50 percent are over 45 years old, with an estimated 24 percent leakage of water [4]. The loss estimate for the sewage system is unclear, although it may be presumed to be similar. Furthermore, these water losses can cause soil erosion, decompaction, and the formation of voids under road infrastructure in metropolitan settings. During any excavation operation, it is possible to come across ancient pipelines that are not indicated on the schematic designs. As a result, the problem cannot be remedied unless all such assets are properly mapped.

Furthermore, fatal incidents in France in 2007 and 2008 prompted the revision of work guidelines in the vicinity of pipelines on July 1, 2012, comprising legislation, four decrees and a standard (NF S 70-003 - Part 1 to Part 3 [5]). The standard categorizes pipeline localisation accuracy as Class A whenever the positioning uncertainty is less than 40 cm, Class B when the uncertainty is 1.5 m, and Class C when the uncertainty is larger than 1.5 m. On the other hand, geographical information system databases applied to networks have become the primary focus of municipal governments, necessitating significant expenditures in geomatics expertise. Furthermore, the new legislation requires network operators to submit a map of new networks in precision Class A, as well as the need to do so for all critical networks buried in urban highways, basements, and Geo-referenced tracks by 2019. The existing regulations, however, do not address any measurement error for pipe size estimation. In addition, utility network identification and mapping have become widespread across the world as a damage prevention tool in conformity with rules. For example, United States defined no-mechanical dig zone boundary around buried infrastructures [6].

The most accurate method of detecting the location of subsurface infrastructure is to (carefully) drill a hole to expose it, and then bring in a survey crew to examine the area. However, this is time-consuming and costly. It can also potentially be hazardous, depending on the technology employed to dig the hole. To save digging, more safe excavation methods such as hydraulic and vacuum excavation are being deployed, but still slow for a large scale locating. Traditional destructive testing procedures, on the other hand, are frequently expensive

and time-consuming, and they cause damage to the tested buildings. Some non-destructive techniques such as acoustics, electromagnetic or RFID technologies are used to locate pipes in the underground [7]. However, existing Non-Destructive Technique (NDT) based mapping methodologies are not very economical and precise to meet the expectations. Furthermore, underground utility network survey is more challenging and difficult as the amount of deployments rapidly increasing. Thus, it requires large scale fast, robust and precise mapping solution to cater the expectation of national agencies.

In this respect, Ground-Penetrating Radar (GPR) is a NDT technology that transmits electromagnetic pulses into the subsurface for various civil engineering applications. Due to its sensitivity to material characteristics, GPR can also be used to detect buried gas pipes. However, it has a slower acquisition rate, and it does not directly provide a 3D positioning of the pipes. To overcome the technical limitation of conventional time-domain impulse GPR, a Stepped Frequency Radar (SFR) can be used, that is relatively faster and high in resolution due to ultra-wideband signals. In this context, SFR array systems has been introduced by commercial manufacturers like 3D Radar. Though, the system is black box and expensive. Further, the available SFR array system or any GPR doesn't provide any robust, automatic signal processing methods for large scale utility mapping. Whereas, the regulations demand high accurate localisation as mentioned above.

Extensive studies have been already performed by researchers to develop varieties of signal processing techniques for automatic detection, depth and diameter estimation of utility pipes. However, none of them demonstrated its robustness nor did they provide any validation on the unpredictable dynamic ground conditions and/or on large spatial field stacked data. Therefore, this thesis has been focused firstly on identifying the necessary steps to resolve the above outlined problems, draw a framework of possible solution with proof of concept conclusively leading to an industrial operational solution. The scope has been organized into three different domains: (a) Automatic pipe detection and (b) Parameters estimation such as depth and radius of the pipe, and considering multi-antenna array SFR as the suitable sensor for data acquisition.

This study entails the research and development of essential signal processing techniques for automatic pipe detection, as well as to estimate the depth and diameters of pipes using physical and machine learning models. In addition, a multi-antenna array step frequency radar prototype was developed to demonstrate array architecture and its operating principles.

In this respect, the overall research work answers the following main questions arise from the above discussed challenges.

- What are the essential procedures for utility mapping using GPR data ?.
- What are the visible attributes and physical behaviours of a buried pipe in a B-scan ?.
- How to create an automatic pipe detection system capable of detecting several pipes in a B-scan ?.
- What is the simplest signal processing sequence, with only single setting, for large-scale utility detection and localisation ?.
- How to correlate GPR signal characteristics with the depth, radius, and stratified media of a pipe ?.
- How to create an algorithm that uses discovered signal properties to precisely estimate the depth and radius of the pipe based on GPR data ?.
- How to construct a multi-antenna array SFR and understand the concepts, architecture, and design specifications. This may be used for research purposes without the need for blackbox commercial array GPRs ?.

- How to provide the principle of a full data processing pipeline capable of automatically detecting and localizing pipe based on GPR data ?.

The summary of the proposed solution is presented below, that answers the key research questions. Furthermore, a state of the art in terms of French utility mapping regulations and practices, global overview of large scale utility mapping projects and GPR operating principles have been discussed in Appendix B.

1.4 Summary of proposed solution

According to the literature, the critical phases of the large scale 3D utility mapping procedure with high precision and speed are identified and arrived to the following solution proposal:

1. Multi-antenna array UWB SFR based data acquisition.
2. Automatic pipe detection using deep convolutional neural network algorithms.
3. Geometric parameter estimation using supervised machine learning.
4. 3D mapping of utility detection using geo coordinates and estimated geometrical parameters.

In the context of answering the research questions listed in the problem statement, the above proposed solution phases are kept as reference components. Hence, all research work has been included within the scope of these key steps. According to the proposed phases, the identified concept of high level processing steps are illustrated in Figure 1.1.

The steps to be followed in the whole sequence are, GPR data acquisition, pipe detection, geometric parameter estimation, and 2D/3D mapping respectively. As stated before, Ground Penetrating Radar (GPR) is a Non-Destructive Testing (NDT) method used to assess the subsurface conditions of a structure and locate buried objects using electromagnetic waves [8]. Thanks to its sensitivity to the material characteristics (such as permittivity, conductivity, *etc.*), GPR can be used to detect both metallic and non-metallic targets. As previously said, the suggested concept of high level processing steps in 3D utility mapping is shown in Figure 1.1. GPR data acquisition, pipe detection, geometric parameter estimation, and 2D/3D mapping are the stages to be taken in the overall process. As stated before, Ground Penetrating Radar (GPR) is a Non-Destructive Testing (NDT) approach that uses electromagnetic waves to assess the subsurface conditions of a structure and discover buried objects [8]. GPR can detect both metallic and non-metallic objects because of its sensitivity to material properties (such as permittivity, conductivity, *etc.*). Furthermore, SFR is a form of ground penetrating radar that operates in the frequency domain rather than the time domain like impulse GPR. Whereas,

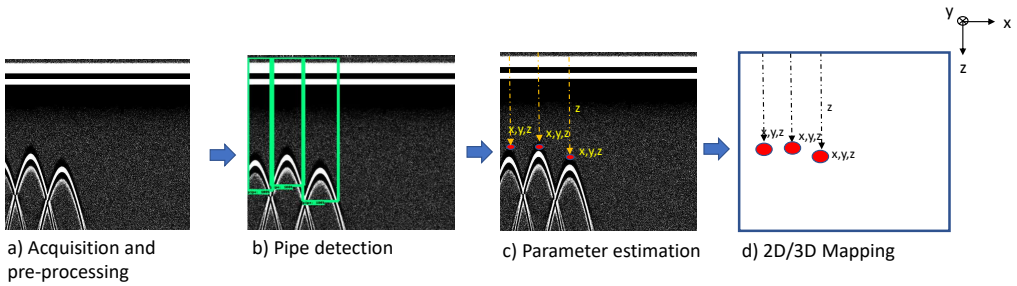

Figure 1.1: Utility locating geometric parameters estimation and mapping process.

the frequency signals transformed to time signal (A-scan) through Inverse Fourier Transform (IFT). And such SFR with multi array system can facilitate parallel B-scan profiles to produce 3D subsurface matrix. Then, their Ultra-wide band characteristics offer high resolution B-scan. Thus, such high resolution volume matrix can be utilised for 3D mapping of utilities using automatic signal processing methods in large scale perspective. Moreover, since the speed of acquisition must be fast enough to acquire large scale of data, the multi-antenna array step frequency radar has been identified as the data acquisition technology.

In this context, pipe detection is the second phase in the overall process towards 2D / 3D localisation in automated 3D utility mapping, as shown in Figure 1.1. Normally, GPR does not immediately offer the pipe's position, but rather a 2D B-scan that must be interpreted by an expert. The hyperbola signature on the B-scan is the most important local characteristic for determining the existence of pipes in the target material. Human interpretation the hyperbola position is used after GPR signal processing for limited data sets, and it is frequently insufficient.

However, automated hyperbola identification is required for large-scale GPR acquisitions based utility mapping. This is done largely to reduce time and cost on data processing while reducing human error, as well as to give speedy 3D localisation and mapping. Such an autonomous hyperbola detection approach may necessitate more accuracy and durability. As a result of the literature study, and considering the disadvantages of the existing approaches and advantages of AI (Artificial Intelligence) based approaches, this thesis proposes automatic pipes detection models based on DCNN object identification methods such as Faster R-CNN and YOLOv4. Before executing the machine learning models, physical signal processing techniques such as time zero offset, gain, noise reduction, and frequency filters were used in all scenarios. The amount of work, methodology, findings, and discussions in this regard may be found in the below Chapters. Furthermore, as illustrated in Figure 1.1, depth estimation is the third phase in the total process leading to 2D or 3D localisation in large scale GPR-based utility mapping. The procedure finds pipes in the shape of hyperbolas using automatic detection models during the pipe identification step, as shown in Figure 1.1. The process of detection and estimation is depicted in Figure 1.1. As shown in Figure 3.2, each recognized "bounding box" in the automated detection must be mapped with its coordinates on the raw B-can. The required region will then be cropped, split, and processed in order to estimate depth (d), radius (r), and any other desired characteristics like velocity of the subsurface medium around the pipe.

With the use of GNSS RTK global positioning, 3D global precision may be attained, provided that the depth is precisely measured using GPR. Meanwhile, the industry is looking for radius (r) to increase mapping data quality and safety boundary precision. Furthermore, radius improves network safety by accounting for pipe size when defining the no-dig zone around the pipe. In general, no dig zone border should be specified from the pipe's surface. For example, if the pipe's radius (r) is unknown, the NDZ (No-Dig Zone) boundary is measured from the pipe's centre, assuming the pipe is a point target, as shown in Figure 1.2, When radius (r) information is given, however, the NDZ (No-dig zone) boundary equals "r + NDZ" from the centre. As a consequence, the radius (r) information broadens the boundary and improves security.

Based on a survey of the literature, multiple methodologies for automated parameter (depth and radius) estimate were developed, each with advantages and limitations for a large GPR-based utility mapping application. To estimate the velocity (v), depth (r), and radius (r) of underground cylindrical pipes, the approaches include physical Ray-based methods and machine learning models such as multi-class SVM classification, SVR regression, ANN regression, DCNN multi class classification, and DCNN regression. Meanwhile, physical signal processing methods such as time zero offset, gain, noise reduction, frequency filters, and peak picking have been introduced, followed by feature engineering for machine learning approaches. The relevant work

in this regard is covered in Chapters 3 and 4 of this report.

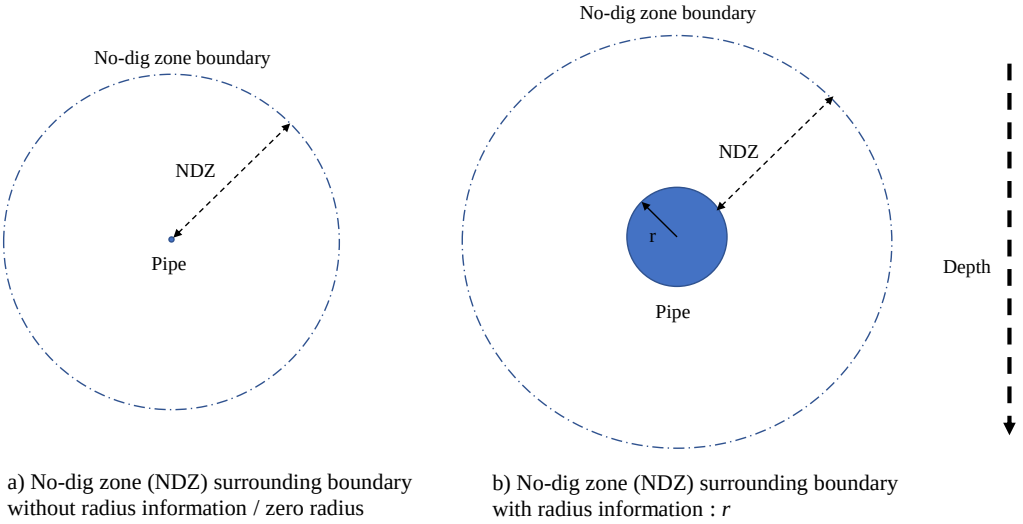

Figure 1.2: No-dig zone boundary with and without radius (r) information.

Despite the fact that the concept was addressed in Figures 1.1, the thesis work was examined scientifically at each stage independently without developing the entire automated data flow from the sensor up to the 3D mapping. Each phase necessitates complete experimental and field validation to finalise the model and parameters for the final data pipeline engineering development. Therefore, the development towards a fully operational automated solution is carefully analysed and evaluated individually in this thesis as standalone components. As a result, the remaining work is scheduled for a future scope in this direction, with this thesis serving as a baseline. In particular, as the fourth and final step of the 3D mapping process after populating all estimated geometrical parameters, the 3D geometrical visualisation of the pipes or the safety boundary can be mapped by connecting the 3D coordinates of the detected pipes in each parallel B-scans, using interpolation techniques (see Figure 1.3). However, the steps requires heavy engineering pipeline developments, which are outside the scope of this thesis.

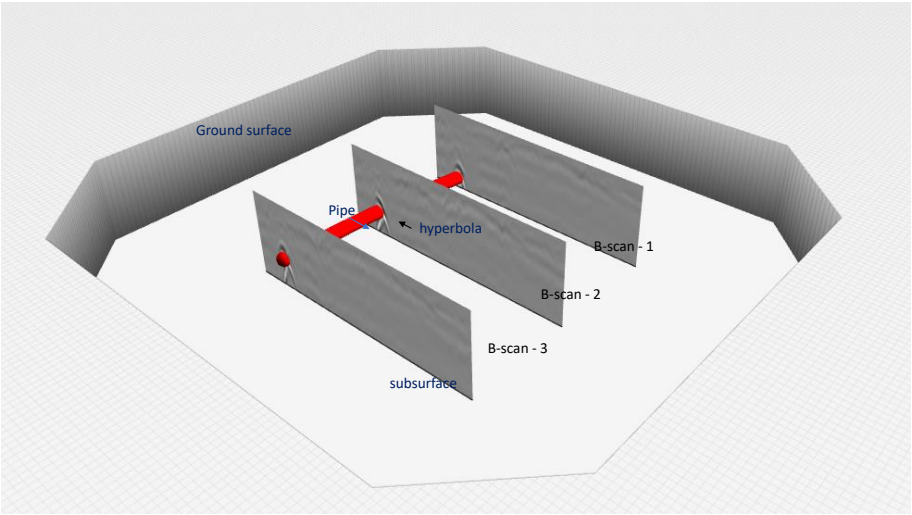

Figure 1.3: 3D mapping of utility networks by connecting parallel hyperbola.

The subsections that follow provide a quick overview of the proposed automatic detection and parameter estimation context, as well as a summary of the multi-antenna array SFR concept.

1.4.1 Introduction to automatic detection

In automatic utility localisation, GPR data acquisition, pipe detection, physical and geometrical parameter estimation and 2D/3D mapping are the high level process steps to follow. Whereas pipe detection is the second step in the over all process towards the 2D or 3D localisation as presented in the Figure 1.1. Normally, GPR does not directly provide the pipe's position, but a 2D B-scan that requires interpretation by an expert or automatic detection model is required. The hyperbola signature on the B-scan is the ultimate local feature to investigate the presence of pipes in the target medium. For small data sets, human interpretation the hyperbola location is practised after GPR signal processing. Thus, any GPR-based signal processing methods have been focused on identifying and quantifying such hyperbolic features on the radargram (B-scan) with the help of human interpretation. However, in case of large scale GPR acquisitions in utility survey, automatic hyperbola detection is necessary. This is primarily to save time and data processing costs while minimizing human error, as well as to provide rapid 2D localisation. Perhaps, such automatic hyperbola detection model requires higher accuracy and robustness. In the literature, several studies have been conducted to develop automatic hyperbola detection models based on physical methods and machine learning approaches, in utility and other GPR applications. Many studies have previously been conducted in this regard on the automated detection issue in B-scans. In this respect, the following key approaches are to highlight.
Hyperbola fitting is a conventional method of identifying underground utilities by detecting hyperbolas induced by target reflections, according to [9]. However, the main disadvantage of presenting this technique is that it produces random outcomes. In addition, it suffers from false detection when signal resolution is low. In this respect, machine learning research conducted by researchers relied on supervised learning methods. In particular in automatic hyperbola detection, [10] proposed a classification method from A-scan based on an adaptive dictionary of 1D wavelets, followed by Support Vector Machine (SVM). However, substantial training data sets and complicated feature extraction are required for these outcome models. The authors used the algorithm “Viola Jones" in [11]. Then the neural network was tested by [12]. Whereas, the prediction results of such supervised machine learning methods are dependent on the quality of the feature, which is becoming more difficult as the volume of data rises. Apart from that, several publications also have provided detecting methods for GPR data processing based on Convolutional Neural Network (CNN). The CNN skips the traditional manual “feature engineering" stage associated with machine learning, and instead learns the feature representations of buried objects automatically directly from GPR B-scan images, as done in [13]. In [14], D. Reichman. et al. examined the pretraining CNN initialisation stage to solve a few labelled samples of GPR data for target identification. While CNN-based algorithms for hyperbola identification have significantly advanced in recent years, the size and amount of input GPR on-site images are frequently limited, and most systems simply performs classifications and misses the target very often. In addition, the basic CNN models require sliding window for the multiple hyperbola detection. In this context, among the CNN-based object detection algorithms, CNN models evolved from simple CNN, R-CNN, Fast R-CNN and to Faster R-CNN throughout the time in order to overcome the drawbacks of each model by the other, by its detection speed and automatic features extraction to sliding window features. Thus, the evolution facilitated rapid object detection and proven in many applications in other domains. Whereas, in Faster R-CNN, selective search method was replaced with region proposal network, which

makes the algorithm to work much faster [15] than Fast R-CNN. The prediction time for one image would be around 0.2 s. This algorithm works better with less computation time when compared with other algorithms. Further, YOLO is used for the detection of objects in real time using convolutional neural networks. Because of its speed and precision, this algorithm is very popular. To detect objects, the approach just takes a single forward propagation through a neural network, as the name suggests [16]. Hence, in this advancement of Deep-CNN object detection algorithms, and many others have studied Faster R-CNN based hyperbola detection model. J. Feng [17] applied Faster R-CNN on raw B-scans and yields performance of more than 90%. Since the number of training samples were huge, Faster R-CNN is not compatible yet for a real time detection due to its processing delay. However, it has the potential to be deployed as post-processing model. On the other hand, to facilitate real-time automatic hyperbola detection, Y. Li [18] has introduced YOLO-3 based technique that produced test results accuracy more than 80% from only 300 training samples. In this context, by considering the large scale detection challenges, and advantages of Faster R-CNN and YOLO by its automatic feature extraction, inbuilt sliding window techniques, and due to the ability to locate multiple hyperbolas in single image, we have studied Faster R-CNN and YOLOv4 with two different annotation approaches in this research work. Furthermore, multiple non-separable overlapped hyperbolas were considered as single target in high densely non-separable overlapped pipe scenarios. This is done because, from the safety perspective, the detection of one or more pipes in the same location or trench is sufficient to draw the safety boundary (no-dig zone) of the utility assets during excavation. To minimize the false positives (due to multiple reflections effects), the subsurface or a layer interface echo also included in the annotation strategy to observe if the false alarms can be minimized by including horizontal subsurface features in the annotation. In this respect, proposed Faster R-CNN and YOLOv4 based automatic hyperbola detection algorithms were numerically and experimentally validated in this thesis. The findings are presented in the Chapter 2 and 4.

1.4.2 Introduction to parameter estimation

In automatic utility locating, GPR data acquisition, pipe detection, physical and geometrical parameter estimation and 2D/3D mapping are the high level process steps to follow. Whereas parameters estimation is the third step in the over all process towards the 2D or 3D localisation as presented in the Figure 1.1. In the literature, the estimation of depth (d) and radius (r) has been widely studied by other researchers in the past using Ray-based method [19], Full-Wave Inversion (FWI) [20], Hough transforms [21] and machine learning techniques [22]. Recently, [20] used Ray-based and FWI approaches to develop a novel method to estimate radius (r), depth and relative permittivity (ε) of utility pipes. However, the latter approach demands heavy computational resources and none of the methods has proven to be robust and accurate enough to convince the Class A expectation of depth localisation in utility application. In particular in large scale mapping.

The Ray-based method was used in [19] to detect buried rebars using inverse problem approach, whereas [23] used it to estimate radius (r) of the buried pipe at pre-known velocity (v) condition. [24] tried to invert the radius (r) of buried pipes using Ray-based method coupled with least square fitting techniques. [25] developed a unique VA (velocity analysis) technique for a bistatic GPR that predicts velocity around a hyperbola using a modified Ray-based approach. However, in all the above cases, the depth and radius values are known in advance. In contrast to the literature, for our case, the depth, radius, and velocity are all unknown, which is extremely challenging. [26] proposes non-linear hyperbola fitting approach to invert the velocity (v) and radius (r) simultaneously. Both approaches were developed for monostatic

antenna configuration and derived the hyperbola as a function of depth (d), radius (r) and velocity (v). Although these methods are promising, the error made on the peak localisation in the time signal lead to large errors in the radius (r) estimation [27]. Therefore, there is a need for a more robust approach. In this context, among a family of several machine learning algorithms, Support Vector Machines (SVMs) have shown promising results for different applications. Moreover, SVM has been extended for regression problems by support vector machine method (SVR). SVM techniques have shown promising results for underground utility applications. SVM has been used in the detection of utilities by automatic hyperbola detection [28]. [29] worked on SVM-based automatic hyperbola detection for utility network detection. In terms of parameter estimation, [30] proposes to use the features extracted from the rebar hyperbola, whereas [22] uses the skeletonisation technique to estimate radius (r) and depth of rebars in concrete structures. However, the latter approach is applied on images, and it suffers from fitting errors on the skeleton compared with the theoretical hyperbola. In addition, [31] proposes to use the features extracted from the hyperbola and with a SVR models to estimate radius (r) and depth of subsurface cylindrical objects. Hence, Multi-class SVM and SVR are the potential methods and retained for the parameter estimation study in this thesis.
Additionally, Artificial Neural Networks (ANN) are relatively new computational tools that have found extensive utilisation in solving many complex real-world problems. The attractiveness of ANN comes from their remarkable information processing characteristics appropriate mainly to non-linearity, high parallelism, fault, and noise tolerance, and learning and generalisation capabilities [32]. In the GPR applications, [33] adopted ANN for the detection and localisation of rebars, while [32] has used Multi-layer perceptron-based ANN for the assessment of rebar size in the reinforcement concrete. However, the approaches were validated only in few rebars and the robustness is still to be contested for broad applications with robust features. In this respect, ANN was also an interest of this study. Moreover, since input features highly dominate the machine learning model's performance [31] along with other factors such as database size and data set's morphology, the objective of this study is to evaluate the performance of Machine learning models combined with set of local features proposed in [31] to estimate velocity (v), depth and radius (r) of buried cylindrical pipes considered as three unique and independent parameters. Even though the velocity (v) is correlated to the depth, the conversion of velocity (v) from the depth information represents only the group velocity (v) of the stratified medium between the ground surface and the object at the vertex of the hyperbola. Thus, to overcome this limitation, velocity (v) is considered as an independent parameter in this study.

In addition, all above methods are based on a prior extraction of local features from the data (B-scan). However, identification of the correct local features still remains a challenge. Deep learning approaches brought great attention due to their proven ability to automatically extract features from the input data in order to perform classification or estimation. However, the deep learning models were seldom evaluated for the estimation of geometrical parameters such as depth and radius (r) of the buried pipes. Most of such machine learning methods for GPR are based on an analysis of B-scans in image format. The annotation is done on the images, relying on pixels. Such signal to image conversion and colour scale normalisation causes degradation in the information. Hence, it limits the applicability of DCNN based algorithms for the GPR based parameter estimation purposes (depth and radius). As a result, we have studied a DCNN based parameter estimation model that can work on B-scan signals instead of images. The objective of the proposed DCNN model work is to evaluate the ability of a deep learning method applied to GPR B-scans instead of "images" for the depth and radius (r) estimation of the pipe. Thus, as objective, the complex and sequential GPR signal pre-processing steps can be avoided in the localisation of the buried pipes.

Furthermore, in addition to the parametric study proposed above, the study is also extended to evaluate a possible method to classify the type of detected pipes, whether it is a

metal or PVC. The few works discovered in the literature for buried object classification on GPR data are [34–37]. In this context [34] investigated a method for classifying underground objects between cavities and pipes using a physical signal processing method. The suggested approach uses Instantaneous Phase Analysis of Ground-Penetrating Radar (GPR) Data. Three-dimensional CNN were utilised in [34] to recognise spatial underground objects such as pipe, cavity, manhole, and subsoil, [35] in particular explored machine learning based classification of underground utility pipes. To classify utility pipe type from GPR data, the author used wavelet transform, Fourier transform, and SVM. To identify buried utility materials, [37] used discrete cosine transform (DCT) coefficients as characteristics fed to the support vector machine (SVM) classifier. In both [35], the author achieved good results at various levels. The mentioned research served as the impetus for the proposed direction of study in this work. However, all these works were not supported to be robust and automated for large scale databases. Therefore, in order to provide a more robust approach, we have proposed to use both KNN (K-nearest neighbours) and SVM machine learning algorithms to measure classification performance using the A-scan.

All the proposed models were validated numerically using 2D gprMax data as preliminary study. The, SVM, SVR and ANN were validated in open-air controller experiment settings. The relevant detail literature review, methodology and findings are presented in Chapter 3 and 4.

1.4.3 Multi Antenna Array UWB Step Frequency Radar

Multi Antenna Array UWB Step Frequency Radar is the data acquisition sensor in the proposed solution to meet the global scope. Hence, it is made-up of multiple SFR channels. Whereas SFR is a GPR that operates in frequency domain as defined in previous section. In the utility application, GPR-based approaches have been shown to have various benefits over other non-destructive techniques, making them of special relevance as a potential solution to the utility network detection, localisation, and classification problem mentioned throughout this chapter. GPR [38] is a non-destructive technology for locating objects or interfaces buried under the earth's surface or within any electromagnetic wave penetrable structure. GPR is capable of detecting both metallic and non-metallic objects. When we look at the GPR's operating principles, we can see that it uses single or multiple antennas to transmit controlled electromagnetic pulses to the subsurface at frequencies ranging from 20 MHz to 3 GHz or higher depending on the type of GPR [38–40]. The pulses that penetrate the ground are reflected back to a receiver by the various subsurface layers and any objects or features within the antenna's radiation visibility. The impulse GPR pulse, for instance a ricker wavelet, is emitted. The reflected pulse response is then recorded as a function of time. Then, several A-scans recorded in equal horizontal step size stacked together forms a signal image called B-scan. In the presence of a pipe, a hyperbola signature is created on a B-scan when a GPR is run over a pipe. The scattered echoes record a peak signal amplitude that changes with the distance between the GPR and the target at the reflection point on the pipe in each trace location. The traces are then piled together to generate a B-scan picture, which consists of the shape of a hyperbola formed by multiple traces (A-scans).

Meanwhile, SFR is a GPR that operates in the frequency domain rather than the time domain like impulse GPR. In its simplest architecture, a basic monostatic SFR can consist of an equivalent circuit or a Vector Network Analyzer (VNA), and an antenna. At each frequency point, the VNA measures the complex reflection coefficient (S_{11}) between the VNA and the coupled target medium through the attached single antenna in the monostatic mode. Nevertheless, in the bistatic configuration, two ports VNA is attached to two antennas and measures S_{12}. The operating principle of a VNA is to produce very narrow electromagnetic pulses (al-

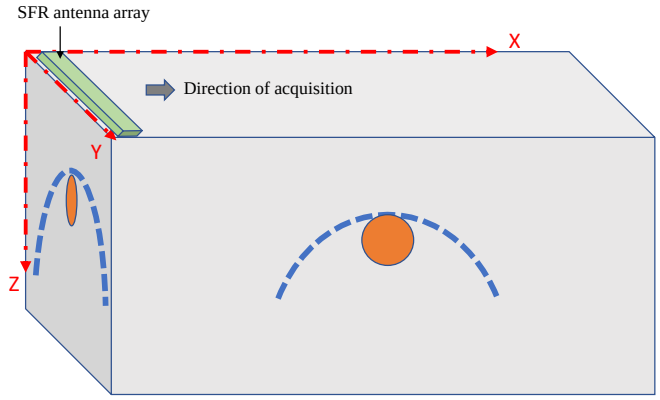

Figure 1.4: 3D matrix formed by B-scan (XZ), Cross view (YZ), C-scan (XY) from multi-antenna array SFR.

most a discrete pulse) at given frequency intervals. The discrete pulses form an ultra-wideband electromagnetic pulse in time domain, resulting in high resolution B-scans. Nevertheless, the resolution fades down the depth as the medium acts as a frequency filter. Therefore, as the high frequency components are attenuated, pulse width becomes wider and, consequently, resolution is dropped. Hence, an optimal frequency band is chosen. However, in commercial SFRs for utility applications, the frequency band is observed between 0.1 and 3 GHz in utility applications. Therefore, ultra-wide bandwidth, dynamic bandwidth control, and high speed measurement are the key attractions for using SFR in GPR applications such as utility surveying. Because the pulse width narrows as the bandwidth increases, high-resolution B-scans may be obtained for precise pipe localisation. In the process of forming a B-scan in a monostatic setup, for example, the measured (S_{11}) is used to perform IFFT to build an A-scan and then a B-scan by stacks. For example, in this thesis, the operating frequency was arbitrarily chosen between 400 MHz and 4.5 GHz.

In this context, from the literature study and industry analysis, a multi-antenna array step frequency radar technique has been discovered for data acquisition, which can fulfil the large scale GPR survey. Since the multi-antenna array SFR can acquire concurrent B-scans profiles and create 3D volume data in a single sweep utilizing an array, the pipe in every direction may be seen in a single pass. As a result, the multi-antenna array step frequency radar design has been created to evaluate the concept, and the proof of concept has been confirmed in this thesis.

The development aims at understanding the architecture and design process of SFR array that can potentially help scale-up for the low cost, high speed system in the future. This development will further help the research community to build their own SFR system for scientific studies, using raw data, without investing in black box and expensive commercial systems.

According to the preceding discussions, the engineering aspects of the thesis are directed at developing a multi-antenna array ultra-wideband step frequency radar [41] for three-dimensional mapping of subsoil, as well as detection, positioning, and localisation of underground utility networks. To realise our objectives, the appropriate architecture and hardware selection is critical, not only for the system's construction but also for building an optimized solution in terms of cost, speed, higher penetration depth, higher bandwidth, minimal coupling noise, larger parallel profiles (B-scans) *etc.*

Figure 1.4 shows a 3D subsurface and an SFR array in a utility survey. The pipe, on the other hand, can be buried in both the parallel and perpendicular to the road (assume the X

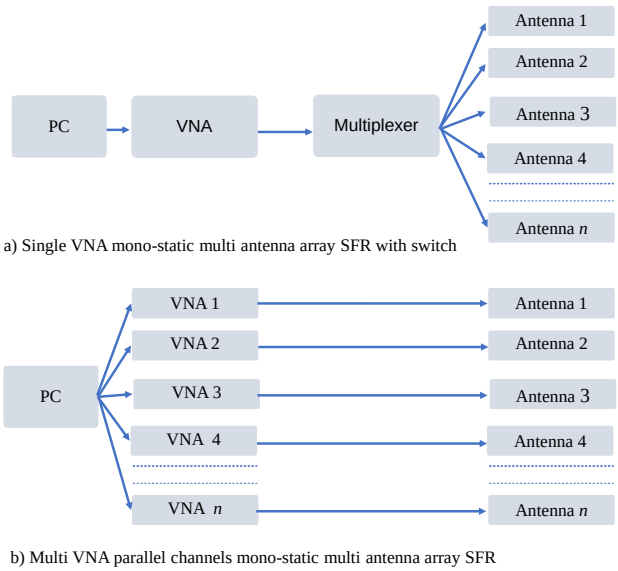

Figure 1.5: Example of two different multi-antenna array SFR topologies.

is the horizontal trajectory of the road). Thus, the purpose of the proposed SFR system is to create parallel B-scan profiles (in the XZ plane) that span the whole width of the road (wider as much as possible in Y axis). As a result, it can reduce survey time while also producing a B-scan in the YZ plane in a single pass in the X direction. As a consequence, any pipes orientated in Y should be visible in XZ B-scan, whereas pipes oriented in X should be visible in YZ B-scan. A broader and denser array are required to meet this requirement, since the number of array channels determines the A-scan stack resolution of the YZ B-scan (cross view). As a result, the number of points in a hyperbola is restricted by the size of the array. In the meantime, a faster system is essential for large scale utility mapping demand. In the context of proposed prototyping, the Figure 1.5 proposes two distinct topologies. In Figure 1.5.a, a single VNA-based multi-antenna array SFR design in monostatic mode with a switch. Then in Figure 1.5.b, there's a multi-VNA array with parallel channels that does not use a switch. To make the SFR prototype development phase easier, we opted to start with a simple design and gradually expand the complexity via consecutive generations. In this context, we have developed two antenna array SFR according to both proposed architectures. Then, the proof of concept was implemented in the thesis via field validation. Thus, the results produce parallel B-scan with hyperbolas. Hence, the detail discussion and findings are presented in the Chapter 4.

All above proposed detection and parameter estimation signal processing methodologies, numerical and experimental studies are well discussed in the below chapters and arranged as described below. In addition, the multi-antenna array step frequency radar prototyping and field validation are included in the manuscript.

1.5 Thesis report structure

The report is arranged in 5 Chapters and 2 Appendices to cover all aspects of the works to accomplish the scope of the thesis works, in the following order.

1. Chapter 1: Outline a brief introduction to the thesis background, objective, literature, proposed methodologies and conducted work.

2. Chapter 2: The chapter discusses the literature review, methodology, implementation of the proposed methods, necessary signal processing techniques, and numerical study of proposed Faster R-CNN and YOLOv4 based automatic pipe detection algorithm.

3. Chapter 3: In this chapter, the parameter estimation process methods are discussed, supported by numerical study. The methods such as, Support Vector Machines (SVM) classifications, Support Vector Machines regression (SVR), Artificial Neural Network (ANN), convolutional neural network (CNN), and Ray-based methods are presented that used in parameter estimation to correlate information about the radius (r) and depth of embedded pipes with the velocity (v) of stratified media in various numerical configurations.

4. Chapter 4: The chapter presents, firstly, the field validation of automatic pipe detection technique using Faster R-CNN and YOLOv4, whereas the data collected by commercial impulse GPR. Secondly, the experimental validation of SVM, SVR and ANN based depth and radius estimation methods was performed in open-air controlled SFR settings. Finally, the proposed multi-antenna array prototype, its literature, hardware selection, software development, and field validation with results have been presented.

5. Chapter 5: Draw a global conclusion of the conducted study, and an outline of prospective future works.

Chapter 2

Automatic Pipe Detection

This chapter discusses the literature review of automatic pipe detection in the process of underground utility network mapping; previous studies and outcomes; automatic pipes detection methodologies based on algorithms such as Faster R-CNN and YOLOv4 proposed in this thesis; and numerical validations of the proposed models. The relevant experimental validation is included in the CHAPTER 4. The models were investigated from the perspective of large scale GPR data processing. Thus, in the case of non-separable overlapping pipes, a global hypothesis is maintained that at least single pipe detection is adequate to detect. As a result, drawing a no-dig zone around the pipes is adequate.

2.1 Introduction

In the recent period, Ground Penetrating Radar (GPR) has been widely used in civil engineering applications as a Non-Destructive Testing (NDT) method for structural monitoring and locating buried objects. Among these, the adoption of GPR has been emerging rapidly in the underground utility survey. Utility surveying refers to the detection, positioning and identification of buried utility pipes, cables, and ducts. The need for precise utility mapping and 3D localisation has grown due to the catastrophic damages incurred on the existing utility networks while attempting excavations around existing facilities. Thus, 3D localisation of underground utility pipes has been regulated to avoid accidents during excavation.

Traditional destructive testing methods and physical manhole verification techniques are usually expensive and time-consuming, and further the borehole tests cause damage to the tested structure. However, these drawbacks can be overcome by using NDT methods for evaluation. Conventional NDT methods such as acoustics, electromagnetic or RFID technologies have been used in the past to find underground pipes. However, these methodologies are not very economical and precise to meet the expectations, as several methods are limited to metallic pipes. On the other hand, GPR is a NDT technology based on electromagnetic pulse which is applied in various civil engineering applications. Thanks to its sensitivity to the material characteristics (such as permittivity, conductivity), GPR can be used to detect both metallic and non-metallic targets.

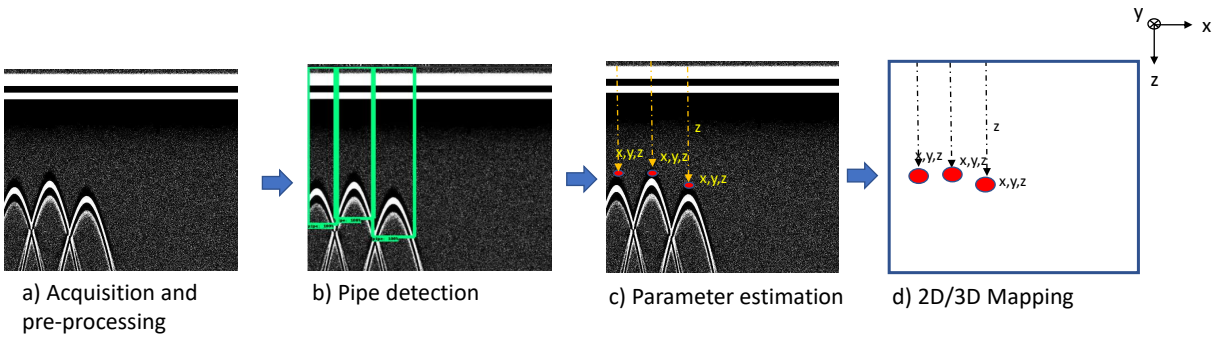

Figure 2.1: Utility locating, parameters estimation and mapping process.

In utility locating, GPR data acquisition, pipe detection, physical and geometrical parameter estimation and 2D/3D mapping are the high level process steps to follow. Whereas pipe detection is the second step in the over all process towards the 2D or 3D localisation as presented in the Figure 2.1. Normally, GPR does not directly provide the pipe's position, but a 2D B-scan that requires interpretation by an expert or automatic detection model is required. The hyperbola signature on the B-scan is the ultimate local feature to investigate the presence of pipes in the target medium. For small data sets, human interpretation the hyperbola location is practised after GPR signal preprocessing and often not sufficient. Thus, any GPR-based signal processing methods have been focused on identifying and quantifying such hyperbolic features on the radargram (B-scan) with the help of human interpretation. However, in case of large scale GPR acquisitions in utility survey, automatic hyperbola detection is necessary. This is primarily to save time and data processing costs while minimizing human error, as well provides rapid 2D localisation. Perhaps, such automatic hyperbola detection model requires higher accuracy and robustness. From the literature, several studies have been already conducted to develop automatic hyperbola detection models based on physical methods and machine learning approaches [9, 42], in utility and other GPR applications. Many studies have previously been conducted in this regard on the automated detection issue in B-scans. In this respect, the following key approaches are to highlight.

Hough Transform: It is a conventional method of identifying underground utilities by detecting hyperbolas induced by target reflections, according to [9]. It is a method for finding complicated patterns in binary image processing by determining precise values of parameters that describe these patterns [43]. According to [9], the Hough transform may also be used to locate circles and hyperbolas. The technique's goal is to use a voting mechanism to locate imperfect examples of objects inside a specific class of forms. This voting mechanism takes place in a parameter space. However, the main disadvantage of presenting this technique is that it has higher computational complexity, and the process uses a large amount of calculation time while producing random outcomes. In addition, it suffers from false detection when signal resolution is low.

Least square method (LS): Unlike the Hough transform, quadratic curves in GPR images may be looked for and distinguished using the LS approach. Although the LS algorithms are specifically intended for hyperbola fitting with the use of forward analytical hyperbola equation, most of them can only recognize one curve in an image and are not relevant to multi-hyperbola detection due to the lack of an image segmentation stage. Noises could not be totally eliminated in practice, and one picture may contain numerous hyperbolas.

Machine Learning: The use of machine learning in the GPR and utility applications are

described in Chapter 3 and below in this chapter. In this respect, the majority of machine learning research relied on supervised learning methods. In particular in automatic hyperbola detection, [10] proposed a classification method from A-scan based on an adaptive dictionary of 1D Gabor wavelets to compute a sparse decomposition of the signal, followed by Support Vector Machine (SVM) [7] obtained a detection rate ranging from 91.7 to 99.3%. However, substantial training data sets and complicated feature extraction are required for these outcome models. The authors used the algorithm "Viola Jones" in [11]. This algorithm uses the Haar wavelet as the input to a boosting learning algorithm called "Adaboost," which achieved a detection rate of 59% to 76% on three different test sets; then neural Network was tested by [12]. Machine learning-based algorithms are also used to GPR images, avoiding template matching and narrowing down the searching regions to include hyperbola. Then, [44] describes a method for classifying noise signals by neural nets during the detection phase. The Viola-Jones (VJ) technique was used by Maas and Schmalzl [45] to extract the target areas in GPR data. Most application characteristics must be identified by specialists for these tasks, and the classification results are dependent on the quality of the feature, which is becoming more difficult as the volume of data rises.

Deep Convolution Neural Networks: According to [46], several publications have provided detecting methods for GPR data processing based on Convolution Neural Network (CNN). The CNN skips the traditional manual "feature engineering" stage associated with machine learning, and instead learns the feature representations of buried objects automatically directly from GPR B-scan images, as done in [13]. Furthermore, [2] utilised CNN to extract and identify important events from GPR B-scans.

In [14], D. Reichman. et al. examined the pretraining CNN initialisation stage to solve a few labelled samples of GPR data for target identification. While CNN-based algorithms for hyperbola identification have significantly advanced in recent years, however the size and amount of input GPR on-site images are frequently limited, and most systems simply performs classifications and misses the target very often. In addition, the basic CNN models require sliding window for the multiple hyperbola detection.

In this context, among the CNN-based object detection algorithms, CNN models evolved from simple CNN, R-CNN, Fast R-CNN and to Faster R-CNN throughout the time in order to overcome the drawbacks of each model by the other, by its detection speed and automatic features extraction to sliding window features. Thus, the evolution facilitated rapid object detection and proven in many applications in other domains. Whereas,

Faster-Region-based Convolution Neural Network (faster R-CNN): In this algorithm, selective search method was replaced with region proposal network, which makes the algorithm to work much faster [15] than Fast R-CNN. The prediction time for one image would be around 0.2 s. This algorithm works faster when compared with other algorithms.

YOLO: YOLO (You Only Look Once) is a popular algorithm that detects objects in real time using convolution neural networks. Because of its speed and precision, this algorithm is very popular. To detect objects, the approach just takes a single forward propagation through a neural network, as the name suggests [16]. The CNN is used to predict multiple bounding boxes and class probabilities at the same time. Hence, in this advancement of Deep-CNN object detection algorithms, and many others have studied Faster R-CNN based hyperbola detection model. J. Feng [17] applied Faster R-CNN on raw B-scans and yields performance of more than 90%. However, the number of training samples were huge and Faster R-CNN is not compatible yet for a real time detection due to its processing delay. However, it has potential to be deployed as post-processing model. On the other hand, to facilitate real-time automatic

hyperbola detection, Y. Li [18] has introduced YOLO-3 based technique that produced test results accuracy more than 80% from only 300 training samples.

Summary of existing automatic detection models: In addition, the performance of various automatic approaches on GPR applications are stated in the Table 2.1, in particular, the utility detection and the findings are summarised on the below Table 2.2.

Réf	Year	Pre-processing	Algorithm	Database	Evaluation
[47]	2009	Standard median filter Background removal procedure Non linear time-varying gain Absolute value of each pixel Binarisation (Kapur's thresholding)	Genetic Algorithm	Train: 900 Test: 2500 400 × 400 pixel A-scan every 0.02 m	62 % correct detection localised with a maximum positioning error equal to 10 cm
[48]	2014	Hilbert transform Salt and pepper noise with HT Hoff algorithm	Artificial bee colony algorithm	400 × 300 pixel GPR image	The computational time of this algorithm is significantly better in compare with classic Hough transform
[49]	2016	No pre-processing	Scale Invariant Feature Transform (SIFT)	Three different GPR images	Mean execution time and Recall for SIFT algorithm gives good results in comparison with the previously tested algorithm of modified Hough transform
[50]	2016	Homogeneous Gaussian modeling SIRV process	Huber's estimator	Single GPR image	Application on real data showed the interest of the approach, especially in detecting pipes having a weak response level
[51]	2017	Profile focusing technique image resolution median filter Hyperbola-profile focusing Gaussian mean filtering	Distinctive Similarity Rendering Approach	Single GPR image	Precision: 0.799, Recall: 0.761 F measure: 0.772. The proposed approach results a better hyperbola apices reconstruction in high noise GPR images
[52]	2017	Moving average filter Adaptive thresholding algorithm	Column-Connection- Clustering Algorithm with Neural Networks	Single GPR image	Precision: 0.799, Recall: 0.761 F measure: 0.772. The proposed method exhibits good performance compared with a state-of-the-art method, in terms of robustness to noise, efficiency, and accuracy
[53]	2018	Normalisation	Deep CNN	21,879 GPR images	With 90% training images Accuracy 0.945 True positive rate (TPR) = 0.741 True negative rate (TNR) = 0.964
[54]	2018	No pre-processing	Faster R-CNN	100 real B-scan images	By the simulations, The model

Réf	Year	Pre-processing	Algorithm	Database	Evaluation
				Train: 60 Test: 40 50 simulated images Train: 40 Test: 10	outperforms detectors using classical features such as HOG and Haar
[55]	2018	Data Augmentation	Faster R-CNN (ResNet-50)	5866 GPR images. Initially these were synthetic data (748 images) and on-site data (90 images) With DA obtained, 5866 images Synthetic:5236 on-site:630 images	With 5000 iterations the accuracy without DA is 87.61 the accuracy with DA is 90.37
[17]	2020	No pre-processing	Faster R-CNN (ResNet-101)	350 GPR images	mean Average Precision (mAP) mAP(0.5): 90.5, mAP(0.75): 89 Average Recall(AR) AR(10): 92.2, AR(100): 92.2
[18]	2020	Static correction cut Removing DC drift Horizontal smoothing Removing Direct ground wave, High and low freq signals	YOLOv3	331 GPR images Training 70% Validation 20% Test 10%	mean Average Precision (mAP) mAP(0.5): 82.71, mAP(0.75): 75.90
[56]	2021	No pre-processing	YOLOv3 YOLOv5	350 GPR images Training 263 GPR images validation 44 GPR images Test 43 GPR images	YOLOv3 - Precision=0.73, Recall=0.86 mAP=80.11 YOLOv5 - Precision=0.77, Recall=0.95 mAP=91.59
[57]	2021	Inverse discrete Fourier transform (ISDFT) Data autoscale Background removal (BGR)	YOLOv3 YOLOv4 YOLOv5	303 GPR images Training 242 GPR images Validation 31 GPR images Test 30 GPR images	YOLOv3 - Precision=0.71, Recall=0.84 mAP=77.20 YOLOv54 - Precision=0.67, Recall=0.74 mAP= 76.33 YOLOv5 - Precision=0.74, Recall=0.94 mAP=94.39

Table 2.1: Bibliography of automatic detection models in GPR applications.

Réf	Year	Pre-processing	Algorithm	Database	Evaluation
[47]	2009	Standard median filter Background removal procedure Non linear time-varying gain Absolute value of each pixel Binarisation (Kapur's thresholding)	Genetic Algorithm	Train: 900 Test: 2500 400 × 400 pixel A-scan every 0.02 m	62 % correct detection localised with a maximum positioning error equal to 10 cm
[48]	2014	Hilbert transform Salt and pepper noise with HT Hoff algorithm	Artificial bee colony algorithm	400 × 300 pixel GPR image	The computational time of this algorithm is significantly better in compare with classic Hough transform
[49]	2016	No pre-processing	Scale Invariant Feature Transform (SIFT)	Three different GPR images	Mean execution time and Recall for SIFT algorithm gives good results in comparison with the previously tested algorithm of modified Hough transform
[51]	2017	Profile focusing technique image resolution median filter Hyperbola-profile focusing Gaussian mean filtering	Distinctive Similarity Rendering Approach	Single GPR image	Precision: 0.799 , Recall: 0.761 F measure: 0.772. The proposed approach results a better hyperbola apices reconstruction in high noise GPR images
[52]	2017	Moving average filter Adaptive threshold algorithm	Column-Connection- Clustering Algorithm with Neural Networks	Single GPR image	Precision: 0.799 , Recall: 0.761 F measure: 0.772. The proposed method exhibits good performance compared with a state of-the-art method, in terms of robustness to noise, efficiency, and accuracy
[53]	2018	Normalisation	Deep CNN	21,879 GPR images	With 90% training images Accuracy 0.945 True positive rate(TPR) = 0.741 True negative rate(TNR) = 0.964
[54]	2018	No pre-processing	Faster R-CNN	100 real B-scan images Train: 60 Test: 40 50 simulated images	By the simulations, The model outperforms detectors using classical features such as HOG and Haar

Réf	Year	Pre-processing	Algorithm	Database	Evaluation
				Train: 40 Test: 10	
[55]	2018	Data Augmentation	Faster R-CNN (ResNet-50)	5866 GPR images. Initially it was synthetic data (748 images) and on-site data (90 images) With DA obtained, 5866 images Synthetic:5236 on-site:630 images	With 5000 iterations the accuracy without DA is 87.61 the accuracy with DA is 90.37
[56]	2021	No pre-processing	YOLOv3 YOLOv5	350 GPR images Training 263 GPR images Validation 44 GPR images Test 43 GPR images	YOLOv3 - Precision=0.73, Recall=0.86 mAP=80.11 YOLOv5 - Precision=0.77, Recall=0.95 mAP=91.59
[57]	2021	Inverse discrete Fourier transform (ISDFT) Data autoscale Background removal (BGR)	YOLOv3 YOLOv4 YOLOv5	303 GPR images Training 242 GPR images Validation 31 GPR images Test 30 GPR images	YOLOv3 - Precision=0.71, Recall=0.84 mAP=77.20 YOLOv54 - Precision=0.67, Recall=0.74 mAP= 76.33 YOLOv5 - Precision=0.74, Recall=0.94 mAP=94.39

Table 2.2: Bibliography of automatic hyperbola detection models.

In summary, based on the broad literature review, the performance and robustness of existing deep learning based models varied depending on the signal pre-processing techniques, annotation strategy and adopted machine learning algorithms. The most common drawback of the existing DCNN models were higher false positives or false negatives as any hyperbola formed by scattering and ringing effects were detected as pipes, and it miss the pipe (create false negative) when the contrast is low or at high dense atmosphere. This results in poor overall accuracy of the models. Meanwhile, the false negatives are higher when multiple hyperbolas are overlapped due to densely present utility pipes. However, distinguishing all individual pipes are not mandatory in the excavation safety perspective, but at least the detection of top pipe is important to draw the no-dig zone.

In this context, by considering the large scale detection challenges, and advantages of Faster R-CNN and YOLO by its automatic feature extraction, inbuilt sliding window techniques, and due to the ability to locate multiple hyperbolas in single image, we have studied Faster R-CNN and YOLOv4 with two different annotation approaches in this research work. The reason behind YOLOv4 is to facilitate real-time detection capability, which is not the case in Faster R-CNN. Furthermore, single hyperbola and multiple non-separable overlapped hyperbolas were considered as single target in highly dense non-separable pipes scenarios. This is done because, from the safety perspective, the detection of one or more pipes in the same location or trench is sufficient to draw the safety boundary (no-dig zone) of the utility assets during excavation. To minimize the false positives (due to multiple reflections effects), the subsurface or a layer interface echo also included in the annotation strategy to observe if the false alarms can be minimised by including horizontal subsurface features in the annotation.

Further, as discussed above, the adopted methodologies use sliding window or similar approach across the large B-scans and hyperbolas are detected with the rectangle bounding box around the target. Moreover, since the bounding box is symmetric to the shape of hyperbole as in Figure 2.1, the lateral centre position of the bounding box coincides with the top of the hyperbola where this feature is potentially facilitates 2D localisation (x, y) of the pipe.

The work was first numerically evaluated using 2D gprMax data sets, then experimentally validated using GPR data obtained by the GSSI SIR-4000 (a commercial impulse radar associated to a 350 MHz antenna) in the site where the pipes are buried with and without trenches. The numerical findings and discussions for Faster R-CNN and YOLOv4-based models are provided in this chapter. As it is expected that the algorithms seek for the shape and properties of the hyperbola, the numerical investigation keeps the stratified medium's dispersion and inhomogeneity constant. As a result, shape deformation caused by dispersion and inhomogeneity has less influence on the shape. Though this assumption can not be evaluated without a controlled site, the field validation of the Faster R-CNN and YOLO methods justifies the hypothesis. Whereas, the experimental study is presented in the CHAPTER 4.

In this context, the next section discusses the methodology of the proposed DCNN algorithms, intuition and signal processing steps.

2.2 Automatic pipe detection methodology

The study proposes Faster R-CNN and YOLOv4 based automatic pipe detection technique that uses GPR B-scan images as input to the model and hyperbola signatures on it. Faster R-CNN was adopted for post-processing scope, while YOLOv4 is proposed for both post-processing and real time pipe detection approaches. Both the algorithms facilitate sliding window approach for the detection of multiple pipes in a single B-scan like shown in 2.1.b. In the event of non-

distinguishable multiple hyperbolas in a location, it has been approximated as a single target from a safety perspective. Likewise, both Faster R-CNN and YOLOv4 models were built with two different annotation strategies. In addition, Faster R-CNN models were incorporated with 3 different convolution network backbones. Thus, the total numerically studied models were six of Faster R-CNN and two of YOLOv4, as shown in flowchart Figure 2.2. Subsequently, two from each were shortlisted for experimental validation.

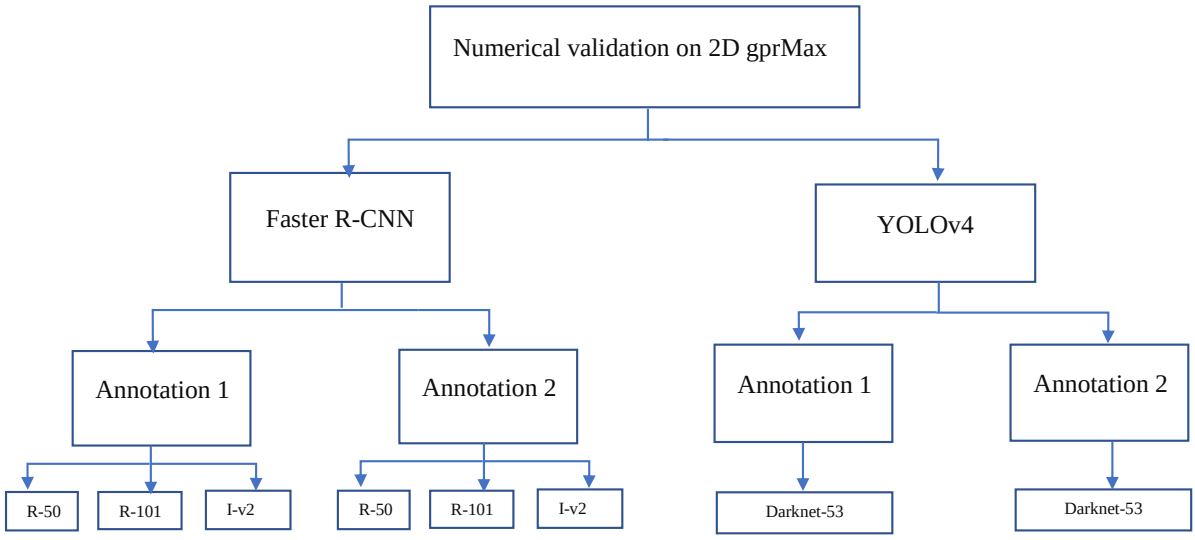

Figure 2.2: Studied automatic detection models. Whereas R-50, R-101 and Iv2 denotes ResNet-50, ResNet-101, and Inception-v2 convolution networks respectively.

2.2.1 Faster R-CNN (Faster Region-based Convolution Neural Network)

Faster R-CNN was proposed by [15] in 2016. As the name itself suggests, Faster R-CNN is a faster version of R-CNN family. The major difference from the other R-CNNs is that it utilises Region Proposal Network (RPN) [15]. As shown in the Figure 2.3, a Faster R-CNN object detection network is designed with an automatic feature extraction network which is a predesigned convolution network like ResNet-50, ResNet-101 [58] or Inception-v2, which is used to automatically extract features from the input B-scan. The process is then followed by two key stages. The first step, called a Region Proposal Network (RPN) that proposes bounding boxes of probable pipes (in the form of hyperbola), which identifies Region-of-Interest (ROI) in the feature map. Then, Region-of-Interest (ROI) pooling operation that populates and flatten the features of ROI for ANN. Finally, an ANN based classifier and bounding box regressor are included for classification of object class, and define the bounding box coordinates, respectively. Hence, these features of Faster R-CNN facilitates automatic detection of multiple pipes in a single B-scan automatically like shown in figure 2.1.b.

2.2.1.a Region proposal network (RPN)

RPN is the key feature of the Faster R-CNN network. Whereas, the region proposals are generated using a network that could be trained and customized according to the detection task, such as hyperbola detection. Because the proposals are generated using a network, this can be trained end-to-end to be customized on the detection task. Though, the RPN processes the input image using the same convolution layers used in the Fast R-CNN detection network.

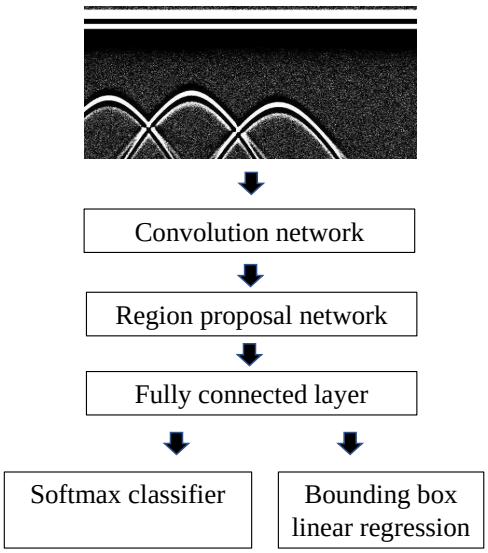

Figure 2.3: Faster R-CNN architecture.

RPN learns to generate candidate boxes from feature maps (output of the multilayer convoluted B-scan) that is the output by the convolution layer used, and generate the proposal for the pipes (hyperbolas). To generate these proposals for the region where the pipes (hyperbolas) exist, a small sliding window over a convolution feature map is applied. The size of this sliding window is n*n (where n is an arbitrarily fixed value by the user; here n = 3). The Anchor is the central point of the sliding window. For each sliding window, a particular set of anchors are generated but with 4 different scales (*i.e.*, 32, 64, 128 and 256) and with 3 different aspect ratios. Thus, twelve (4 x 3) proposals are possible for each pixel. Therefore, total number of Anchor Boxes with feature map of size w * h, and k number of anchors for each position of feature map, can be stated as w * h * k. Whereas, w and h are the width and height of the feature map, respectively. RPN has a classifier and a regressor, where the classifier determines the probability of a proposal having the target object while regression regresses the coordinates of the proposals [6].

The RPN works basically on the feature map returned from the last convolution layer shared with the Fast R-CNN. Based on a rectangular window of size n*n, a sliding window passes through the feature map. For each window, several candidate region proposals are generated. These proposals are not the final ones, as they will be filtered based on their objectness score [15].

Anchors The anchor boxes are the part of RPN operation. In the principle, the feature map of the last convolution layer is passed through a rectangular sliding window of size n*n. For each window, k region proposals are generated. Each proposal is parametrized according to a reference box, which is called an anchor box. The two parameters of the anchor box is scale and aspect ratio. If suppose there are 3 scales and 3 aspect ratios, and thus there is a total of k=9 anchor boxes. But k may be different from 9. In other words, k regions are produced from each region proposal, where each of the k regions varies in either the scale or the aspect ratio. Some anchor variations are shown in the Figure 2.4.

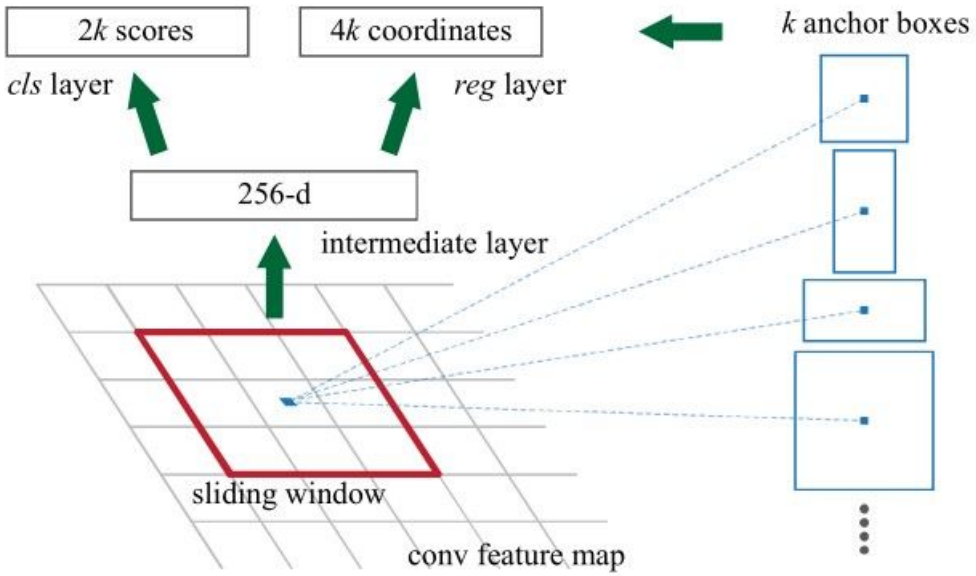

Figure 2.4: Anchors of RPN [59].

In this particular application with GPR data, hyperbola shape highly varies depending on the subsurface permittivity, depth and radius of the pipe, acquisition pulse width, resolution etc. For example, the Figures 2.5 illustrate how the hyperbola thumbnail could change with different scales and aspect ratios for a given configuration, whereas figures [a) 1:1, b) 1:2, c) 2:1 with width : height aspect ratio, and d) x 1, e) x 2 f) x 3 scales respectively]. Likewise, the higher k proposals is preferred to represent all possible combinations of the aspect ratio and scales, considering the variation imposed by the factors discussed above. Thus, the total number of trained combinations shall be equal to training images * k proposals. As the results, high k proposals in the training stage would increase the confidence of the trained model by including more possible combinations of hyperbola shapes. Subsequently, it could increase the number of true positive targets with higher IOU (Intersection Over Union) score, since the correlation between the trained ground truth and predicted anchor will be higher. However, the larger k also may produce false detection by falsely detect small diffraction effect hyperbola as real pipes. Therefore, the k proposal's values are fixed to a specific convolution network and arbitrarily selected. In this case, k=9 was chosen to cater the hyperbola shape and sizes to allow various pipes sizes, depth and permittivity variations. However, the optimised k values required to be studied, which requires very high computing resources. Thus, the k value is kept at 3 and k optimisation is retained for future work in-order to optimise the performance of the model.

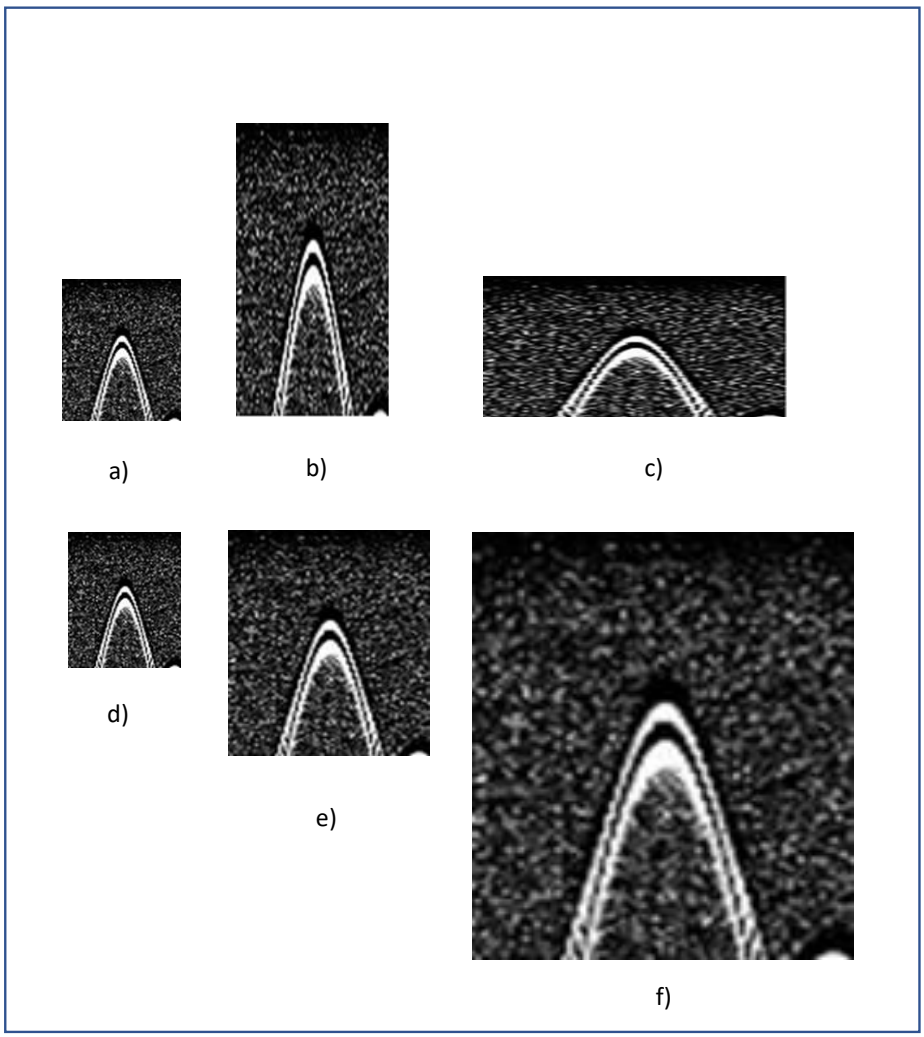

Figure 2.5: k proposals of a B-scan hyperbola thumbnail. a) 1:1, b) 1:2, c)2:1 width : height aspect ratio, and d) x1, e) x2, f) x3 respectively. Whereas a) and d) are similar in size.

In this context, upon selection of k proposals of anchor-boxes, for each n*n region proposal, a feature vector is extracted. The ROI pooling layer arrange 2D features obtained from RPN into a flattened vector appropriate for ANN (fully connected neural network). This vector is then fed to 2 sibling fully-connected (FC) layers. The first FC layer is named *cls*, and represents a binary classifier that generates the objectness score for each region proposal. The second FC layer is named *reg* which returns a 4-D vector defining the bounding box of the region.The first FC layer (*i.e.* binary classifier) has 2 outputs. The first is for classifying the region as a background (B-scan sections without hyperbola), and the second is for classifying the region as an object (hyperbola as the object in this work).

Intersection over union During the model training with RPN, each anchor is given a positive or negative object score based on the IoU as describer in the condition below (Equation 2.1). The IoU is given as the ratio between the area of intersection between the proposed anchor box and the annotated ground-truth box to the area of union of both. The IoU ranges from 0.0 to 1.0. The value is zero when no intersection and IoU is 1.0 if both anchor box and ground truth are fully overlapped. In this study, if an anchor that has an IoU value above 0.7 is given a positive object label. If IoU greater than 0.7 is never found, then a positive label is assigned to the anchors that have highest IoU. A negative object score is assigned to a non-positive

anchor when the IoU overlap is less than 0.3. This score means the anchor is classified as the background. Anchors that are neither positive nor negative do not contribute to the training objective. Anchor boxes at each spatial location, mark an object as foreground or background based on its IoU threshold.

$$IoU = \begin{cases} \text{Positive objectness } \rightarrow IoU > 0.7 \\ \text{Conditional Positive } \rightarrow 0.5 < IoU \leq 0.7 \\ \text{Negative objectness } \rightarrow IoU < 0.3 \\ \text{Not Negative / Positive } \rightarrow 0.3 \leq IoU \leq 0.5 \end{cases} \tag{2.1}$$

This IoU value argument is a default settings defined by the author of Faster R-CNN for the optimal performance. Thus, similar condition parameters were maintained in this study. Nevertheless, the values can have influence in discriminating between the background and the hyperbola. However, optimizing such parameters necessitates customizing existing Faster R-CNN architecture and high speed computing resources, which are not considered at this level, considering that a single model training needs at least 12 hours on a GPU-based computer. As a result, optimizing IoU values may need significant computational power and time, limiting the scope of the research. However, it may be the scope of future studies if high-performance computer resources become available in the future.

ROI-pooling

In Faster RCNN, the Region proposal network is used to predict objectness and regression box differences (with respect to anchors).These region proposals are often at the size of the input image rather than the feature layer. Thus, the proposals need to be scaled down to the feature map level. Additionally, the proposals can be of different width, height and aspect ratios. These need to be standardized for a downstream CNN layer to extract features. ROI Pool aims to solve both these problems. ROI pooling extracts a fixed-length feature vector from the feature map and does by flattening the obtained feature maps by doing max pooling [60].

Losses

Based on the definitions in [15], the class of each anchor is considered for RPN training. Finally, the loss function is applied to each image for training. Faster R-CNN uses Smooth L1-Loss for the regressors and Cross-Entropy for the classifier to calculate the loss. Where Smooth L1-Loss, also known as Huber loss [15].

In this context, for bounding box regression, and in the predictions, the characterisations of the 4 coordinates are defined in [15] based on 4 basic geometrical parameters as follows: where x, y, w and h denote the box's centre coordinates, its width and height. The Figure 2.6 illustrates how the label coordinates of a B-scan have been adopted according to the definition described in [15]. The Figure 2.6 shows a label as an example. However, the number of label shall be depending on the number of hyperbola presents in a B-scan.

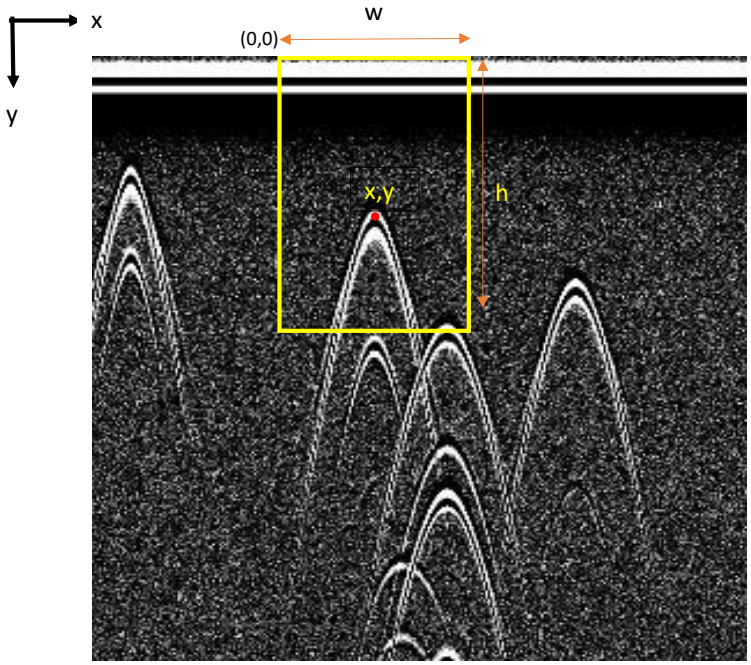

Figure 2.6: Example of a hyperbola with label.

Furthermore, as shown in Figure 2.3, a convolution network is deployed in the first layer of the Faster R-CNN to automatically extract features from the input B-scan, while the next paragraph discusses the principles.

2.2.1.b Convolution network

According to the architecture of Faster R-CNN presented in the Figure 2.3, convolution network is the first key stage of the model prior to RPN. In the proposed utility detection algorithm, convolution network extracts automatic features from the B-scan through multiple layers of convolution operation. Hence, using sliding window approach, it differentiates unique hyperbola features from the background. In definition, Convolution Neural Network (ConvNet/CNN) is a deep learning algorithm which can extract important differential features from in an input image (learnable weights and biases). Hence, the model be able to differentiate one from the other class (in this case hyperbola and background). In the field of deep learning, the CNN is the most famous and commonly employed algorithm, according to [61–63]. And in any given machine learning models, the pre-processing required in a ConvNet is much lower as compared with other classification algorithms. Compared with common supervised machine learning models, CNN network skips complex and time-consuming feature engineering step as shown in the Figure 2.7, and ease the development of classification models by automating feature extraction.

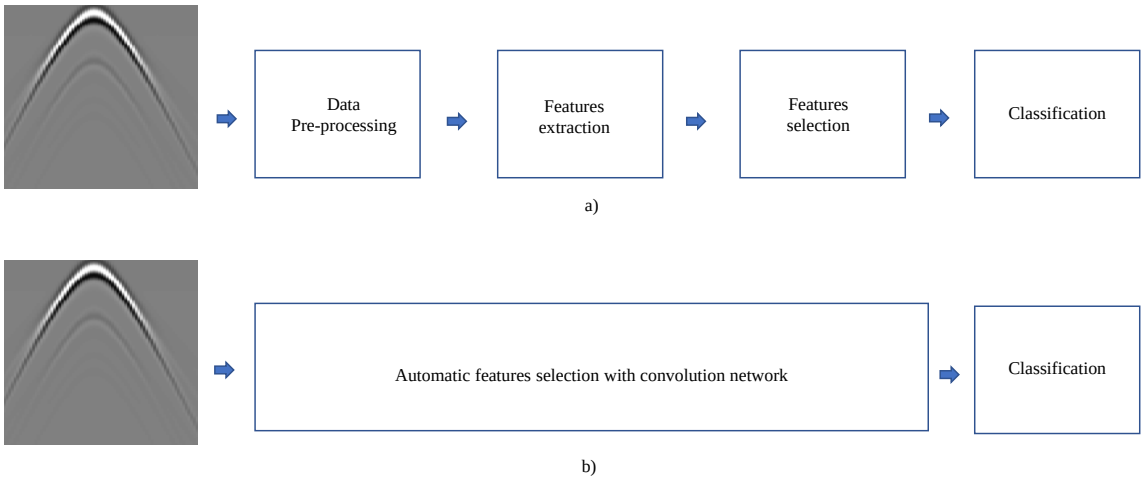

Figure 2.7: Comparison between a) machine learning and b) deep learning approaches in object classification.

The Figure 2.7.a explains the flow of a supervised machine learning. Whereas, normally, the hyperbola features must be already known by global or local features. Thus, the set of features will be used for classification at the end. In contrast, according to the Figure 2.7.b a deep convolution network can automate the feature extraction in the event where the unique hyperbola features are unknown. So that, using the multi layer and complex convolution network operation, the algorithm learns unique features itself from the input image. Hence, the pre-built convolution networks such as ResNet and Inception are already validated for more complex object detection like human, and other objects. Therefore, applying such deep neural network for automatic feature detection in B-scan can identify the automatic features from B-scan.

In this specific application, the process of convolution down samples the hyperbola information on the picture to a low dimensional feature map via the process of convolution utilizing predetermined filters and pooling (for example, max pooling), as shown in Figure 2.8.

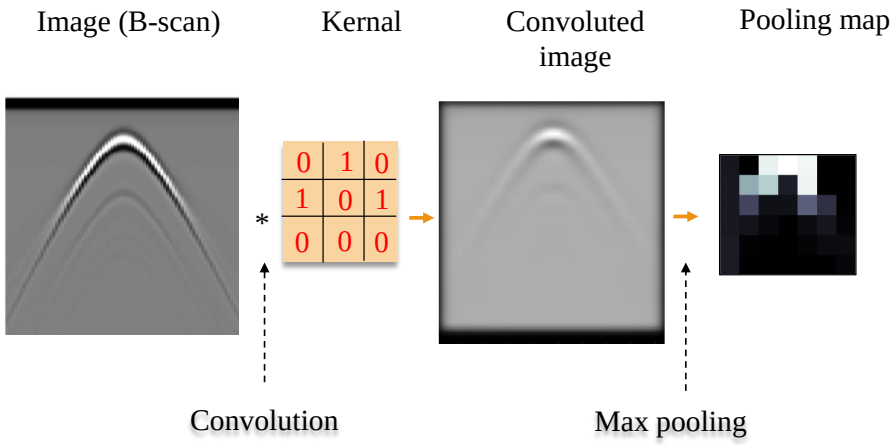

Figure 2.8: Example of a simple convolution layer process.

For an example, in numerical term, the pixel values of a large image is shrunk to a low dimensional feature image (as seen in Figure 2.9 and then to be flattened for the classification

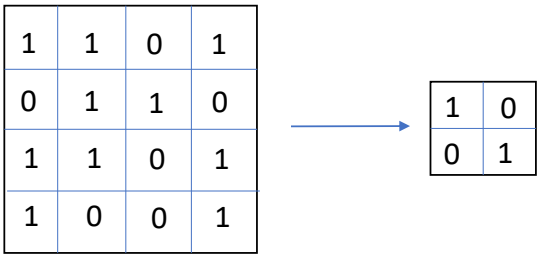

Figure 2.9: An example of a large image pixel values on the left, transformed to low dimension image (pooling map) through convolution process on the right through the process shown in 2.8.

layer. However, a deep convolution neural network will have several CNN layers in sequence like this in its network.

Hence, the convolution Layer and the Pooling Layer (the process chain shown in Figure 2.8), together form the i-th layer of a convolution Network. Depending on the complexities in the images, the number of such layers may be increased for capturing low levels details even further, but at the cost of more computational power. Whereas resnet-50 has 50 layers while resnet-101 has 101 convolution layers. A detail explanation of convolution principles can be seen in [64].

ConvNet for the proposed Faster R-CNN model Though several pre-designed deep convolution networks sophisticated for object detection exist, in this thesis, the following three proven convolution networks were investigated at this stage. Because, these deep networks were already validated on high complex object patterns [65] and using Faster R-CNN [66]. Perhaps in the literature, [55] and [17] adopted ResNet-50 and Resnet-101 for the automatic detection of hyperbola on GPR data respectively. Moreover, relatively the shape of the hyperbola is less complex in pattern. Thus, the adoption of existing convolution networks can avoid complex customisation. Because, the computational complexity and cost are very high for deep learning model training. Thus, the study was limited to the following three architectures.

- Residual Networks with 50 layers (ResNets-50)
- Residual Networks with 101 layers (ResNets-101)
- Inception-v2

However, the customised convolution network can be implemented for the hyperbola detection for further improvements.

ResNet Residual Network (ResNet) is a type of neural network introduced by Kaiming He *et al.* [65] to resolve a complex problem. In fact, many deep learning algorithms used the plain network that connects a convolution layer to a RELU activation function. Normally, we stack many layers within the Convolution Networks to result in improved performance and accuracy. The intuition behind adding more layers is that these additional layers progressively learn more complex features. For instance, in case of recognizing hyperbola, the primary layer may learn to detect edges and the second layer may learn to spot vertex and similarly the third layer can learn to detect other properties and so on. Still, the optimised number of convolution layers

to distinguish hyperbola on B-scan was not confirmed in the literature. Hence, higher number of convolution layers is preferred for global and local feature extraction. However, increasing CNN layers is not that easy. For a sufficient deep model, adding another layer results in the degradation problem and therefore the performance can start to suffer [65].

To overcome this problem of degradation, a building block of the convolution network is proposed by [65] in the ResNet architecture which won the ImageNet competition in 2015 to deal with the deeper levels while overcome gradient vanishing problem. The key difference in ResNet architecture compared to plain network is known as shortcut connections, which uses the preceding convolution layer's input to the next output and sums the output in the ReLu activation function [65] to resolve gradient vanishing problem with increasing number of layers in the network. Whereas, [65] proposed ResNet architecture with 18, 34, 50, and 101 layers of depth (convolution layers). e.g. a ResNet-50 has fifty layers.

Furthermore, based on the conclusions of the paper [65] ResNet works well with the adoption of the Faster R-CNN and gives better performance results in object detection datasets. Hence, due to the relative advantage of the ResNet architecture, the ResNet 50 and 101 was studied as an automatic feature extraction network (convolution network) in the proposed Faster R-CNN based automatic hyperbola detection model. Furthermore, the Inception ConvNet was also applied to compare the robustness of the model across different ConvNet architectures.

Inception: The inception network [67] is a form of Convolution Network that solves different aspects of current problems, like how ResNet addressed gradient vanishing. The goal was to make multi kernel parallel convolutions easier to do while maintaining good accuracy and low computing cost. The reason behind this is that the size of salient sections in the input image might vary hugely. A B-scan with a hyperbola, for example, might have varied sizes and shapes depending on the horizontal resolution, pulse bandwidth, relative permittivity of the medium, and pipe depth. Because of the variation in the shape and location of the hyperbola information, choosing the right kernel size for the convolution operation becomes a challenge. For information that is distributed more globally, a larger kernel is desired, while for information that is distributed more locally, a smaller kernel is preferred. So, that multi kernels learning is required to identify the most appropriate kernel size. Nevertheless, it's computationally time-consuming. At the same time, very deep plain networks are prone to over fitting and the vanishing gradient problem too [65]. As a solution, allowing multi kernels in a network with varied kernel sizes to function on the same level too would basically make the network "wider" rather than "deeper," lowering the computing cost of the network while maintaining high accuracy. Though the target object's size and aspect ratio variation (k proposals) can be handled by RPN network in Faster R-CNN, the performance of the model also depends on the convolution kernels size of the Convolution network that takes place prior to the RPN network. Hence, a CNN network that learns a single B-scan with multiple kernels is necessary to test the Faster R-CNN model's performance. In this respect, the inception resolves the optimised k proposals alternatively. Detail intuition and network architecture of inception can be seen in [67].

In this thesis, for the proposed Faster R-CNN model, inception-v2 is investigated for the automatic hyperbola detection.

To be summarised, due to automatic feature extraction architecture and ability to detect multiple pipes in single B-scan, the Faster R-CNN is proposed for automatic utility pipe detection. Moreover, Faster R-CNN is already studied by other researchers in hyperbola detection and already validated on several object detection applications. In addition, the proposed ConvNet architectures are widely used in the Faster R-CNN applications, including GPR application. Hence, the Faster R-CNN with proposed ConvNets have been studied. However, Faster

R-CNN's detection speed is not sufficient yet to deploy for real time detection task. Therefore, in order to investigate a feasible real-time pipe detection model, YOLO algorithm was also studied and hence methodology is briefed in the next section. Whereas, from literature, YOLO is already proven for real-time object detection in several applications.

2.2.2 YOLO (You Only Look Once)

You only look once (YOLO) is a real-time object detection system that is well discussed in the literature. The role of Faster R-CNN in automatic pipe detection is to provide automatic hyperbola detection in the post-processing step of large GPR data processing. However, in other circumstances, real-time pipe detection in the field is also essential before excavation operations can begin. In this case, Faster R-CNN has yet to attain the required temporal performance for real-time object detection. Nonetheless, [16] introduced the YOLO technique to be suitable for real-time object detection applications without sacrificing performance. On PASCAL VOC 2007 (an object detection challenge competition), the Faster R-CNN VGG-16 model processes 7 frames per second with a mean average Precision (mAP) of 73.2%, whereas the YOLO VGG-16 model processes 21 frames per second with a mAP of 66.4%. Though the performance of the YOLO has dropped a bit while the detection speed is 3 times faster. As a result, such a property of YOLO models motivates the research of YOLO for suitability of real-time hyperbola recognition at acceptable performance level. Furthermore, [18, 56, 57] have used YOLO for real time automatic hyperbola detection with GPR data. As a result, the adoption's motivation was kept in this thesis.

Workflow

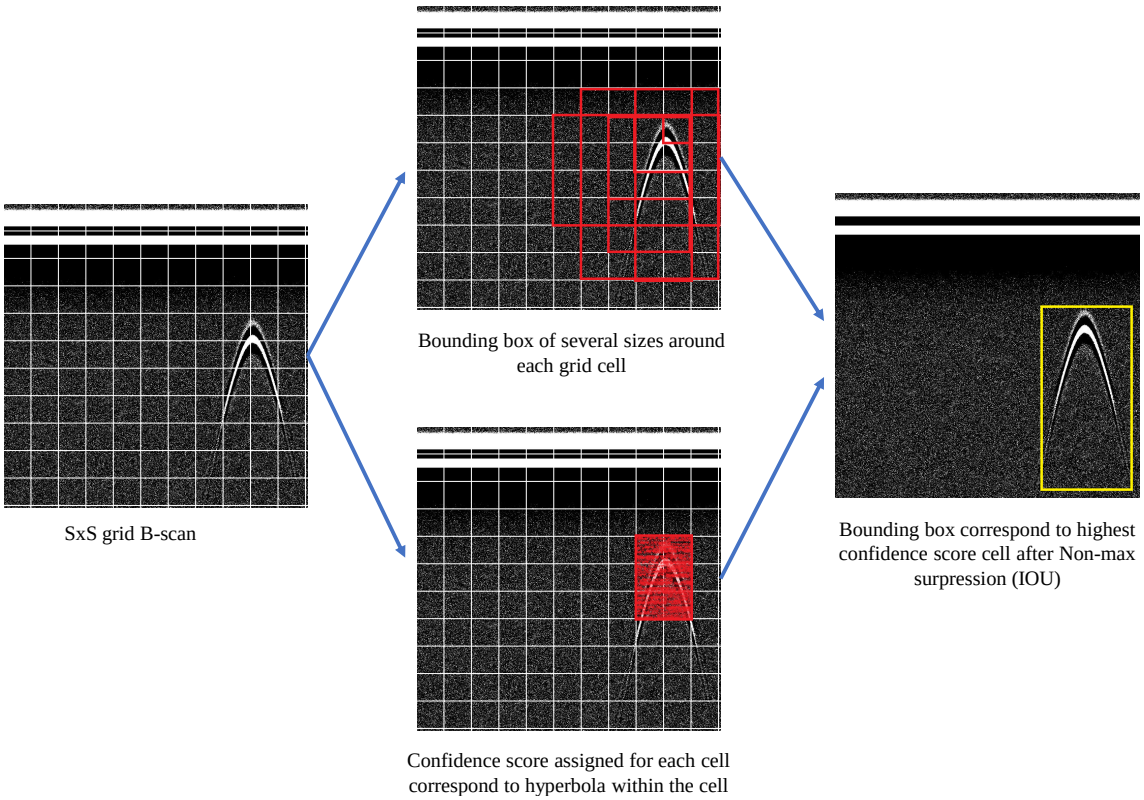

Figure 2.10: High level workflow of YOLO.

In the data workflow of simple YOLO architecture, the network predicts each bounding box of existing hyperbola targets using features from the full B-scans. It also predicts all bounding boxes for an image across all classes at the same time. This means that our network considers the entire image as well as all the objects within it. End-to-end training and real-time speeds are possible thanks to the YOLO design, which maintains excellent average Precision. Target hyperbola is often defined as a single class in the proposed automatic hyperbola detection scope. The scenario can also be expanded to include multi-class hyperbola. For example, class 1 refers to single pipes, while class 2 refers to several pipes. At this level, however, the number of classes is limited to one. Because, the model tries to discriminate between a hyperbola and the background.

As explained by [16] and according to the illustrative Figure 2.10, the input image is divided into a $S \times S$ grid by the YOLO technique. If the object's centre falls inside a cell grid, that cell grid is in charge of detecting the object. Each cell grid forecasts B bounding boxes and their confidence scores. These confidence scores represent the model's belief that the box contains a target item (such as a hyperbola) as well as the accuracy with which it forecasts the box. In formal terms, confidence is defined as

$$CS = \Pr_{(\text{Object})} * \text{IOU}\ {}^{\text{truth}}_{\text{pred}} \tag{2.2}$$

If no object exists in that cell, the confidence scores CS is zero. Otherwise, the confidence score equals to the intersection over union (IOU) between the predicted box and the ground truth. Whereas, $\Pr_{(\text{Object})}$ is the probability of the objectness. Each bounding box consists of

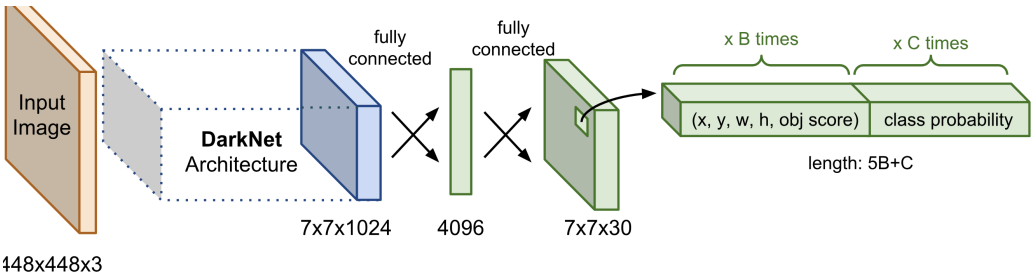

Figure 2.11: Example of high level YOLO architecture [68].

5 predictions: x, y, w, h, and confidence. The (x, y) coordinates represent the centre of the box relative to the bounds of the cell grid. The width (s) and height (h) are predicted relative to the whole image. Finally, the confidence prediction represents the IOU between the predicted box and any ground truth box. Each cell grid also predicts C a number of conditional class probabilities, $\Pr(\text{Class}_i \mid \text{Object})$. Then, it divides the image into a $S \times S$ grid and for each cell grid predicts B bounding boxes, confidence for those boxes, and C class probabilities. These predictions are encoded as an $S \times S \times (B * 5 + C)$ tensor.

2.2.2.a Architecture

The network of YOLO looks like a standard CNN, with convolutions layers, followed by two fully connected layers in the end.

With reference to the Figure 2.11, the convolution architecture (ConvNet) of the automatic features extraction in YOLO is Darknet (instead of Resnet / Inception in Faster R-CNN). Whereas, the base model is comparable to Inception. The input B-scan is followed by Darknet convolution network and then, over the entire conv feature map, two completely connected layers provide the final prediction of shape $S \times S \times (B * 5 + C)$. Where $S \times S$ denotes the number of cell grids, B denotes the number of bounding boxes with bounding box coordinates (b_x, b_y, b_w, b_h) and confidence (p_c), and C denotes the C number of class probabilities (*i.e.*, c_1 that of hyperbola). The loss function for the YOLO model is described in [16].

Note: The preceding section was created to demonstrate YOLO and its intuition. The proposed automatic hyperbola detection model, on the other hand, was investigated using Yolo-4, a more complex and advanced version of YOLO. A short brief about Yolo-4 architecture is discussed below due to the complex nature of the architecture and workflow of Yolo-4.

YOLOv4

YOLO comes in a variety of flavours, including YOLO [16],YOLOv2 [69],YOLOv3 [70], YOLOv4 [71] and YOLOv5 [72]. The convolution network and architectures, on the other hand, differ from one another in order to improve accuracy and reduce latency. YOLO version 4 (YOLOv4) [71] and YOLO version 5 (YOLOv5) [72] are the most recent additions to the YOLO series. Hence, the both series built with YOLOv3 backbone. The YOLO version 3 method is one of the most widely used single-stage detection methods (YOLOv3). YOLOv3 provides a great blend of fast detection speed and excellent detection accuracy in a one-stage detection approach. Several applications have previously demonstrated effective deployment, such as optical crack detection [73], pavement pothole identification [74], traffic sign detection [75], and traffic flow detection [76]. More detail intuition can be referred in papers published by relevant authors. Also, the motivation of YOLOv4 was to be used in this study since it was similar to the work

done by [57] for pavement crack detection. The results of [57] shows YOLOv4 is much faster and accurate than YOLOv3 on crack detection. However, in the scope of this work, YOLOv4 for the real time pipe's detection is implemented. Its intuition, network architecture and loss function schemes and bounding box regression principles can be seen in [70] and [71].

Note: In summary, the thesis explored YOLOv4-based real-time automatic pipe detection with two distinct Annotation techniques and signal processing sequences according to the data and model. The both Faster R-CNN and YOLOv4 model, uses the same annotation techniques. As a result, the annotation techniques, model performance measures and involved signal pre-processing fundamentals will be discussed below.

2.2.3 Implementation principles

The preceding subsections examine the approaches used for automatic pipe detection. The proposed models, on the other hand, allow for the identification of many pipes inside a single B-scan. In this context, Faster R-CNN and YOLO are both supervised machine learning models that necessitates model development, training and testing prior to operational deployment. As part of concept validation, model building involves training and performance testing. However, both training and testing B-scans must be labelled with ground truth, which is referred to as 'annotation'. The B-scans will then be divided into training and testing databases, with the training data used for model training. The model's performance will next be evaluated through testing the predicted results against annotated ground truth. Prior to model input, required pre-processing procedures are used in this process to improve the readability of hyperbolas in B-scans. This section has covered all of these techniques.

2.2.3.a Annotation techniques

The input image labelling is required for both Faster R-CNN and YOLO. In definition, the process of labelling the training images (B-scan) of a dataset in order to train supervised deep learning models is known as image Annotation. As a result, the Annotation is utilised to label the B-scans with hyperbola that required for the training of proposed deep learning models to perform convolution operation within the bounding box and recognize hyperbola features (depending on the Annotation approach and aim). In this situation, B-scan Annotation is necessary to mark the ground truth with single or multiple hyperbola, depending on the task's aim. Then, the annotated B-scans, as well as annotation bounding box coordinates, will be utilised for model training and validation. Whereas, the coordinates was adhered to the format of coordinates parameters discussed in section 2.2.1.a and 2.2.2.a relevant to the applied DCNN model. Because, the annotated bounding box coordinates are the key parameters for the model's loss function and overlap minimisation.

In this context, manual Annotation was used in this thesis work, which was done with the help of an open source software called "Labelimg", which was written in the Python environment. The individual will predetermine the labels "classes" and carefully construct the bounding box around the "ground truth signature, such as single hyperbola or multiple hyperbola in case of highly overlapped scenarios; with or without subsurface echo" depending on the Annotation technique. However, each model contains only a single annotation technique. After the model has been trained and deployed, it can predict and detect certain features in non-annotated B-scans. Importantly, as a result of the human error during Annotation, the model's performance may decrease considerably [77]. Remembering the two major ideas for automatic pipe identification, the Faster R-CNN was explored for post-processing, while the YOLO was investigated for real-time detection capability. In this regard, two Annotation techniques were developed for both algorithms in order to observe the performance differences in the

models related to the Annotation approach. The Figures 2.12 explains how the two scenarios of Annotations were performed on B-scan.

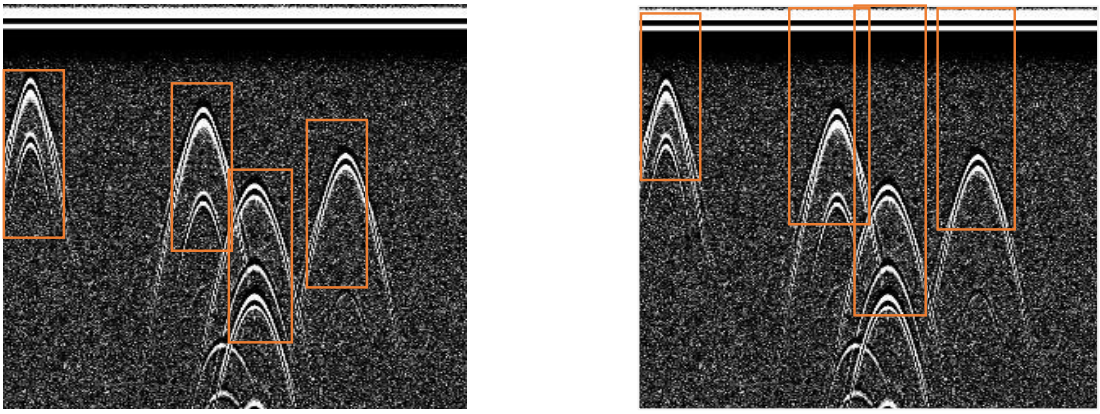

a) b)

Figure 2.12: Figures a) B-scan Annotation scenario-1, b) B-scan Annotation scenario-2.

The motivation behind these Annotation scenarios are; the most common drawback of the existing DCNN models are higher in false positives in automatic hyperbola detection applications, as any hyperbolas formed by scattering and ringing effects are also detected as true pipes. This results in poor overall accuracy of the models. Meanwhile, the false negatives are higher when multiple hyperbolas are overlapped due to densely present utility pipes. However, distinguishing individual pipes are not mandatory in the excavation safety perspective, but the detection of top pipe is important. Therefore, single hyperbola or highly overlapped multiple non-separable hyperbolas are considered as one target. This is done because, from the safety perspective, the detection of one or more pipes in the same location or trench is sufficient to draw the safety boundary of the utility assets during excavation works. So both Annotation strategies consider this approach. Furthermore, as an alternative approach, to minimize the false positives (false detection of artefacts such as multiple reflections effects as true pipes), the subsurface or a layer interface echo is also included as the Annotation scenario-2, while the scenario-1 is a conventional approach to detect the hyperbolas on B-scan. Hence, both annotation techniques never mixed within a single trained model.

For example, in terms of Annotation scenarios, the studied models can be categorised as

1. Faster R-CNN models with Annotation scenario-1
2. Faster R-CNN models with Annotation scenario-2
3. YOLO models with Annotation scenario-1
4. YOLO models with Annotation scenario-2

2.2.3.b Signal pre-processing

To increase the readability of the information in the B-scans, GPR B-scans usually require multiple pre-processing stages such as time zero correction, 1D and 2D noise / clutter removal filters, and gain. Binarisation or edge filters are occasionally used to increase the visibility of the hyperbola edges if necessary. For the detection model based on SVM dictionary, [78] utilised a curvelet filter to remove noise and improve hyperbola readability. Several studies and actual evidence show that different processing tools and sequences are acceptable for different B-scans;

for example, referring to the Table 2.2, authors used a variety of pre-processing approaches in their works. In addition, frequency filters and background removal are also frequently used for GPR signal processing. However, removing the background might destroy useful horizontal information such as subsurface or layer interfaces, as well as the vertex of a hyperbola, and commercial GPRs already have a band-pass filter built in. As a result, the need for frequency filters is also determined by the quality of the data and the collecting equipment.

Considering all the finding and facts from literature, pre-processing has a significant impact on model performance, and the pre-processing approaches depend on the kind of detection model. As a result, both are interdependent. The order in which the pre-processing phases are performed, on the other hand, is highly dependent on the kind of GPR, the noise quality of the B-scan, and the subsurface circumstances. However, the existing methods and sequences are not well oriented on large scale GPR processing. As a result, selecting a single pre-processing step or a certain sequence as a static processing flow for a big GPR data set is quite challenging. On the other hand, the subsurface quality varies considerably across the survey region, especially in the massive GPR data processing of utility mapping prospects. As a result, sticking to a single sequence for all data is difficult and ineffective, resulting in false alarms.

As a solution, huge GPR data can be divided into small B-scan portions, with distinct signal processing procedures applied to each little section. However, it increases the amount of human interaction and, as a result, the overall processing time. Furthermore, it contradicts the primary goal of the automatic hyperbola identification method. To complete the work, it is important to keep to basic processing steps with single global settings while processing big utility data sets. In addition, after converting from signal matrix to 2D picture formats, deep learning models learn the input based on normalised pixel values. In this situation, the convolution network may be unable to detect any hidden or non-visible hyperbola within a B-scan.

In support of this reasoning, [56] and [17] used Faster R-CNN and YOLO on 'raw B-scans' and achieved model performance of more than 80%. Because of the Deep Convolution Neural Network models' capacity to auto extract hyperbola features, which has been demonstrated on complicated objects like COCO data sets. Furthermore, the purpose of this application is to identify the shape of the hyperbola. As a result, for the utility identification application, any basic algorithm that detect the hyperbola is adequate. This is amply supported by the findings of [56] and [17]. As a consequence, complex and dynamic signal processing techniques were avoided in this thesis. And for hyperbolas enhancement, time zero adjustment and gain were judged to be sufficient, therefore they were used in the implementation. In terms of automatic large scale utility mapping, the objective is to reduce preprocessing to get closer to raw data and keep to a single configuration suitable to large data processing.

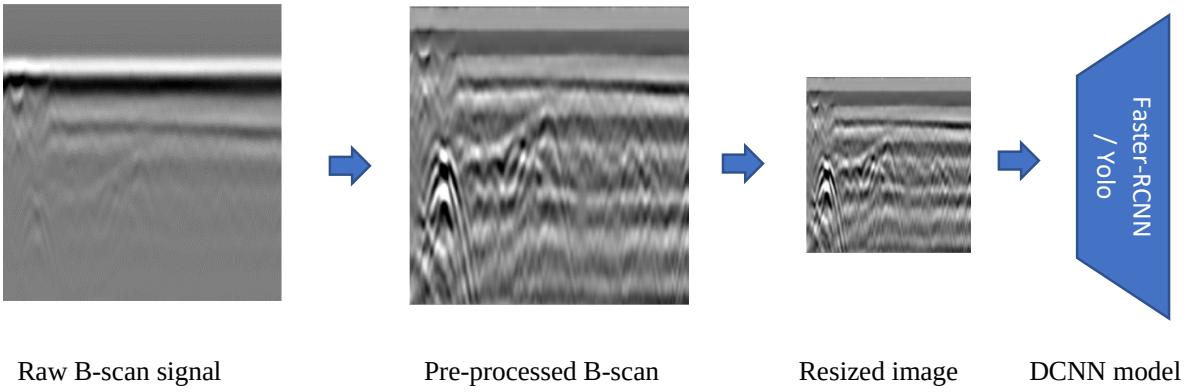

Figure 2.13: Data pre-processing flow.

The Figure 2.13 demonstrate the simple processing flow from the raw signal image to the DCNN model (Faster R-CNN or YOLO). Whereas, in the sequence of data processing for the proposed deep learning algorithms, in final steps of the pre-processing sequence, B-scan is meant to be transformed to gray scale or binary 2D images (jpg) at pre-defined pixel sizes after the signal processing stages. The B-scan must be resized to the normal pixel size without compromising too much information. Furthermore, the optimized resize is highly depended on used machine learning model, the type of GPR, acquisition time samples resolution and centre frequency etc. However, in this work, the x-axis resolution is kept as similar to raw B-scan. In this context, the intuition behind time-zero adjustment, gain, and image resizing approaches is addressed below, with any data-specific techniques re-explained in the subsection 2.3.2.

Time zero referencing: In utility surveys, a stable and unique reference as a time-zero point for the GPR data is required in order to compare the travel time and, potentially, estimate the depth of hyperbolas situated at various points along the survey. The bounding box coordinates relative to the surface interface would then be generated. Due to a variety of factors, such as the different lengths of the connecting cables or the change in antenna height induced by vibration of the GPR equipped vehicle [23] or the GPR, this is typically not achievable in an air-coupled configuration. Furthermore, in bistatic air coupled antenna configuration, the time zero of the emitter and receiver antenna can be different and desynchronized during mechanical vibrations. So, that it creates anomaly in the A-scan. However, in the detection aspects, the time zero is an optional process as it doesn't impact on the model's performance. Because, the proposed Faster R-CNN or YOLO algorithms look for the shape and pattern characteristics in the B-scan with the use of image in pixels. Nevertheless, the time zero reference is required if the detected target to be utilised for further parameter inversion like depth estimation with use of Ray-based methods. In contrast, if the objective of the model is limited to automatic detection only. The time zero referencing becomes more optional than mandatory.

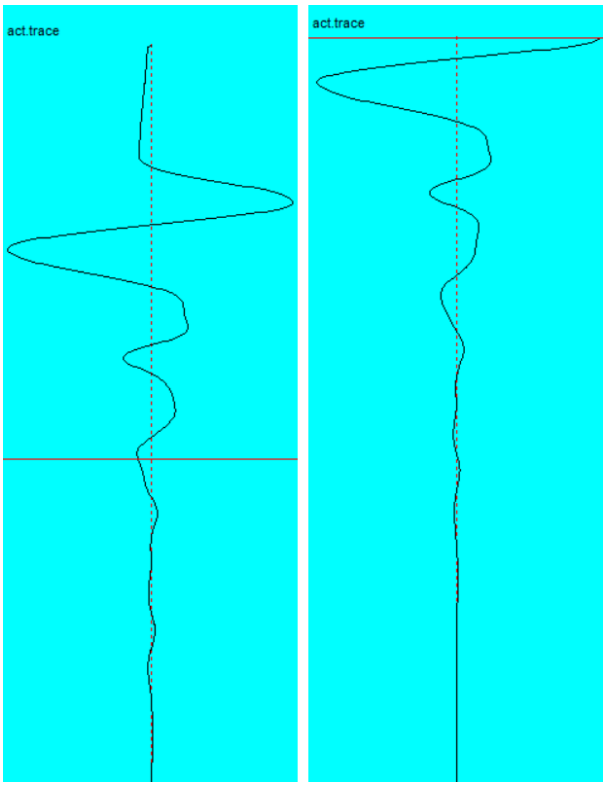

Figure 2.14: $left$: A-scan before time zero referencing $right$: A-scan after time zero referencing.

As discussed above, due to the vibration of GPR antenna, the position of the reflection from the air-subsurface interface in various A-scans may change. The hyperbola shape can also be distorted as a result of this (depending on the level of vibration). To avoid the apparent interpretation issues that come from a variable time-zero reference, the data must be adjusted to set a consistent time-zero position. However, even if the vibration is low and the surface echo always overlaps the direct coupling echo in a ground coupled antenna arrangement, a common time zero reference is necessary to remove the transit time between the radiation zero point and the air-subsurface interface. As a result, the coordinates of the bounding box are specified in relation to the ground surface, which enhances depth conversion and hyperbola fitting.

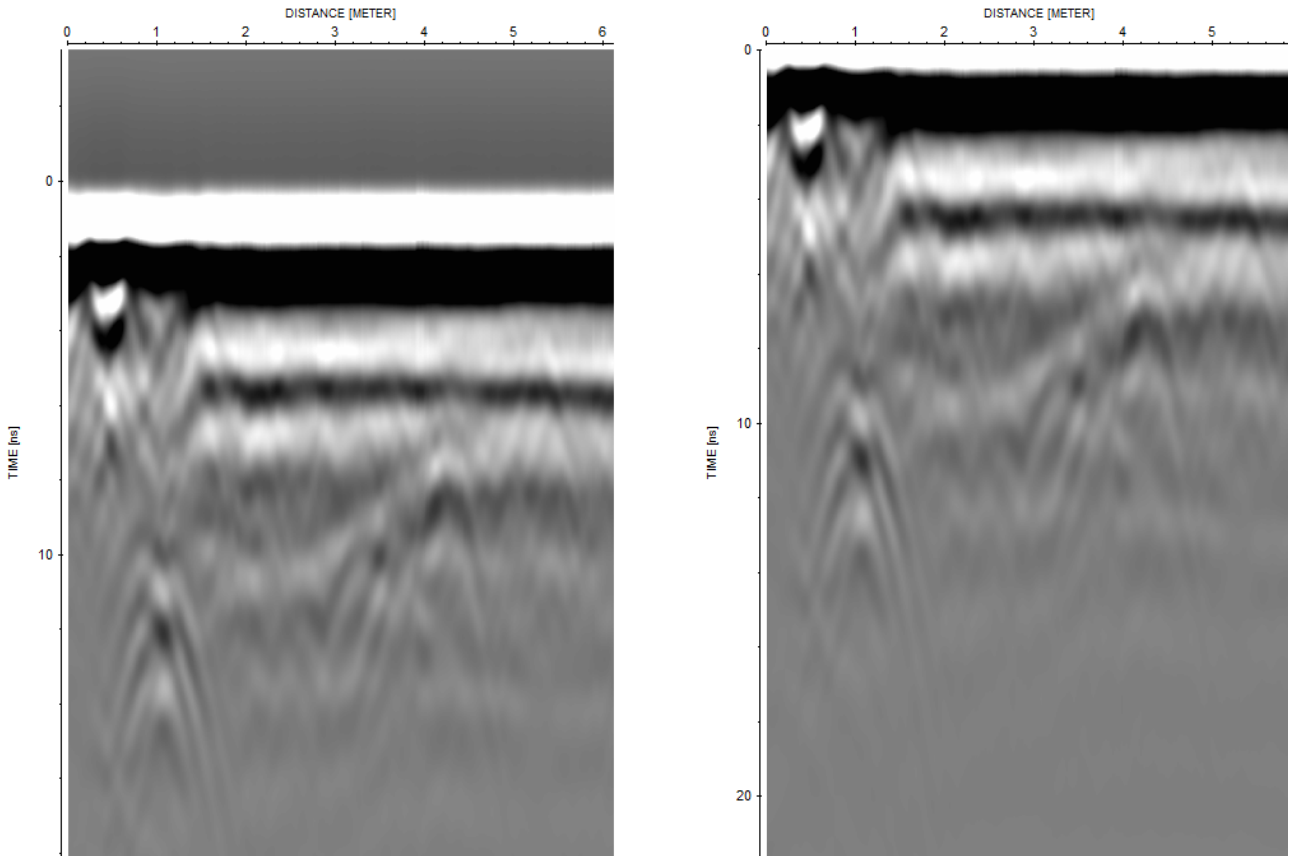

Figure 2.15: *left*: B-scan before time zero referencing *right*: B-scan after time zero referencing.

Generally, this problem is resolved by cutting the air layer up to a specific first echo reference. Setting the appropriate position of this threshold along the A-scan has an impact on the accuracy of the results, depending on both the kind of antenna and the central frequency of study. According to [25], the most commonly used and recommended thresholds are: a) the first break-point, b) the first negative peak, c) the zero-amplitude point between the negative and positive peaks, d) the mid-amplitude point between the negative and positive peaks, and e) the first negative peak. However, with certain GPR equipment, on-site calibration of the time-zero is feasible, and the selection of any hyperbola reflection characteristics within the A-scans must take the time-zero reference point into consideration. This situation, however, is less sensitive at the detection stage. However, picking a correct travel time is indeed critical for depth conversion. Figures 2.14 and 2.15 demonstrate the impact of changing the time zero in relation to the first positive peak. Whereas, the A-scans and B-scans are shown in the respective figures.

Signal gain: Normally, signals detected at earlier times are significantly stronger than signals measured at later times in a raw GPR A-scan, as seen in Figure 2.16 (left).

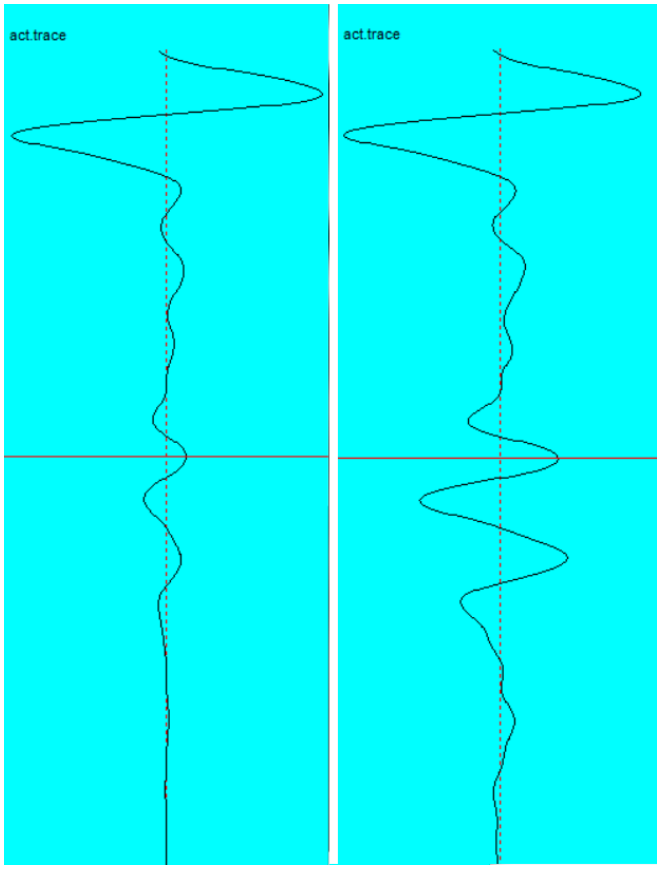

Figure 2.16: *left*: A-scan before gain, *right*: A-scan after gain.

This might be attributed to geometrical and frequency dependent material dispersion (depends on the permittivity and conductivity of the medium, and geometric spreading). The amplitude losses at a three-dimensional level are referred to as geometrical spreading, and it is considered independent of frequency. Higher frequency harmonics are attenuated more than lower frequency harmonics via frequency-dependent attenuation. The frequency-dependent attenuation of propagating EM waves is caused by the dispersive EM nature of materials in the subsurface. The rate of dispersion, on the other hand, is proportional to the electrical conductivity of the travelling medium [79]. As a result, all the aforementioned variables contribute to an EM signal's significant attenuation over time. As a result, distinguishing important features in the data at a later time may be difficult. Due to the weak signal intensity of the reflected echo down the time axis, such signal loss in 2D prospect causes the hyperbola traces to vanish. Signal gain is defined as a time-varying amplification of signal amplitudes in this context. Regardless of the specific process, it is utilised to recover a portion of the losses caused by attenuation (e.g., absorption and spherical divergence). To do so, multiply the raw A-scan data $A_{raw}(t)$ by a gain function g(t) for each discrete amplitude value of an A-scan as follows:

$$A^{'}(t) = g(t) \times A_{raw}(t) \tag{2.3}$$

where $A^{'}(t)$ is the data in the A-scan. As a result, it is equally applied to each A-scan via the B-scans. The gain function is almost always a positive function that grows in magnitude as time passes (negative gain also applied in certain cases). Then, raw data are subjected to a bigger gain at a later period. As can be seen, the gain function grows exponentially in value over time to accommodate for the exponential decline in return signal intensity. However, in some cases, negative gain is used to reduce the amplitude of the saturated signal in order to boost the contrast in other areas. Figures 2.16 and 2.17 show how an exponential gain boosts the amplitude of signal points in A-scan and, as a result, the visibility of the hyperbola signature in B-scan.

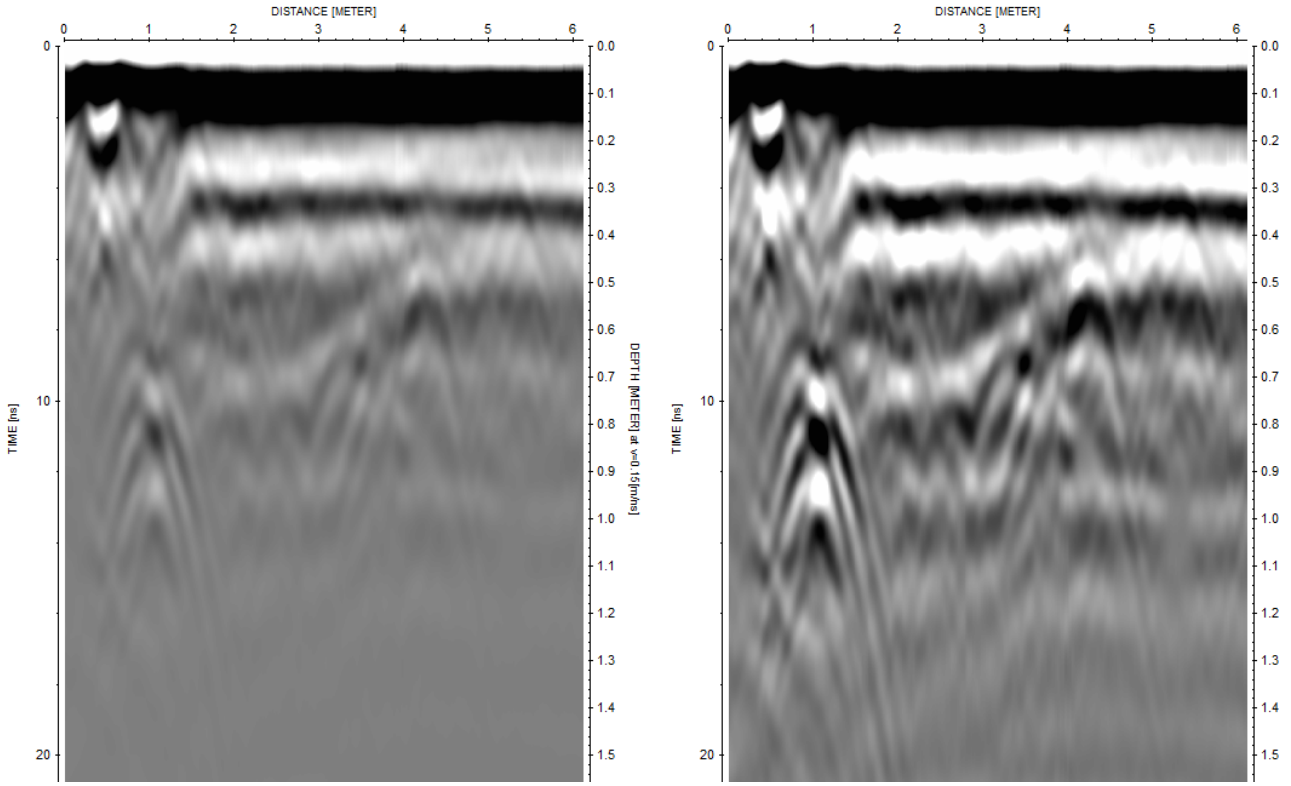

Figure 2.17: *left*: B-scan before gain *right*: B-scan after gain.

However, all aspects of late arrivals, including noise contributions, are enhanced in the positive gain process, and additional artefacts may be generated. Because, global signal-to-noise ratio (SNR) of a B-scan is modified depending on the Gain function. Consequently, the effect can be sometimes degraded the quality of signal. Hence, an optimised gain function is required for each data sets. In general, it's important to note that signal gain in pipe detection model is utilised for improving visual and interpretation of hyperbolas, because, the B-scan to be transformed to grayscale images prior to DCNN model input. Meanwhile, gain functions make significant changes to the recorded signal amplitude, which could result in data manipulation. Hence, such data can not be used for parameter inversion that involves amplitude.

Gain adoption is also heavily influenced by the GPR type, quality, and contrast of the acquisition data. For example, the GSSI SIR 3000 already has semi-processed file output, therefore extra gain treatment for hyperbola visualisation in post-processing may not be required, however the SIR 4000 just provides raw B-scan, which may require gain treatment. As a result, any described gain process in this chapter is limited to the detection process, after which the detected bounding box must be mapped on the raw B-scan to start a separate inversion process.

To summarize, in our study, the exponential gain was applied to the pre-processing step. In this case, single gain parameters were maintained across both the training and testing datasets.

Because large GPR data processing necessitates a single configuration in the automatic pipe detection models for full data sets. Meanwhile, time zero referencing was addressed, however it is not required for the proposed models because the models check for hyperbola and its properties in the B-scan. Furthermore, the deep learning models accept a specific picture size as input. As a result, the picture resizing procedure is divided into two parts. Firstly, B-scans must be scaled to meet the input size requirement. Secondly, the scaled B-scan was transformed to a greyscale image with the appropriate pixel size, as detailed in the next paragraphs.

B-scan resizing and image conversion: Only images with a fixed pixel dimension are accepted by the YOLOv4 model. For example, YOLOv4 algorithm accepts 600 x 600. As a result, the GPR B-scans should be resized and converted to greyscale 16-bit images that have been normalised to 256 values, where maximum positive amplitude is assigned 255 while minimum negative amplitude constitutes 0, and then shrunk using the bi-linear and anti-aliasing image resizing techniques. In fact, the Faster R-CNN can be very flexible to dynamic input sizes. Hence, the fixed image size is maintained throughout the study to retain similar dimension between Faster R-CNN and YOLOv4. Furthermore, in the size reduction process, the time samples dimension was shrunk considerably more than the horizontal dimension in order to preserve the distance resolution as close to the original B-scan as possible without losing any major information. Though the SNR is modified during the resize, the effect is negligible as long as the shape and visibility of the hyperbolas are conserved for the detection stage. Hence, the SNR effect was not carried out here.

The impact of resizing on an A-scan and a B-scan is seen in Figures 2.18, 2.19 and 2.20 respectively. The size of a B-scan was reduced from 600 A-scans (width) x 7200 time samples (height) to 600 x 600. Based on our observations in Figures 2.18, 2.19 and 2.20, the reflection wavelet form does not change after scaling down. In addition, some extent of floor noise is filtered by Bilinear resizing process. In theory, bilinear interpolation determines the inserted

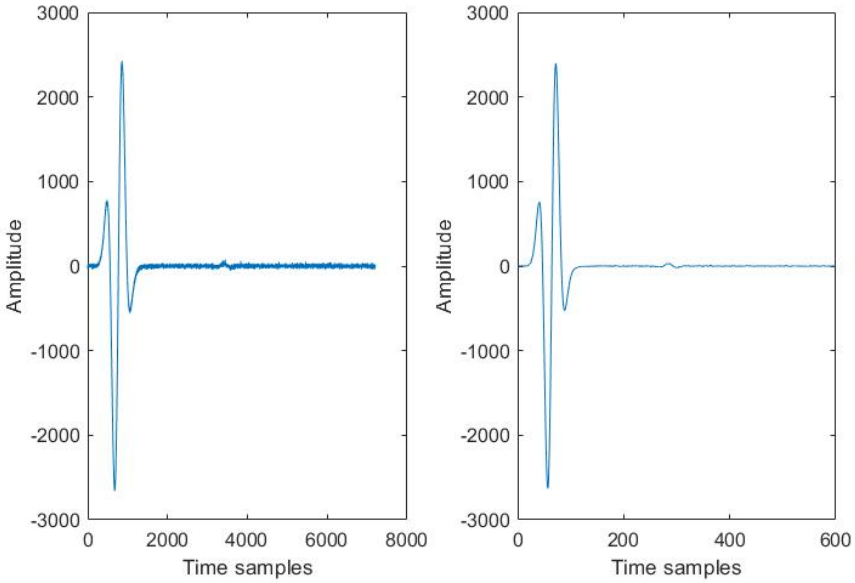

a) A-scan before resize

b) A-scan after resize

Figure 2.18: a) A-scan (1 x 2000) before bi-linear resize; b) A-scan (1 x 600) after bi-linear resize.

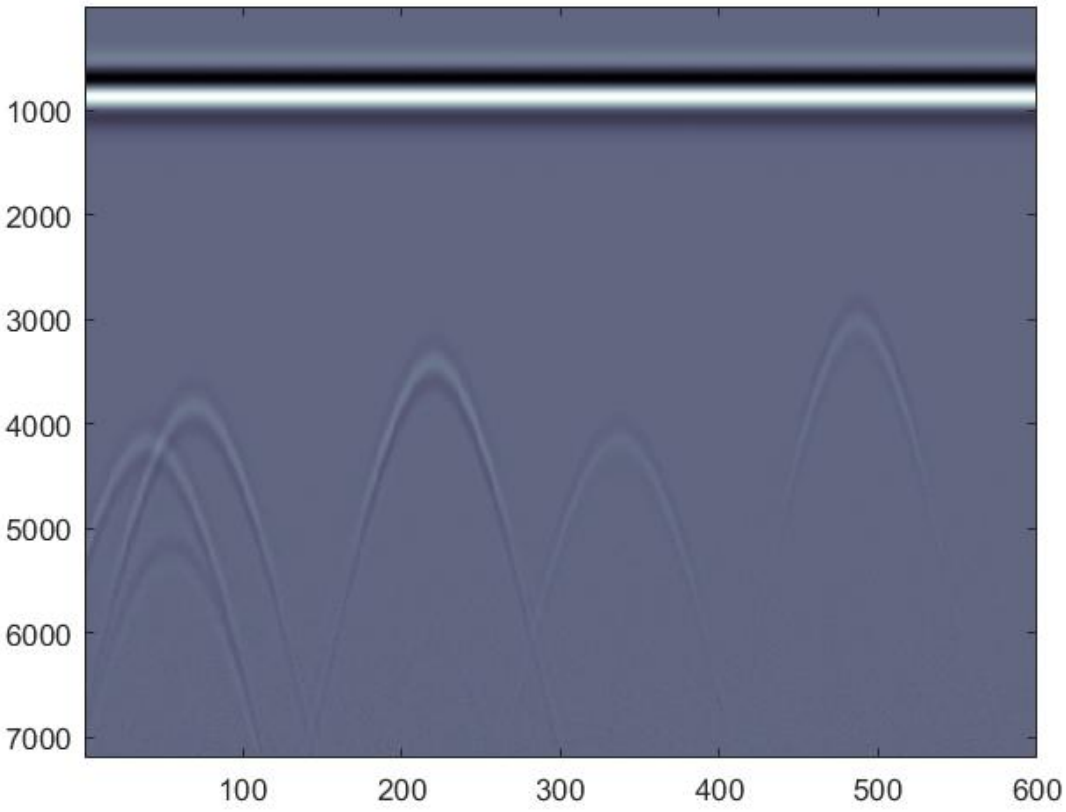

Figure 2.19: B-scan before bi-linear resize (7200 x 600).

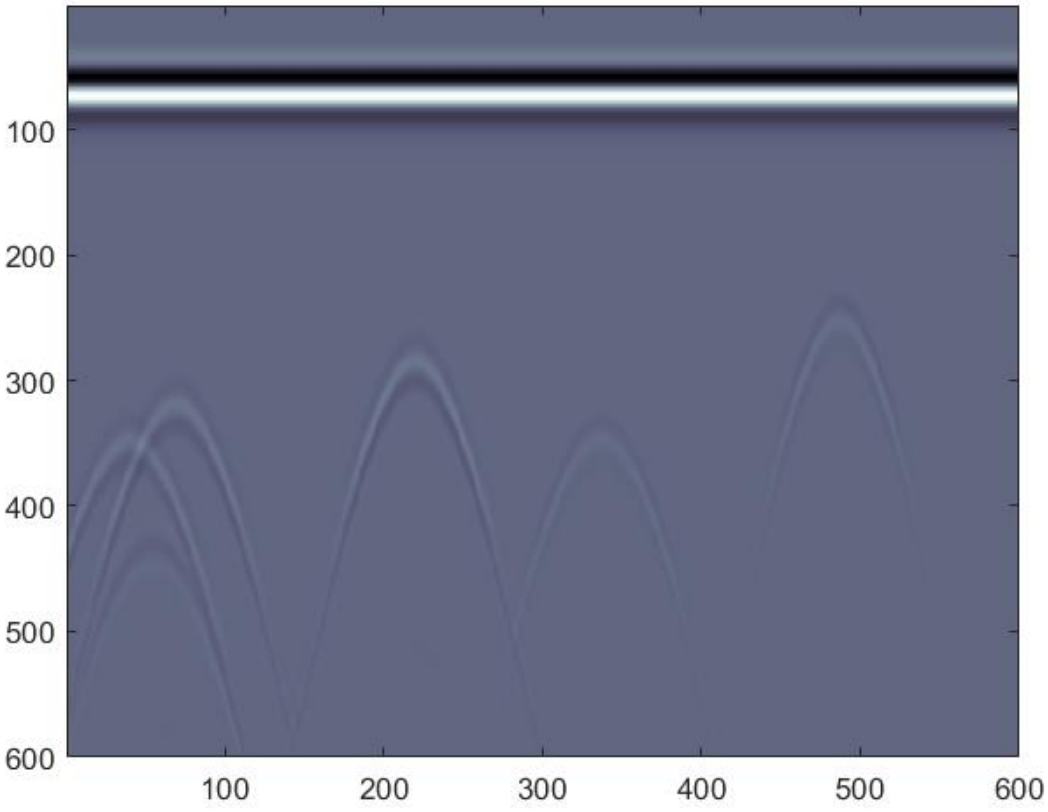

Figure 2.20: B-scan after bi-linear resize (600 x 600). x-axis resize factor kept at 1:1.

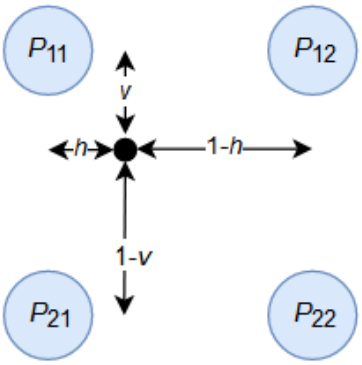

Figure 2.21: Intuition of bi-linear image interpolation.

pixel value by taking the weighted average of the four input pixels closest to the inserted place. Given that P11,P12,P21,P22 are the 4 neighbouring pixels of a 2 x 2 grid, horizontal and vertical scales are computed independently and represented by h and v. As a result, the value for each output pixel determined by [80],

$$P = (P_{11}h + P_{12}(1-h))\,v + (P_{21}h + P_{22}(1-h))\,(1-v) \tag{2.4}$$

The number of A-scans in the B-scan is also the horizontal dimension of the original B-scan. In comparison with the high dimension (time samples), down sampling the horizontal dimension is particularly susceptible to hyperbola information. Hence, the resized B-scan's horizontal dimension was kept near to that of the original B-scan. As a result of the scaling technique, the hyperbola shapes were retained. In order to remap the bounding box coordinates to the original B-scan, the scale ratio is painstakingly recorded.

2.2.3.c Performance matrices

The performance matrices discuss the adopted approach for measuring the performance of proposed DCNN object detection models. In object detection algorithms, the *precision* (Equation 2.5), *recall* (Equation 2.6), average Precision (AP) and mean average Precision (mAP) are the most frequent matrices that used to assess the accuracy of detections [15,16,81]. Hence, similar terms were adopted in this thesis.

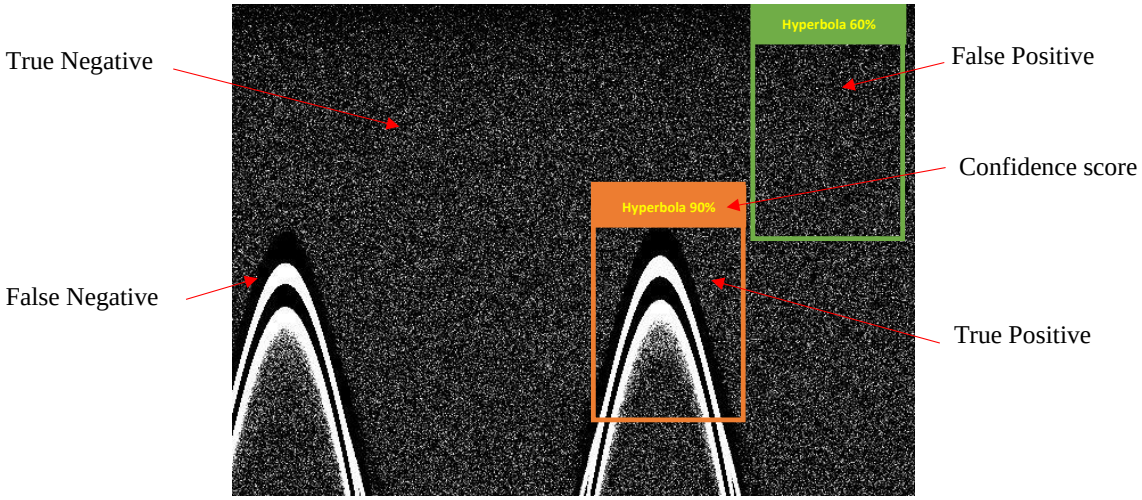

Figure 2.22: Detection model's basic performance indicators.

The basics of independent variable relevant to the above assigned terms are listed below and illustrated in the Figure 2.22. In terms of utility detection, which may be interpreted based on the term pipe existence in order to quantify the performance indicators.

- True positive (TP): A correct detection of ground truth (Pipe detected as a pipe)
- False positive (FP): An incorrect detection of a non-existent object (Pipe detected as a Non-pipe)
- False negative (FN): An undetected ground-truth (Non-pipe detected as a pipe)
- True Negative (TN): A correct detection of non targets (Non-pipe detected as a Non-pipe)

Because there are an infinite number of areas inside any given B-scan that are not target (non-hyperbola), a true negative (TN) result does not apply and is not accounted for in performance analysis in the context of object detection (ex: background) [82]. As a result, TN is the theoretical equivalent of infinity. Hence, all signs that include TN are avoided. The evaluation of object detection algorithms, on the other hand, is mostly dependent on the *precision* and *recall* notions, which are described in equations 2.5 and 2.6 below:

$$Precision = \frac{\mathrm{TP}}{\mathrm{TP} + \mathrm{FP}} \tag{2.5}$$

$$Recall = \frac{\mathrm{TP}}{\mathrm{TP} + \mathrm{FN}} \tag{2.6}$$

By definition, Precision refers to a model's ability to detect only relevant objects. It's the percentage of positive predictions that are right. The capacity of a model to discover all relevant cases (all ground-truth bounding boxes) is referred to as 'Recall'. It's the proportion of positive predictions that are correct out of all the available ground truths.

As a result, more Precision equals less false positives (FP), which means fewer non-pipes are recognized as genuine pipes. In the meanwhile, the strong Recall means that fewer pipes are misinterpreted as non-pipes (model failed to detect). Hence, in terms of the utility detection's safety prospects, the model favoured a greater Recall over a higher Precision.

Based on the intersection over union (IOU) and confidence score [35], the above listed definitions imply determining what qualifies a "right detection" and an "incorrect detection". Confidence score is the likelihood that an anchor box includes an object in the object detection scope. A classifier is generally used to predict it. The IOU is calculated by dividing the overlapping area between the predicted bounding box B_p and the ground-truth bounding box B_{gt} by the area of union between both.Where,

$$\mathrm{IOU} = \frac{\mathrm{Area}\,(B_p \cap B_{gt})}{\mathrm{Area}\,(B_p \cup B_{gt})}, \tag{2.7}$$

We can categorize a detection as "right detection" and an "incorrect detection" by comparing the IOU with a specified confidence score threshold t. If IOU $>$ t, the detection is thought to be correct. If IOU $<$ t is present, the detection is deemed erroneous. Similarly, various pairs of Precision and Recall may be obtained for the entire test data sets by setting the confidence score threshold (t) at different values. Precision-Recall curves can be plotted with Recall on the x-axis and Precision on the y-axis to show the relationship between the two measures. As a result, the area under the Precision-Recall curve may be described as AP (average Precision):

$$\mathrm{AP} = \int_0^1 p(r)dr \tag{2.8}$$

where r is the Recall values and p is the Precision value in the function of r since the p varies with r according to AUC (Area Under the Curve).

The value of AP ranges from 0 to 1. The model with the greatest AP is the most stable. The average of APs from multiple classes is called mAP. The mAP is the same as the AP in single class object detection, such as hyperbola detection. However, in the proposed models, target models are not exactly a single hyperbola. In the other hand, the target ground truth varies based on the Annotation approaches explained in the section above. In summary, the model's performance is evaluated based on Precision, Recall and AP.

In brief, the proposed Faster R-CNN and YOLOv4 based automatic pipe identification model were numerically verified first, followed by experimental validation, taking into consideration all recommended techniques, signal pre-processing, and performance matrices.

2.3 Numerical validation of automatic pipe detection

The objective of the numerical study is to validate the proposed Faster R-CNN and YOLOv4 based hyperbola detection models on synthetic GPR data. The Faster R-CNN and YOLOv4 models requires tens of training B-scans to build the model. Whereas, each B-scan must be created with different configurations with multiple hyperbolas in a single B-scan and closer to realistic situation. Hence, the numerical modelling is a viable tool to control the ground truth and perform parametric studies, in order to observe the performance behaviours of the model in different subsurface and pipe configurations. In contrast, experimental data are less useful for parametric studies due to their limitation on configuration control in terms of subsurface characteristics such as permittivity of the stratified medium (ε_r), pipe type, depth (d) and radius (r), the space between two pipes etc. In terms of GPR, the model's behaviour also needs to be analysed in terms of bandwidth (BW) and noise level. In order to facilitate such detail parametric studies, numerical validation was chosen as the first step before concluding the appropriate DCNN model and optimal GPR configuration for automatic hyperbola detection for field validation.

In order to validate the proposed hyperbola detection approaches, simple homogeneous dispersive 2D gprMax models were used [83]. gprMax is an open source simulation software developed in Python environment for forward modelling of GPR [83]. The detail introduction was given in the Chapter 1.

The numerical study's main scope is listed below and presented in Figure 2.23 accordingly. Further, the study extended to various parametric studies to draw a conclusion, which were described later in the section:

- Measure and analyse the performance of Faster R-CNN based automatic hyperbola detection models in terms of detection accuracy on 2 different annotation approaches and 3 different ConvNet architectures.
- Measure and analyse the performance of YOLOv4 based automatic hyperbola detection models in terms of detection accuracy on 2 different annotation approaches.

2.3.1 Numeric database generation: modelling using gprMax

The numerical study for the validation of proposed automatic pipe detection models is based on synthetic GPR B-scans generated using gprMax, which is an open source tool used to simulate the electromagnetic wave propagation within a material (and multiple materials as

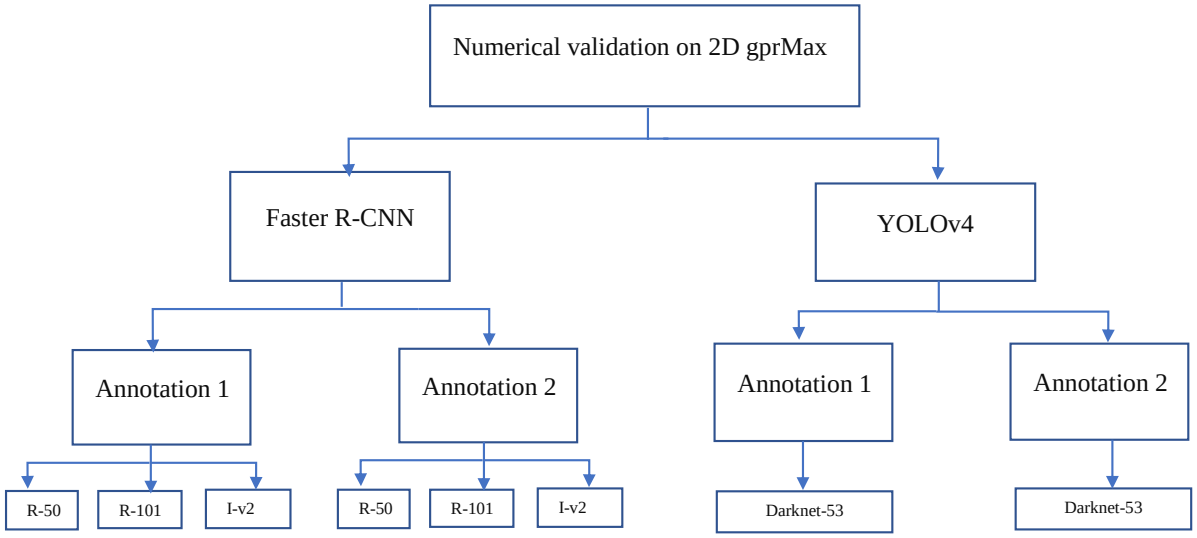

Figure 2.23: Numerical study plan for detection model validation. Whereas R-50, R-100 and Iv2 denotes ResNet-50, ResNet-101, and Inception - v2 convolution networks respectively.

well). To Recall a brief introduction and gprMax here, with the help of Maxwell's equations projected in 2D using the Finite-Difference Time-Domain (FDTD) method [84, 85], gprMax is capable of creating various subsurface models for different radar configurations operating at different bandwidth. It was developed in 1995 [86, 87], and the last upgrade was openly distributed by Giannopoulos and Giannakis [83] in 2015. It uses both Python and Cython for background programming whereas the user interface is a high-level programming unique to gprMax. Extensive user manuals on gprMax are available in [83, 88–90].

With regard to the data sets created in this study, the comparable generated data-sets were utilised in all model configurations listed in Figure 2.23 to preserve data and configuration similarity for the model's performance comparison. As a result, the gprMax model configuration is given in Table 2.3.

With the given GPR configuration, 175 random B-scans were generated. An example of the designed geometrical is presented in the Figure 2.24. In addition, similar number of B-scans also generated at 900 MHz for a model performance comparative study. In this case, the gprMax model configuration was similar except the centre frequency.

Configuration	Values
Pulse type and centre frequency (f_c)	Ricker pulse, 400MHz
Antenna off-set, type	Zero-offset, hertzian dipole
Antenna coupling	0.5 cm height
Medium's relative permittivity (ε_r)	6 to 9
Medium's conductivity (σ)	1×10^{-5} S/m
Acquisition step size (Δx)	2 cm
PML boundary	10 discrete boxes + 10 cm clearance
Pipe's depth (d)	0.5 m to 1.2 m
Pipe's radius (r)	10 mm to 75 mm
Pipe's type	metal, PVC + air, PVC + water
Time window (T)	35 ns
Number or Pipe's per B-scan	1-6
Number of A-scans per B-scan	600 (12 m)
B-scans dimension	$600 * 7200$ (A-scans x time samples)
Number of B-scans	272

Table 2.3: gprMax model configuration.

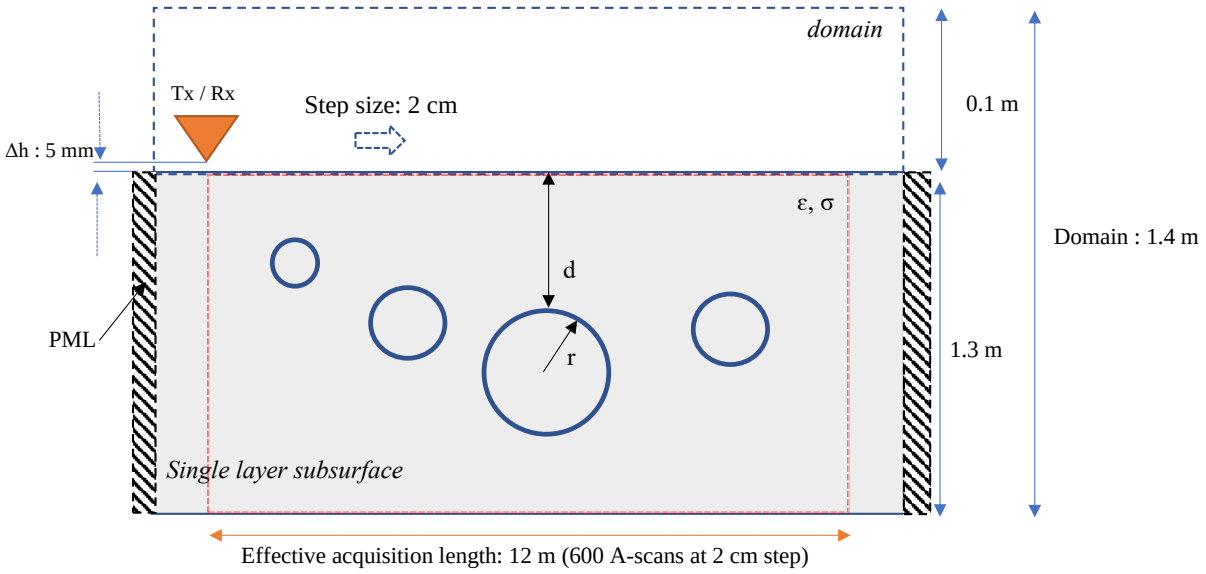

Figure 2.24: gprMax geometrical model configuration used for the simulation with an example of 4 embedded pipes.

According to the Figure 2.24, in this simulation work, the domain size was defined as 12.2 m × 1.4 m in order to allow multiple hyperbolas in single B-scan, and to insert minimum 600 A-scans per B-scan to retain the required input image dimension for YOLOv4. Likewise, totally 272 B-scans were generated to be sufficient for the proposed detection models. Hence, A-scan the time window was defined to 35 ns to cover the entire depth of the subsurface at permittivity of 9.

400 MHz was chosen as the central frequency. Because of its capacity to penetrate further into dispersive, noisy subsurface, the frequency range is employed in commercial GPRs for

applications such as utility detection. The commercial GSSI system, for example, has the Model 50400S, which is a 400 MHz [91] antenna. This antenna can operate with the commercial GSSI GPR systems such as SIR-30, SIR-3000 and SIR-4000. It can penetrate up to a depth of 5 m at relative permittivity of 9. As a result, the frequency is highly suited for utility detection.

Then, to keep the model as general as possible, a zero-offset hertzian dipole was chosen as the antenna type. This assured that the hyperbola shape creation was not biased by the antenna type and offset at this stage. Due to the antenna's gain, the position and strength of the reflected echo may vary. It's not a significant factor at this point in the detection process (without parameter inversion). And rather than examining the influence of antenna design differences, the study's goal is to evaluate the performance of deep learning models. Antenna offset analysis is required only when the training and test models are from different GPR types. Furthermore, the gprMax tool lacks a validated custom antenna modelling at a chosen centre frequency (400 MHz).As a result, the model's parameters were adjusted to zero-offset hertzian dipole; ground coupled for greater penetration and in line with commercial GPRs; and ricker pulse, which is also often used in commercial GPRs.

The relative permittivity was set between 6 and 9 to correspond to the average subsurface state of the pavement. In addition, the σ of 1×10^{-5} S/m implies that the medium is dispersiveness. To rule out any bias caused by high conductivity dispersion effects, low conductivity was chosen. Gain adjustment, on the other hand, can compensate for attenuation caused by larger dispersion.

To construct hyperbola, the acquisition step size is 2 cm to allow for sufficient lateral resolution. Because of this, 600 acquisitions may produce the requisite picture width of 600 pixels (one pixel width per acquisition) for the YOLOv4 input. As a result, the overall acquisition length is 12 m. On the other hand, a 5 cm step is adequate. However, it raises the needed acquisition length (B-scan width) from 12 m to 30 m for 600 A-scans per B-scan. Owing to this, the computational cost has skyrocketed. Furthermore, impulse GPRs may acquire data with high resolution, such as 5 mm-5 cm step sizes. Hence, 2 cm is considered a suitable value.

The domain mesh (cell) sizes are $\Delta x = 2 \times 10^{-3}$ m, $\Delta y = 2 \times 10^{-3}$ m, respectively. Though a smaller cell size would be preferable, the number was chosen to decrease simulation time while preserving sufficient resolution to show hyperbola without losing data. The FDTD method, on the other hand, discretizes both the space and time domains in order to solve Maxwell's equations numerically. As a result, the spatial discretisation plays a critical part in the modelling method's performance.

The three axes of the 2D gprMax model are discretized as Δx (spatial discretisation), Δy (temporal discretisation) and Δz (lateral discretisation). Despite the fact that the model is 2D, gprMax requires a minimum value for Δz in its modelling procedure. The discretisation size (mesh size) in the time axis may be defined as follows in order to notice a satisfactory resolution of the time domain GPR signal:

$$\Delta y = \frac{\lambda}{10} \tag{2.9}$$

Whereas, λ is the wavelength of the highest frequency component of the pulse.

The subsurface model created using gprMax consists of: single layer with assumption that an infinite multi layer can be approximated to a single layer with average dielectric characteristics as shown in Figure. 2.24. Let λ_1, and λ_2 be respectively the wavelength of the impulse within the layer of permittivity respectively ε_{min} and ε_{max}. Then, from Equation 2.9, the optimal temporal discretisation can be obtained from the condition defined in [88]:

$$\Delta y = \min \left\{ \frac{\lambda_1}{10}, \frac{\lambda_2}{10} \right\} \tag{2.10}$$

In order to maintain regularity, we use $\Delta x = \Delta y = \Delta z$ and the selected value must satisfy this condition such as below these values. Hence, the smaller the value is, the higher the resolution.

$$\lambda = \frac{c}{f_{max}\sqrt{\varepsilon}} \tag{2.11}$$

Based on [92], the maximum frequency components of the ricker pulse spectrum may be calculated as roughly (f_c * 2.5) = ($f_{\max}$) = 1000 MHz for the specified centre frequency (fc) of 400 MHz. The wavelength (λ) at relative permittivity (εr) ranges 6 and 9 must be 12.5 cm and 10 cm, respectively, based on the Equation 2.11 derived from [93]. As a result of Equation 2.10, the selected $\Delta x = \Delta y = \Delta z$ must be smaller than $\frac{\lambda}{10}$, which is 1 cm in this case. The condition is satisfied since the chosen values are 2 mm. Furthermore, until the centre frequency value of 2 GHz, the stated mesh size would meet the criterion. As a result, the mesh size may be kept for a higher frequency comparison research later in this chapter. Furthermore, the mesh resolution error is expected to be no more than 2 mm in this case. Moreover, the number of cells in the domain affects the computing cost significantly. As a result, increasing the mesh size can significantly reduce simulation time. As a result, a proper mesh size, domain size, and simulation time balance is required. For example, on a 4 core processor PC, the simulation time for a single B-scan for the given configuration is 6 hours per B-scan. As a result, while choosing a mesh size, all considerations were taken into account.

In the meantime, the time window (T) of the A-scan was chosen to be 35 ns. The time sampling resolution is $\Delta t = 4.8611 \times 10^{-12}$ s which satisfies Courant, Freidrichs and Lewy condition [94]. According to Equation 2.12, the required time window ($T_{\max}$) to visualise the entire depth ($h_{\max}$) of 1.4 m at permittivity (ε) of 9 shall be, 28 ns. For a worse case scenario when the GPR is 1 m away from the pipe at 1.4 m depth, the travel path of the pulse is 1.7 m (diagonal distance). Thus, the required travel time window is 34 ns. Therefore, 35 ns is chosen to meet this constrains with a safety margin.

$$T_{\max} = \sqrt{\varepsilon}\frac{2h_{\max}}{c} \tag{2.12}$$

The geometrical model consists of one or more pipes with combination of pipe's materials such as metallic, PVC with air, PVC with water embedded within a single layer as described in Figures 2.24. Cylindrical pipe's positioning depth (d) varies between 50 cm to 120 cm randomly. The radius of the pipe on the other hand are between 1 cm, 7.5 cm with 3 different conductivity (σ) levels at 1×10^{-5} S/m, 1×10^{-3} S/m, 1×10^{-1} S/m. The spatial resolution between adjacent A-scans is 2 cm. Thus, a total of 272 unique B-scans were created, with each B-scan made up of 600 A-scans. Thus, the B-scan size made up of 600 x 7200 (A-scans x time samples). Furthermore, the simulation accounted PML (Perfectly Matched Layer) effects and default settings of 10 domain mesh boxes, and additional 10 cm clearance were maintained on both side of the geometry.

Creating a 2D gprMax model script The input script for the gprMax simulation should be written in a *.in text file, and it runs in a Python environment. The model was programmed in text editor using the gprMax manual's instructions, taking into consideration all the following design factors. The Listings contain an example of a model script. The compiled script is for a specific B-scan situation. Similarly, an automated python script was built to modify the input parameters at random based on the Table 2.3 parameters. As a result, all 272 B-scans were produced.

The origin of spatial coordinates is in the lower left corner, using a right-handed Cartesian coordinate system (0,0,0). To begin, the GPR domain is determined, as well as the total acquisition time ($T_{\max}$) and the domain discretisation ($\Delta x = \Delta y = \Delta z$) as seen in Listing 2.1.

```
#title: B scan of buried multi pipes in a dielectric half-space
#domain: 12.2 1.4 0.002
#dx_dy_dz: 0.002 0.002 0.002
#time_window: 3.5e-08
```

Listing 2.1: gprMax modeling: Specifying the domain parameters, mesh size and time window

The subsurface's material parameters, such as permittivity, conductivity, and permeability, are also determined, as well as its size. However, as shown in line 2 of Listing 2.2, the 3D coordinates of the subsurface are always specified as follows: the first three values represent the bottom left corner, while the next three coordinates indicate the top right corner of the single layer pavement. A unique name tag for each material is defined, for instance "half_space" and assigned to the created subsurface layer.

```
#material: 8.54 1e-05 1 0 half_space
#box: 0 0 0 12.2 1.3 0.002 half_space
```

Listing 2.2: gprMax modeling: Initializing material characteristics

Followed by that, all the pipes and its 3D centre coordinates of both side faces of the cylindrical pipe are defined with its corresponding radius and permittivity of the pipe material as presented in Listing 2.2. More detail explanation can be found in [88].

Then, as shown in Listing 2.3, all the pipes (4) and their 3D centre coordinates of both side faces of the cylindrical pipe are defined with their appropriate radius and permittivity of the pipe material. Inner and outer circle of the pipe's geometry is defined in separate lines as seen in Listing 2.3 In [88], more detailed explanation is provided by authors.

```
#material: 81.73 0.04 1 0 water
#cylinder: 8.97 0.70 0 8.97 0.70 0.002 0.085 pec
#material: 3.66 0 1 0 pvc1
#cylinder: 3.21 0.35 0 3.21 0.35 0.002 0.077 pvc1
#cylinder: 3.21 0.35 0 3.21015 0.35 0.002 0.072 pvc1
#material: 5.34 0 1 0 pvc2
#cylinder: 2.83 0.53 0 2.83 0.53 0.002 0.056 pvc2
#cylinder: 2.83 0.53 0 2.83 0.53 0.002 0.051 free_space
#material: 5.38 0 1 0 pvc3
#cylinder: 0.50 0.53 0 0.50 0.53 0.002 0.089 pvc3
#cylinder: 0.50 0.53 0 0.50 0.53 0.002 0.084 pec
```

Listing 2.3: gprMax modeling: Initializing material characteristics

The waveform, centre frequency, and a name tag for the pulse are next defined, as shown in Listing 2.4, followed by the antenna type and coordinates of the transmitter's antenna position. The receiver location is then specified in a separate line. Finally, in the last two lines, the displacement step size for both Tx and Rx is defined.

```
#waveform: ricker 1 400000000.0 my_ricker
#hertzian_dipole: z 0.1 1.305 0 my_ricker
#rx: 0.1 1.305 0
#src_steps: 0.02 0 0
#rx_steps: 0.02 0 0
```

Listing 2.4: gprMax modeling: Initializing material characteristics

2.3.2 Data pre-processing

The suggested Faster R-CNN and YOLOv4 models need the pre-processing of output B-scans prior to the input. In this context, 272 B-scans were obtained using the settings and technique described above. For the simulation, numerous computers and high-performance computing clusters were used. The gprMax, as shown in the Figure 2.25, produces impulse responses for both electrical (E) and magnetic (H) fields in all three polarisations (x,y,z). Perhaps it is observed that the reflection is particularly strong in the direction of Ez. Because, the polarisation component is perpendicular to the axis of displacement and parallel to the pipe. As a result, the Ez signal has been chosen for further processing. The reflections are not apparent at this level due to attenuation and the dominance of the tx/rx direct coupling effects. After gprMax output data conversion to Matlab, the signal was pre-processed. White gaussian noise was introduced in the pre-processing processes to bring the B-scans closer to realistic. Following that, Gain for gray scale or binarisation is done to improve hyperbola readability, followed by resizing B-scans to 600 x 600 dimensions. Whereas, the image binarisation is an alternative to Gain and explained below in this subsection. Finally, the B-scans were converted to “jpg" format. Furthermore, the images were divided into two groups, with training and validation images saved in one group and test images saved in the other. Finally, the training and validation sets were independently annotated using the suggested annotation approaches and used for model learning. Meanwhile, test data were saved for model testing. The sequence is illustrated in the Figure 2.26. The result of the data pre-processing phase is introduced into Faster R-CNN or YOLOv4 models, as shown in the figure. In addition, feature extraction and detection are included into the Faster R-CNN / YOLOv4 architecture.

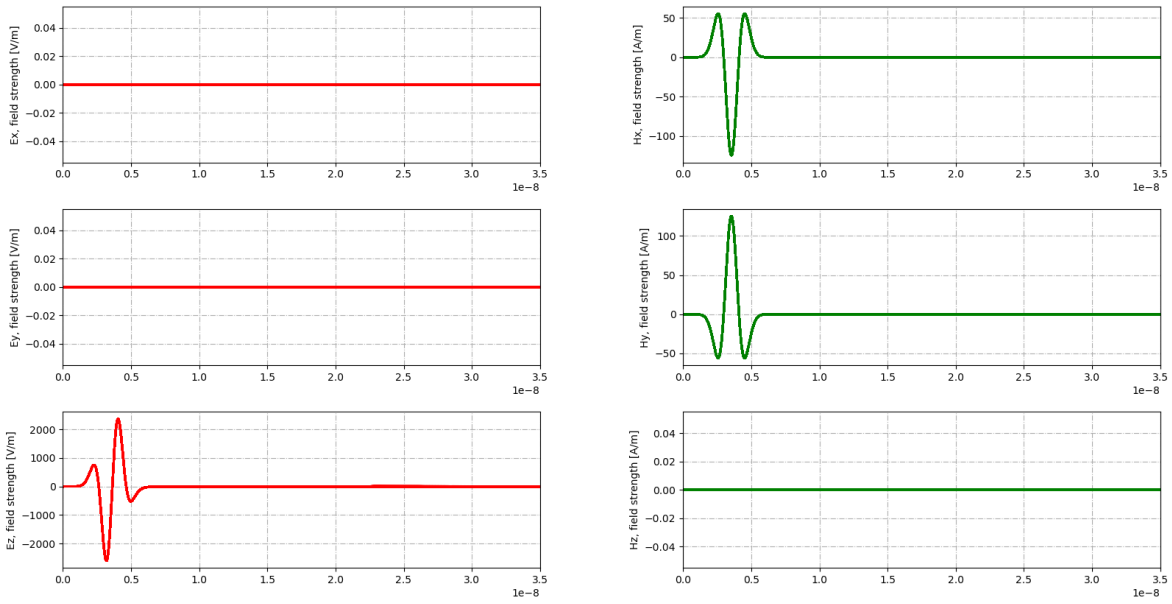

Figure 2.25: Example of A-scan output plot of gprMax. $left$: electrical response; $right$ figures indicate magnetic response.

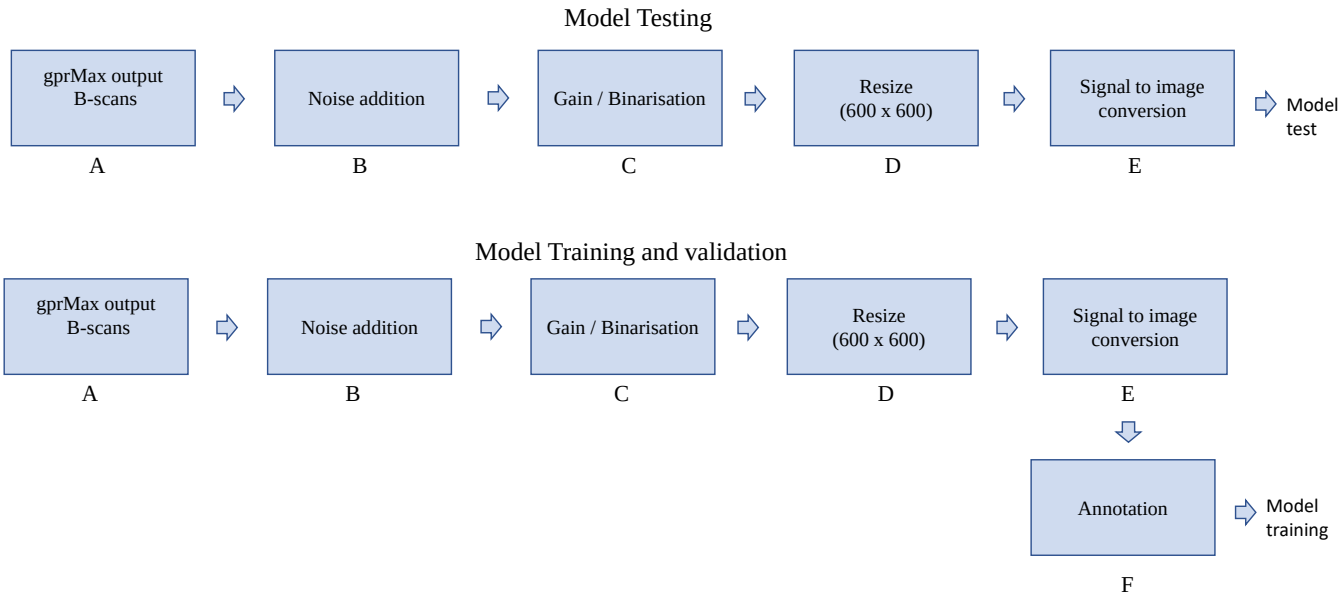

Figure 2.26: Data pre-processing flow.

Gain process: An example of a B-scan is presented in Figures 2.27, as seen in the gprMax output. The hyperbolas are not apparent due to distortion of signal with the depth and the prominence of the Tx/Rx direct coupling effects. As a result of the exponential gain enhancement and gray scale conversion, the hyperbola was improved, bringing B-scan closer to reality as seen in 2.28.

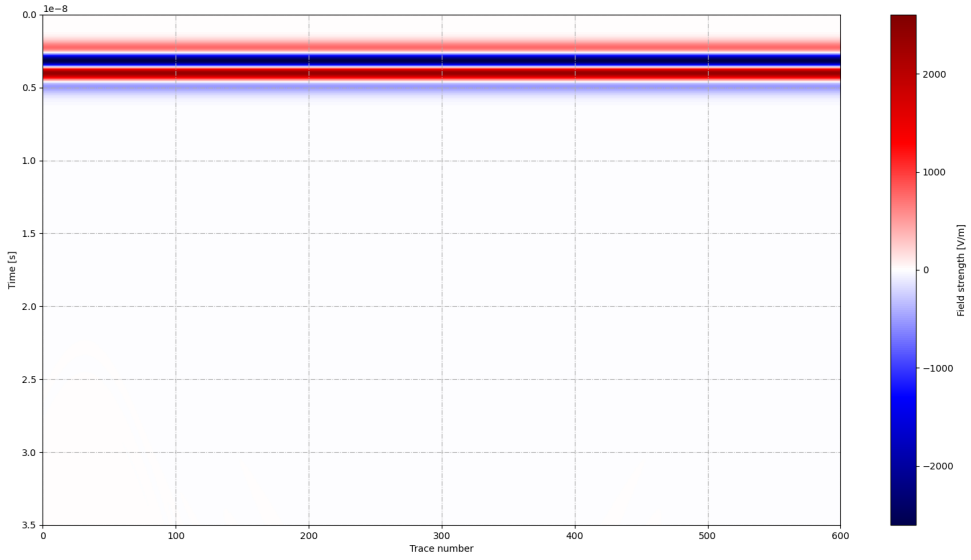

Figure 2.27: Example of a B-scan output plot of gprMax for E_z component, plotted in gprMax Python library.

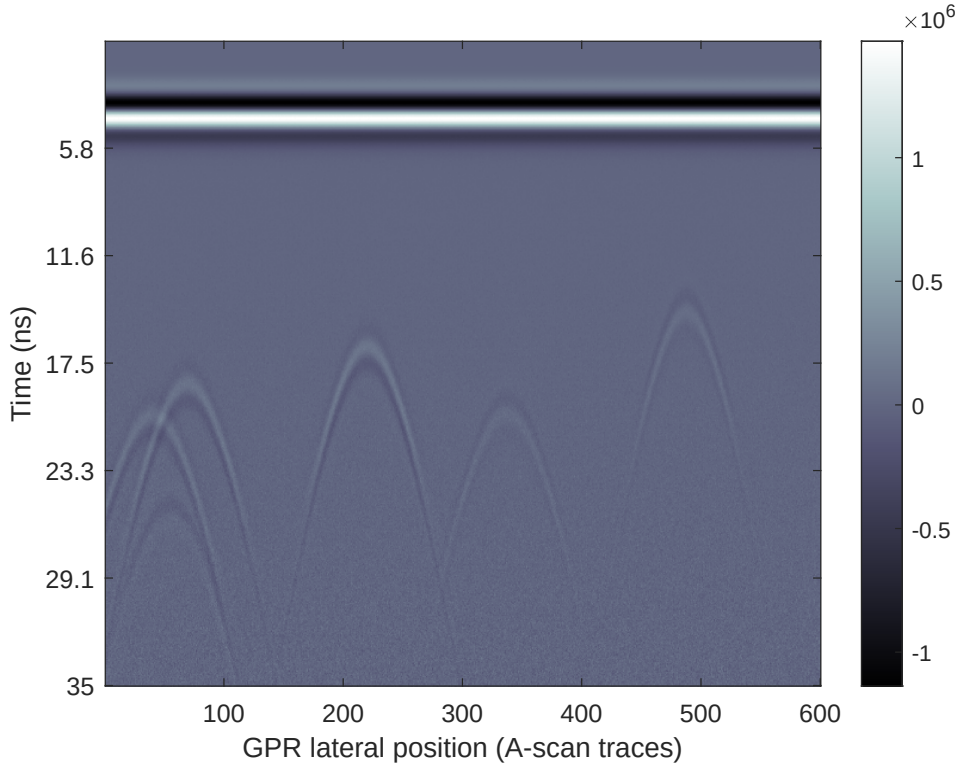

Figure 2.28: Example of a B-scan after exponential gain and greyscale plot, plotted in Matlab.

Noise addition: Furthermore, because the gprMax does not contain noise a random controlled noise variation models within the B-scan, an extra white gaussian noise is inserted to produce a more realistic B-scan in order to assess the efficacy of the detection algorithms in a realistic noisy environment. Hence, in order to add white gaussian noise to noiseless B-scans at certain signal-to-noise ratio (SNR) levels, the conventional additive noise model is assumed, as formulated by Equation 2.13 on each B-scan. The noise is usually a White Gaussian Noise (WGN) with zero mean $\mu = 0$ and standard deviation $\sigma = \sigma_N$.

Hence, the SNR is defined in the time domain with respect to the signal-to-noise ratio between the positive peak according to :

$$SNR_{dB} = 20 * log_{10} \frac{M}{\sigma_N} \tag{2.13}$$

where,

- M is the maximum magnitude of the first echo of the entire B-scan,
- σ_N is the standard deviation of the noise added.

Owing to this definition, a weaker SNR is likely observed over the depth. Inversely, for a selected SNR, the standard deviation of the noise to add to the noiseless simulated data is given by:

$$\sigma_N = M \times 10^{-\frac{SNR}{20}} \tag{2.14}$$

The SNR levels of 15 dB, 30 dB and 50 dB were applied to examine the noise impact followed by a resizing process using bilinear interpolation (discussed earlier in the chapter) and as shown in the Figures 2.29(a). Because of the direct coupling effect, the contrast between

the hyperbola and the noise is quite low. However, after removing the direct coupling echo, the noise level at the high depth is highly dominant in comparison with the signal level, as shown in Figures 2.30(a). When the gain is applied, both the signal and the noise are enhanced at the same time. As a result, 30 dB was picked for further investigation at this time due to limited computing resources and time constrains. However, The model's performance against each noise level was examined for one specific circumstance later in this chapter. Furthermore, at this step, the mid-level noise is chosen to eliminate any performance bias induced by noise severity. Since the focus is limited to deep learning model performance, once a suggested model scenario is chosen, noise variation will be studied as part of the model's robustness parametric research in the future.

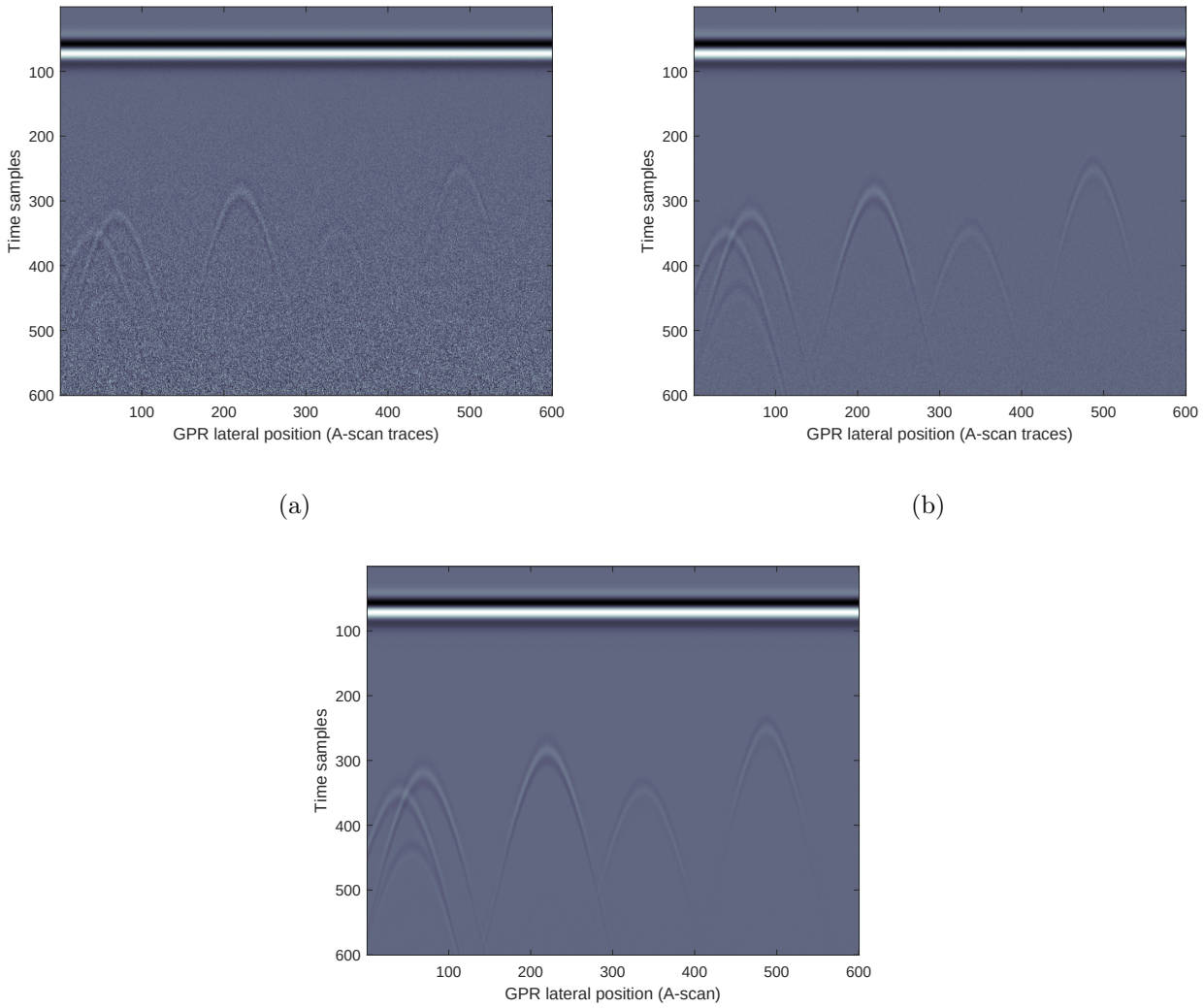

Figure 2.29: B-scans with Added White Gaussian Noise (AWGN) at SNR levels of (a) 15 dB, (b) 30 dB and (c) 50 dB.

In this regard, in the numerical study data pre-processing (as shown in Figure 2.13), the output of gprMax was introduced with white gaussian noise to apply extra noise to the B-scans inorder to make the simulated B-scan more realistic. The B-scan was then processed with gain or binarisation (both are alternative approaches). The binarisation, on the other hand, is detailed further down. Separate models were created using both methodologies to examine the differences in model performance (Faster R-CNN and YOLOv4).

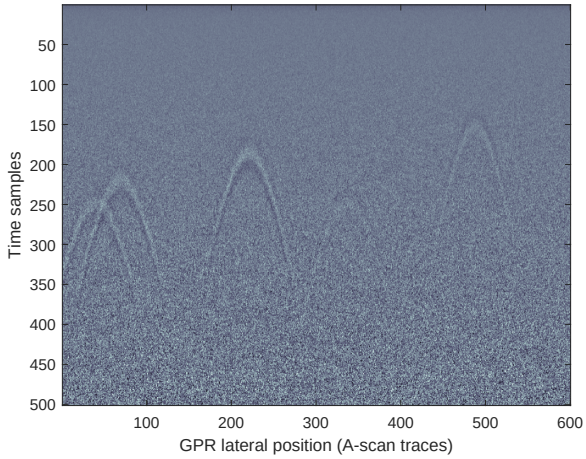

(a)

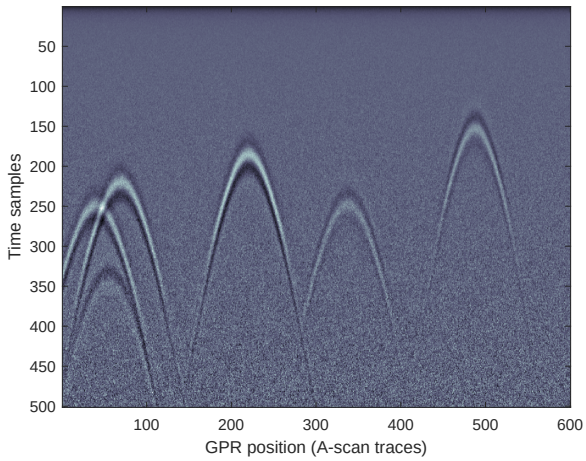

(b)

Figure 2.30: B-scans with AWGN at SNR levels of (a) 15 dB and (b) 30 dB without direct coupling echo.

Image binarisation: The resized picture may be directly utilised as input for the Faster R-CNN and YOLOv4 models. Binarisation, on the other hand, is utilised to bypass the difficult gain procedure. As mentioned in the preceding sections, gain settings are extremely specific to a certain location, data quality, GPR type, subsurface condition, and so on. As a result, for large GPR data processing, single global settings are chosen to minimize time without sacrificing hyperbola visibility within the data. Hence, binarisation is a promising strategy for improving hyperbola readability right from the raw B-scan without having to go through the gain process, allowing it to be utilised as a single setting for a huge data set. Thus, Binarisation can bypass the gain step in a noise-free B-scan, which improves the edge of the hyperbola. As a result, the numerical investigation was continued using a binarisation-based technique due to the nature of the new approach. The flow chart 2.31 shows the differences between two pre-processing procedures for enhancing hyperbola visibility: with and without gain, respectively. In the Figures 2.32, the processed output is compared. Binarisation also improves hyperbola readability without adding processing gain, as seen in the figures. So, a single setup for a large data processing is made easier. However, the limitation depends on the noise complexity of the raw B-scan.

Note: The produced B-scans were subjected to the aforementioned pre-processing procedures, and the resulting resized B-scans were transformed to 600 x 600 pixels jpg image format, after which the data set was utilised for annotation, learning, and testing of both Faster R-CNN and YOLOv4. As a result, the next subsections compare and contrast the model implementations of Faster R-CNN and YOLOv4 utilizing the identical pre-processed image sets.

2.3.3 Faster R-CNN model validation

This subsection presents the numerical validation of the proposed Faster R-CNN based automatic pipe detection models, using the above-mentioned B-scan images. Faster R-CNN models were trained, validated, and tested using two different annotation scenarios as stated in section 2.2.3.a, utilizing the above-mentioned B-scan images. The performance of the Faster R-CNN models generated from each annotation scenario was evaluated using three alternative convolution architectures, including ResNet-50, ResNet-101, and Inception-V2, as shown in Figure 2.12. Hence, 175 B-scans were divided into 50, 25 and 100 for the training, validation

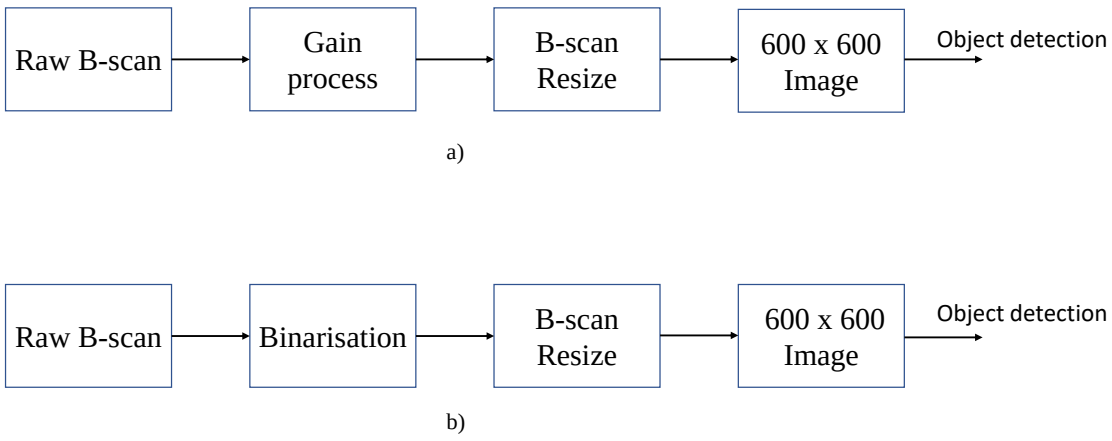

Figure 2.31: (a): Hyperbola enhancement with Gain, (b): Hyperbola enhancement with binarisation without gain.

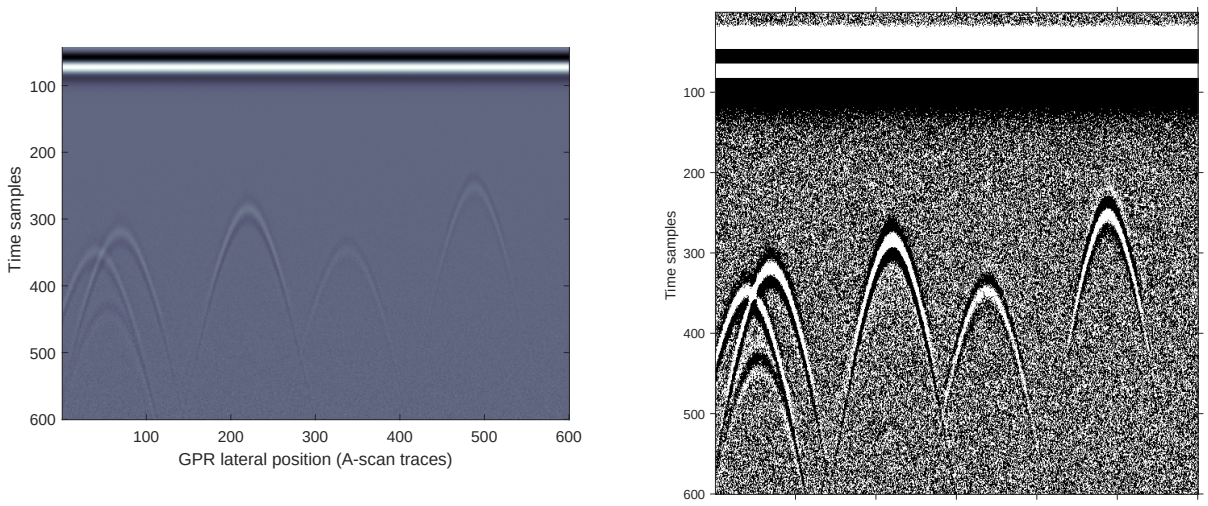

(a) (b)

Figure 2.32: B-scans at SNR = 30 dB, (a) with gain and binarisation (b) without gain and binarisation.

and testing respectively. However, the diagram in Figure 2.23 that discussed earlier, show the combination of Faster R-CNN models based on binary or greyscale inputs. For each input type, there are six separate models studied as stated in the Figure 2.23

Note: The study concentrated on two primary hypotheses: first, the pipe detection model is meant for large-scale GPR acquisition, and second, the pipe detection focused on network safety (single pipe detection in overlapping pipe atmosphere is sufficient to draw the no-dig zone boundary).

2.3.3.a Model training

For training, validation, and testing, the database was separated into 50, 25 and 100 groups, respectively. The training and validation sets were then labelled with an open source Python program called 'Lablimg'. The annotation was performed for both annotation scenarios (Annotation-1, Annotation-2) separately. The annotation is the process of labelling the ground truth that is drawn around the single / set of hyperbolas. As the results, the output of the annotation provides coordinates of the bounding box such as x, y, w and h which indicates the box's centre coordinates, its width and height as shown in Figure 2.33. The detail explanation of the coordinates and its relevance to the loss function is explained in the section 2.2.1.a. Further, the objective of two annotation approaches in this study are well explained in the section 2.2.3.a. Both annotation scenarios (Annotation-1, Annotation-2) were performed individually. The procedure of labelling the ground truth that is drawn around the single / set of hyperbolas is known as annotation. As a result, the annotation's output includes bounding box coordinates like x, y, w, and h, which indicate the box's centre coordinates, width, and height, as shown in Figure 2.33. Even though the binary images were presented in this subsection, the gray scale also have gone through similar procedures.

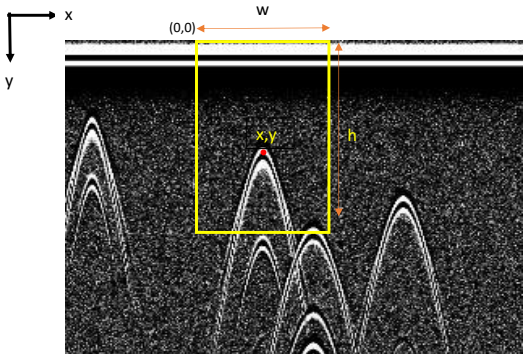

Figure 2.33: Example of a hyperbola with annotation scenario-2 on binary image.

In the section 2.2.1.a, we go through the coordinates in detail and how they relate to the loss function. In addition, the section 2.2.3.a clearly explains the goals of two annotation methodologies used in this work. The output of the annotation tool is illustrated in Table 2.2.3.a, where each hyperbola target is recorded with its input image filename, dimension of the image, class of the target named 'hyperbola' in this case, and four coordinates of the bounding box. Despite the fact that the tool's output coordinates deviate from the model's requirements, the script converts them to the model format.

Followed by the annotation, the annotated data sets of training and validation sets were separated for model training. The model was built with the support of 'tensorflow' which is an open source library for numerical computation and large-scale machine learning, and implemented using the 'Google Colab' to overcome heavy computational cost.

Filename	Width	Height	Class	Xmin	Ymin	Xmax	Ymax
$\text{Bscan}_1.00.jpg$	600	600	hyperbola	418	292	483	599
$\text{Bscan}_1.00.jpg$	600	600	hyperbola	485	292	571	594
$\text{Bscan}_10.00.jpg$	600	600	hyperbola	307	181	469	594
$\text{Bscan}_10.00.jpg$	600	600	hyperbola	471	182	600	600
$\text{Bscan}_11.00.jpg$	600	600	hyperbola	4	179	78	599
$\text{Bscan}_11.00.jpg$	600	600	hyperbola	79	178	159	600
$\text{Bscan}_11.00.jpg$	600	600	hyperbola	158	177	272	595
$\text{Bscan}_12.00.jpg$	600	600	hyperbola	1	230	100	600

Table 2.4: Example of annotation output file with bounding box coordinates as an example. Xmin, Ymin are the top left, and Xmax, Ymax are the bottom right of the bounding box, whereas the top left corner of the image is (0,0).

Model parameters : The model configuration parameters of the trained Faster R-CNN model are shown in Table 2.5. Scales, aspect ratios, k proposals, max pool kernels, and Non Max Suppression (NMS) threshold are therefore crucial factors that can have a significant impact on the model. All parameters, however, may be modified for a detailed parametric analysis to observe the behaviour with hyperbola detection. However, due to the computational expenses, model parameters are theoretically established with logical expectations based on the nature of GPR and utility applications. For example, training a single model on Google Colab takes at

least 6 hours. As a result, studying all parametric studies at this time and with the resources available is very improbable.

Model parameters	Values
RPN kernel Scales	$[0.25, 0.5, 1.0, 2.0]$
RPN kernel Aspect ratios	$[0.5, 1.0, 2.0]$
K proposals	$12 (= 4^*3)$
Height stride	16
Width stride	16
Nms IOU threshold	0.7
Maxpool kernel size:	2×2
Maxpool stride	2
Initial learning rate	0.0003
Step	900000
Momentum optimizer value	0.9
Optimizer	Momentum optimizer
Localisation loss weight	2.0
Objectness loss weight	1.0

Table 2.5: Faster R-CNN model parameters for the training.

The section 2.2.1.a elaborates K proposals (scales * aspect ratios) and their link between scales and aspect ratios. The kernel scales (0.25, 0.5, 1.0, 2.0) and aspect ratios (0.5, 1.0, 2.0) were chosen to improve the model's ability to predict on varied sizes of the hyperbola that differed from the training database. Scale size and aspect ratio higher than 2.0 are not useful, and they can lead to false alarms because, the hyperbola shape is seldom expanded by its width. As a result, larger K suggestions may potentially tolerate hyperbola shape change caused by permittivity, depth, horizontal step size variation, and varied temporal resolution. The higher number of K proposals, on the other hand, can significantly enhance the computation. As a result, the best value is determined at this point.

Similarly, stride settings determine how far the kernel window must jump at a time to reach the next place. As a result, we defined 16 for both width and height strides. For a B-scan with a step size of 1 cm, 16 is comparable to 16 cm in width and roughly 1 ns (6 cm) in depth resolution. It is critical to get the best deal possible, because extremely large stride values can overlook hyperbola between two places, whilst modest values can result in a huge number of overlapping 'false positives.' The numbers specified guarantee that at least one hyperbola is recognized between two adjacent lateral points. Height strides, on the other hand, has a resolution of roughly 6 cm. That's enough to split 6 cm dense pipes. However, because the detection's goal is to define the non-separable pipes as a single target, the stride values chosen are enough. However, if adequate computational resources are available, additional fine-tuning can be investigated in the future.

Finally, the model is trained in Google colab using 50 annotated training examples and 25 annotated validation samples. Similarly, 6 separate models were trained using the convolution network combination depicted in Figure 2.23.

Training loss and validation indicators: The learning loss has converged to a global minimum between 30,000 and 50,000 cycles. As a result, the learning rate has been restricted to a maximum of 60,000 to optimise the training time. The Figure 2.34 shows examples of how the total loss function converges. The loss iterations were supported by momentum optimizer

algorithm. Each model has taken around 6 hours for the learning. Also, the best model's Mean Squared Error (M.S.E) error was minimised to $1 * 10^{-4}$.

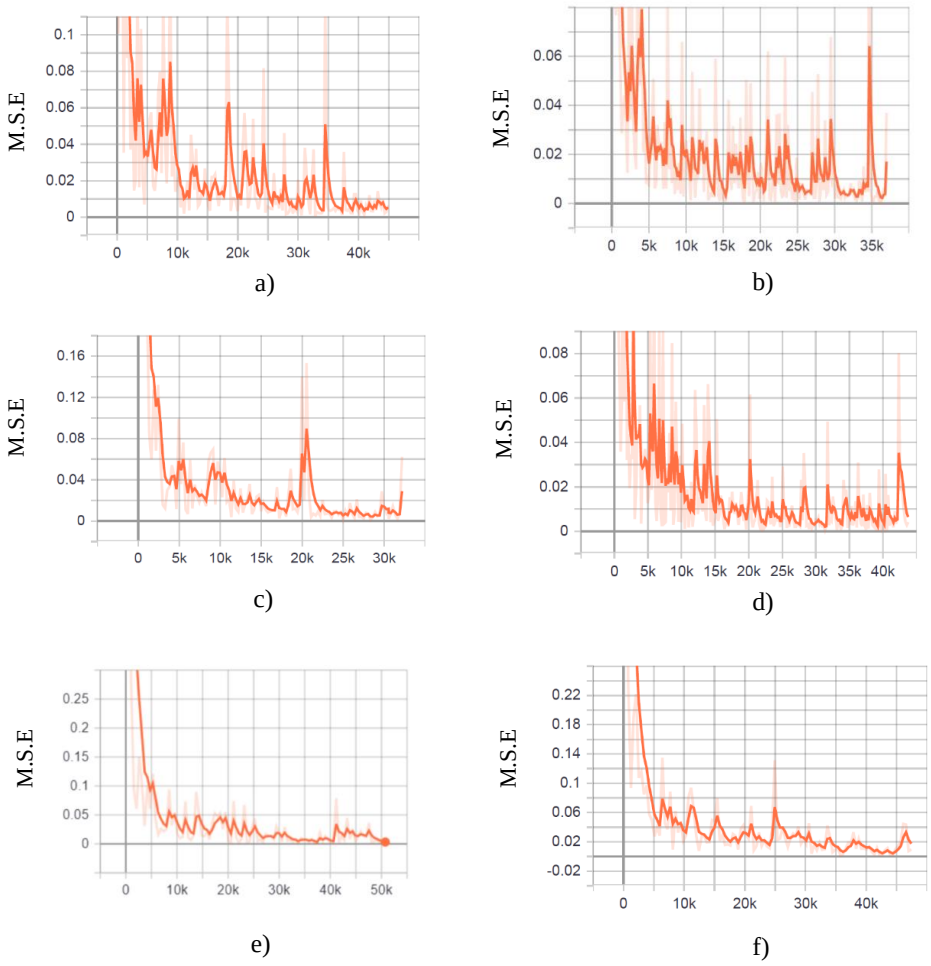

Figure 2.34: Example of model training loss function of Faster R-CNN with a) ResNet-50 + Annotation-1, b) ResNet-50 + Annotation-2, c) ResNet-101 + Annotation-1, d) ResNet-101 + Annotation-2, e) Inception-v2 + Annotation-1, d) Inception-v2 + Annotation-2. X-axis represents iteration numbers, while Y-axis indicates Mean Square Error (M.S.E). The dark high contrast plots are the smooth curves plotted over the actual curve with low contrast.

.

In the validation stage, the performance indicators show that, the built Faster R-CNN models have mAP and AR higher than 80% in the Annotation-1, and 72% in the Annotation-2 respectively. The Tables 2.7 and 2.6 present validation performance of all six models.

Convolution Models	mAP at IoU=0.50:0.95	AR at IoU=0.50:0.95
ResNet-50	0.722	0.771
ResNet-101	0.72	0.77
Inception-V2	0.703	0.758

Table 2.6: Training validation performance of Faster R-CNN model using annotation scenario-1 (on 25 images).

Convolution Models	mAP at IoU=0.50:0.95	AR at IoU=0.50:0.95
ResNet-50	0.824	0.869
ResNet-101	0.814	0.850
Inception-V2	0.801	0.834

Table 2.7: Training validation performance of Faster R-CNN model using annotation scenario-2 (on 25 images).

The Tables 2.7 and 2.6 show the training validation results of different Faster R-CNN models, built using two different annotation techniques and 3 ConvNets. The Table 2.6 presents the results of 3 ConvNets based Faster R-CNN models based on Annotation-1. While the Table 2.7 refers to 3 ConvNets based Faster R-CNN models based on Annotation-2. According to the validation findings, the model ResNet-50 consistently performed well with the provided dataset. The ResNet-50 model outperforms the ResNet-101 model because the depth of the convolution layers is increased in the ResNet-101 model, resulting in a loss in performance owing to the degradation problem explained in the section 2.2.1.b. Meanwhile, because of the nature of the Inception architecture and the increasing number of kernel scales, the Inception can potentially generate more false positives. As a result, the inception indicates a decrease in Average Precision (AP) and Average Recall (AR). However, the results are more oriented to a specific data set, and the performance difference of Faster R-CNN across three convolution networks is minimal (ResNet-50, ResNet-101 and Inception-v2). Furthermore, it is observed that the Annotation-2 approached outperforms Annotation-1, in all cases. And the ResNet-50 is relatively better and light. As a result, ResNet-50 is utilised for numerical data testing of both annotation scenarios. However, all three ConvNet models were assessed during field validation using both annotation scenarios.

2.3.3.b Results and discussion

The trained models were tested with 100 testing B-scan images. The performance of Faster R-CNN + ResNet-50 automatic pipe detection models (two separate models based on annotation-1 and annotation-2) were measured in terms of Precision and Recall that explained in the sub-section 2.2.3.c. In this study, the pipe refers to a single hyperbola or multiple hyperbola in the case of non-separable cases. The presented results firstly focused on the models based on binary image inputs, then later the greyscale models performances were presented for comparison later in the section

Faster R-CNN + ResNet-50 + Annotation scenario-1 model with binary image input: The Table 2.8 presents the performance of the model based on Faster R-CNN + ResNet-50 + Annotation scenario-1 tested for the given 'binarised' synthetic B-scan image inputs. The performance is measured in terms of Precision and Recall. Then supported by few examples of model predicted true positive and false alarms (false positives and false negatives) results with bounding box as illustrated in Figures 2.35 and 2.36 respectively.

Testing Images	Total Hyperbolas	TP	FN	FP	TN	Precision (%)	Recall(%)
100	272	267	5	9	-	96.7	98.1

Table 2.8: Performance of Faster R-CNN + ResNet-50 model using Annotation-1 model with 50 binarised training images.

Testing Images	Total Hyperbolas	TP	FN	FP	TN	Precision (%)	Recall(%)
100	272	271	1	9	-	96.7	99.6

Table 2.9: Performance of Faster R-CNN + ResNet-50 model using Annotation-1 model with 50 binarised training images (with single zone hypothesis)

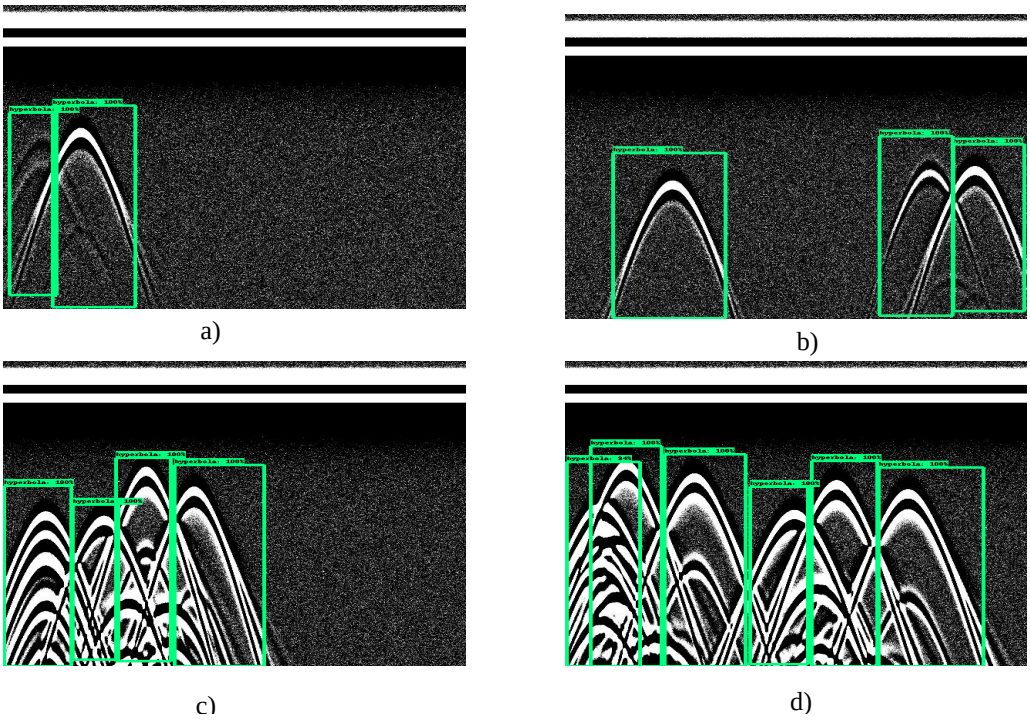

Figure 2.35: Example for True-Positive detection with Faster R-CNN + ResNet-50 model using annotation scenario-1, distinguishing individual hyperbola.

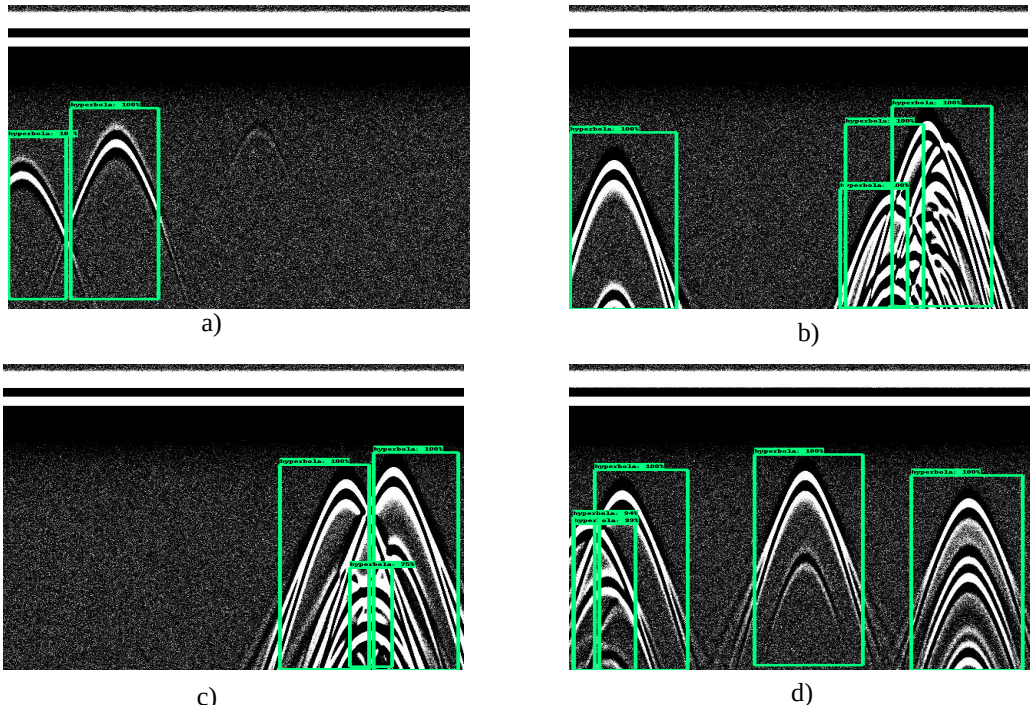

Figure 2.36: Example for false alarms with Faster R-CNN + ResNet-50 model using annotation scenario-2, distinguishing individual hyperbola.

According to Table 2.8, the model's Precision and Recall are 96.7 and 98.1%, respectively. As a result, Recall is slightly higher than Precision. Because it has produced less false negatives (5) than false positives (9). Despite the fact that the study's goal is to assume non-separable multiple hyperbola as a single target, the table demonstrates the model's ability to distinguish each hyperbola in order to assess the model's resilience. For example, in Figure 2.36.a, the model failed to detect a low contrast hyperbola (false negative), while in the Figure 2.36.b, only 4 hyperbolas were accurately recognized, but one non-separable hyperbola on the right side was missed. As a result, it was classified as a false negative. Similarly, the test results contained five false negatives in the data set. If the results were reorganized according to the primary hypothesis, as shown in Table 2.9, by considering it as a single zone, the number of false negatives in the total test results would be 1 (There is one exceptional where, the model failed to detect a well separated hyperbola in the Figure 2.36.a due to poor visibility). As a consequence, the number of true positives will be 271. As a result, the Recall must be 99.6%, as shown in Table 2.9. However, the status of false positive does not change as a result of the objective difference, whereas Figure 2.36 exhibits scenarios with a few examples of false positives and false negatives encountered by the model. Like shown in the images in Figure 2.36, several false positives was recorded as expected. It is the case where multiple reflection effects are detected as true targets. In terms of safety, false positives are less dangerous than false negatives. However, the ultimate motivation of the annotation scenario-2 is to avoid such false positives caused by multiple reflections to improve the overall performance.

Faster R-CNN + ResNet-50 + Annotation scenario-2 model with binary image input: Similarly, the performance of the model based on Faster R-CNN + ResNet-50 + Annotation scenario-2 is presented in Table 2.10, corroborated by a few examples of real positive and false alarm outcomes, as shown in Figures 2.37 and 2.38 respectively.

Testing Images	Total Hyperbolas	TP	FN	FP	TN	Precision (%)	Recall(%)
100	272	262	10	3	-	98.8	96.3

Table 2.10: Performance of Faster R-CNN + ResNet-50 model using Annotation-2 model With 50 binarised training images.

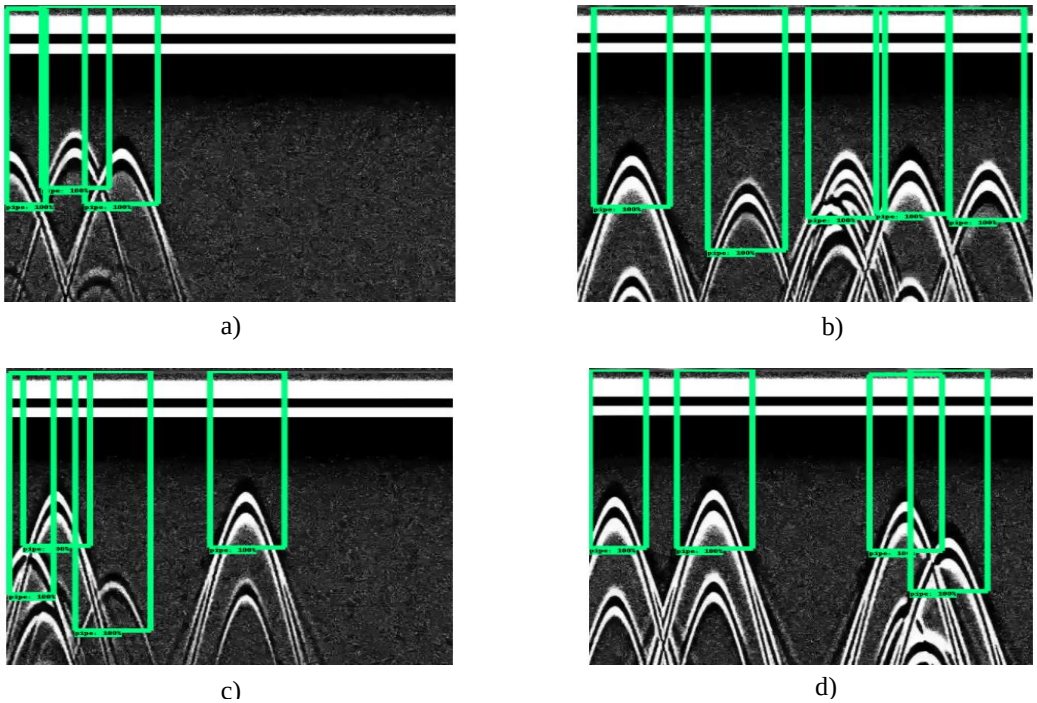

Figure 2.37: Example for True-Positive detection with Faster R-CNN + ResNet-50 model using annotation scenario-2. Distinguishing individual hyperbola.

The model's Precision and Recall are 98.8 and 96.3%, respectively, according to Table 2.10. As a result, in contrast with the Annotation-1 based model presented in the preceding section, Precision is somewhat greater than Recall. This model produced higher false negatives (10) than false positives (3). Due to the fact that the study's aim is to assume non-separable multiple hyperbolas as a single target, the table shows the model's potential to recognize distinct hyperbola in order to evaluate the model's robustness. Particularly in Figure 2.37.b, for example, only 5 hyperbolas were correctly identified, but one non-separable hyperbola in the centre was missing. As a result, it was deemed a false negative. Similarly, the entire data set had 10 false negatives in the test findings. The amount of false negatives in the entire test results would be zero if the data were restructured according to the principal hypothesis, as shown in Table 2.11, by treating it as a single zone. As a result, the total number of true positives will be 272. Hence, the Recall must become 100% as stated in Table 2.11. The status of false positive, on the other hand, does not alter as a result of the objective difference, whereas Figure 2.38 depicts scenarios with a few false positives.There was one false positive on each of the images in Figure 2.38. This is caused in part by highly dense pipes. False positives are less harmful than false negatives in terms of safety. However, it can be mitigated by adding another NMS (Non Max Suppression) layer. That is something to consider in the future. To be noted that, the false positives were significantly reduced in annotation scenario-2.

As previously indicated, when the non-separable hyperbolas in a location were treated as a single target, accuracy remains more than 98% and Recall reaches 100%. Nonetheless, the model's performance in terms of individual distinct hyperbola recognition is evaluated over a

Testing Images	Total Hyperbolas	TP	FN	FP	TN	Precision (%)	Recall(%)
100	272	272	0	3	-	98.9	100

Table 2.11: Performance of Faster R-CNN + ResNet-50 model using Annotation-2 model With 50 binarised training images, assuming non-seperable hyperbola as single zone

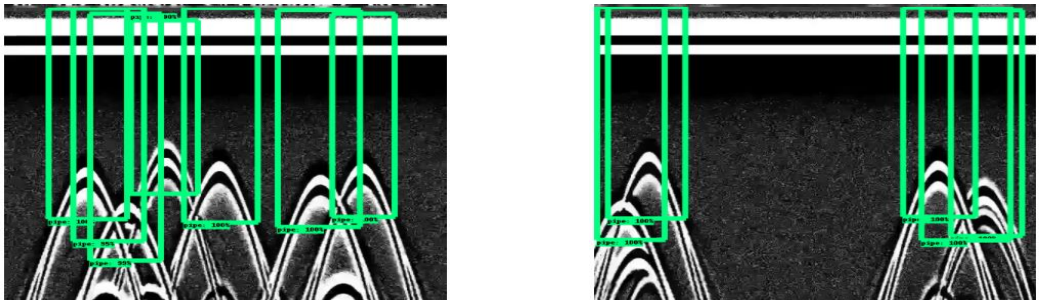

a) b)

Figure 2.38: Example for false positives with Faster R-CNN + ResNet-50 model using annotation scenarion-2.

range of different training database sizes and IOU thresholds. Figures 2.39 and 2.40 demonstrate this variation in accuracy and Recall performance. The findings reveal that regardless of the number of training sets used, overall accuracy remains above 90%. Furthermore, with a training size of 60 and an IOU value of 0.7, the accuracy is close to 98%. However, when the IOU amount increases, accuracy increases. The Recall value approaches 96% with a training set size of 60. It also does not change much across different IOU values. And, once again, when the dense hyperbolas are meant to represent a single target, the Recall becomes 100%.

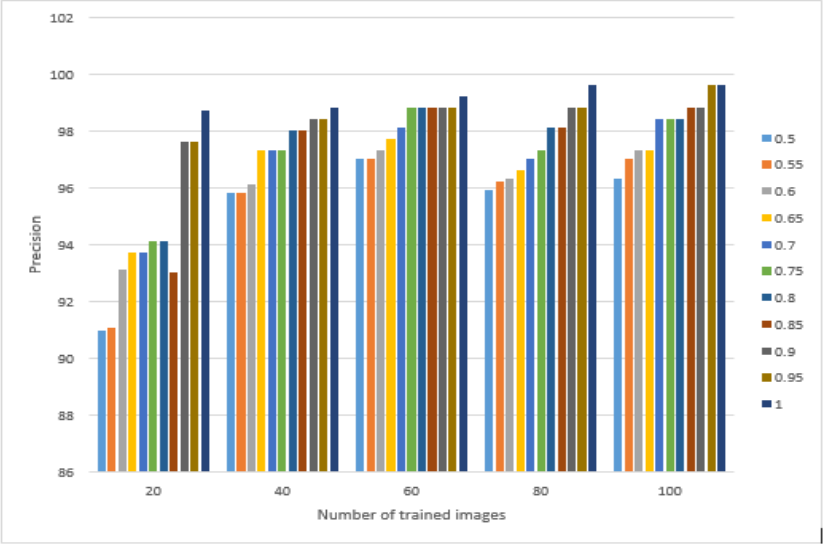

Figure 2.39: Precision variation of Faster R-CNN + ResNet-50 + Annotation scenario-2 model across various training database size and IOU threshold values.

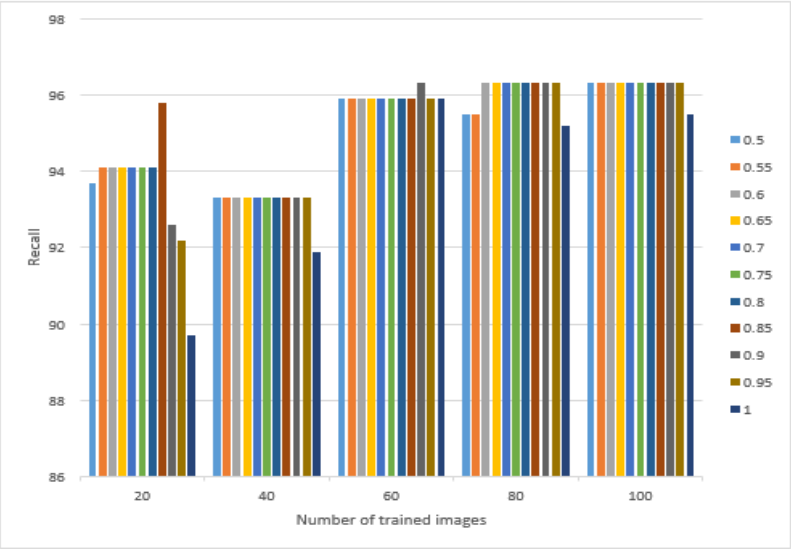

Figure 2.40: Recall variation of Faster R-CNN + ResNet-50 + Annotation scenario-2 model across various training database size and IOU threshold values.

By summary, the above results discusses the performance of 02 different ResNet-50 based Faster R-CNN models using Annotation-1 and Annotation-2 respectively. According to the test results, among two annotation techniques, both models able to detect (distinct detection) multiple hyperbolas in a single B-scan with minimum accuracy and Recall are above 96%. Hence, the Annotation-1 is relatively better in “Recall" (98%). Whereas, higher “Recall" is more preferred than “Precision" in terms of pipe’s safety. In this context, due to the fact that, the ConvNet has influence on the pipe detection model’s performance, the comparison of the Faster R-CNN model’s performance that built using three different ConvNets (ResNet-50, ResNet-101 and Inception-v2) are discussed below.

Performance comparison of Faster R-CNN models with binary image input: The paragraphs that follow compare the performance of a proposed faster R-CNN constructed using three ConvNets (three separate models per annotation technique, each using ResNet-50, ResNet-101 and Inception-v2). In addition, further discussion expanded also shows how the Faster R-CNN + ResNet-50 model operates under varied noise levels and GPR centre frequency conditions (bandwidth). At this time, relatively limited scenarios are investigated due to a lack of sufficient computing resources.

In order to compare 03 ConvNets based Faster R-CNN models, each with two annotation techniques. All together, six models were trained as shown in the Table 2.12. Each model uses the identical training and validation data, as well as annotation labels, as mentioned in the preceding paragraphs. The models were then evaluated using the same test sets. As a result, the performance of all six models is displayed in Table 2.12 at a glance for easier comparison. Nevertheless, to be emphasised here that, the mentioned six models were trained using the ‘binary image’ inputs. According to the data, the ResNet-50 method with Annotation-1 has the greatest “Recall" (98.1%), whereas the ResNet-50 approach with Annotation-2 has the highest “Precision" (98.8%). However, while stronger Recall is preferable to Precision in terms of pipe safety, ResNet-50 with Annotation-1 performs pretty well overall. ResNet-101 outperforms ResNet-50 owing to convolution network deterioration caused by the increased number of convolution layers in ResNet-101. ResNet-101 Precision reduced dramatically in the Annotation-2 approach. The Recall of Inception-v2 is remains equivalent to ResNet-50,

however the Precision of the Annotation-2 approach has reduced. Furthermore, when comparing annotations 1 and 2, the ResNet-50 outperforms both. Annotation-2 achieves the annotation approach's main goal by reducing false positives. However, performance varies depending on the data set. As a result, additional diversified research is required in the future to reach a reliable conclusion.

On the other hand, when the non-separable hyperbolas are considered as a single target (herein after referred to as single zone hypothesis), the false negatives become nearly zero, as the results the Recall values of all six models would reach minimum 99%, except in ResNet-50 where the Recall reaches 100% that can be noticed in the Table 2.13. Furthermore, false positives also can be minimised by introducing additional NMS layer, which is left for future investigation.

All false alarms are recorded inside densely overlapping hyperbolas. In addition, false positives are caused by overlapping bounding boxes pointing to the same target or by multiple reflection effects. Apart from that, a false positive is recorded when the hyperbola visibility is very low, which is a signal pre-processing problem (gain and contrast). However, false positives were never produced by incorrectly recognizing background as the true target. While the ResNet-50 currently outperform other models, the margin is rather small. As a consequence, only Faster R-CNN + ResNet-50 models were chosen for experimental validation using field data.

Model	Testing Images	Total Hyperbolas	TP	FN	FP	Precision (%)	Recall (%)
ResNet-50 + Annotation-1	100	272	267	5	9	96.7	98.1
ResNet-101 + Annotation-1	100	272	266	6	11	96.0	97.7
Inceptionv2 + Annotation-1	100	272	266	6	6	97.7	97.7
ResNet-50 + Annotation-2	100	272	262	10	3	98.8	96.3
ResNet-101 + Annotation-2	100	272	265	7	36	88.0	97.4
Inception-v2 + Annotation-2	100	272	266	6	19	93.3	97.7

Table 2.12: Performance of automatic pipe detection Faster R-CNN models for individual hyperbola distinction.

Model	Testing Images	Total Hyperbolas	TP	FN	FP	Precision (%)	Recall (%)
ResNet-50 + Annotation-1	100	272	271	1	9	96.7	99.6
ResNet-101 + Annotation-1	100	272	271	1	11	96.0	99.6
Inception-v2 + Annotation-1	100	272	271	1	6	97.8	99.6
ResNet-50 + Annotation-2	100	272	271	0	3	98.9	100
ResNet-101 + Annotation-2	100	272	271	0	36	88.2	100
Inception-v2 + Annotation-2	100	272	271	1	19	93.4	99.6

Table 2.13: Performance of automatic pipe detection Faster R-CNN models for single zone hypothesis.

Then, one configuration of three ConvNets (ResNet-50, ResNet-101, and Inception-v2) based Faster R-CNN models was evaluated for greater noise scenario to examine its behaviour in higher noisy data. As a result, while the trained model was at 30 dB SNR, a second test data set with 20 dB SNR B-scans was constructed and evaluated with the model trained with 30 dB SNR B-scans. Thus, the ResNet-50 + Annotation-1 and Annotation-2 models were chosen for this

purpose since they performed substantially better overall in the prior study. The Figures 2.41 illustrate some cases with true positives and false alarms. Whereas, Figure 2.41.a has one true positives and two false negatives. Likewise, in Figure 2.41.b, there are two true positives, one false positive, and one false negative. Further, in Figure 2.41.c contains three true positives and two false negatives. Similarly, all figures can be interpreted with true positives, false positives and false negatives. However, based on the statistics shown in the Table 2.13, it is clear that both ResNet-50 models suffer from much larger false negatives, that is evident from the figures 2.41. As a result, the Recall has decreased considerably (69.5%).

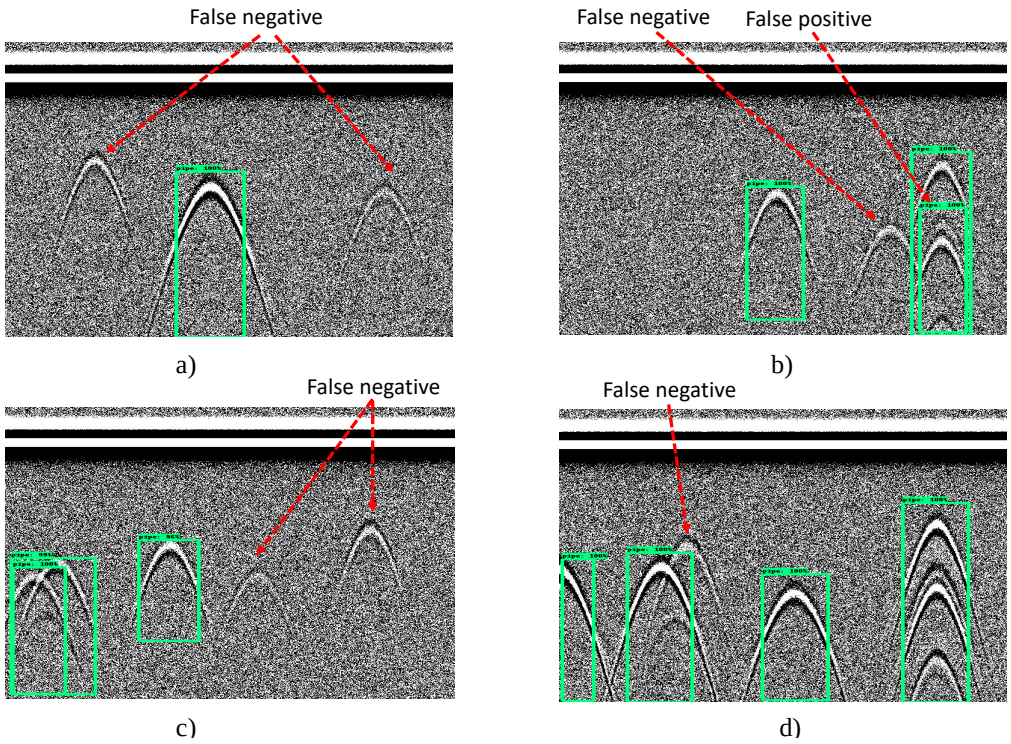

Figure 2.41: Example for true positives and false alarms detection with Faster R-CNN + ResNet-50 model using annotation scenario-1 on binarised images. Trained with SNR = 30 dB (400 MHz) and tested with SNR = 20 dB.

Model	Testing Images	Total Hyperbolas	TP	FN	FP	Precision (%)	Recall (%)
ResNet-50 + Annotation-1	33	92	64	28	3	95.5	69.5
ResNet-50 + Annotation-2	33	92	64	28	1	98.4	69.5

Table 2.14: Performance of automatic pipe detection Faster R-CNN models, trained with SNR = 30 dB (400 MHz) and tested with SNR = 20 dB.

In addition to the noise variation investigation, the model's ability was evaluated on different frequency. As an example, the centre frequency on the trained GPR B-scans is 400 MHz. During this time, 900 MHz test B-scans were generated and tested using a 400 MHz model that had already been trained. The Table 2.15 demonstrates how it behaves in this context. It was discovered that in the Annotation-1 situation of the evaluated ResNet-50 based Faster R-CNN model, cross frequency detection still performs well, although accuracy has decreased. Cross frequency detection is enabled by the dynamic kernel features (k proposals: aspect ratio and scaling concept) in the Faster R-CNN principles, because the frequency changes, so does

the wavelet width. The network can recognize the new frequency hyperbola by its shape and other common characteristics when the varied wavelet is comparable to the scaled or scale down dimension of the initial wavelet (trained wavelet). The examples of some test results are demonstrated in the Figure 2.42 and a couple of false alarms scenarios presented in the figure 2.43

Model	Testing Images	Total Hyperbolas	TP	FN	FP	Precision (%)	Recall (%)
ResNet-50 + Annotation-1	100	269	264	5	36	88.00	98.1
ResNet-50 + Annotation-2	100	269	251	18	5	98.00	93.3

Table 2.15: Performance of automatic pipe detection Faster R-CNN models, trained with centre frequency (f_c) of 400 MHz and tested with 900 MHz dataset.

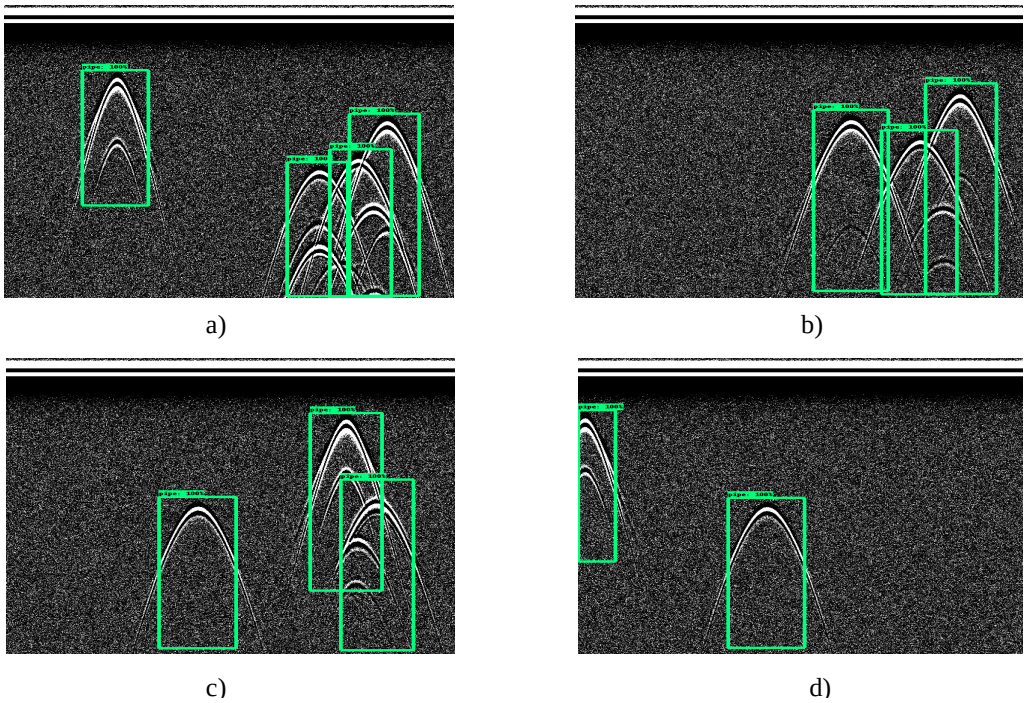

Figure 2.42: Example for True-Positive detection with Faster R-CNN + ResNet-50 model using annotation scenario-2 on binarised images. Trained with centre frequency (f_c) of 400 MHz and tested with 900 MHz dataset.

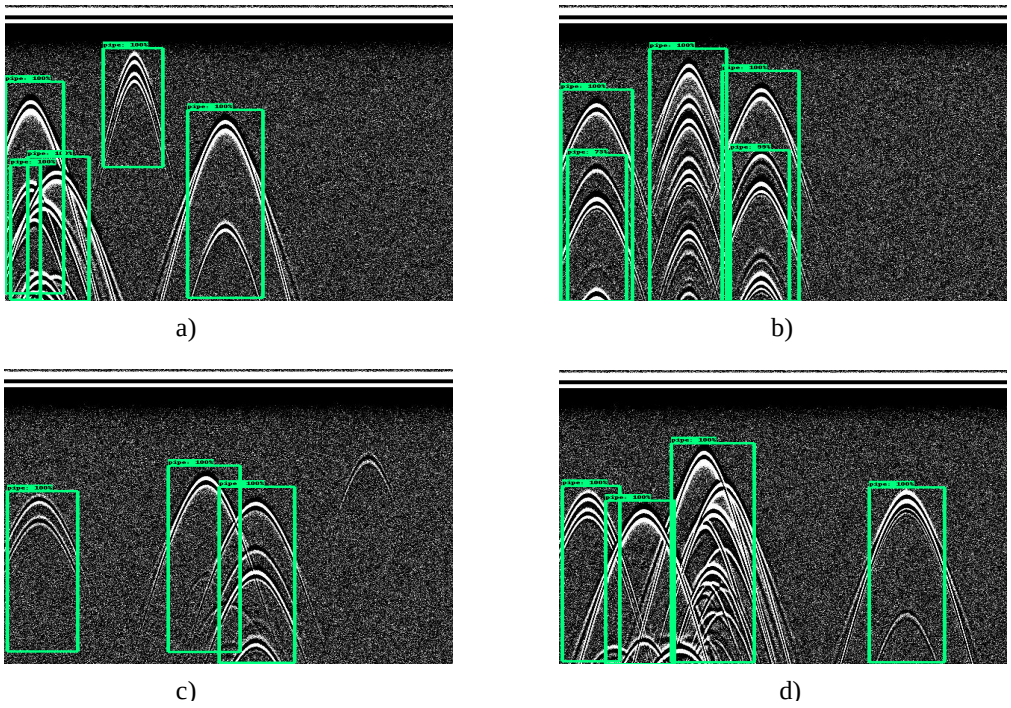

Figure 2.43: Example for false alarms of Faster R-CNN + ResNet-50 model using annotation scenario-2 on binarised images. Trained with centre frequency (f_c) of 400 MHz and tested with 900 MHz dataset.

Based on the findings above, when binary images are utilised as the input of the Faster R-CNN model, the ResNet-50-based model has the highest “Recall" values among all three ConvNets, but “accuracy" stays nearly the same. Higher Recall levels, on the other hand, are desired in pipe detection to minimize false negatives. Nonetheless, the performance gap between the three ConvNets is minimal. Annotation-1 is more accurate than Annotation-2 in terms of annotation approaches. Furthermore, when test B-scan noise is increased from 30 dB to 20 dB, the Recall value of binary images declines from 98 percent to 70% (SNR). Meanwhile, when the test data set's centre frequency differs from the training data, Recall does not decrease while accuracy falls from 98% to 88%. However, the Recall value remains constant (98%). This pattern suggests that various frequency GPR devices may be utilised to construct a global detection model using binary inputs. Furthermore, in the preceding work, binary pictures were used as input to Faster R-CNN rather than greyscale images. Because the binary conversion eliminates the gain process. As a result, it streamlines pre-processing of large-scale data. Alternatively, the part that follows compares the performance on greyscale images.

Faster R-CNN models performance comparison between binary and grey-scale inputs: In order to eliminate gain pre-processing, the six models outlined above were developed using binary B-scan image inputs, because achieving a single gain setting for large volumes of data is difficult. As a result, under some subsurface circumstances, such as dispersive and high moisture media, hyperbola may disappear owing to a lack of gain or contrast. As a result, the model detection may skip the hyperbola, resulting in a ‘false negative’.

As a result, the binary image was employed, as mentioned in the subsection 2.3.2. However, binary images are often used for synthetic data because they are relatively homogeneous and have a normal and symmetric amplitude value distribution. As a result, the goal is excellent for a noise-free environment. This can be accomplished by using high-performance noise or clutter filters on real-world B-scan data, which is not developed in this thesis. As a result,

Model	Testing Images	Total Hyperbolas	TP	FN	FP	Precision (%)	Recall (%)
ResNet-50 + Annotation-1	100	272	266	6	2	99.2	97.7
ResNet-101 + Annotation-1	100	272	269	3	3	98.2	98.8
Inception-v2 + Annotation-1	100	272	270	2	5	98.8	99.2
ResNet-50 + Annotation-2	100	272	267	5	2	99.2	98.1
ResNet-101 + Annotation-2	100	272	269	3	2	99.2	98.8
Inception-v2 + Annotation-2	100	272	268	4	6	97.8	98.5

Table 2.16: Performance of automatic pipe detection Faster R-CNN models with greyscale B-scan input images.

the binarisation is subject to high effective noise removal filters or noise free GPR images. Furthermore, commercial GPR may have varied colour, amplitude, and dynamic scaling, as well as quality. Because of this, traditional greyscale B-scan input is not ruled out for the time being.

Based on these reasons, the greyscale approach were tested on all six models using the same set of training data, but annotated on greyscale images, in order to evaluate its performances. The Table 2.16 presents the test results of all six combination model of Faster R-CNN.

According to the Table 2.16, the performance of greyscale models seems better than binary images. However, the single gain setting works better in the synthetic GPR B-scans. Hence, it's still a question of the robustness in the real data. All model's Precision and Recall remain above minimum 97%. However, the Inception-v2 has the highest Recall in the Annotation-1 scenario, while it shows the least 'Precision' in the Annotation-2.

Furthermore, Figures 2.44 and 2.48 provide a few instances of test results based on Faster R-CNN + ResNet-50 + Annotation-1 and Annotation-2, respectively, demonstrating that the models are capable of identifying low contrast images that are sometimes not interpretable by the human eye. However, it would remain a difficulty for the human operator to determine whether the result is a 'real positive' or a 'false positive'. The ground truth is uncertain in the actual world scenario.

In addition, Figures 2.45 and 2.46 are provided to indicate some false alarms. The models in both annotation techniques react similarly to binary image-based models. False positives have been observed in multiple reflection conditions, whereas, false negatives have been observed in low contrast hyperbolas. An extra NMS filter can be used to eliminate some false positives. This has not yet been deployed and left for future work.

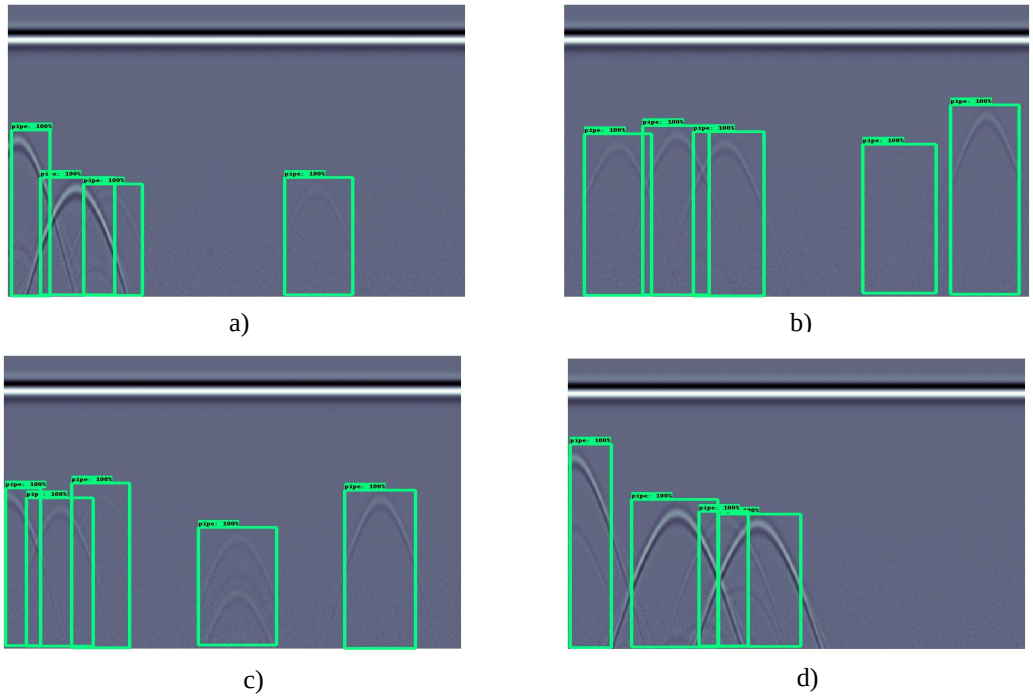

Figure 2.44: Example for true positives of Faster R-CNN + ResNet-50 model using annotation scenario-1 on gray scale B-scan images.

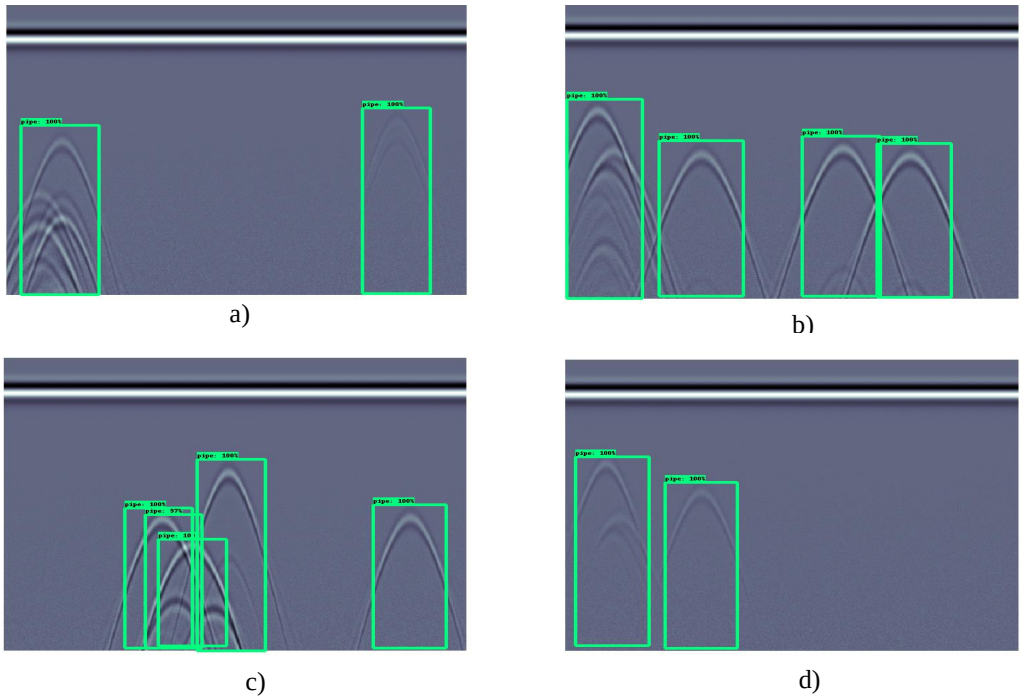

Figure 2.45: Example for true positives with some false alarms. Faster R-CNN + ResNet-50 model using annotation scenario-1 on gray scale B-scan images.

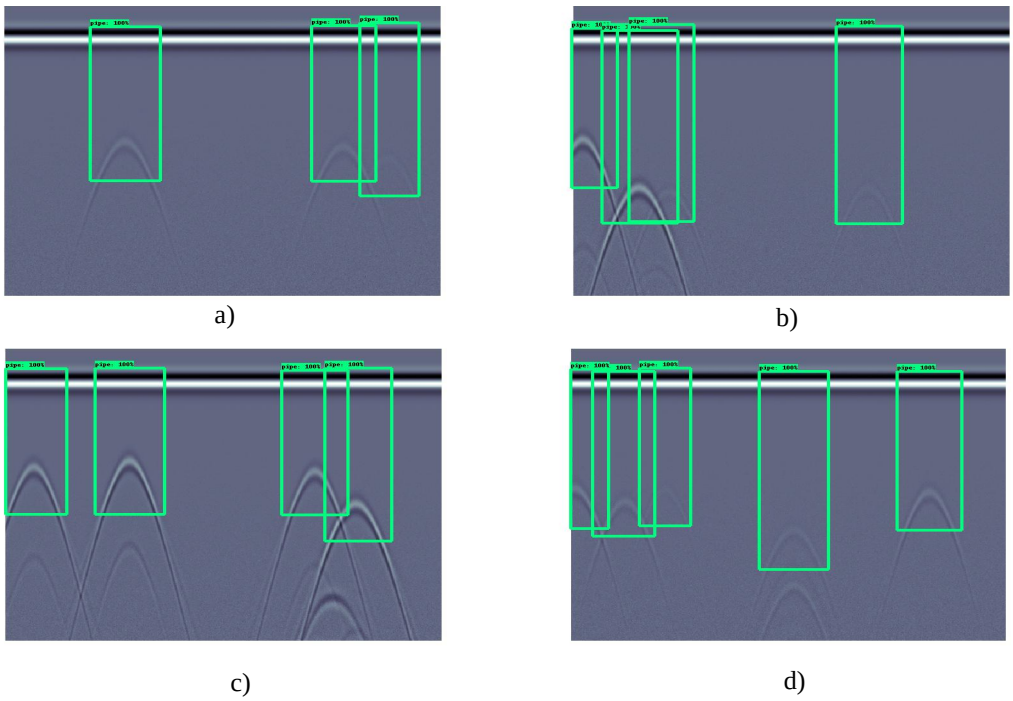

Figure 2.46: Example for true positives and false alarms of Faster R-CNN + ResNet-50 model using annotation scenario-2 on gray scale B-scan images.

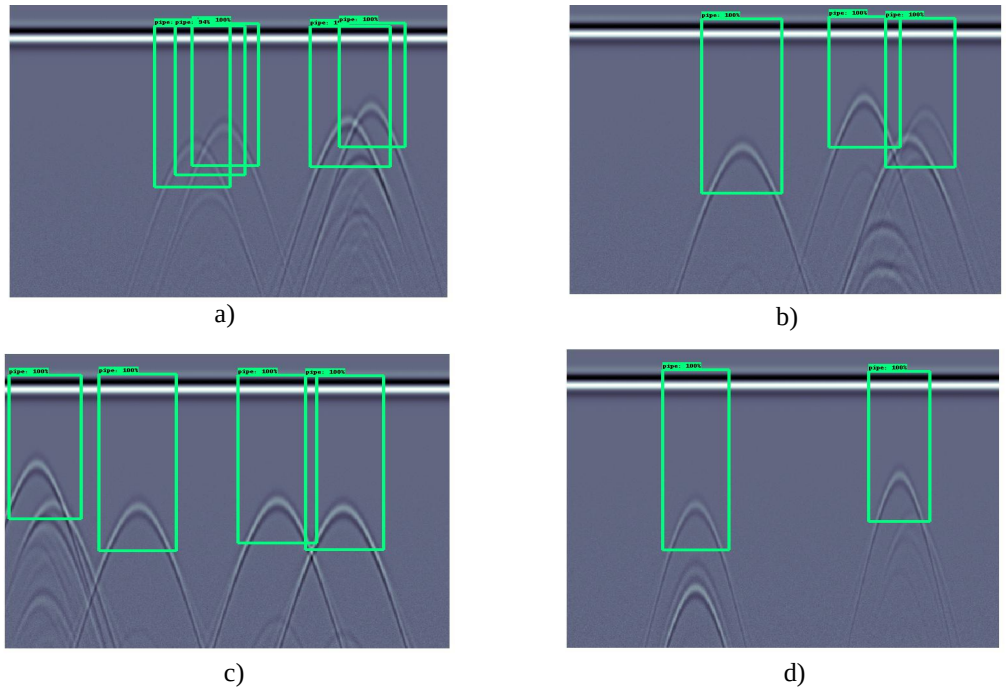

Figure 2.47: Example for true positives with some false alarms. Faster R-CNN + ResNet-50 model using annotation scenario-2 on gray scale B-scan images.

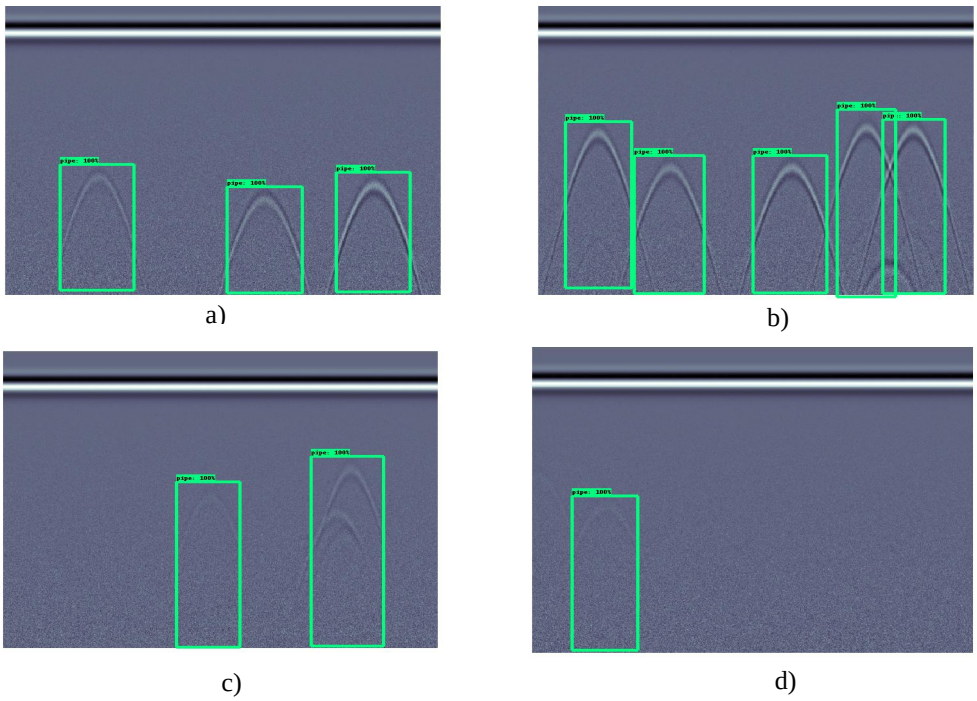

Figure 2.48: Example for true positives and false alarms. Faster R-CNN + ResNet-50 model using annotation scenario-1 on gray scale B-scan images. Training with SNR = 30 dB (400 MHz) and tested with SNR = 20 dB.

From the Table 2.17, the Inception-v2 models were picked to evaluate the models' performance on high noise data such as 20 dB SNR (white gaussian noise), whereas the previous models were tested on 30 dB SNR B-scan images. As a consequence, the table results relate to the test results corresponding to the 30 dB SNR based training model with test data of 20 dB SNR. As a result, accuracy and Recall have increased marginally. However, the performance difference is not significant, and it is clear that the presented models might potentially operate on noisy data. Surprisingly, the number of 'false positives' reach zero.

Aside from that, the trained model at 400 MHz (synthetic images with a central frequency of 400 MHz) was evaluated on 900 MHz based (synthetic images with a centre frequency of 900 MHz) test data. Figure 2.18 indicates the results. Whereas, the findings demonstrate that the model can detect pipes from GPR images derived from higher centre frequency GPRs thought the training images are at low frequency. However, the accuracy has dropped significantly while the Recall has remains high. In contrast, the number of false positives is relatively large in comparison with the number of false negatives. As a result, models are less likely to miss the target when evaluated on frequency data that differs from the frequency of the training data. The ability of the model's adaptability between different frequencies come from the dynamic kernel sizes (k-proposals) of the Faster R-CNN architecture and the nature of Inception-v2 convolution network. The k proposals have been explained in the subsection 2.2.1.a.

Model	Testing Images	Total Hyperbolas	TP	FN	FP	Precision (%)	Recall (%)
Inception-v2 + Annotation-1	33	85	82	3	1	98.7	96.4
Inception-v2 + Annotation-2	33	85	82	3	0	100.0	96.4

Table 2.17: Performance of automatic pipe detection Faster R-CNN models, training with SNR = 30 dB (400 MHz) and tested with SNR = 20 dB.

Model	Testing Images	Total Hyperbolas	TP	FN	FP	Precision (%)	Recall (%)
Inception-v2 + Annotation-1	100	269	263	6	34	88.50	97.7
Inception-v2 + Annotation-2	100	269	265	4	47	84.90	98.5

Table 2.18: Performance of automatic pipe detection Faster R-CNN model with greyscale B-scan image input, training with centre frequency (f_c) of 400 MHz, and tested with 900 MHz dataset.

In summary, the numerical findings provided above are based on Faster R-CNN automatic pipe detection models that use greyscale B-scans. all studied models automatically detects multiple pipes within a single B-scans. When comparing the performance of binary image inputs with greyscale inputs, the model based on greyscale B-scan inputs performs much better in terms of "Recall" and "Precision." Among the three ConvNets, the Inception-v2 based model outperforms the others. Meanwhile, the Annotation-1 is marginally better in terms of annotation methods. In all circumstances, however, the performance difference between ConvNets and annotation approaches is relatively small. In addition, as compared with binary image-based models, greyscale-based models are more resilient to noise. As a result, when test data noise rose from 30 dB to 20 dB, Recall decreased from 99 to 96% (SNR). In contrast, the "Recall" in the binary image model declined to 70%. Furthermore, "Recall" did not diminish considerably as frequency increased. However, accuracy has fallen to 88.5%, given that Recall has greater weight than accuracy, as noted previously. As a result, greyscale-based Faster R-CNN outperforms binary inputs. Though the suggested numerical research of Faster R-CNN is promising, the detection speed of Faster R-CNN is theoretically insufficient for real-time detection applications. As a result, the YOLOv4 was created to test its algorithm and determine whether the YOLOv4 can be implemented alternatively with its real-time detection capability and without sacrificing performance. Alternatively, YOLOv4-based models can be used as an approximation tool post-processing stage, the goal for studying YOLO is to investigate its usefulness for real-time or near real-time pipe detecting capabilities without sacrificing performance. If the performance is better than Faster R-CNN, it might potentially replace Faster R-CNN in post-processing as well. Indeed, YOLO has previously been demonstrated to be quicker and more deployable for real-time object detection applications. Furthermore, it has different convolution architectures and localisation approaches compared with Faster R-CNN. As a consequence, the YOLOv4-based automatic hyperbola detection model has been studied and numerically validated at this level using a synthetic B-scan database and pre-processing steps (similar training, validation, and labelling to the Faster R-CNN models described in the preceding subsections). However, because of the unique nature of the YOLOv4 built environment, training was carried out on HPC (high performance computing) clusters. To recap, the YOLOv4 is constructed on a convolution network backbone based on Darknet-53 rather than ResNet or Inception (refer to 2.2.2.a for more information). Hence, the YOLOv4 based model shall have only one variation in the study, such as YOLOv4 with annotation scenario-2 as mentioned in the Figure 2.23. However, the below section presents the results obtained in Annotation-2 approach in this report, with the hypothesis that, the performance doesn't vary much between Annotation-1 and Annotation-2 based on the findings in Faster R-CNN.

Testing Images	Total Hyperbolas	TP	FN	FP	TN	Precision (%)	Recall(%)
100	272	266	6	0	-	100	97.8

Table 2.19: Performance of YOLOv4 using Annotation-2 model with 50 binarised training images, distinguishing individual hyperbola.

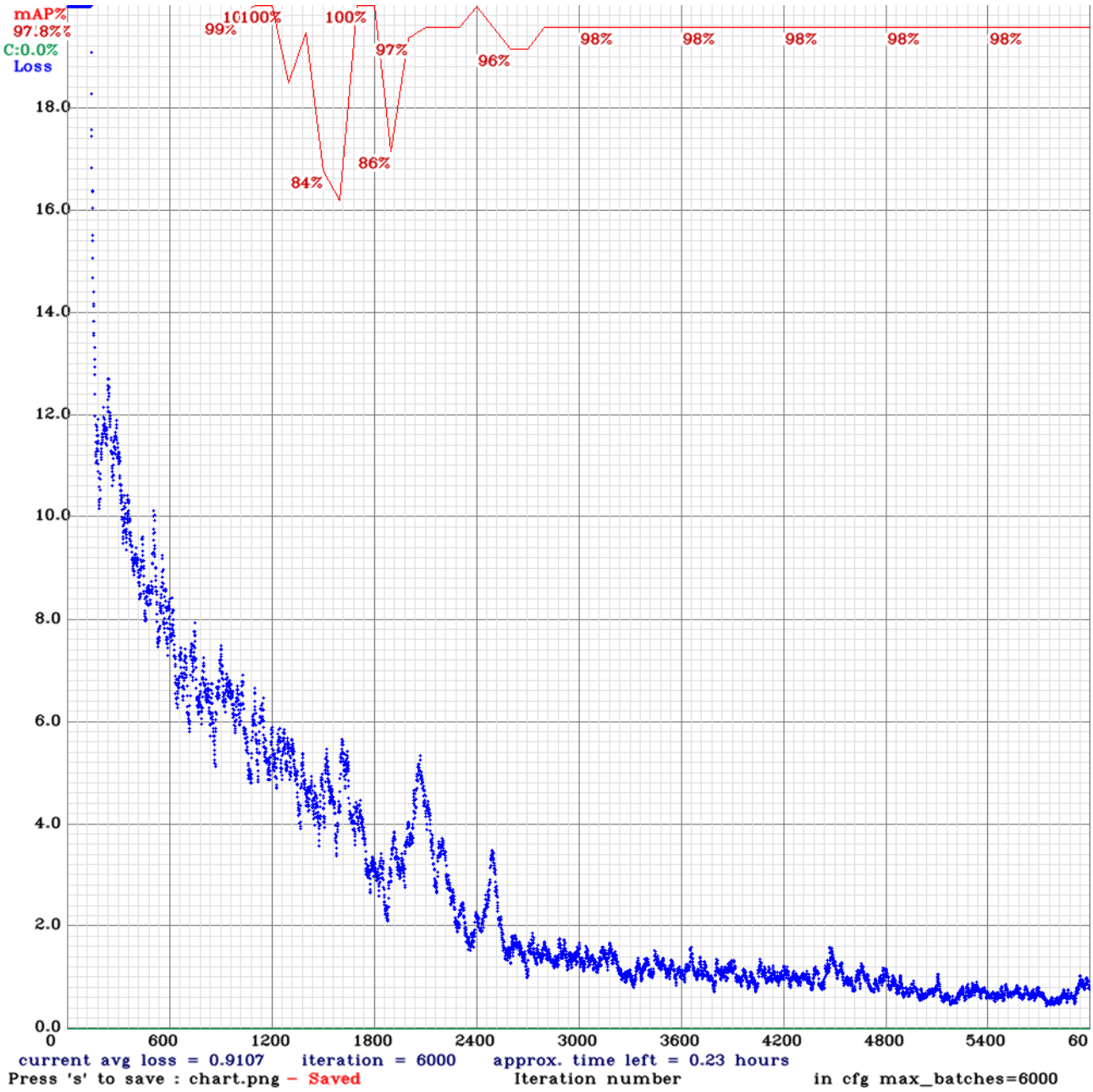

Figure 2.49: System generated loss convergence graph at training phase for YOLOv4 + Annotation-2 model.

The system produced validation plot in Figure 2.49 shows that the training model's mean average Precision (mAP) is 98% and the maximum iteration is set to 6000 according to best practice. Finally, the loss is converged to its minimal as iteration cycle progress. In addition, the most recent best model was employed for testing. Furthermore, as described below, the validation mAP performance reflects on the test results.

According to Table 2.19, the Precision of the YOLOv4 model based on annotation scenario-2 has reached 100% in Precision and 97.8% in Recall. Thus, YOLOv4 has completely eliminated false positives in comparison with Faster R-CNN. The reason for the YOLOv4's out performance in the false positive counts could have influenced by its features extraction convolution architecture (Darknet-53 + FPN) or YOLO architecture that can not be concluded precisely at this stage. In the other-hand, six false negatives have been recorded in high density overlapping hyperbolas. If these situations are viewed as separate zones, the Recall also exceeds

100%. Figures 2.50 and 2.51 show the prediction outcomes and false alarms, respectively. Figure 2.51 shows that on each picture, one of the high densely overlapped hyperbolas is not recognized (false negative). However, if the site is regarded as a single zone, it is presumed as actual positive targets. That leads to 100% Recall performance of the model.

Similar to the Faster R-CNN study, the YOLOv4 also was tested for cross frequency and cross noise scenarios, whereas the trained model data was based on 400 MHz centre frequency and 30 dB SNR. While the two additional data sets tested with this trained model, that of

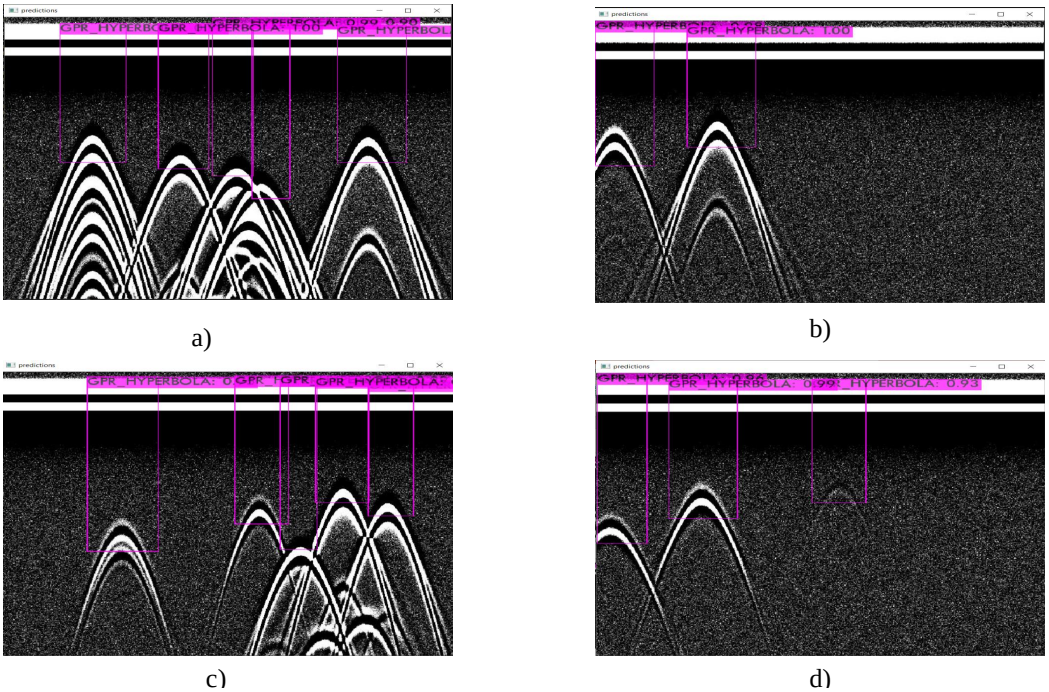

Figure 2.50: Example for True-Positive detection with YOLOv4 using Annotation-2 model.

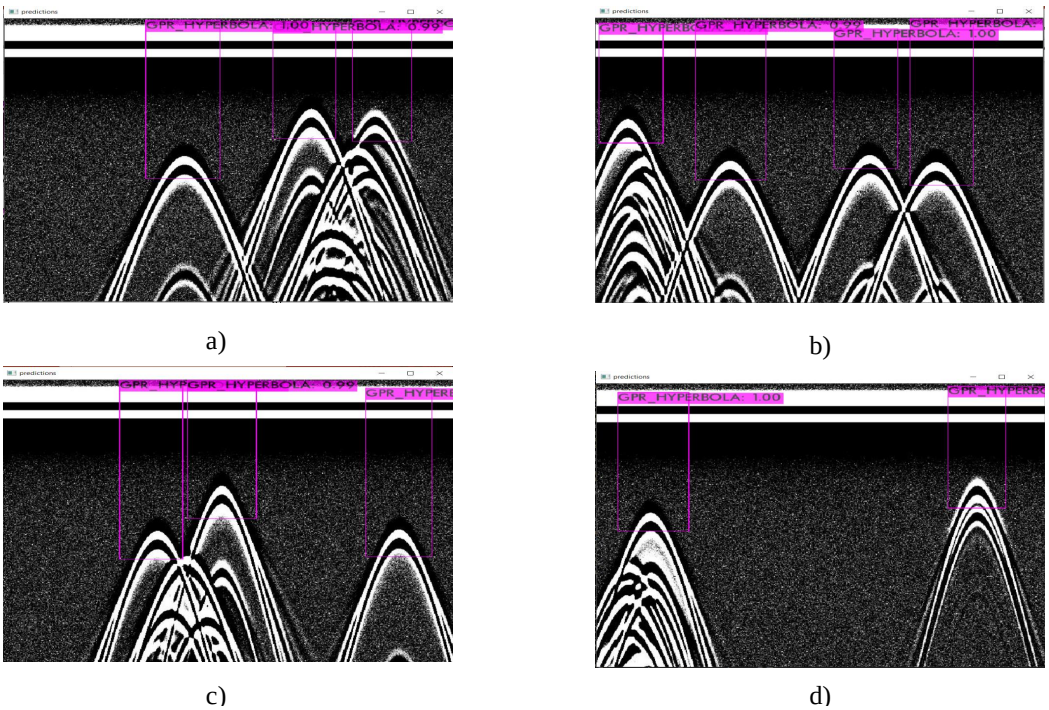

Figure 2.51: Example for false negative detection with YOLOv4 using Annotation-2 model.

YOLOv4 + Annotation-2.

The data in Table 2.20 illustrate how the 400 MHz YOLOv4 model behaved on 900 MHz B-scans. The performance decreased in the Table 2.20 when compared with the 400 MHz to 400 MHz test shown in the Table 2.19. The model has an increasing number of false negatives and false positives. Precision fell more than Recall. Figure 2.52 exhibits various instances of detection findings, which include both true positives and false alarms. However, when it was evaluated in a greater noise environment with 20 dB SNR test data sets, the Precision stayed at 100% although Recall decreased substantially to 56.4%, according to Table 2.21.

Testing Images	Total Hyperbolas	TP	FN	FP	TN	Precision (%)	Recall(%)
100	269	257	12	28	-	90.2	95.6

Table 2.20: Performance of automatic pipe detection YOLOv4 model with binarised B-scan image input, training with centre frequency (f_c) of 400 MHz, and tested with 900 MHz dataset.

Testing Images	Total Hyperbolas	TP	FN	FP	TN	Precision (%)	Recall(%)
100	269	232	37	0	-	100.0	56.4

Table 2.21: Performance of automatic pipe detection YOLOv4 model with binarised B-scan image input, training with SNR = 30 dB (400 MHz) and tested with SNR = 20 dB.

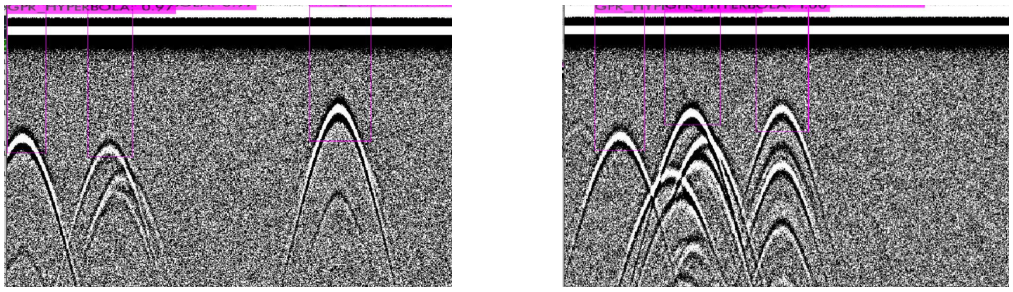

a) b)

Figure 2.52: Example for true positives and false negatives detection with YOLOv4 using Annotation-2 model, training with SNR = 30 dB (400 MHz), and tested with SNR = 20 dB.

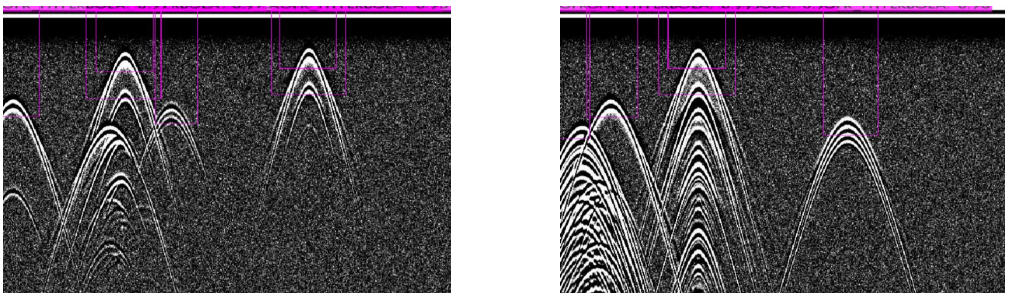

a) b)

Figure 2.53: Example for true positives and False negatives detection with YOLOv4 using Annotation-2 model, training with centre frequency (f_c) of 400 MHz and tested with 900 MHz dataset.

According to the numerical analysis, YOLOv4 automatically recognizes multiple hyperbolas in a single B-scan with a “Precision" of 100% and a “Recall" of 97.8%. However, when the SNR of the test data was decreased to 20 dB, the Recall value plummeted to 56%. This shows that the model performs poorly in noisy environments and is more likely to miss detecting individual pipes. As a result, it poses a risk to the network's security. But when overlapping pipes are assumed a single target (single zone hypothesis), the Precision reaches 100% and Recall also increased to more than 90%. Nevertheless, because of time and resource constraints, numerical research is confined to Annotation-2 with binary picture input only. Greyscale input models must be examined in order to evaluate their performance and generate conclusions about the YOLOv4 input format and annotation technique. It's being kept for now as a future prospect. In any case, YOLOv4 was included in the experimental validation. As a result, a good performance indication in experimental validation may be used to rule out further numerical investigation of YOLOv4.

2.4 Conclusion

The chapter discusses automatic pipe detection algorithms that are focused on large-scale GPR data processing for utility mapping. As a result, the chapter analyses the possible applicability of two deep learning algorithms, Faster R-CNN and YOLOv4. The detail literature review, methodology of the suggested models and their operational principles, signal and data pre-processing procedures, and numerical validation study utilizing 2D gprMax were all given.

The numerical validation shows that both Faster R-CNN models and YOLOv4-based automatic pipe detection models have the potential to solve the main goal of automatic detection. Thus, all the investigated models were able to automatically detect multiple hyperbolas in a single B-scan. Further, the models performance matrices are evaluated for its ability to distinguish individual pipes even in overlapping situation. Nevertheless, the model's performance reaches nearly 99-100% when the single zone hypothesis is adopted. However, the presented key findings are based on individual pipe distinction. The models detected individual multiple pipes in a single B-scan very quickly, with an overall Precision and Recall of 85 - 98% regardless of its overlapping nature.

The performance gap between Faster R-CNN and YOLOv4 is very small. Furthermore, the influence of different convolution networks in the Faster R-CNN is visible. Nonetheless, it is quite small. Annotation techniques and pre-processing (greyscale or binary image), on the other hand, have a significant impact on model performance. The binary B-scan has a

significant advantage in that it eliminates gain processing. In the meantime, greyscale is a conventional approach that sometimes be able to detect hyperbola that's not interpretable by a human eye. Though it is an advantage, in practical situation, the processing engineer won't be able to distinguish these cases between true positive and false positive.

Furthermore, the performance of both annotation systems is good. Indeed, the Annotation-2 removes false positives caused by the multiple reflection effect. However, the numerical findings show that the performance difference is modest. The models can still recognize data that differs from training data at varied frequencies. Furthermore, except the YOLOv4 models, the models operate in higher noise test data with minimal deterioration. The applicability of the binary B-scan image input is dependent on the GPR type, data quality, and signal scale. If the greyscale data is sufficient to visualise all hyperbola in single settings, stage binarisation or the greyscale are optional at this point. As a result, if the quality of the obtained GPR is sufficient, the greyscale can be used. Furthermore, in the future, the numerical study can be expanded by kernel size and the hyperparameters study, as well as on more complex models. That has been limited in this thesis due to limited high performance computing resources at this stage. Because the numerical data sets studied are relatively homogeneous. Finally, the models must be evaluated on field data in order to understand their behaviour in extremely non-homogeneous and noisy data, as well as on particular GPR equipment data. The experimental validation can confirm that the model can be deployed in real-world circumstances and noisy situation. In this regard, four models were chosen for experimental validation:'Faster R-CNN + ResNet-50 + Annotation-1', 'Faster R-CNN + ResNet-50 + Annotation-2', 'YOLOv4 + Annotation-1', and 'YOLOv4 + Annotation-2'. Due to the lack of large scale data collection systems, such as a high speed array GPR system, impulse GPR has been employed for experimental validation. The specifics are described in the next section.

Chapter 3

Parameter estimation and classification

In this chapter, we evaluate and optimise the performance of multiple methods for estimating the depth (d) and radius (r) of utility pipes using GPR data, using both physical and machine learning approaches. Whereas depth (d) estimate is required for accurate 3D pipe localisation. The radius (r) estimation is important that increases the mapping process's accuracy. Furthermore, it increases network safety by taking pipe size into account when determining the no-dig zone surrounding the pipe. For example, in France, Class A Precision of all critical underground utility networks are regulated by legislation, with a maximum 3D localisation error of +-40 cm for rigid pipes. In such case, precise depth and size information will enhance the mapping accuracy, thus the legal requirement. Furthermore, research for the classification of pipe type using machine learning methodologies was also presented.

In the parameter estimation process, Support Vector Machine (SVM) classifications, Support Vector Machines regression (SVR), Artificial Neural Network (ANN), convolution neural network (CNN), and Ray-based methods are used in parameter estimation to correlate information about the radius (r) and depth (d) of embedded pipes with the velocity (v) of stratified media in various numerical configurations and objectives. The techniques are based on the hyperbola trace that emerges from a sequence of B-scans, and the shape of the hyperbola changes greatly depending on the depth (d) and radius (r) of the pipe, as well as the velocity (v) of the medium. In the Ray-based method, the wave velocity (v) and pipe radius (r) were inverted using an appropriate non-linear least mean squares inversion methodology. The information gathered from observed hyperbola travel time was also used to choose features within machine learning models.

Regarding pipe type classification, Support vector machine (SVM) and K-Nearest Neighbour (KNN) were used in this work to categorise the type of pipe material based on the A-scan signature of the reflected echo on top of the pipes.

All the study is numerically validated in this chapter with simulated data acquired using the Finite-Difference Time-Domain (FDTD) approach and the numerical tool 2D, gprMax. The study is based on monostatic, ground coupled GPR data sets. Because monostatic configurations is compatible with the SFR that is currently under development. Further, the monostatic arrangement, on the other hand, reduces the array size by half while increasing speed of acquisition. In addition, a parametric comparison of the performance of the proposed estimation models also presented in terms of absolute relative error between estimated values and the ground truth. Furthermore, the proposed parameter estimation models assume that the hyperbola has already been detected using the methods described in Chapter 2.

3.1 Introduction

As introduced in the previous chapters, Ground Penetrating Radar (GPR) is a Non-Destructive Testing (NDT) method used to assess the subsurface conditions of a structure and locate buried

objects using electromagnetic waves [8]. Thanks to its sensitivity to the material characteristics (such as permittivity, conductivity, *etc.*), GPR can be used to detect both metallic and non-metallic targets. In addition to the wide range of GPR applications listed in [95], depth (d) estimation of the buried cylindrical pipes has become an important task in underground utility networks localisation [20]. In the meantime, the industry looks for radius (r) to improve the mapping data quality and precision of safety boundary.

However, regardless of the information acquired using GPR, each application requires suitable processing techniques in order to interpret GPR data. Within the scope of utility networks, 3D locating of the underground utility pipes became mandatory to avoid accidents during excavations. As the results, 3D localisation and mapping of underground utility pipes has been regulated by governments. In France, for example, Class A precision is regulated by legislation, with a maximum 3D localisation error of 40 cm allowed for rigid pipes (50 cm for flexible pipes).

In fact, traditional destructive testing methods and physical manhole verification techniques are widely used and are usually expensive and time consuming, and further the borehole tests cause damage to the tested structure. However, these drawbacks can be overcome by using NDT methods for evaluation. Conventional NDT methods such as acoustics, electromagnetic or RFID technologies have been used in the past to find underground pipes. Hence, GPR can be used to detect both metallic and non-metallic targets.

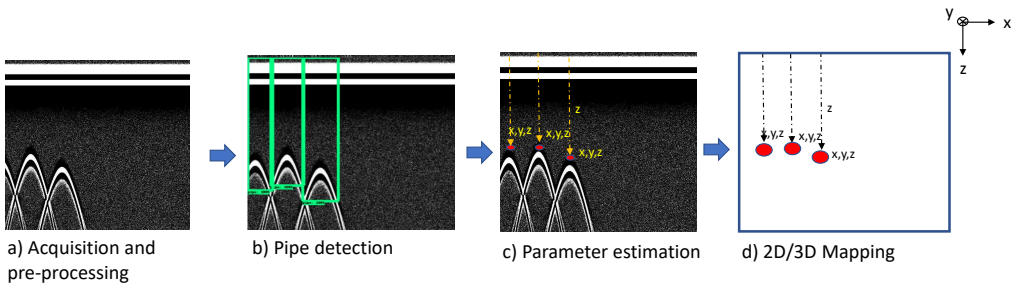

Figure 3.1: Utility locating geometric parameters estimation and mapping process principle.

In 3D utility locating, the identified concept of high level processing steps are illustrated in Figure 3.1. The steps to be followed in the whole sequence are, GPR data acquisition, pipe detection, geometric parameter estimation, and 2D/3D mapping respectively. Whereas in large scale GPR-based utility mapping, depth estimate is the third phase in the overall process leading to 2D or 3D localisation. In the pipe detection stage, the process identifies pipes in the form of hyperbolas using the automated detection models provided in Chapter 2. The process between detection and estimation is demonstrated in the Figure 3.2. As in Figure 3.2, each identified "bounding box" in automatic detection needs to be mapped on the raw B-can with its coordinates. Then, relevant area can be cropped, separated and processed to estimate depth (d), radius (r) and any intended parameters.

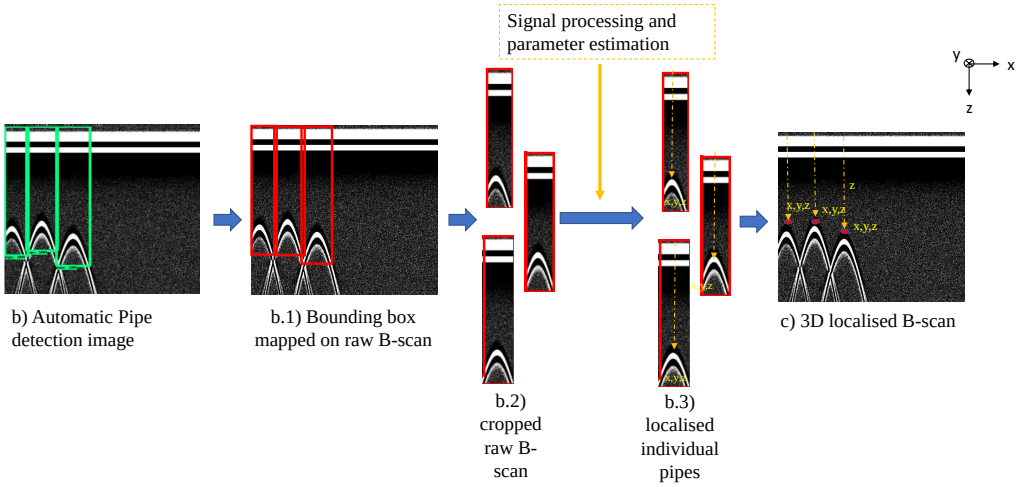

Figure 3.2: Utility parameter estimation process. The steps between Figure 2.1.b and Figure 2.1.c.

In this situation, a single or more non-separable hyperbola may coexist within a single bounding box window. In the case of non-separable multiple hyperbolas, at minimum the top hyperbola can be used to estimate depth (d) according to the single zone hypothesis (non-separable pipes considered as single zone). As a result, the parameter estimate investigation in this chapter was limited to single hyperbola configurations. Following that, during the mapping process, the inverted depth (d) information (z coordinates) shall be integrated to the previously collected (x,y) geo-coordinates (*ie.* through GNSS of the GPR) to permit exact 3D localisation precision as required by the law. Furthermore, the radius (r) and pipe type information must be enhanced with complementary information that increases the mapping data's quality. Furthermore, it increases network safety by taking pipe size into account when determining the no-dig zone surrounding the pipe. Generally, no dig zone boundary supposed to be defined from the surface of the pipe. For example, when the radius (r) of the pipe is unknown, the NDZ (No-Dig Zone) border is measured from the centre of the pipe, assuming the pipe is a point target, as illustrated in Figure 3.3, However, when radius (r) information is included, the NDZ (No-dig zone) border equals to "r + NDZ" from the centre. As a result, the radius (r) information expands the border and enhances safety.

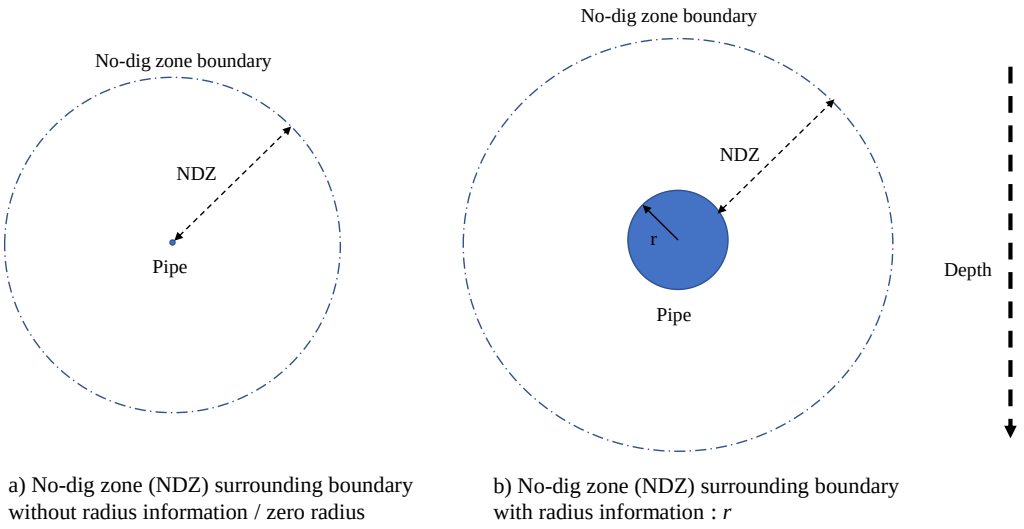

Figure 3.3: No-dig zone boundary with and without radius (r) information.

In overall, every stage shown in Figure 2.1 is evaluated independently using separate data sets without building the whole process flow at this stage. Because, each step must be confirmed with its resilience and limitations before the entire pipeline is built.

In the ground of literature, the estimation of depth (d) and radius (r) has been widely studied by other researchers in the past for example as demonstrated in the literature using Ray-based method [19], Full-Wave Inversion (FWI) [20], Hough transforms [21] and machine learning techniques [96]. Recently, [20] used Ray-based and FWI approaches to develop a novel method to estimate radius (r), depth (d) and relative permittivity (ε) of utility pipes. However, the latter approach demands heavy computational resources. However, none of the methods has proven to be robust and accurate enough to convince the Class A expectation of depth localisation in utility application.

The Ray-based method was used in [19] to detect buried rebars using inverse problem approach, whereas [23] used it to estimate radius (r) of the buried pipe at pre-known velocity (v) condition. [24] tried to invert the radius (r) of buried pipes using Ray-based method coupled with least square fitting techniques. [25] developed a unique VA (velocity analysis) technique for a bistatic GPR that predicts velocity around a hyperbola using a modified Ray-based approach. Whereas, the depth and radius values are known in advance. In our case, the depth, radius, and velocity are all unknown. Which, on the other hand, is extremely challenging to predict. [26] proposes non-linear hyperbola fitting approach to invert the velocity (v) and radius (r) simultaneously. Both approaches were developed for monostatic antenna configuration and derived the hyperbola as a function of depth (d), radius (r) and velocity (v). Although these methods are promising, the error made on the peak localisation in the time signal lead to large errors in the radius (r) estimation [27]. Therefore, there is need of more robust approach.

In this context, among family of several machine learning algorithms, support vector machines (SVMs) have shown promising results for different applications [97–100], including several GPR related applications [101–104]. Moreover, SVM has been extended for regression problems namely Support Vector Regression (SVR). [105] used support vector regression (SVR) based supervised learning method to find the correlation between the complex dielectric permittivity and volumetric water content of the hydraulic concretes based on GPR data. In addition, [106] applied SVR to estimate the thin pavement thickness. Further, [107] used Two-class Support Vector Machines (SVM) to detect debonded sections of the pavement structure. On the

other hand, SVM techniques have shown promising results for underground utility applications. SVMs are used in the detection of utilities by automatic hyperbola detection [28]. [29] worked on SVM-based automatic hyperbola detection for utility network detection. In terms of parameter estimation, [30] proposes to use the features extracted from the rebar hyperbola, whereas [22] uses the skeletonisation technique to estimate radius (r) and depth (d) of rebars in concrete structures. However, the latter approach is applied on images, and it suffers from fitting errors on the skeleton compared with the theoretical hyperbola. In addition, [31] proposes to use the features extracted from the hyperbola and with a SVR models to estimate radius (r) and depth (d) of subsurface cylindrical objects. However, while this approach performed well on synthetic data, it is yet to be validated on real data. Hence, Multi-class SVM and SVR are the potential methods and retained for the parameter estimation study in this thesis.
On the other hand, Artificial Neural Networks (ANNs) are relatively new computational tools that have found extensive utilisation in solving many complex real-world problems. The attractiveness of ANNs comes from their remarkable information processing characteristics appropriate mainly to non-linearity, high parallelism, fault, and noise tolerance, and learning and generalisation capabilities [32]. In GPR applications, [33] adopted ANN and machine learning for the detection and localisation of rebar, while [32] has used Multi-layer perceptron-based ANN for the assessment of rebar size in the reinforcement concrete. However, the approaches were validated only in few rebars and the robustness is still to be contested for broad applications with robust features. Since input features highly dominate the model's performance [31] along with other factors such as database size and data set's morphology, the objective of this study is to evaluate the performance of ANN-based regression model combined with set of local features proposed by [31] to estimate velocity (v), depth (d) and radius (r) of buried cylindrical pipes considered as three unique and independent parameters. Even though the velocity (v) is correlated with depth (d), the conversion of velocity (v) from the depth (d) information represents only the group velocity (v) of the stratified medium between the ground surface and the object at the apex of the hyperbola. Thus, to overcome this limitation, velocity (v) is considered as an independent parameter in this study.

In addition, all above methods are based on a prior extraction of features from the data (B-scan). However, identification of the correct local features still remains a challenge. Deep learning approaches brought great attention due to their proven ability to automatically extract features from the input data in order to perform classification or estimation (by regression) precisely and rigorously in various fields. Faster R-CNN and Yolo models have been found in literature for detection of utility pipe's in two steps: a proposal of region of interest followed by detection of hyperbolas in these regions. However, the deep learning models were seldom evaluated for the estimation of geometrical parameters such as depth (d) and radius (r) of the buried pipes. Most of such machine learning methods for GPR are based on an analysis of B-scans in image format. The annotation is done on the images and the algorithms of detection, classification or estimation (by regression) relying on pixels. Such signal to image conversion and colour scale normalisation causes degradation in the information. Hence, it limits the applicability of DCNN based algorithms for the GPR based parameter estimation purposes (depth and radius). As a result, we have studied a DCNN based parameter estimation model that works on B-scan signals. The objective of the proposed DCNN model work is to evaluate the ability of a deep learning method applied to GPR 2D "raw signals" instead of "pictures" for the depth (d) and radius (r) estimation of the pipe.

Because, normally, the DCNN uses images instead of raw signal. In such a case, the signal's dynamic information is lost by rescaling the signal amplitude to a certain colour scale. Furthermore, many authors used different pre-processing steps on the data to improve the readability of the hyperbola and remove noise and clutter. In some cases, threshold and filtering functions were applied to differentiate the target (hyperbola) from the background (*ie.* refer IOU thresh-

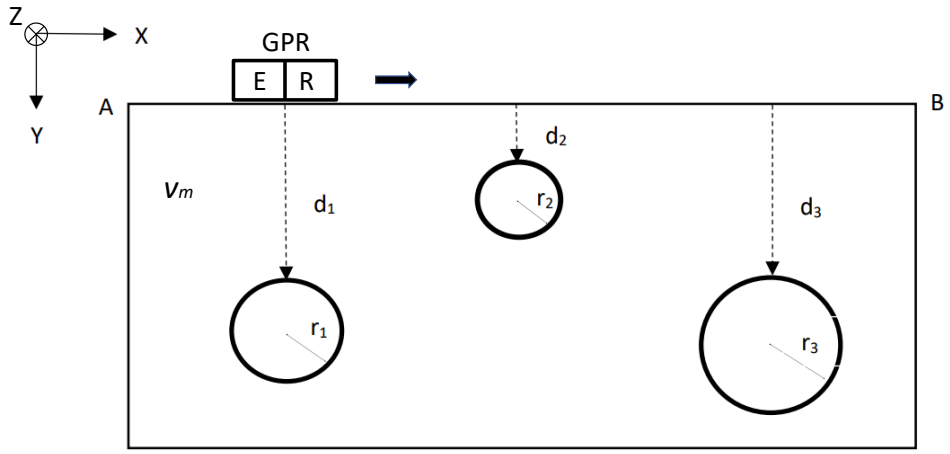

Figure 3.4: Example of a GPR, buried cylinders in the subsurface and estimated parameters. E - emitter, R - receiver of the GPR.

old in chapter 2). However, the pre-processing steps require rescaling of the image, and it causes the loss of information. To overcome this challenges, raw B-scans have been utilised in this particular study. Thus, as an objective, the complex and sequential GPR signal pre-processing steps can be avoided in the localisation of the buried pipes.

To be summarised, based on the literature review, several approaches were adopted for this study considering advantages and disadvantages of each approach for the large GPR based utility mapping application. The objective for the multiple proposed models in this Chapter is to compare the performance of Ray-based method, multi-class SVM classification, and SVR and DCNN to estimate velocity (v), depth (d) and radius (r) of buried cylindrical pipes. The objectives and limitations of each approach are explained in the latter sections of the Chapter. The proposed objectives are illustrated in the Figure 3.4. The depth (d_i) from the surface AB to the top of the cylindrical object; velocity (v_m) of the surrounding medium of the buried cylindrical objects; and radius (r_i) of the buried cylindrical objects are the parameters of interest as seen in the Figure 3.4. Due to the lack of sufficient experimental data with ground truth at this stage of the research, the study is carried out on numerical GPR data (B-scan from various configurations) created using the FDTD based software 2D gprMax [108] and an open-air experimentation and validations were performed for SVM, SVR and ANN, and the results were presented in the Chapter 4.

In addition to the parameter study proposed in the above, the study also extended to evaluate a possible method to classify the type of detected pipes, whether it is a metal or PVC. The few works discovered in the literature for buried object classification on GPR data are [34], [35], [36], [37]. In this context [34] investigated a method for classifying underground objects between cavities and pipes using a physical signal processing method. The suggested approach uses Instantaneous Phase Analysis of GPR Data. Three-dimensional convolutional networks were utilised in [34] to recognise spatial underground objects such as pipe, cavity, manhole, and subsoil. While that, in particular, [35] explored machine learning based classification of underground utility pipes. To classify utility pipe type from GPR data, the author used wavelet transform, Fourier transform, and SVM. To identify buried utility materials, [37] used discrete cosine transform (DCT) coefficients as characteristics fed to the support vector machine (SVM) classifier. In both [35], the author achieved good results at various levels.

The mentioned research served as the impetus for the proposed direction of study in this work. However, in this work, we have used both KNN (K-nearest neighbour) and SVM machine learning algorithms to evaluate the performance using the A-scan. The model was validated

numerically using 2D gprMax data as preliminary study.

The physical and machine learning algorithms covered in this chapter are illustrated in the Figure 3.5.

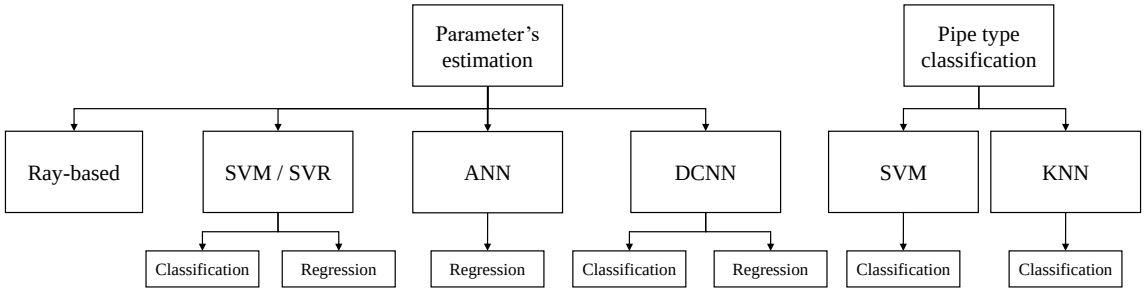

Figure 3.5: Physical and machine learning algorithms covered in this chapter with their objectives.

3.2 Estimation models: Ray-based, SVM and ANN

3.2.1 Methodology

In this section, three parameters related to embedded pipes will be estimated: radius (r), and depth (d) of the pipe and the propagation velocity (v). In order to do so, four approaches have been considered, broadly categorised into two groups: Ray-based and Machine learning models. The Ray-based method can be implemented in two ways: concurrent estimation of v, d and r parameters and, perform radius (r) estimation at a pre-known propagation velocity (v) of the medium. This is achieved using an appropriate non-linear least-square optimisation algorithm on the extracted hyperbola against analytical geometrical Ray-based objective function.

On the other hand, the machine learning method namely, SVM is used. SVM is implemented as either a Multi-class classification model or a regression model, the SVR to estimate the v, d and r parameters. In addition, Artificial Neural Networks (ANNs) was studied for the estimation of v, d and r by overcoming limitations in SVR.

3.2.1.a Ray-based method

The hyperbolic signatures in GPR data are created by reflections that occur on the target surface and due to changing distance between the antenna and the target.
As shown in Figure 3.6, it is the case of monostatic antenna configuration, assuming that the reflection takes place on the line between the antenna phase centre and the centre of the cylinder. When the pipe orientation axis is perpendicular to the horizontal displacement axis of the GPR, two-way travel time t_i of the reflected wave on the cylindrical surface appears at two-way travel time distance $t_i^{'}$ on A-scan of particular GPR position. Whereas, the $t_i = t_i^{'}$. Hence, the geometrical relationship can be defined as in Equation 3.1 [19]:

$$\Delta x_i^2 = \frac{v^2 t_i^2}{4} + vrt_i - (d^2 + 2dr) \tag{3.1}$$

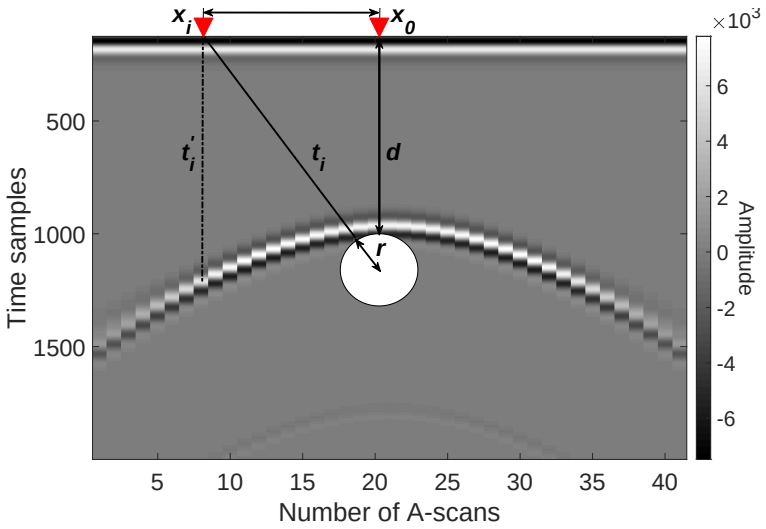

Figure 3.6: Geometrical Ray-based relationship of a buried metallic pipe.

where, $\Delta x_i^2 = (x_i - x_0)^2$ is derived as a polynomial function of v, r, d and t_i, i denotes the GPR's horizontal spatial position. From , for a given hyperbola, the v, r, d parameters can be inverted as they remain constant while Δx_i and t_i are the variable components. To do so, unconstrained Newton quasi non-linear optimisation algorithm was adopted based on the assumption that v of the medium is constant around the hyperbola (homogeneous and dispersiveness medium without anisotropic properties). The unconstrained solver was chosen because the inversion results are highly sensitive to the boundary conditions and starting values. In addition, each hyperbola requires fine-tuning of the boundary conditions, which is difficult for large data sets with broad configurations in terms of velocity (v), depth (d) and radius (r). Hence, the unconstrained Newton quasi non-linear optimisation algorithm was adopted to generalise the model, which is independent of boundary conditions.

$$(v, d, r) = \text{argmin}_{(\xi,\tau,\zeta)} \sum_{i=1}^{N} \left[\Delta x^2 \left(\xi, \tau, \zeta, t_i\right) - \Delta x_i^2\right]^2 \tag{3.2}$$

whereas ξ, τ, ζ are the intermediate values of v, d and r respectively.

3.2.1.b Support vector machine (SVM) classification and regression

The second family of methods studied in this thesis are the SVM and the SVR. These methods are adapted to estimate the v, d and r parameters with three independent trained models. For each parameter estimation, the extracted hyperbola features are considered as inputs while v, d and r parameters are the predicted values.
While SVM is based on the structural risk minimisation principle, SVR is a very specific class of non-parametric regression methods based on SVM. Among two different approaches of SVR, ϵ-SVR is adopted for this study. Multi class SVM is applied with the perception that the labeled parameters are classified into set of different classes. While SVR is adopted when parameters are considered as continuous value problem.

Let $\mathbf{T_S} = \{(\mathbf{z_1}, S_1), \ldots, (\mathbf{z_N}, S_N)\}$ be composed of N pairs of observation, with $\mathbf{z_i}$ being the features vector associated with the ith B-scan and S_i is the label. In case of radius (r) estimation, we have $S_i \in r$, for velocity, we have $S_i \in v$ and for depth (d) estimation, we have $S_i \in d$; where r, v and d are as defined in the next section. We begin by describing the case of the linear function f, given by [109]:

$$f(\mathbf{z}) = \langle \mathbf{a}, \mathbf{z} \rangle + \mathbf{b} \text{ with } \mathbf{z} \in \mathbb{X}, b \in \mathbb{R} \tag{3.3}$$

where a,b are weight vector and bias respectively. $\langle \cdot, \cdot \rangle$ represents the dot product in $\mathbb{X}$ (where $\mathbb{X}$ denotes the space of the input patterns).
In case of classification, the optimisation problem is expressed as ([107]):

$$\begin{aligned} &\text{minimize}_{a,b,\xi} \quad \frac{1}{2}a^T a + C\sum_{i=1}^{N}\xi_i \\ &\text{subject to} \begin{cases} S_i(a^T\Phi(\mathbf{z}_i)+b) \geq 1-\xi_i, \\ \xi_i \geq 0, i = 1,2,\ldots,N \end{cases} \end{aligned} \tag{3.4}$$

where Φ is the kernel function that maps vectors into higher dimensional functions, ξ is the slack variable introduced to reduce training errors and $C > 0$ is the regularisation parameter. The solution $f(\mathbf{x})$ uses Lagrange multipliers and is given by [107]:

$$f(\mathbf{z}) = sgn\left\{\sum_{i=1}^{N} S_i\alpha_i\Phi(\mathbf{z}_i,\mathbf{z}) + b\right\} \tag{3.5}$$

where sgn is the sign function and, α_i are Lagrange multipliers and S_i are the class labels.
In case of regression, an additional parameter $\mathfrak{e}$ is introduced. In addition, in this case ξ and ξ_i^* are the slack variables included to reduce training errors. Thus, Equation 3.4 will be rewritten as [109]:

$$\begin{aligned} &\text{minimize}_{a,b,\xi} \quad \frac{1}{2}a^T a + C\sum_{i=1}^{N}(\xi_i+\xi_i^*) \\ &\text{subject to} \begin{cases} S_i - \langle a,\mathbf{z}_i\rangle - b \leq \mathfrak{e}+\xi_i, \\ \langle a,\mathbf{z}_i\rangle + b - S_i \leq \mathfrak{e}+\xi_i^* \\ \xi_i,\xi_i^* \geq 0, i = 1,2,\ldots,N \end{cases} \end{aligned} \tag{3.6}$$

The solution for non-linear regression is given by [109] as:

$$f(\mathbf{z}) = \sum_{i=0}^{N}(\alpha_i - \alpha_i^*)\Phi(\mathbf{z}_i,\mathbf{z}) + b \tag{3.7}$$

where α_i and α_i^* are Lagrange multipliers. Further, in case of a gaussian kernal function, Φ can be defined as,

$$\Phi(\mathbf{z},\mathbf{z}_i) = e^{-\frac{|\mathbf{z}-\mathbf{z}_i|^2}{2\sigma^2}} \tag{3.8}$$

and this is often simplified as,

$$\Phi(\mathbf{z},\mathbf{z}_i) = e^{-\gamma|\mathbf{z}-\mathbf{z}_i|^2} \tag{3.9}$$

whereas the γ, C and $\mathfrak{e}$ are optimised in LIBSVM which is a machine learning library in Matlab for one or multi class classification using SVM.

There were three separate multi-class SVM models (SVM_r, SVM_d, SVM_v) and three separate ϵ-SVR models (SVR_r, SVR_d, SVR_v) were trained independently with its corresponding labels. Whereas, separate models enable single parameter inversion at a time by solely depend on the proposed six features. Further, the same set of training and testing data were utilised in all models to avoid any bias in the results due to data set difference.

3.2.1.c Artificial Neural Network - MLP

On the other hand, Artificial Neural Networks (ANNs) are relatively new computational tools that have found extensive utilisation in solving many complex real-world problems. The attractiveness of ANNs comes from their remarkable information processing characteristics appropriate mainly to non-linearity, high parallelism, fault, and noise tolerance, and learning and generalisation capabilities [32]. In the GPR applications, [33] adopted ANN and machine learning for the detection and localisation of rebar, while [32] has used Multi-layer perceptron-based ANN for the assessment of rebar size in the reinforcement concrete. However, the approaches were validated only in few rebars and the robustness is still to be contested for broad applications with robust features. Since input features highly dominate the model's performance [31] along with other factors such as database size and data set's morphology, the objective of this study is therefore to evaluate the performance of ANN-based regression model combined with a set of local features proposed by [31] to estimate velocity (v), depth (d) and radius (r) of buried cylindrical pipes considered as three unique and independent parameters. Even though the velocity (v) is correlated with depth (d), the conversion of velocity (v) from the depth (d) information represents only the group velocity (v) of the stratified medium between the ground surface and the object at the apex of the hyperbola. Thus, to overcome this limitation, velocity (v) is considered as an independent parameter in this study. Due to the lack of suitable experimental data at this stage of the research, the evaluation is carried out on numerical GPR data (B-scan from various configurations) created using the FDTD based software 2D gprMax [108].

Three parameters related to embedded pipes namely, radius (r) and depth (d) of the pipe and the propagation velocity (v) will be estimated in this work using 3 separate ANN models corresponding to each parameter. Hence, the ANN model used in this study was a Multi-Layer Perceptron (MLP), a feed-forward neural network. MLP-based ANN is characterized by three layers of neurons (input layer, hidden layer and output layer) with non-linear activation functions at the hidden layer units. In order to identify the best correlation between the independent (6 features) and the dependent variables (v or d or r), two feed-forward MLPs were used, one for non-linear mapping of standardised independent variables (z) into a single predicted score named α, the other one for linear mapping of the dependent variable (s) into a predicted score named β. These two networks simultaneously mapped from the inputs z and s to the scores α and β, respectively. A particular cost function forced the correlation between α and β to be maximized by finding the optimal values of weights and bias. For both MLP, the input variable vectors z and s were mapped to the neurons in the hidden layer α and β as follows:

$$\begin{cases} h_z = \tanh\left(W_z \cdot z + b_z\right) \\ h_s = W_s \cdot s + b_s \end{cases} \tag{3.10}$$

where W_z and W_s are the weight matrices between input layer and hidden layer and b_z and b_s are the bias parameter vectors of hidden layer units. The scores α and β were obtained from a linear combination of the hidden neurons vectors h_z and h_s, respectively, with

$$\begin{cases} \alpha = \tilde{W}_z \cdot h_z + \tilde{b}_z \\ \beta = \tilde{W}_s \cdot h_s + \tilde{b}_s \end{cases} \tag{3.11}$$

The cost function $\Gamma = -\operatorname{corr}(\alpha, \beta)$ was used to maximize the correlation between α and β, and was minimized by finding the optimal values of W_z, W_s, b_z, b_s, $\tilde{W}_z$, $\tilde{W}_s$, $\tilde{b}_z$ and $\tilde{b}_s$ (where $\tilde{W}$ represent the weight matrices of the respective hidden layers). In addition, the constraints $\langle\alpha\rangle = \langle\beta\rangle = 0$ and $\langle\alpha^2\rangle = \langle\beta^2\rangle = 1$ were applied, which were input into a modified cost function (Γ_{m}):

$$\Gamma_m = -\operatorname{corr}(\alpha, \beta) + \langle\alpha\rangle + \langle\beta\rangle + \sqrt{\langle\alpha^2\rangle - 1} + \sqrt{\langle\beta^2\rangle - 1} \tag{3.12}$$

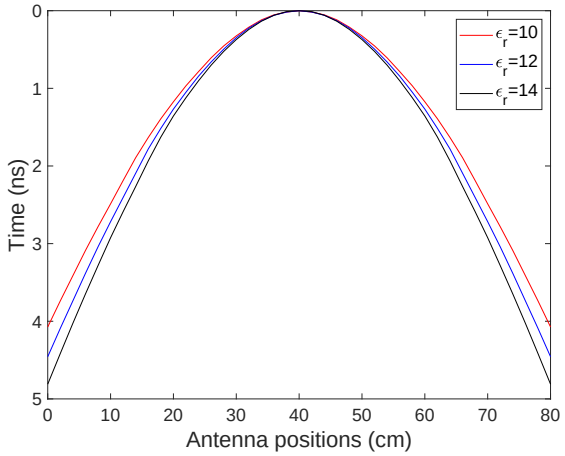

Figure 3.7: Examples of hyperbola shape variation across different velocity (v) at same depth (d) and radius (r), normalised at the apex.

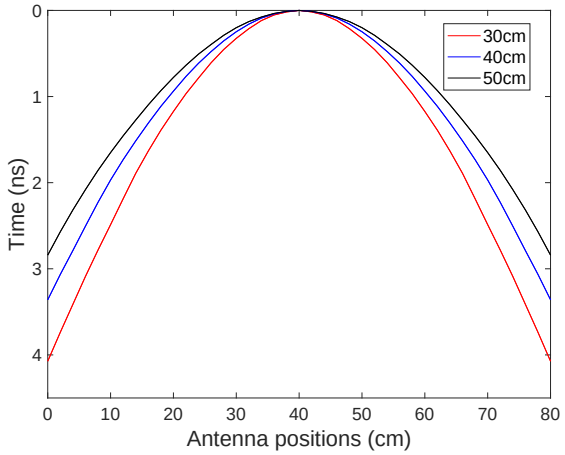

Figure 3.8: Examples of hyperbola shape variation across different depth (d) at same velocity (v) and radius (r), normalised at the apex.

3.2.1.d Feature Selection

The feature selection for the proposed machine learning models is based on the hypothesis that a pipe with a large radius (r) yields flatter hyperbola and the tail of the hyperbola is observed to become more parallel in the same medium velocity (v) as observed from experiments (argued by [27]). This pattern correlation relates the hyperbola sector with the three parameters under study, namely, v, d and r. Whereas, $v = C/\sqrt{\varepsilon}$, and C is the speed of electromagnetic waves in free space.

The Figures 3.7, 3.8, 3.9 illustrate how hyperbola shape varies across different v, d and r. The physical reason for such fluctuation, on the other hand, may be found in the Figure 3.6, and the Equation 3.1. The travel time t_i at every given horizontal position x_i defines the form of a hyperbola. The value of t_i relatively increases with increasing relative permittivity of the medium at a given depth and radius configuration. As a result, the steep of the hyperbola rises. As a result, the shape narrows as seen in Figure 3.7. For a given medium permittivity and radius configuration, the ratio of ti to $t0$ (travel time at apex) rises as depth drops ($t0$ decreases). As a consequence, as shown in Figure 3.8, the hyperbola is narrower with decreasing depth and larger with increased depth. This is in contrast to the permittivity fluctuation. In the case of radius, however, when permittivity and depth are constant, ti becomes substantially shorter as

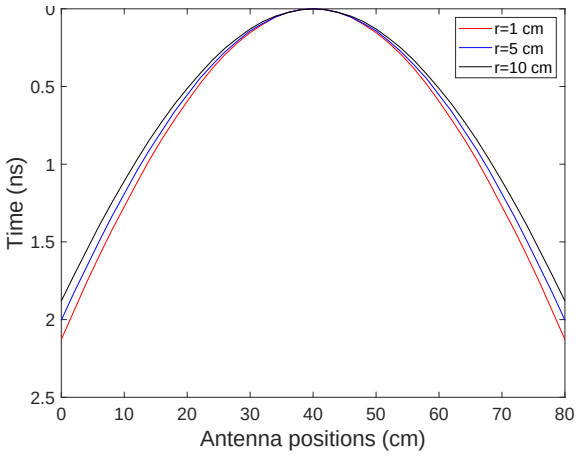

Figure 3.9: Examples of hyperbola shape variation across different radii at same velocity (v) and depth (d), normalised at the apex.

the pipe's size grows. As a result, the Hyperbola becomes wider as the pipe radius increases, as shown in Figure 3.9.

Furthermore, the Equation 3.1 may be rearranged to calculate the hyperbola's slope at any horizontal location x_i. As a result, the t as a function x can be constructed. As a result, the slope of the hyperbola, which is the first derivative ($\frac{dt}{dx}$), can be defined as follows:

$$\frac{dt}{dx} = \frac{4 \cdot \sqrt{\varepsilon} \cdot x}{C \cdot \sqrt{x^2 + (d+r)^2}} \tag{3.13}$$

Thus, according to the Equation 3.13, it is obvious that the slope ($\frac{dt}{dx}$) is,

- Proportional to the permittivity (ε). So, the hyperbola shape is narrower with high permittivity (validating the trend in Figure 3.7).
- Inversely proportional to the depth (d). As a result, the slope will be low at higher depth (validating the trend in Figure 3.8).
- Inversely proportional to the radius (r), and validating the pattern in Figure 3.9.

Furthermore, when x » (d+r) (x is very much greater than (d+r)), the fraction of x and $\sqrt{x^2 + (d+r)^2}$, becomes nearly 1. Therefore, the slope can be approximated to as asymptote,

$$\frac{dt}{dx} \approx \frac{4 \cdot \sqrt{\varepsilon}}{C} \tag{3.14}$$

This indicates that, when x » (d+R), the slope of the hyperbola can yield the value of relative permittivity (ε) of the medium according to Equation 3.14. This method may be used to make an approximation of relative permittivity. Furthermore, it establishes that, the hyperbola slope at infinity of x for a given homogeneous material will be the same regardless of the depth and radius of the pipe (slopes are parallel).

For example, when a pipe at d = 1 - 2 m, r = 0.01 m, if the slope ($\frac{dt}{dx}$) is measured at 1 - 10 m far from the apex, the relative estimation error of relative permittivity (ε) can vary as shown in the Figure 3.10.

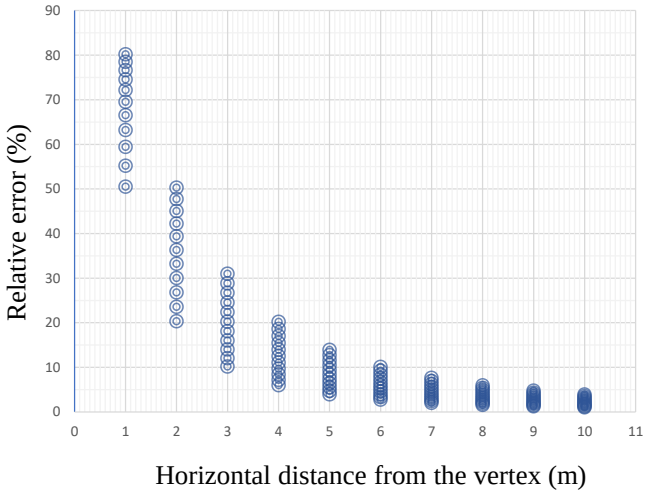

Figure 3.10: Example of relative error variation in hyperbola slope based relative permittivity estimation. When a pipe at d = 1 - 2 m, r = 0.01 m.

According to Figure 3.10, the slope-based permittivity estimation produces substantial estimation error closer to the vertices. Nonetheless, when x = 10, the relative error was reduced to less than 5%. However, it is difficult to extend a hyperbola beyond 10 m since the B-scan signal clarity (visibility of the hyperbola's leg) is weak at long distances and is further restricted by the radiation pattern of the GPR antenna. As a result, the approach cannot be utilised to estimate permittivity precisely for utility applications. It is, however, an alternate strategy for approximation. This study does not include any further examination of this method.

Based on the observed hyperbola shape variation pattern, the features for machine learning were selected to fully represent the hyperbola shape from the apex and closer proximity, while minimising the dimension of the features. In this context, the B-scan data are initially preprocessed to obtain the six features (t_a, t_b, t_c, t_d, t_e, t_f) for a B-scan as showed in Figure 3.11. These features are described as follows: t_a is the two-way travel time from the ground to the apex of the hyperbola, t_b is the mean of first 25 % of hyperbola data points, t_c is the mean of 25 % to 75 % of hyperbola data points, t_d is the mean of 75 % to 100 % of hyperbola data points, t_f is the maximum travel time within the window and t_e is the travel time difference (*i.e.* $t_f - t_a$).

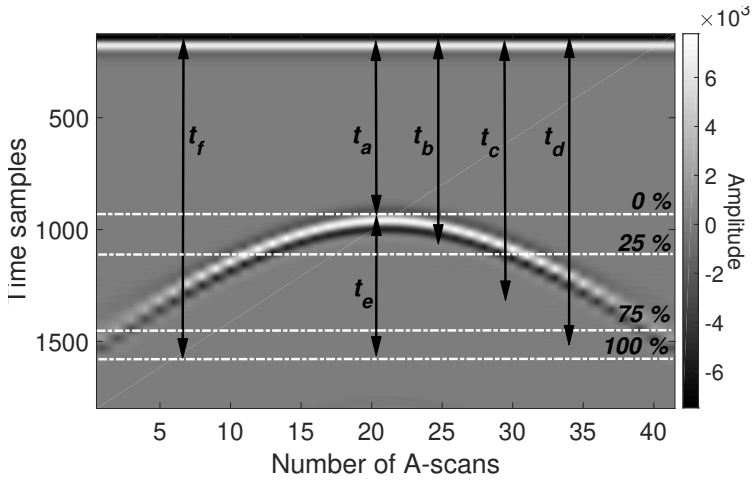

Figure 3.11: Representation of travel-time based feature selection from the hyperbola on a B-scan; $\varepsilon_r = 6$, $r = 1$ cm, $d = 30$ cm, due to a metallic pipe.

The adopted Ray-based and machine learning methods presented hereafter are implemented using the resulting feature sets of the B-scans. In this work, t_i was picked as shown in the Figure 3.12. The minimum peak of the direct wave and the maximum peak of the reflected wave was considered as the actual travel time between the source and the object. Because, in this case, the antenna radiation source, ground surface and direct coupling wavelets are overlapped each other.The GPR configuration of the synthetic data are described in the section below.

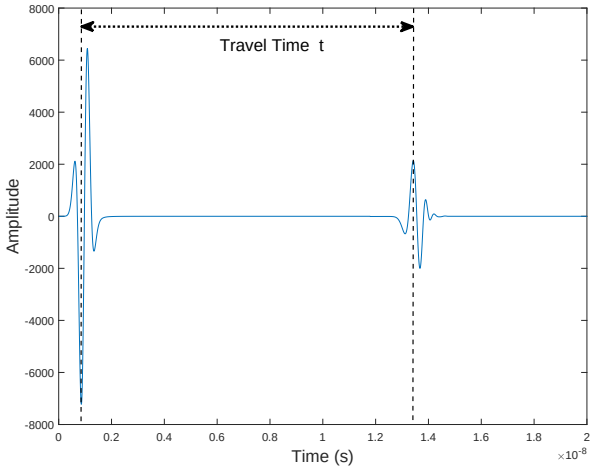

Figure 3.12: Travel time estimation from A-scan for hyperbola formation. Whereas t = t_i.

In summary, the parameters estimation models were developed and numerically validated using simulated gprMax based GPR data and then in open-air experimentation. Whereas, the models utilise the above-mentioned machine learning approaches such as SVM, ANN, and SVR, and coupled with the suggested features as input. As a result, the numerical analysis is described in the section below.

3.2.2 Numerical validation on noiseless data

In order to validate the proposed estimation approaches, simple homogeneous dispersive 2D gprMax model is used [108]. gprMax is an open source simulation software developed in Python environment for forward modelling of GPR that uses Finite Difference Time Domain (FDTD) to simulate EM wave propagation solving Maxwell's equations [108].

In our work, the domain size is defined as 1.0 m × 1.0 m. The domain mesh sizes are $\Delta x = 2.5 \times 10^{-3}$ m, $\Delta y = 2.5 \times 10^{-3}$ m and the time sampling resolution is $\Delta t = 5.89 \times 10^{-12}$ s which satisfies Courant, Freidrichs and Lewy condition [108]. In terms of the source, a Hertzian dipole is excited with a point source at zero antenna offset, and at a height of 5 mm, from the surface. The excitation waveform was the ricker wavelet, centred at $f_c = 1.5$ GHz.
The model consists of a metallic cylindrical pipe embedded within a single layer as described in Figure 3.6. The permittivity of the layer (ε_r) is varied between 6 and 16 with steps of 0.33. The cylindrical pipe's positioning depth (d) varies between 30 cm to 70 cm with incremental steps of 10 cm. The radius (r) of the pipe on the other hand are 1 cm, 2 cm, 3 cm, 5 cm, 7 cm, 10 cm with 3 different conductivity (σ) levels at 1×10^{-5} S/m, 1×10^{-3} S/m, 1×10^{-1} S/m. The spatial resolution between adjacent A-scans is 2 cm. Thus, a total of 2610 unique B-scans were created, with each B-scan made up of 41 A-scans. The summary of configuration is presented in the Table 3.1

Configuration	Values
Pulse type and centre frequency (f_c)	Ricker pulse, 1500 MHz
Antenna off-set, type	Zero-offset, hertzian dipole
Antenna height	5 mm
Medium's relative permittivity (ε_r)	6 to 16
Medium's conductivity (σ)	1×10^{-5} S/m, 1×10^{-3} S/m , 1×10^{-2} S/m
Acquisition step size (Δx)	2 cm
PML boundary	10 discrete boxes + 10 cm clearance
Pipe's depth (d)	0.3 m to 0.7 m
Pipe's radius (r)	$10, 20, 30, 50, 70, 100$ mm
Number of A-scans per B-scan	41 (0.8 m)
B-scans dimension	$41 * 7200$ (A-scans * time samples)
Pipe's type	all metallic
Number of B-scans	2610

Table 3.1: The summary of gprMax model configurations.

3.2.2.a Implementation of SVM and SVR

Feature extraction is performed on each B-scan signals to obtain the features' matrix **Z**. The data is then divided into two sets: learning and testing, with learn-to-test ratio 80 %:20 %. The ratio was chosen as an optimised value in terms of model performance while maximising the size of training data with reasonable amount of test data. The test data is independent of the learning data. Both SVM and SVR are then implemented using the SVM toolbox in MATLAB® 2020a. A k-fold cross validation technique is used (with $k = 5$) in the learning stage to validate the model in the learning phase, avoid over-fitting [107] and also provide insight on the model's behaviour to unknown data sets.
A loss function, namely average root mean square error (RMSE) is used to determine the optimal values for each method. While SVM adopted fine-Gaussian kernel one-to-one multi-class classification, ϵ-SVR adopted fine-Gaussian kernel. In case of SVM, two parameters namely c and γ are optimized whereas an additional ϵ parameter in case of ϵ-SVR were optimised against the RMSE loss function. In this study, described hyperparameters were optimised using Bayesian optimisation algorithm. The Table 3.2 below is an example of how the input features and labels are organized for model training. In fact, each row provides the features and label for a single hyperbola. The features are attributed to the first six columns, and the label (ground truth) is assigned to the last column, in this case v, d, or r.

t_a (ns)	t_b (ns)	t_c (ns)	t_d (ns)	t_f (ns)	t_e (ns)	Label
10.1	10.2	11.0	12.9	14.1	4.01	0.783528
11.2	11.3	11.9	13.3	14.3	3.06	0.866025
12.1	12.2	12.9	14.4	15.4	3.29	0.801784
6.94	7.04	7.80	9.46	10.5	3.56	0.878561
13.3	13.3	13.7	14.7	15.3	1.97	1.019441
5.24	5.31	5.90	7.14	7.90	2.66	1.162476
10.7	10.8	11.2	12.2	12.9	2.18	1.039438

Table 3.2: Example of input feature and label layout for model training.

3.2.2.b Results and Discussion

Table 3.3 compares the performance results of the mean relative error (mean err) and the maximum relative error in terms of 95^{th} percentile (P_{95}) were computed using the Equation 3.15:

$$err = \left| \frac{(M_{est} - M_{act})}{M_{act}} \right| \times 100 \tag{3.15}$$

where, M_{est} is the estimated value and M_{act} is the actual value.
The relative error (err) of the predicted value with reference to its actual value of every tested data (in this case hyperbolas or their features) was estimated. Then, the relative errors (err) are populated for the whole test results in order to obtain the mean relative error (mean err). Like wise, the mean relative error (mean err) of each parameter estimation (for radius (r), depth (d) and velocity (v)) was calculated separately for every proposed model (Ray-based, SVM_m and SVR_m), that are presented in the Table 3.3.

Method	$err(r)\%$		$err(d)\%$		$err(v)\%$	
	mean	P_{95}	mean	P_{95}	mean	P_{95}
Ray-based concurrent	260%	464%	25.1%	65%	11.3%	22%
Ray-based fixed velocity	120%	353%	-	-	-	-
Regression (SVR)	6.3%	26.5%	0.39%	1%	0.22%	0.5%
Classification (SVM)	2% (10/500)		0% (0/500)		1% (5/500)	

Table 3.3: mean relative error (mean err) and maximum relative error in terms of 95^{th} percentiles (P_{95}) $w.r.t$ radius (r), depth (d) and velocity (v) estimation. The last row represents the number of false alarms in SVM.

In particular, the proposed Ray-based parameter estimation method was applied in two different approaches. First, all parameters such as v, d and r were estimated concurrently. Second, r was estimated for pre-known values of v and d (assuming that the values were already estimated by other methods precisely or ground truth is known). Both approaches adhere to the objective function described in the Equation 3.1 followed by the best fit error minimisation function mentioned in Equation 3.2. Hyperbola obtained from numerical B-scans were fitted with analytical objective function to invert the best value of the coefficients such as v, d and r. From concurrent Ray-based estimation method, mean err are 260%, 25.1%, 11.3%, for r, d and v respectively. Thus, the concurrent parameter estimation's performance is very poor among all tested methods, according to the results in Table 3.3. However, fixed velocity (v) Ray-based method shows relatively better performance for the radius (r) estimation with 120% of mean err. Nevertheless, the mean err is still higher compared with machine learning based methods. The possible contribution of higher uncertainty in Ray-based method arises from the bias in the travel time picking and lack of regularisation techniques. Furthermore, error increases with medium's conductivity (σ) due to the fact that the pulse's high frequency components are attenuated by the medium, and it causes a shift in the signal peak and causes more travel time picking error. Additionally, it is observed that, the estimated results' are highly sensitive to the boundary conditions and starting values of the optimisation process. When optimisation technique is applied to a broad range of r, d and v configurations with single boundary conditions, it sticks in the local minima instead of global minima. Thus, the optimisation requires

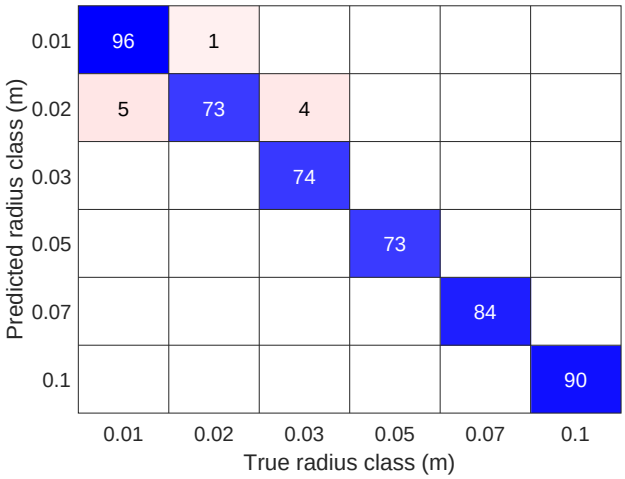

Figure 3.13: Confusion matrix of predicted results for radius (r) estimation based on multi-class SVM classification model. radius (r) classes: 0.01 m, 0.02 m, 0.03 m, 0.05 m, 0.07 m and 0.1 m respectively. Blue boxes indicate number of correct predictions and pink boxes represents number of false alarms.

fine-tuning boundary conditions for each hyperbola, which is not feasible for broad configurations at this stage. Therefore, considering all above drawbacks, the objective function for the Ray-based method must be revised along with more innovative unconstrained optimisation techniques to further improve the performance of the Ray-based method. Furthermore, the objective function may vary based on the frequency configurations, antenna type and antenna offset of the GPR. Due to the time complexity of further parametric study in this direction, the scope of this study is limited to the proposed objective function.

In overall, as seen in Table 3.3, both SVM and SVR show promising results for estimation of v, d and r. SVM shows the highest performance with false alarm of 10/500 for radius (r) estimation, and SVR shows 6.3% mean relative error (mean err) for continuous value problems in the radius (r) estimation. Among Ray-based method, performance of radius (r) estimation is slightly increasing when velocity (v) is pre-known, but not significantly. The obtained mean err of depth (d) and velocity (v) estimation is comparatively very low in the SVR and SVM approach whereas the err is less than 1%.

In the SVM classification approach, multi class one-to-one SVM classification is adopted as another approach for the proposed estimation problem in this study. Nowadays, in new underground utilities installations, the depth (d) and radius (r) are being standardised and motivates to implement the multi-class SVM classifier in order to predict the closest possible class. In this context, each design parameter value of v, d and r of the training data set was trained as a classification label so that the model could predict the closest class for an input data. In this context, three separate SVM models were trained for v, d and r. In this respect, the SVM model results shows 1%, 0%, 2% false alarm rate for v, d and r inversions respectively.

In the radius (r) estimation, as demonstrated in Figure 3.13, the boxes highlighted in blue indicate correct class predictions while pink boxes correspond to false alarms. SVM's false alarms are higher at, 1 cm and the false alarm rate decreases with the increasing radius (r) size. Noticeably, the false alarms are only one class away from the actual value. For example, when the true radius (r) value is 1 cm, the model predicts 96 cases correctly while in 5 cases it falsely classifies as 2 cm. In overall, only 10/500 predictions were found to be false alarms particularly

which come from 1 cm, 2 cm and 3 cm classes with the medium's relative permittivity range of 6-7 (over all permittivity (ε) range of studied data: 6-16). Furthermore, according to the confusion matrix, if all the pipes with a radius of 1 - 3 cm are categorized into a single class, the overall radius estimation can be '100%' accurate. Because false alarms are only seen in 1 - 3 cm classes. Though, the performance of SVM models are better than other approaches, due to the lack of radius (r) standardisation between pipe fabricators it limits the applicability of SVM. SVR models trained based on proposed features as a continuous value problem. Three separate SVR models were trained for r, d and v with the same data sets. According to the Table 3.3, it's observed that, the mean *err* obtained from SVR models are very low compared with ray based methods, whereas the estimated mean *err* corresponds to the SVR models are 6.3%, 0.39%, 1% for r, d and v respectively. According to Figure 3.14 and Figure 3.15, the *err* significantly drops from 120% to 6.3% in case of SVR compared with Ray-based approach. The errors are significantly low at larger radius (r) classes, and relatively higher at high conductivity (σ).

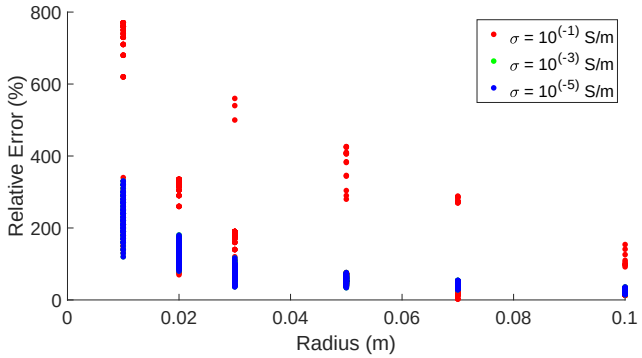

Figure 3.14: Absolute relative error (*err*) in Ray-based estimation of radius (r) at fixed velocity (v) scenario across different radius.

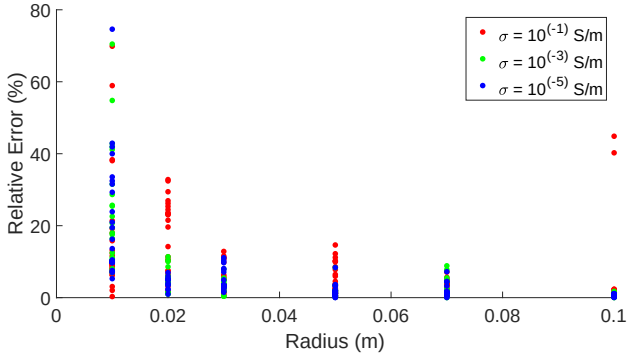

Figure 3.15: Absolute relative error (*err*) in SVR based radius (r) estimation across different radius classes.

Overall mean *err* of the radius (r) estimation is 6.3% as seen from Table 3.3, and based on the Figure 3.16 and Figure 3.17, radius *err* shows an increasing trend with depth (d) and the velocity (v), and it is relatively higher when the medium's conductivity (σ) level is at 1×10^{-1} S/m.

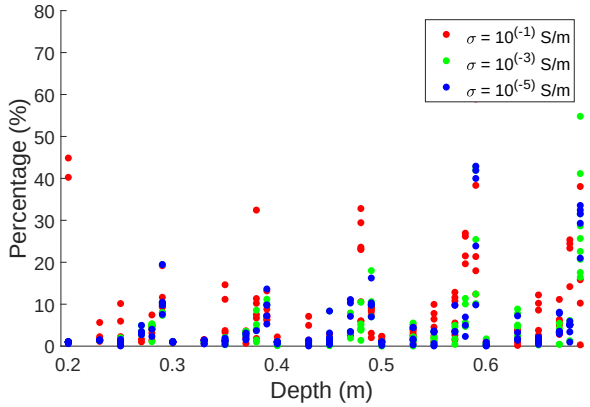

Figure 3.16: Absolute relative error (err) variation in SVR based radius (r) estimation across different depths (d).

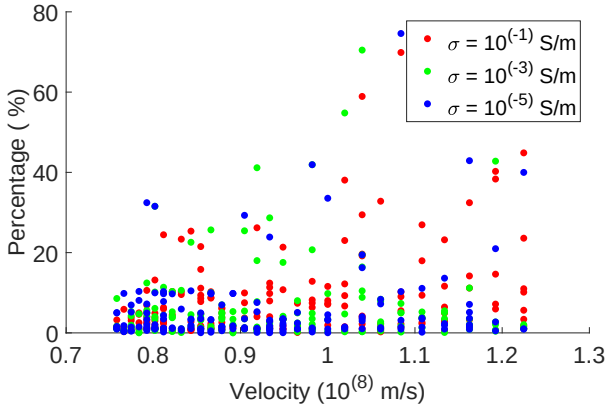

Figure 3.17: Absolute relative error (err) variation in SVR based radius (r) estimation across different velocities (v) of medium.

$$l.e = (M_{est} - M_{act}) \tag{3.16}$$

$$a.l.e = |(M_{est} - M_{act})| \tag{3.17}$$

Referring to histogram in Figure 3.18 based on Equation 3.16, it shows that the linear error (l.e) of the radius estimation varies within the range of -1 to 1 cm; and from Figure 3.20 which is based on Equation 3.17, maximum linear absolute error ($a.l.e$) is nearly 1 cm, it's comparatively low at 10 cm radius class and higher at high conductivity (σ) medium which is plotted in red.

In terms of depth (d) estimation errors in SVR, overall mean err is as low as 0.39% as per the Table 3.3. Furthermore, as shown in the Figure 3.22, the err of the depth (d) estimation remains consistent across the depth classes. Nevertheless, according to Figure 3.23, the depth (d) estimation error is slightly increasing with the velocity (v). Meanwhile, both the figures indicate that depth estimation error is less sensitive to medium's conductivity (σ) variation in contrast to radius (r) estimation.

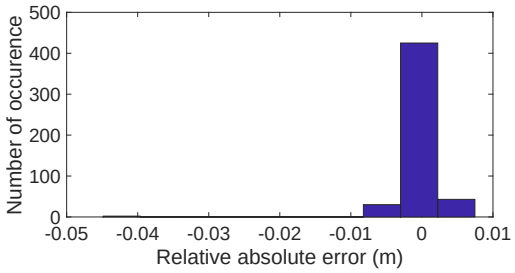

Figure 3.18: SVR-linear error $(l.e)$ of radius estimation.

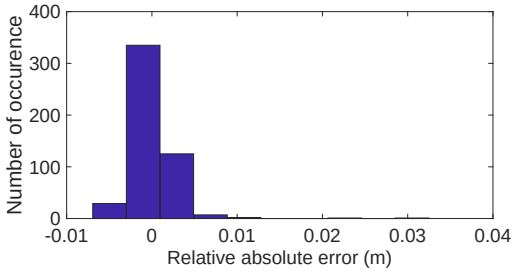

Figure 3.19: SVR-linear error $(l.e)$ of depth estimation.

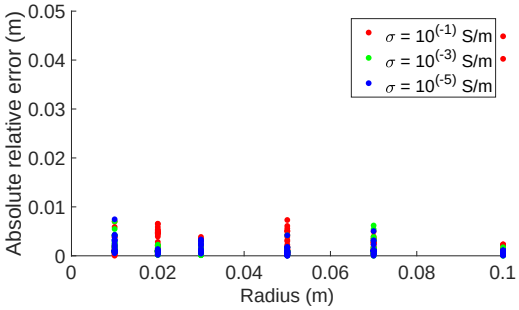

Figure 3.20: SVR-linear absolute relative error $(a.l.e)$ of radius estimation.

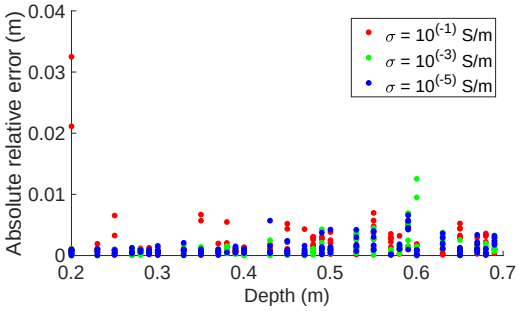

Figure 3.21: SVR-linear absolute relative error $(a.l.e)$ of depth estimation.

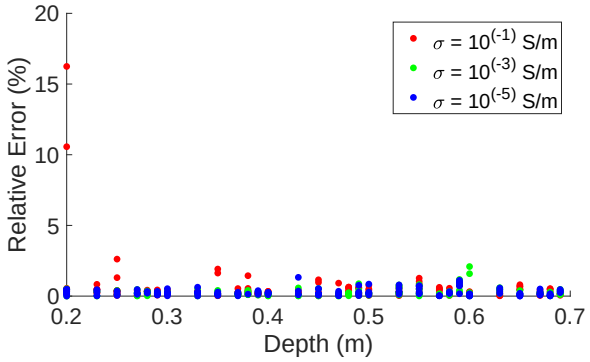

Figure 3.22: Absolute relative error (err) variation in SVR based depth estimation across different depth.

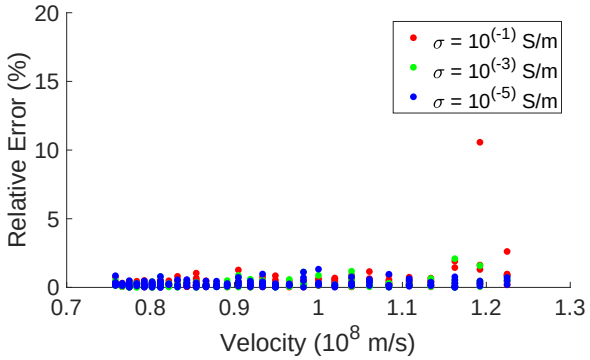

Figure 3.23: Absolute relative error (err) variation in SVR based depth estimation across different velocity (v) of medium.

Likewise, in the linear error terms, according to the Figure 3.19 linear error $l.e$ varies approximately between -5 mm to 5 mm range, and it's increased with higher depth classes as in Figure 3.21.

In the Figure 3.24 and Figure 3.25, it presents the velocity (v) estimation's err variation within different depth (d) and velocity (v) classes, respectively. Overall mean err of velocity (v) estimation remains below 0.5%, however, there are few outliers noticed in the lower depth classes between 0.2 m to 0.25 m, but error level is consistent across other depth classes. In the meantime, err is slightly increasing with the velocity (v), and it doesn't show any significant variation with medium's conductivity except few outliers observed in the higher velocity (v) classes.

The impact of the buried medium's conductivity in the SVR's model performance was analysed in terms of mean err at predefined three conductivity levels such as (σ) $1\times10^{-5}\,\mathrm{S\,m^{-1}}$, $1\times10^{-3}\,\mathrm{S\,m^{-1}}$ and $1\times10^{-1}\,\mathrm{S\,m^{-1}}$, which is presented in the Table 3.4. Overall mean err and the 95th percentile of err increases with the conductivity in r, d and v estimations. For example, though the mean err is 6.3% in radius (r) estimation, the error has increased from 5.3% to 7.7% when (σ) is increased from $1\times10^{-5}\,\mathrm{S\,m^{-1}}$ to $1\times10^{-1}\,\mathrm{S\,m^{-1}}$. However, the error difference is very small between (σ) levels $1\times10^{-5}\,\mathrm{S\,m^{-1}}$, and $1\times10^{-3}\,\mathrm{S\,m^{-1}}$. The trend is similar for both depth d and velocity v as well. However, The depth d and velocity v estimation mean err are well remained below 1%. Radius estimation mean err are larger at higher conductivity medium

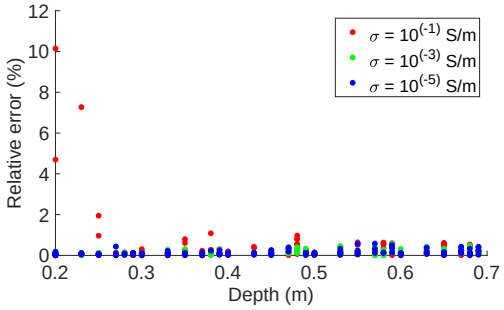

Figure 3.24: Absolute relative error (err) across depth classes.

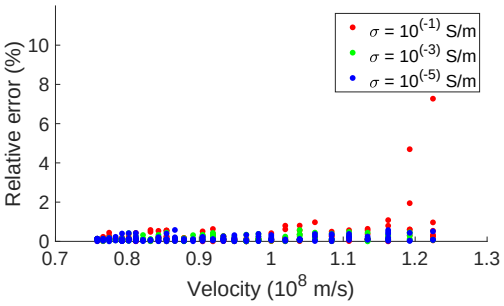

Figure 3.25: SVR- velocity error (err) across velocity (v) classes.

due to the fact that the pulse's frequency components are attenuated by the medium, and it causes changes in the pulse shape and shifts the signal peak and causes travel time picking error. Since the radius (r) is highly sensitive to the travel time error, it leads to large error in the radius (r) estimation.

Furthermore, the findings presented above were produced using estimated features derived from 41 hyperbola points (41 points construct a symmetric hyperbola). It is, in reality, 21 points on a single side of a symmetric hyperbola. The Figures 3.26.a and b, examine the performance of the SVR model in different numbers of hyperbola points used for feature extraction, depth (d) estimation, and radius (r) estimation. The 'step size' between two neighbouring A-scans, on the other hand, stayed at 2 cm. In this scenario, the relative mean absolute error of the SVR models is notably different when the number of hyperbola points is between 10 and 20. However, when the number of participants was increased from 20 to 40, the performance did not significantly improve. As a result, with a step size of 2 cm, 20 points per half hyperbola (40 points in whole hyperbola) are enough for the required feature extraction. As shown, the trend can be seen in both depth (d) and radius (r) estimation.

	$err(r)\%$		$err(d)\%$		$err(v)\%$	
	mean	P_{95}	mean	P_{95}	Mean	P_{95}
Conductivity (σ) $1 \times 10^{-5}\,\mathrm{S\,m^{-1}}$	5.3%	26.04%	0.25%	0.74%	0.12%	0.39%
Conductivity (σ) $1 \times 10^{-3}\,\mathrm{S\,m^{-1}}$	5.9%	25.5%	0.26%	0.75%	0.14%	0.42%
Conductivity (σ) $1 \times 10^{-1}\,\mathrm{S\,m^{-1}}$	7.7%	28.4%	0.52%	1.1%	0.32%	0.79%

Table 3.4: Mean absolute relative error and 95^{th} percentiles (P_{95}) *w.r.t* radius (r), depth (d) and velocity (v) estimation in SVR approach.

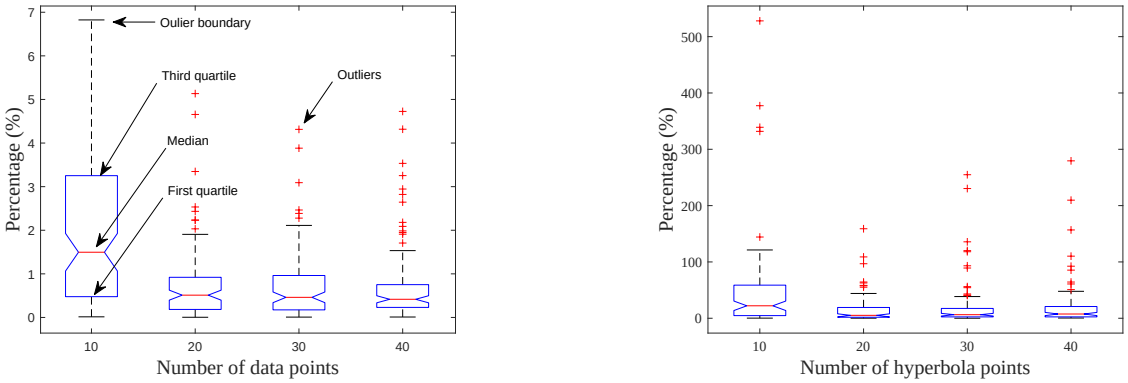

(a) Relative absolute error of depth (d) estimation at different hyperbola points

(b) Relative absolute error of radius (r) estimation at different hyperbola points

Figure 3.26: Relative absolute error of depth (d) and radius (r) estimation at different hyperbola points considered for feature extraction at 2 cm horizontal step size.

Similarly, at 21 points per half hyperbola, the performance of SVR was examined across multiple horizontal resolutions of the hyperbola in terms of varied horizontal step size ranging from 1 cm to 10 cm. In contrast, the Figure 3.27 illustrates that, in depth estimation, the model is not very sensitive to horizontal resolution. As a result, it keeps the mean relative error (mean *err*) below 1%. The error distribution at 2 cm, on the other hand, is significantly narrower. At 1 cm - 4 cm, the radius (r) estimate performance is substantially better.

In summary, for radius estimate, a step size resolution of 1 - 4 cm is recommended, while depth estimation can tolerate up to 1 - 10 cm without a major performance reduction. In fact, a larger step size can speed up GPR acquisition. In the meanwhile, 20 points is adequate in terms of hyperbola points.

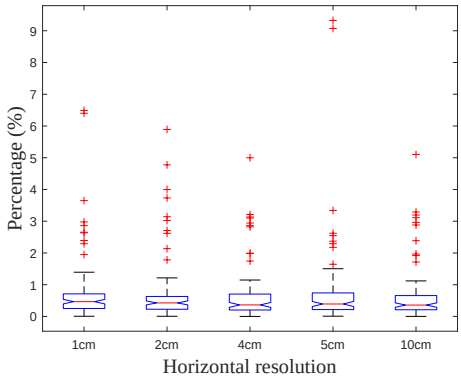

(a) Relative absolute error of depth (d) estimation at different horizontal resolution step sizes

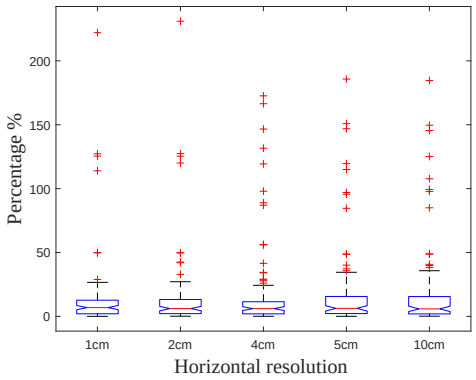

(b) Relative absolute error of radius (r) estimation at different horizontal resolution step sizes

Figure 3.27: Relative absolute error of depth (d) and radius (r) estimation at different horizontal resolution step size and at 21 points of half hyperbola.

In this subsection, we presented a comparative study to analyse the performance of Ray-based method, SVM and SVR to estimate velocity (v), depth (d) and radius (r) of buried cylindrical pipes. It shows that in this particular study with the proposed feature set, the SVM and SVR performance were much better than the Ray-based method. A detail analysis *w.r.t.* radius (r), depth (d) and velocity (v) estimation was presented. The overall results suggest that the depth (d) and velocity (v) estimation accuracy is more robust than the radius (r) estimation in the proposed model. Furthermore, between SVR and SVM, due to the lack of radius (r) standardisation between pipe fabricators, it is difficult to obtain a conclusive model for parameter estimation and thereby it constitutes a limit for the applicability of multi-class SVM. Ray-based method suffers from many factors, including trapped in the local minima during the optimisation. However, it's still be a choice for an approximated estimation if objective function and optimisation techniques are further modified accounting all factors discussed in this work, but it requires further study in this direction. The radius (r) estimation is less accurate compared with other parameters (d and v) due to fact that, radius (r) is highly sensitive to the travel time error, and the support vector region size (ξ_i^*) of SVR is comparable to the RMSE difference between adjacent radius (r) classes. Hence, it leads to additional error. Even though the machine learning models produce promising results, the availability of large training data set with known design values (ground truth of v, d and r), are still being the challenge for the field applicability. Hence, it must be overcome by creating a large experimental data set which is unique to a certain GPR equipment. Despite that, the ANN based estimation model was evaluated to observe if the performance can be further improved by overcoming the limitations of SVR, that is discussed in the next subsection. In addition, the influence of noise in the performance of the proposed models are also presented in the subsection 3.2.3.

3.2.2.c Implementation of ANN

The same datasets of SVR was utilised for the ANN implementation, where feature extraction is performed on all B-scan images to obtain the feature matrix $\mathbf{Z}$ composed of feature vectors $\mathbf{z}$.

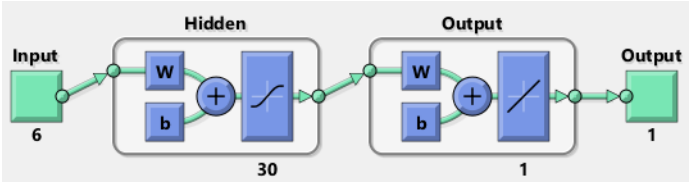

Figure 3.28: Implemented Artificial Neural Network diagram (ANN), generated in MATLAB® 2020a. Whereas, w: weight, b: bias.

The data is then divided into two sets: learning and testing, with learn-to-test ratio being 80:20. ANN is then implemented using the 'Machine learning and Deep Learning' toolbox in MATLAB® 2020a. The proposed ANN-MLP model contains, a feed-forward neural network with 6 input features, 30 hidden neurons with "sigmoid" activation function, followed by single neuron output contains "linear" activation function as described in Figure 3.28. The model is used to map 6 features onto a set of labelled outputs such as (r) or (d) or (v) in three separate models (ANN_r, ANN_d, ANN_v).

3.2.2.d Results and discussion (ANN)

Table 3.5 compares the performance results of the mean relative error (mean err) and the maximum relative error (max err) in terms of 95^{th} percentile (P_{95}) computed using:

$$err = \left| \frac{(L_{est} - L_{act})}{L_{act}} \right| \times 100 \tag{3.18}$$

where, L_{est} is the estimated value and L_{act} is the actual value.

According to the Table 3.5, ANN model shows err of 0.16%, 0.2%, 2.49% for the estimation of v, d and r respectively. Meanwhile, P_{95} the percentile of r estimation is relatively higher compared with v and d thereby indicating a wider err distribution. We can therefore infer that the estimations of v, d are highly robuster than the r estimation. Since the radius (r) information is highly sensitive to the variation of the shape of the hyperbola as argued by [31], the err was observed to be higher in case of r estimation.

Method	$err(r)\%$		$err(d)\%$		$err(v)\%$	
	Mean	P_{95}	mean	P_{95}	mean	P_{95}
ANN (MLP)	2.49	9.68	0.2	0.5	0.16	0.42

Table 3.5: Mean err and 95^{th} percentiles (P_{95}) err, $w.r.t$ radius (r), depth (d) and velocity (v) estimation (using 3 separate models)

According to the err distribution box plot shown in the Figure 3.29, the depth (d) estimation mean err is approximately 0.16%, Q3 (third quartile) is around 0.23%, and outlier is less than 0.5%, with nearly no outlier reported. Meanwhile, the radius (r) mean err is 3%, and the outlier boundary is 12% with few outliers. As a consequence, the results are somewhat better than SVR for both depth (d) and radius (r) estimate. Likewise Figure 3.30 illustrates the ANN model's performance on velocity (v) estimation. Hence, the mean err is around 0.15%.

Figure 3.31 indicates that err is higher at lower radius (r) classes, and it drops with increasing radius (r) size. Likewise, at lower radius (r) classes, err is relatively larger at higher material conductivity (1×10^{-1} S/m) while this trend is not observed at higher radius (r) cases.

In addition, in the ANN architecture, the number of hidden neurons (indicated in the Figure 3.28) has influence on the performance of the model. Hence, the radius (r) estimation model was undergone the performance evaluation across different number of hidden neurons to identify the optimised numbers for the best minimum hidden neurons. Whereas, the Figure 3.32 demonstrate the radius (r) estimation mean err for different number of hidden neurons. At scenario when the hidden neurons numbers are 30, the err was relatively lower, that motivates to chose 30 hidden neurons in the architecture.

Furthermore, the size of the learning database was also analysed to obtain the best minimum learning database size. Whereas, the Figure 3.33 shows the performance of the ANN model for velocity (v), depth (d), radius (r) estimation with 500 test data at different sizes of learning database. The mean err of depth (d) and velocity (v) model don't vary significantly with increasing training database size, and remains below 1%. However, the radius (r) mean err decreases with data-sets. However, the radius (r) model's performance difference between training database size of 300 and 1800 is only 3%. Thus, 300 learning database size is sufficient at this level in terms of depth (d), while a marginal compromising on radius (r) performance.

In the above part of the subsection, we presented a study to analyse the performance of MLP-based ANN model to estimate velocity (v), depth (d) and radius (r) of buried cylindrical pipes using GPR signals. The database consisted of 2610 unique B-scans which were preprocessed to obtain a feature matrix consisting of 6 signal features for each B-scan. The proposed model demonstrated promising results in the estimation of r, d and v-parameters. The mean relative errors (mean err) in the estimation were below 1% for velocity (v) and depth (d) and below 3% for radius (r) estimation respectively. In addition, a detailed analysis $w.r.t.$ on pipe radius (r) was also presented. Further, the study was extended to identify the optimised ANN architecture and learning database size.

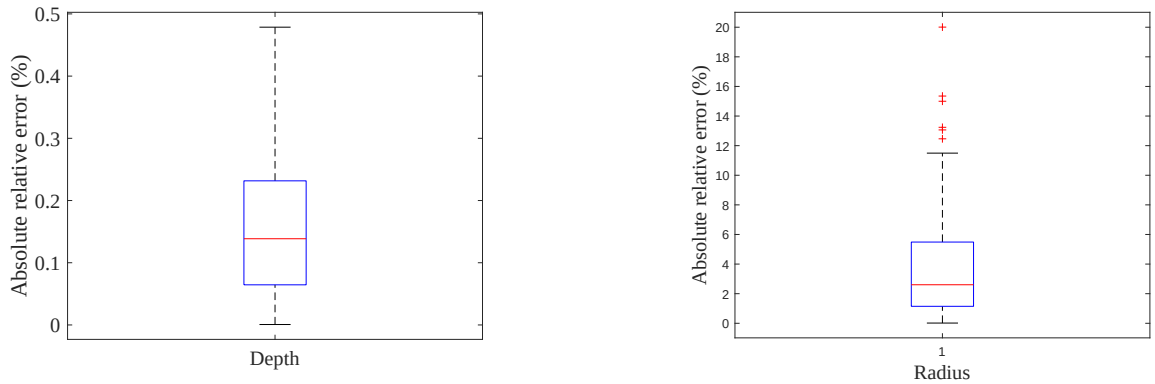

(a) Absolute relative error of depth (d) estimation of ANN

(b) Absolute relative error of radius (r) estimation of ANN

Figure 3.29: Absolute relative error of depth (d) and radius (r) estimation of ANN.

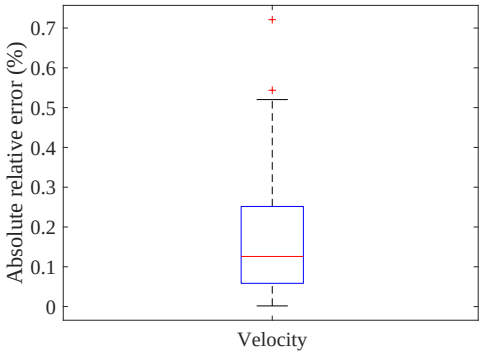

Figure 3.30: Absolute relative error of velocity (v) estimation of ANN.

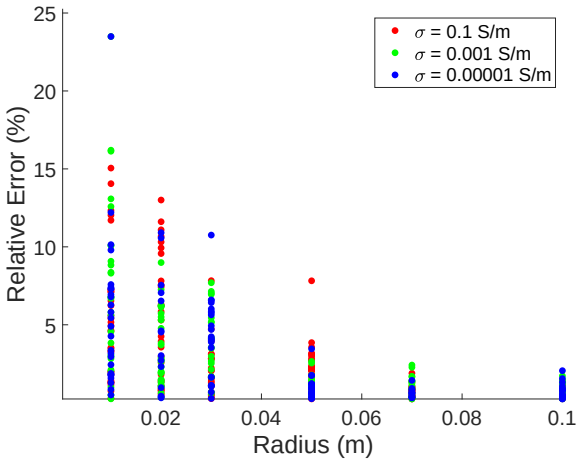

Figure 3.31: Error distribution (err) for radius estimation at various levels of σ.

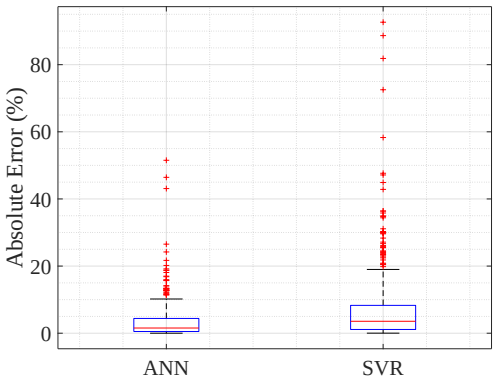

Figure 3.34: Radius estimation performance comparison between ANN and SVR.

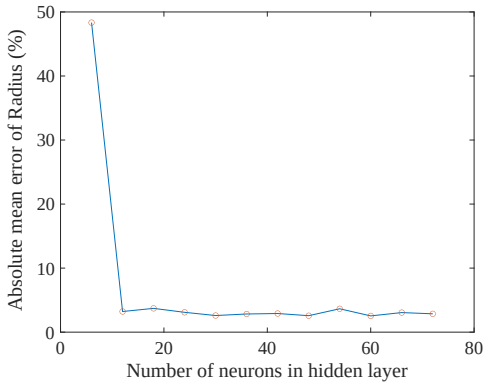

Figure 3.32: Radius estimation performance across different number of ANN hidden neurons.

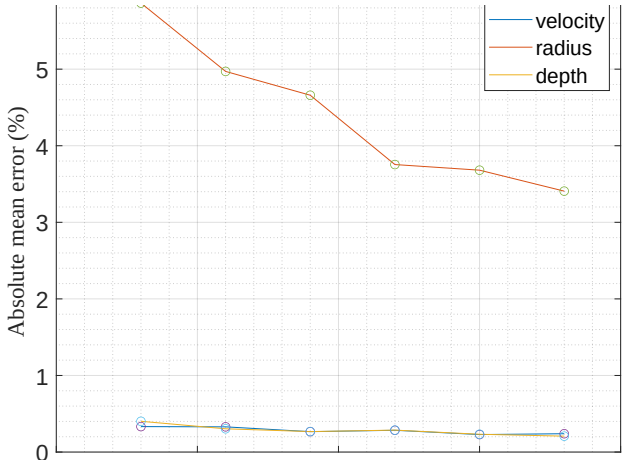

Figure 3.33: Mean error variation (err) for different training data size.

Method	$err(r)\%$		$err(d)\%$		$err(v)\%$	
	mean	P_{95}	mean	P_{95}	mean	P_{95}
Ray-based concurrent	260%	464%	25.1%	65%	11.3%	22%
Ray-based fixed velocity	120%	353%	-	-	-	-
Regression (SVR)	7.03%	26%	0.39%	1%	0.22%	0.5%
Classification (SVM)	10/500		0/500		5/500	
Regression (ANN)	2.49%	9.68%	0.2%	0.5%	0.16%	0.42%

Table 3.6: Mean relative error (mean err) and maximum relative error in terms of 95^{th} percentiles (P_{95}) $w.r.t$ radius (r), depth (d) and velocity (v) estimation

In context to the performance of SVR and ANN in terms of depth (d) and radius estimation, Table 3.6 presents the mean relative error (mean err) and percentile 95 of Ray-based, SVM, SVR, and ANN at a glance to compare the performance in the same test data-sets. The ANN, on the other hand, outperforms in all estimation formats. Because, it overcomes the drawback of SVR that suffers to an extent due to support vector size. Furthermore, Figure 3.34 shows the

relative error (err) distribution of radius (r) estimate. Whereas, the box plot shows that the mean error is lower than SVR, the distribution is narrower, and the outlier border is smaller than SVR. When it comes to depth (d) inaccuracy, the performance difference is negligible. As a result, the distribution is not displayed here.

Finally, both SVR and ANN give adequate performances for predicting all three parameters (velocity (v), depth (d) and radius (r)) for noiseless data. Meanwhile, the ANN performs somewhat better, with roughly identical results in the parametric variations. Acceptable performance is defined as depth (d) estimate at Class A with a linear error of less than $\pm$40 cm. The maximum allowable estimation error to satisfy Class A precision is presented in Figure 3.35. Whereas, the x-axis is the buried ground truth depth (d) in cm, y-axis refers to the allowed error in terms of percentage (%) with reference to the ground truth depth (d). The curve was plotted with the hypothesis that, the 2D localisation shall be done using GNSS RTK with $\pm$ 2 cm accuracy. So that, the 2D error is negligible and full weight error can be included in the depth (d). Whereas at 2 m deep, 40 cm is comparable to a 20% inaccuracy. Thus, both SVR and ANN can satisfy and retained for further studies.

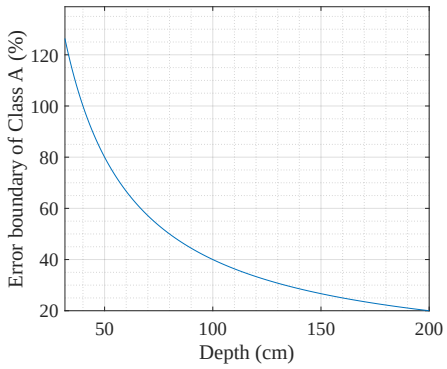

Figure 3.35: Maximum allowable depth (d) estimation error to satisfy Class A precision.

Furthermore, the next part assesses the model's performance on noisy data. The purpose of examining noiseless B-scans in the initial stage is to identify the proposed model's performance and behaviours separately, from the effects of noise on the model's behaviour.

3.2.3 Numerical validation on noisy data

The above subsection evaluates the performance of Ray-based and machine learning methods on noiseless data. Because, the objective was to evaluate the performance of the model in the absence of the noise. The model performances are satisfactory and highly precise in terms of depth (d) and radius (r) regardless of geometrical configuration of the pipes and dielectric of the medium. However, the effect of noise is evaluated by adding additional white Gaussian noise to the B-scans. The noise addition based on SNR is well explained in the Chapter 2, and the procedure applied by [110]. In order to accomplish the objective of this study, the noise scenario varying from 25 dB - 40 dB were evaluated. In fact, the noise addition is not part of the signal pre-processing. The objective of the noise addition is to imitate the signal closer to realistic scenarios. The effect of noise added to Figure 3.36 is presented in the Figure 3.37. For the noise study, the number of database narrow downed to 389 B-scans, which were randomly chosen and divided into 311, 78 for training and testing respectively. The chosen data samples were at relative permittivity (ε_r) between 6 and 10 with conductivity (σ) level at 1×10^{-5} S/m. Because, for instance, from the Table 3.4, the performance of the models doesn't vary much across medium's conductivity and the performance remains stable across different permittivity

according to the above presented findings in Figure 3.25 (the figure was presented in previous subsection). As a result, the aforementioned datasets were chosen for noise analysis.

Thus, the signal pre-processing sequence can be stated as follows.

1. Noise removal with low pass filter
2. Exponential gain
3. Hilbert transform envelop and travel time picking

Whereas, the fundamentals of the signal processing techniques are explained in the Chapter 1 and 2.

In this scenario, frequency filters such as low pass filter is used to remove the noise and clutter. Then, the gain is used to amplify the reflection wavelets. Finally, Hilbert transform envelop was used as a window filter to locate higher energy reflection wavelet. As a result, the peak picking for the travel time feature extraction become easier.

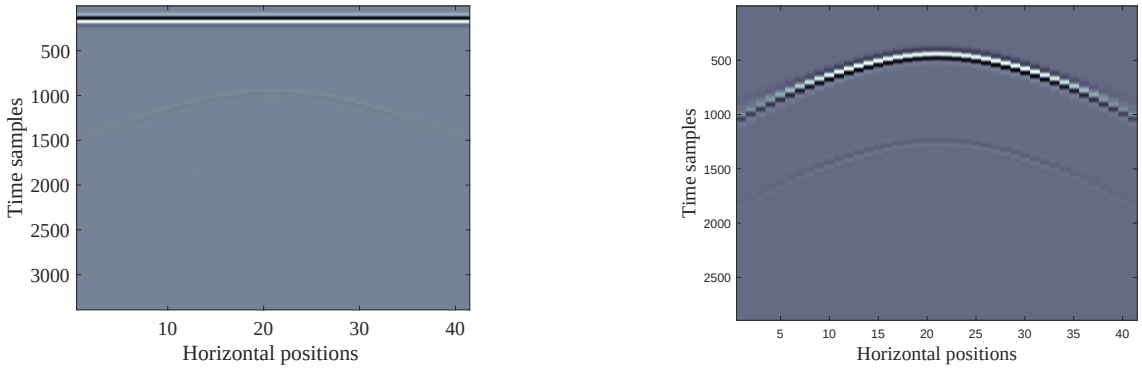

(a) B-scan noiseless

(b) B-scan noiseless without subsurface echo

Figure 3.36: Example of B-scan with and without subsurface echo, whereas (b) is the corresponding B-scan of (a).

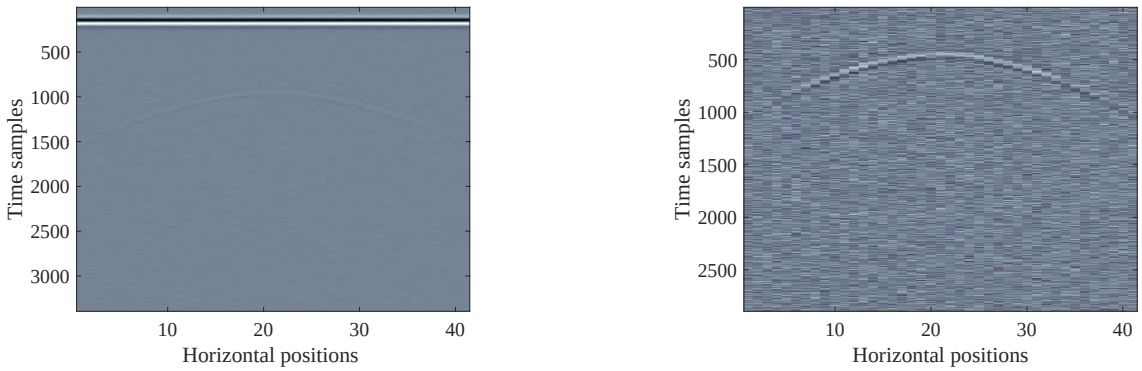

(a) B-scan with 25 dB SNR

(b) B-scan with 25 dB SNR and without subsurface echo

Figure 3.37: Example of B-scan with and without subsurface echo, SNR 25 dB equivalent white gaussian noise added, whereas (b) is the corresponding B-scan of (a)

In the context of noise addition, the Figures 3.36 and 3.37 show the noiseless and noise added B-scans respectively. Whereas, Figures 3.36.a and 3.37.a illustrate the scenarios with

the direct coupling echo, while Figures 3.36.b and 3.37.b are without the direct coupling echo. Hence, the effect of noise is very visible in Figure 3.37.b. When comparing the Figure 3.37.b and 3.38.b, the low pass filter is applied for the noisy B-scan and the output results enhance the visibility of the hyperbola in the Figure 3.38.b.

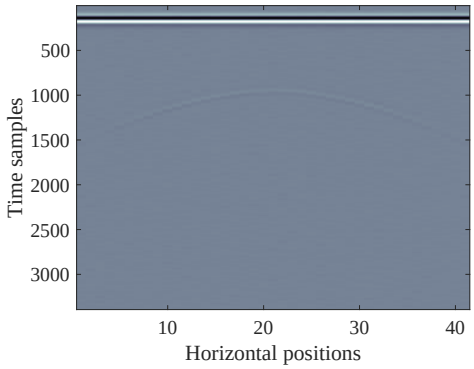

(a) B-scan with 25 dB SNR, low pass filtered

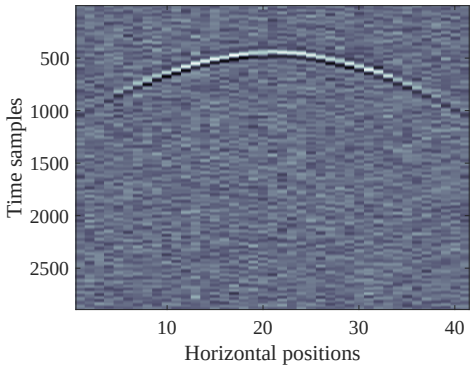

(b) B-scan with 25 dB SNR, low pass filtered and without subsurface echo

Figure 3.38: Example of B-scan with and without subsurface echo, SNR 25 dB equivalent white gaussian noise added and processed with low pass filter, whereas (b) is the corresponding B-scan of (a)

Furthermore, as shown in Figure 3.39, the effect of noise and the low pass filter is illustrated with the support of the A-scan. Whereas, Figure 3.39.a is the complete A-scan extracted at the centre of the hyperbola includes direct coupling, while Figure 3.39.b is a zoomed out window at pipe's surface reflection point. The low pass-filter eliminates the noise and minimise the picking error. The maximum relative picking error encountered was "8 time samples" ($8 * 5.89 \times 10^{-12}$ s) in the whole 389 hyperbolas. The maximum picking error was calculated between the peak to peak travel time difference between the noise removed hyperbola and the ground truth.

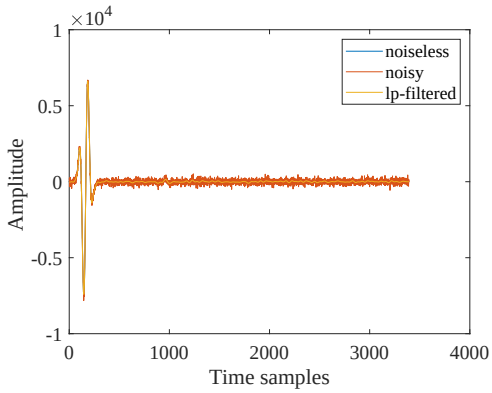

(a) A-scan with without noise, 25 dB SNR, low pass filtered

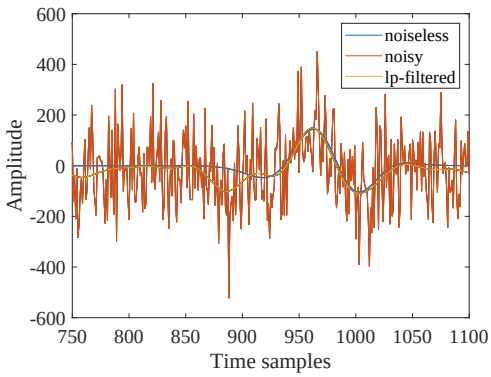

(b) A-scan with without noise, 25 dB SNR, low pass filtered magnified

Figure 3.39: Example of A-scan with and without noise, and processed with low pass filter.

The retrieved hyperbola-based features were trained with ANN and SVR in this context, as recommended in the preceding sections. Furthermore, the models' robustness was assessed in

two separate circumstances. First, the training model was noiseless, but the test set was noisy. Second, both the training and testing sets are noisy. In general, the models may be classified as follows.

- SVR nl-n: SVR model with noiseless training dataset and noisy test set.
- SVR n-n: SVR model with noisy training dataset and noisy test set.
- ANN nl-n: ANN model with noiseless training dataset and noisy test set.
- ANN n-n: ANN model with noisy training dataset and noisy test set.

The listed scenarios were repeated for both depth (d) and radius (r) estimation at several noise level as described in the Figure 3.40.

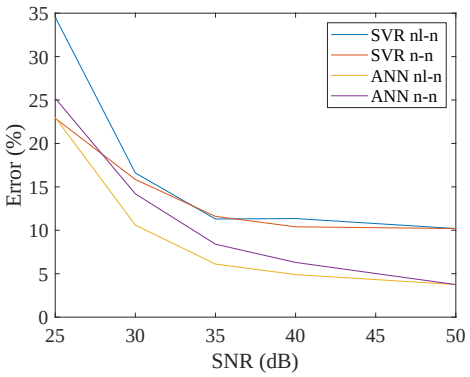

(a) Relative absolute error of radius (r) estimation in different noise level

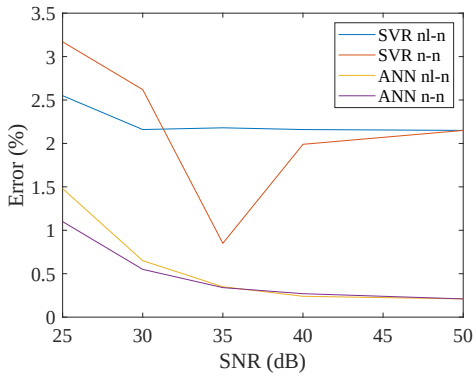

(b) Relative absolute error of depth (d) estimation in different noise level

Figure 3.40: Relative absolute error of radius (r) and depth (d) estimations in different noise level in both SVR and ANN. Whereas in legends, nl-n , n-n refers to train on noiseless - test on noisy, train on noisy - test on noisy data scenarios respectively.

According to Figure 3.40.a, the mean relative error (mean err) of the projected radius (r) estimation rapidly decreases with increasing SNR in all circumstances (decreasing noise). As a result, when SNR changes between 25 dB and 50 dB, ANN outperforms SVR by recording the least error between 25% - 5%. As a result, it is clear that better noise removal techniques can increase the model's accuracy. Meanwhile, as shown in Figure 3.40.b, the mean relative error (mean err) follows the same pattern as in radius (r) estimation. However, in both SVR and ANN in depth (d) estimation models, the plot gradient is relatively low. However, the ANN outperforms the SVR by a small margin. Regardless, the mean error for both models is less than 3%, which meets CLASS A accuracy (according to Figure 3.35).

In conclusion, based on the results of the noisy B-scan, SVR and ANN are still compelling for parameter estimation. Particularly, the depth (d) estimation satisfies Class A precision. The noise, in reality, has a considerable influence on the performance of the presented models. Furthermore, the noise level is greatly dependent on noise removal techniques. As a result, a high precision noise removal technique is necessary to improve the outcomes whilst keeping a greater SNR. Antenna effects elimination and calibration are another possibility in this situation. Whereas the technique is suggested for future research. Because the antenna effects are significantly correlated with the radiation pattern and antenna properties. In the meanwhile, the database utilised is a hertzian dipole, which is quite generic.

gprMax, on the other hand, has a restricted variety of antennas, therefore the available 3D antenna model necessitates 3D simulations and a large processing power to construct a necessary database size. As a result, it is avoided at this level due to a lack of compute resources. Aside from that, the raw signal from the present 2D dipole numerical simulation reveals no substantial noise caused by antenna effects. Furthermore, extra white noise was supplied for assessment, which differed from the realistic nature of antenna effect (ringing or electronic noise). Nevertheless, the removal of antenna effects coupled with FWI can produce high precision depth (d) localisation. Which is yet to be validated for utility applications. Hence, it's highly a potential area of study in the near future.

Simultaneously, the current investigation was expanded to investigate the relative performance behaviour of the suggested machine learning models on PVC pipes and in varying centre frequencies. The results are provided in the next subsection.

3.2.4 Performance on various configurations

The above presented results were validated on metallic and standardised depth (d) and radius (r) values, which were partially continuous and not completely random continuous values. Hence, the study is extended to study the performance and behaviour of the proposed SVR and ANN based estimation models on random continuous depth (d) and radius (r) values, and PVC pipe configuration.

Configuration	**Values**
Pulse type and centre frequency (f_c)	Ricker pulse, 400MHz or 1200MHz or 1500MHz
Antenna off-set, type	Zero-offset, hertzian dipole
Antenna coupling	Ground coupled
Medium's relative permittivity (ε_r)	5 to 9
Medium's conductivity (σ)	1×10^{-5} S/m, 1×10^{-3} S/m , 1×10^{-2} S/m
Acquisition step size (Δx)	2 cm
PML boundary	10 discrete boxes + 10 cm clearance
Pipe's depth (d)	0.2 m to 1 m
Pipe's radius (r)	20 mm : 10 : 100 mm
Number of A-scans per B-scan	41 (0.8 m)
B-scans dimension	$41 * 7200$ (A-scans x time samples)
Pipe's type Configuration A Configuration B	 all metal metal, PVC + air, PVC + water, PVC + metal
Number of B-scans 400 Mhz Training : Test 1200 Mhz Training : Test 1500 Mhz Training : Test	Configuration A (308) : (79) (308) : (79) (308) : (79)
Number of B-scans 400 Mhz Training : Test 1200 Mhz Training : Test 1500 Mhz Training : Test	Configuration B (308) : (79) (308) : (79) (308) : (79)

Table 3.7: gprMax model settings of two types of database whereas configuration A with all metal, configuration B with metal and PVC respectively.

The Numerical study defined in the Table 3.7 to analyse how different GPR centre frequen-

cies, and pipe's materials impact on the performance of the proposed parameter estimation models based on SVR and ANN.

- Numerical study to analyse how the proposed parameter estimation models based performs on random continuous values of depth (d) in training sets.
- Evaluate the model performance when the training database's frequency is different from test data.
- Evaluate the model performance when training database contain mixed frequency data,
- Evaluate the model performance in PVC and metallic pipes together.

In this context, the Figure 3.41 illustrates the B-scans and their corresponding single A-scans of Metal, PVC + water, PVC + air respectively those obtained from simulation (different geometry and diameters). Whereas, the sub-figures (a) and (d) are the B-scan and A-scan of metal; (b) and (e) are the B-scan and A-scan of PVC + water; (c) and (f) are the B-scan and A-scan of PVC + air;

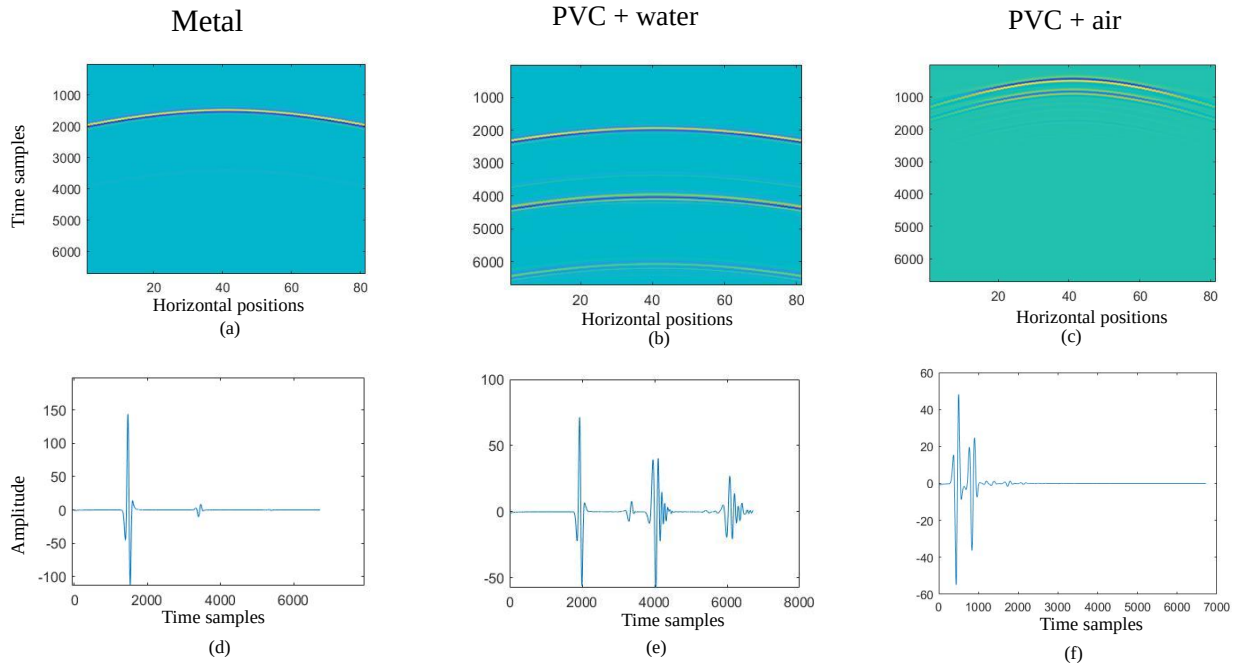

Figure 3.41: B-scan and A-scan signatures of Metal and PVC pipes. Whereas, the sub-figures (a) and (d) are the B-scan and A-scan of metal; (b) and (e) are the B-scan and A-scan of PVC + water; (c) and (f) are the B-scan and A-scan of PVC + air.

The A-scan and an unknown artefact reflection are shown in Figure 3.41.d (direct coupling is already filtered in all cases). Then, Figure 3.41.e depicts three strong reflections such as first on the surface of the pipe, followed by the bottom of the pipe and the multi reflection effect. Meanwhile, in PVC + air pipe as in Figure 3.41.f, double reflection is seen, with a very short travel time gap between the reflections compared with PVC + water. Because, the travel time is higher in water due to slow EM velocity (v) in the water due to higher permittivity ($\varepsilon_r = 81$), while the travel time is very short as the air velocity (v) is very high and equivalent to free space velocity ($\varepsilon_r = 1$). As a result, these A-scan signature variations may be regarded as classification characteristics of the three relevant pipe materials. Hence, the pipe type classification is covered in the section 3.4.

The travel time between the subsurface echo and the first echo on the pipe's surface is used to estimate depth (d) and radius (r) using suggested machine learning algorithms (assuming the emission centre and subsurface echo are overlapped at near ground coupled configuration). Regardless of material types, the first reflection on the pipe is stronger and dominant, therefore the hyperbola shape can be extracted. However, there is a small phase change (signal peak polarity change) in the reflection wavelet on PVC + air because when air is lower in permittivity than PVC ($\varepsilon_r = 2 - 3$) and stratified medium ($\varepsilon_r = 6 - 9$). Even though in PVC + water configuration, the PVC's permittivity (ε) is less than the permittivity (ε) of stratified medium, there are supposed to be phase change in the first reflection, however, it is neglected due to the thin layer of the PVC material compared with the resolution of the wavelet of the pulse. In all cases, the travel time distance was chosen between peak to peak as defined in Figure 3.12.

Data base Training : Testing	ANN		SVR	
	Mean Relative Error % (Depth)	Mean Relative Error % (Radius)	Mean Relative Error % (Depth)	Mean Relative Error % (Radius)
400 MHz : 400 MHz	1.5	47	1.46	55
1200 MHz : 1200 MHz	1.39	34	1.64	37
1500 MHz : 1500 MHz	1.2	36	1.89	32.5
3 Frequency	1.6	40	1.5	38
400 MHz : 1200 MHz	2.2	34.5	2.3	37
400 MHz : 1500 MHz	2.79	38.25	2.3	36
1200 MHz : 400 MHz	4.4	41	2.38	51
1200 MHz : 1500 MHz	1.21	33	1.66	38

Table 3.8: Model performance results on various frequency datasets of training and testing, at noisy and random continuous depth (d) values, metallic pipes.

In terms of database with configuration A (all metal pipes with random continuous depth (d) and radius (r) values), four separate models were built for each machine learning models (ANN and SVR). The four models are 400 MHz, 1200 MHz, 1500 MHz, mixed 3 frequencies. SVR and ANN models were applied to the estimation of depth (d) and radius (r) as seen in Table 3.9 and given that all standard signal processing steps were followed as described in the above sections including noise additions, removal and low-pass filters.

It is found that, the depth (d) estimation's mean relative error (mean err) is still remained lower between 1.2 - 1.5% in ANN , and 1.46 - 1.89% in SVR when training and test data frequencies are the same. Even, the depth (d) accuracy didn't change significantly (1.6%) when the database combined all three frequencies. However, if the training data sets and testing data sets are different in frequencies, the depth (d) estimation mean relative error (mean err) increased upto 4%. However, it still satisfies the Class A requirement. To be noticed, the depth (d) accuracy in ANN is higher at 1500MHz that potentially indicates, the use of high resolution GPR (ultra-wide band) can produce very narrow wavelets thus the estimation accuracy can be improved. But, the trend is opposite in SVR. In both ANN and SVR, the depth (d) estimation accuracy has almost the same level of accuracy.

Nevertheless, the radius (r) estimation error increased above 30%. that indicates the sensitivity of the hyperbola to the radius (r) information in the random continuous atmosphere. And the database size is relatively lower compared with the first study presented in section 3.2.2

Data base Training : Testing	ANN		SVR	
	Mean Relative Error % (Depth)	Mean Relative Error % (Radius)	Mean Relative Error % (Depth)	Mean Relative Error % (Radius)
400 MHz : 400 MHz	3.6	36.9	**3.44**	**35**
1200 MHz : 1200 MHz	2.7	50.4	2.2	52.8
1500 MHz : 1500 MHz	2.1	48.6	2.6	46

Table 3.9: Model performance results on various frequency datasets of training and testing, at noisy and random continuous depth (d) values, PVC pipes.

Configuration B in the Table 3.7 consists of metal and PVC pipes (PVC + air, PVC + water, PVC + metal). Table 3.9 show the depth (d) and radius (r) estimation mean relative error (mean *err*) for ANN and SVR. The results indicate the depth (d) estimation mean relative error (mean *err*) has increased from 1.5% to 3.6% when PVC involves in the material, while the radius (r) estimation error has increased up to 50%. The depth (d) estimation accuracy improves with the centre frequency. The configuration B can be perceived as closer to the realistic configurations compared with other studies. Hence, it is evident that, the depth (d) estimation can achieve the Class A precision though the radius (r) estimation requires more robust approach for utility applications.

In conclusion, the subsection investigated the performance of SVR and ANN on PVC materials and in different GPR bandwidth data. The results of the investigation in PVC pipes indicate that the suggested machine learning approaches (SVR and ANN) may be utilised to estimate the depth (d) with an average precision of at least 97% (3% average relative error). Meanwhile, estimating the radius (r) necessitates a more robust procedure. Furthermore, the GPR bandwidth has no noticeable impact on depth (d) estimation performance. As a result, any GPR bandwidth is permissible. However, 1.5 GHz performs marginally better. Furthermore, the study discovers that data received from a certain GPR bandwidth may be utilised to estimate depth (d) in different GPR bandwidth data.

Conclusion

The section analyses several methods based on Ray-based and machine learning approaches for estimating the depth (d), radius (r) of the pipe, and velocity (v) of the stratified media, with the use of suggested unique feature selection (in the case of machine learning). Overall, the numerical analysis predicts that the proposed machine learning models would outperform Ray-based approaches in all scenarios (with or without noise). Furthermore, depth (d) accuracy may be achieved to meet the French requirements' Class-A precision. When the radius (r) and depth (d) are well standardised, the applicability of SVM multi classification is possible. Nonetheless, in real circumstances, this is not the case; however, standardisation of the depth (d) and radius (r) is becoming common for new installations.

In the meanwhile, the study reveals that SVR or ANN could be implemented in any environment that can perform, with mean relative errors (mean *err*) ranging from 5% to 35% for radius (r) and 2% to 3.5% for depth (d) estimate, respectively. ANN, on the other hand, performs somewhat better. As a result, the SVR is not ruled out at this time. Furthermore, SVR and ANN performance declines with noise, and the radius (r) estimation error has significantly risen in continuous value settings.

However, the depth (d) estimation shows its robustness in noiseless, noisy, random continuous values, metal and PVC pipes configurations (all cases). These findings promise further acceptability of the methods on 3D localisation of utility network upon validation on experimental data. Nevertheless, the radius (r) estimation performance is not convincing for the random value configuration. However, the relative mean error remains below 50% and it's not yet regulated by law like depth (d). But it affects the accuracy of the no dig zone boundary.

However, the proposed approach for radius (r) estimation can be utilised for radius (r) standardised applications or any applications that requires approximate estimations. Then, the non dig zone boundary can be defined in several classes accordingly.

In this regard, due to limited resources, I do not have a controlled location with a sufficient number of pipes of varying depths and diameters to create a supervised machine learning model at this stage. The SVR or ANN, on the other hand, requires hundreds of hyperbolas with ground truth (without overlaps). As a result, the experimental validation is limited to an open air design with a few pipes. The outcomes are provided in Chapter 4. In the future, antenna effects may be eliminated using an antenna calibration (estimating antenna transfer function and radiation centre), and the green function can be evaluated instead of raw B-scan. As a result, more noise-filtered data for machine learning models may be acquired. Because the green function eliminates any noise or multi-reflection effects caused by the antenna radiation pattern, as well as any coupling issues. This strategy has the potential to boost performance. However, it has been recommended for additional work in this area. Furthermore, numerical validation in 3D simulation and pipes at an angle are also required. This job is also avoided since computer resources are limited at this point.

All the above-mentioned models make use of a set of characteristics carefully retrieved from the hyperbola. In the future, the procedures will necessitate a complicated autonomous engineering pipeline in the automation. Instead, the next section of the study explores the feasibility of using B-scan directly with the use of a DCNN (Deep Convolution Neural Network). The goal is to employ a DCNN that can automatically extract features. Furthermore, the methods for determining if the raw signal B-scan can be utilised in place of the B-scan image.

3.3 Estimation model based on CNN

The above proposed methods are based on a prior extraction of features from the B-scan. However, identification of the correct local features remains always challenging. Thus, deep learning approaches brought great attention due to its proven ability to automatically extract features through convolution networks. However, the deep learning was rarely evaluated as a regression model for the estimation of geometrical parameters such as depth (d) and radius (r) of the buried pipes. Most of such machine learning methods for GPR are based on an analysis of B-scans in image format. The labelling is done on the images and the algorithms of detection, classification or regression relying on pixels. Such signal to image conversion and colour scale normalisation causes degradation in the information. Hence, it limits the applicability of DCNN (Deep Convolution Neural Network) based algorithms for the GPR based parameter estimation purposes (depth (d) and radius (r)). As a result, we have studied a DCNN based parameter estimation model that works on B-scan signals. The objective of the proposed CNN model work is to evaluate the ability of a deep learning method applied to GPR 2D "raw signals" instead of "pictures" for the depth (d) and radius (r) estimation of the pipes.

The proposed parameter estimation models based on Deep Convolution Neural Network (DCNN) opted for multi classification and regression have been numerically validated on subsurface raw GPR images (B-scans). However, in this study due to limited computational resources the study is aimed at the specific utility network type. In this regard, according to modern standards, each utility network type is allotted a defined depth (d) range to avoid network overlapping. In this context, among different underground networks, we opted to focus on metallic gas networks for the time being for this study, because gas networks are standardised: it has to be buried at depths between 0.7 and 1 m with the radius (r) classes of 31.5, 55, 100 and 125 mm, according to AFNOR French Standard NP P98-331 [111]. Thus, this problem can be perceived as classification. Meanwhile, the regression approaches also applied for comparison.

In the proposed deep convolution neural networks, the first few steps consist of extracting the features through the process of convolution and max pooling. The process extracts unique features from the input data (raw B-scan) while reducing the dimension and flattens the features (transform to 1D) to a vector appropriate for the fully connected ANN, as shown in Figure 3.42. By contrast, in previous works, we extracted hyperbola travel time based statistical local features through series of processing steps [31].

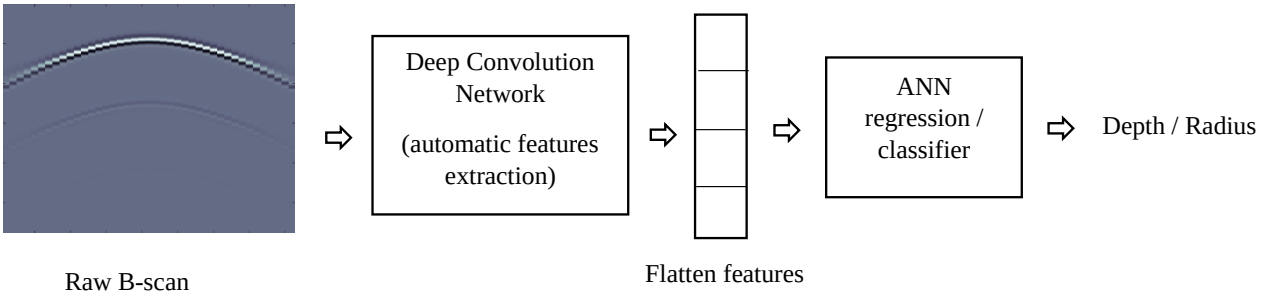

Figure 3.42: DCNN classification and regression architecture.

3.3.1 Numerical Validation

In order to generate the synthetic GPR raw B-scans, simple homogeneous dispersiveness noiseless gprMax 2D model is used [108] with the configuration stated in the Table 3.10.

Configuration	Values
Pulse type and centre frequency	Ricker, 1.5 GHz
Antenna off-set, type and height	Zero-offset, hertzian dipole, 0.5 cm
Medium's relative permittivity	3 - 6
Medium's conductivity	1×10^{-5} S/m
Acquisition step size	5 cm
Pipe's depth	0.7 m - 1 m
Pipe's radius	31.5 mm, 55 mm, 100 mm, 125 mm

Table 3.10: gprMax 2D configurations for synthetic GPR data modelling of metallic gas pipe.

Since the proposed model adopts a supervised learning approach, each B-scan was labelled with its designed parameter values. In terms of radius (r) estimation, the radii of the gas networks are standardised and classified into different radius (r) classes. So that, a multi classification model was deployed by assigning a class label (for each B-scan) for each radius (r) class. The number of classes is defined in advance according to the expected results, here the 4 diameter classes of the pipes such as 31.5, 55, 100 and 125 mm. In the meantime, the depth (d) estimation is considered as regression problem with depth (d) range between 0.7 and 1 m. The labelled 1725 B-scans dataset got split into two sets, such as training and testing. Which then allows learning to be carried out on 894 training B-scans dataset and validated on 430 B-scans with the training : validation ratio of 67% : 33%. The method is then tested

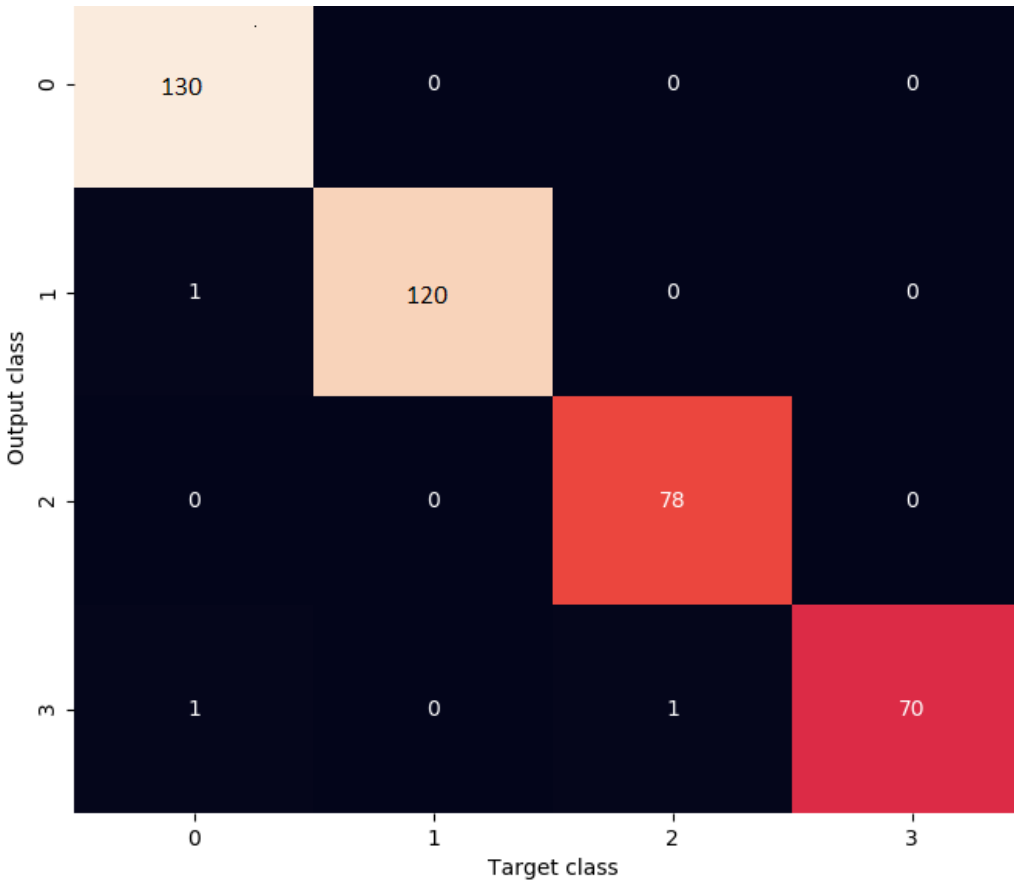

Figure 3.43: Confusion matrix of radius estimation, whereas classes 0,1,2 and 3 indicate radius classes 31.5, 55, 100 and 125 mm respectively.

on the 401 B-scans that has not been used for training. The automatic feature extraction and dimension reduction step is performed directly by the deep convolution layers without any advanced processing. In this case, Resnet-51 was applied for deep convolution layers. Then, in the ANN, for the regression *tanh* activation layer deployed in the output layer of ANN, while the classification has $softmax$ activation function.

3.3.1.a Results and discussion

A DCNN multi-class classification model and a DCNN regression model were trained separately for the estimation of radius (r) and depth (d) respectively. Then, each model was deployed to perform the prediction out of test B-scan data-sets. Hence, its ground truth labelled values are compared with the model prediction. Whereas, the Figure 3.43 presents the confusion matrix of the radius (r) estimation using proposed multi-class classification model.

According to the confusion matrix in Figure 3.43, target class represents the actual values, while output class represents model predicted values. Classes 0,1,2 and 3 indicate radius (r) classes 31.5, 55, 100 and 125 mm respectively. In 398 out of 401 (99.2 %) cases, radius (r) classes were correctly predicted by the trained model while only in 3 out of 401 instances, the false alarms were observed. Among the false alarms, the misclassification was only one class away from the actual value in two instances.

More specifically, the radius of class 0 (31.5 mm pipes) contains 131 pipes. The CNN classification algorithm accurately predicted their radius class 130 times in this class, with only two false alarms. In one case, the model incorrectly classed 31.5 mm pipe as 55 mm pipe, while in another case, the model incorrectly classified 31.5 mm pipe as 125 mm pipe. Similarly, class

1 (a total of 120 pipes of 55 mm) has been properly predicted 120 times. Despite this, one false alert was registered out of 79 pipes in Class 2 (100 mm). As a result, radius values of 78/79 were successfully predicted, with one false alarm. A 100 mm pipe is categorised as 125 mm in this false prediction circumstance. In class 3, which are 125 mm pipes, had been predicted 100% correctly without any false alarms.

Likewise, the proposed DCNN based regression model was evaluated for the estimation of depth (d) and the model provided a mean square error of 0.21 % on 401 B-scan samples of test data within the depth (d) range from 0.7 to 1 m. The predicted depth (d) values were well fitting with its ground truth. Furthermore, detail parametric study is retained for future scope. In addition, the test datasets in section 3.2.2 is tested with CNN approach and produced mean relative error (mean err) of 0.16 %.

Conclusion

The work carried out consists of creating a database of annotated "raw" B-scans to demonstrate the feasibility of a deep learning algorithms for determining the depth (d) and diameter of buried gas pipes using multi classification and regression approach. The methods show very encouraging results, both in classification for diameter and regression for depth (d). Though the research work has focused on gas pipes due to its standardised radius (r) and depth (d) range, the method can be also adapted to all types of underground utility networks. However, limited computational resources is a constraint to continue the study in this direction for the time being. At this stage, due to lack of field data, the model has been numerically validated. Furthermore, the current analysis remains in 2D B-scans, so it would also be interesting to evaluate the model's performance on raw C-scans. Hence, the algorithm will computationally heavier. However, the approach has given a good conceptual foundation.

3.4 Pipe type classification

A technique for identifying the type of pipe in the utility detection and localisation process may improve the safety of the network as well as the excavation workers. Because the identification of the materials may assist in determining the sort of network. For example, metallic in the case of gas or power, and PVC in the case of water. Physical investigation is essential for identification on a modest scale of site inquiry. However, in terms of time and cost, these automatic classifications benefit in the processing of large amounts of GPR data. As a result, the purpose of this early investigation was to determine if GPR signals could be discriminated between metal and PVC based on the A-scan signature. Hence, the GPR B-scan signature varies between metallic, PVC + water, PVC + air, PVC + metal etc. The Figure 3.41 and example of how the signature of B-scan and A-scan could vary according to different pipes materials, and the physical explanation behind such variation was discussed in the section 3.2.4.

3.4.1 Numerical validation

In this context, a database similar to that used in section 3.2.4 (Configuration B: 1.5 GHz) was used to numerically validate an automatic pipe type classification model based on Binary SVM and KNN (k-nearest neighbours) to determine whether the pipe is PVC or metal, with the support of an A-scan in the apex of the hyperbola (top of the pipe) serving as the global feature. Whereas, the k-nearest neighbours (KNN) method is a supervised machine learning technique that can be used for classification as well as for regression problems. KNN works by calculating the distances between test data (features) and K number of nearest neighbours in the closest group in the trained model, then picking the cluster that has the highest neighbours to the test

data and voting for the most frequent label in the case of classification. The authors in [112] provides a detailed tutorial of intuition of KNN. In the case of classification, the optimal K for the data is determined by experimenting with several Ks and selecting the one that performs best using optimisation techniques. Finally, it was discovered that the optimal value of K for the studied pipe classification data-set stayed at 2.

Furthermore, there were 640 B-scans generated (370 of metal pipes, 370 of PVC pipes), shuffled and split into 80:20 for training and testing.

3.4.1.a Results and discussion

According to the obtained results presented in the table 3.11, the binary SVM model with RBF (Radial Basis Function) non-linear kernel produce 85.2% of accuracy. That means the model discriminates a metal and PVC pipes 85.2% correctly. However, the confusion matrix in the Figure 3.44 shows that, the true positive rate of detection in metallic pipes are at 91.2% while the PVC is at 78.9%.

Features	Algorithm	Classification Accuracy
A-scan (Temporal)	SVM	85.2%
A-scan (Temporal)	KNN	90.7%

Table 3.11: Binary SVM based pipe type classification accuracy

Meanwhile, KNN provides 90.7% of accuracy, where 100% for metallic pipes and 81% in PVC pipes. Whereas the k values is 2. That indicates the metal and PVC can be classified into two clusters by KNN algorithm.

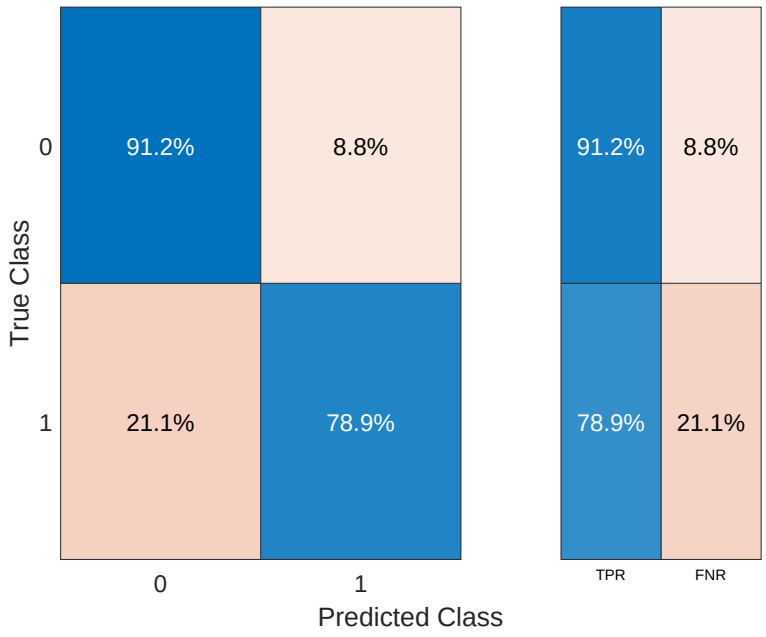

Figure 3.44: SVM confusion matrix of metallic and PVC pipe classifications. Whereas, Class-0: Metal, Class-1: PVC.

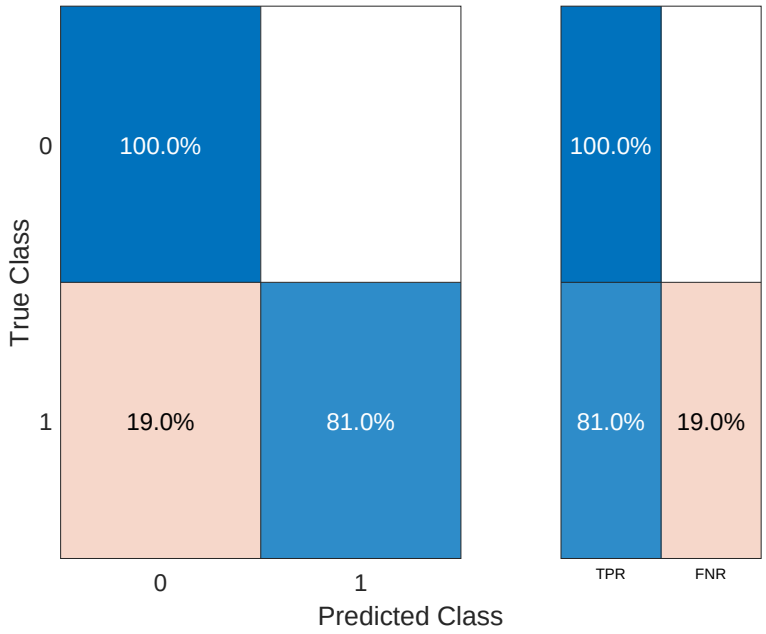

Figure 3.45: KNN Confusion matrix of metallic and PVC pipes classifications. Whereas, Class-0: Metal, Class-1: PVC.

In the context of KNN based pipe type classification performance, Class 0 refers to metallic pipes, whereas Class 1 refers to PVC pipes, as shown in Figure 3.45. The findings show that all metal pipes are accurately predicted with no false alarms (100% accurate). Meanwhile, PVC pipe was properly predicted 81% of the time, while 19% of PVC pipe was misclassified as metallic pipe. As a result, models for recognizing PVC pipes need to be improved further.

At this stage, this preliminary study shows promising results to discriminate between a metallic and PVC pipes based on the A-scan signature using machine learning approach. However, in realistic scenario, more detailed investigation is required to differentiate between different content of pipes (PVC + water or PVC + air or PVC + optical fiber) using multi classification techniques. Due to the similarity of the A-scan signature, for example, the A-scan is identical between large PVC with air and small PVC with water. In this case, the A-scan pattern shall be identical. Also, in this case, further feature engineering is essential as an additional layer of classification with another sets of different features, that is left for future studies. Nevertheless, nowadays, since the new installations of utility pipes are highly classified in terms of depth (d). Hence, combining the depth (d) information with the above classification can predict the network type as an alternative approach.

Conclusion

The section provides a pipe type classification approach that distinguishes between metal and PVC pipes. According to the findings, supervised machine learning techniques such as BSVM or KNN may be utilised to categorise the goal with an accuracy greater than 85%. Furthermore, the proposed model 100% accurately classifies metallic pipes compared with PVC pipes. That's a positive indication that critical pipelines like Gas and Electricity are being well identified as critical network, which consists of metallic materials. Thus, the accurate metallic classification improves in terms of network and human safety. However, there is a need for a multi classification research that can separate various types of pipes, which requires various feature selection instead of A-scans or B-scan input with DCNN, and the scope is retained for future work.

3.5 Conclusion

The chapter studies several parameter (velocity (v), depth (d) and radius (r)) estimation methods and pipe type classification in the global objective of 3D mapping of underground utility networks. In all cases, the hypothesis is taken as the pipes were already detected automatically using the methods proposed in Chapter 2. Hence, the individual pipes within the detected bounding box has been utilised for the parameter estimation. However, the studied numerical database were independent for every aspect at this stage.

The first section analyses several methods based on Ray-based and machine learning approaches (SVM, SVR, ANN) for estimating the depth (d), radius (r) of the pipe, and velocity (v) of the stratified media with the use of suggested unique feature selection (in the case of machine learning). Overall, the numerical analysis predicts that the proposed machine learning models would outperform Ray-based approaches in all scenarios (with or without noise). Furthermore, depth (d) accuracy may be achieved to meet the French requirements' Class-A precision. When the radius (r) and depth (d) are well standardised, the applicability of SVM multi classification is possible. Nonetheless, in on site circumstances, this is not the case; however, standardisation of the depth (d) and radius (r) is becoming common for new installations. In the meanwhile, the study reveals that SVR or ANN could be implemented in any environment that can perform, with mean relative errors (mean err) ranging from 5% to 35% for radius (r) and 2% to 3.5% for depth (d) estimate, respectively. ANN, on the other hand, performs somewhat better. As a result, the SVR is not ruled out at this time. Furthermore, SVR and ANN performance declines with the increase in noise levels, and the radius (r) estimation error has significantly risen in continuous value settings. However, the depth (d) estimation shows its robustness in noiseless, noisy, random continuous values, metal and PVC pipes configurations. This promise further acceptability of the methods on 3D localisation of Utility network upon validation on experimental data. Nevertheless, the radius (r) estimation performance is not convincing for the random value configuration. However, the relative mean error remains below 50%, and it's not yet regulated by law like depth (d). Thus, the proposed approach for radius (r) estimation can be utilised for radius (r) standardised applications or any applications that requires approximate estimations.

In this regard, due to limited resources and the controlled locations with a sufficient number of pipes of varying depths and diameters to create a supervised machine learning model is lacking at this stage. The SVR or ANN, on the other hand, requires hundreds of hyperbolas with ground truth (without overlaps). As a result, the experimental validation is limited to an open air design with a few pipes. The outcomes are provided in Chapter 4. In the future, antenna effects may be eliminated using an antenna calibration (estimating antenna transfer function and radiation centre), and the Green function can be evaluated instead of B-scan. As a result, more noise-filtered data for machine learning models may be acquired. Because the Green function eliminates any noise or multi-reflection effects caused by the antenna radiation pattern, as well as any coupling issues, this strategy has the potential to boost performance. However, it has been recommended for additional work in this area. Furthermore, numerical validation in 3D simulation and pipes at an angle are required. This job is also avoided since computer resources are limited at this point.

In the second section, the content covered depth (d) and radius (r) estimation using DCNN with automatic feature extraction on raw B-scan. Because, all the above-mentioned models make use of a set of characteristics carefully retrieved from the hyperbola. In the future, the procedures will necessitate a complicated autonomous engineering pipeline in the automation. Instead, the next section of the study explores the feasibility of using B-scan directly with the use of a DCNN. The goal was to employ a DCNN that can automatically extract features and the methods to determine if the raw signal B-scan can be utilised instead of the B-scan image.

Further, the work carried out consists of creating a database of annotated "raw" B-scans to demonstrate the feasibility of a deep learning algorithms for determining the depth (d) and diameter of buried gas pipes using multi classification and regression approach. The methods show very encouraging results, both in classification for diameter and regression for depth (d). Though the research work has focused on gas pipes due to its standardised radius (r) and depth (d) range, the method can be also adapted to all types of underground utility networks. This can be included in the future scope of the study.

The third section describes a preliminary study about pipe type classification method that can differentiate between metal and PVC pipes. According to the results, supervised machine learning such as BSVM or KNN can be used to classify the objective with the accuracy more than 85%. In addition, the proposed model classify metallic pipes 100% accurately. That's a promising indication to ensure the critical pipes like gas and power is identified in terms of network and human safety. However, there is a need for multi classification study that can differentiate every type of pipes, which needs different features selection instead of A-scans or B-scan input with DCNN, whereas the scope is left for future works.

In general, for the experimental validation of all proposed models in this chapter, at this stage, due to lack of sufficient field data with ground truth information, all models has been numerically validated. Moreover, since the proposed model is highly sensitive to the shape the hyperbola, the model can work for a specific GPR equipment. Because, the shape the hyperbola varies according to the antenna offset size, height. Therefore, the database for the experimental validation must be built by single equipment. However, the data shall be identical in monostatic configurations even in different equipment. Furthermore, the current analysis remains in 2D B-scans, so it would also be interesting to evaluate the model's performance on 3D data. Hence, the algorithm is computationally heavier and avoided at this stage. Further, the antenna effects removal also suggested. Hence, all the recommendations are retained for future works in this direction. Upon validation in the field, with the fusion of GNSS coordinates data, an automatic data pipeline can be developed for a commercially viable 3D localisation solution.

In the next chapter, the SFR development, experimental validation automatic pipe detection and open air experimental validation of SVR and ANN are presented.

Chapter 4

Experimental validations and SFR development

The first section of the chapter comprises the experimental validation of automatic pipe detection models based on Faster R-CNN and YOLOv4. Second, open-air experimental validation of SVR and ANN-based depth and radius estimation models is covered in the chapter. Finally, the chapter is followed by the development and field validation of a multi-antenna array step frequency radar prototype.

4.1 Experimental validation of automatic pipe detection

The goal of the field validation is to assure and quantify the detection capabilities of the proposed deep learning algorithms on field data (collected from commercial impulse GPRs) in a noisy environment and realistic subsurface circumstances. The prime objective of the automatic pipe detection techniques is to facilitate multiple pipe detection in a single B-scan with acceptable detection rate. Then, the objective of the study is to validate the proposed models in field data. In this respect, four models were chosen for experimental validation, as indicated below. Because of the large-scale data gathering systems, such as a high-speed array GPR systems are unavailable at this stage, single channel impulse GPR has been used for experimental validation. The model is verified using greyscale data rather than binary data. Because the greyscale input model is standard and performed reasonably well in the numerical investigation.

The four studied models are,

- Faster R-CNN + ResNet-50 + Annotation-1 grey-scale image input
- Faster R-CNN + ResNet-50 + Annotation-2 grey-scale image input
- YOLOv4 + Annotation-1 grey-scale image input
- YOLOv4 + Annotation-2 grey-scale image input

In the context, the validation was carried out at Gustave Eiffel University in Nantes, France. In order to conduct the GPR survey, two 350 MHz impulse GPRs (GSSI SIR-4000 type) were used. The reason for choosing 350 MHz centre frequency was, since it is a commonly utilised commercial GPR and frequency range for utility detection application, and it has a penetration range of up to 2 - 5 m depending on the soil condition. The training data were taken around Nantes campus in various locations utilizing two separate GSSI 350 MHz impulse GPRs, and the test data was obtained from the test zone illustrated in Figure 4.1. Hence, the training and test contain GPR B-scans obtained from two different GPRs (but same type, frequency, and settings parameters). Furthermore, because the test site's exact ground truth is unknown,

performance metrics like as accuracy and Recall were calculated based on the global assumption that at least one pipe is recognized at high density overlapping hyperbola. As a result, several pipes in a single location are treated as a single target (already defined hypothesis). In this case, already existing schematic CAD drawings of the site are used as a probable ground truth to confirm the existence of the pipes (without depth and size information). Whereas, depth and radius are not mandated in the pipe detection stage.

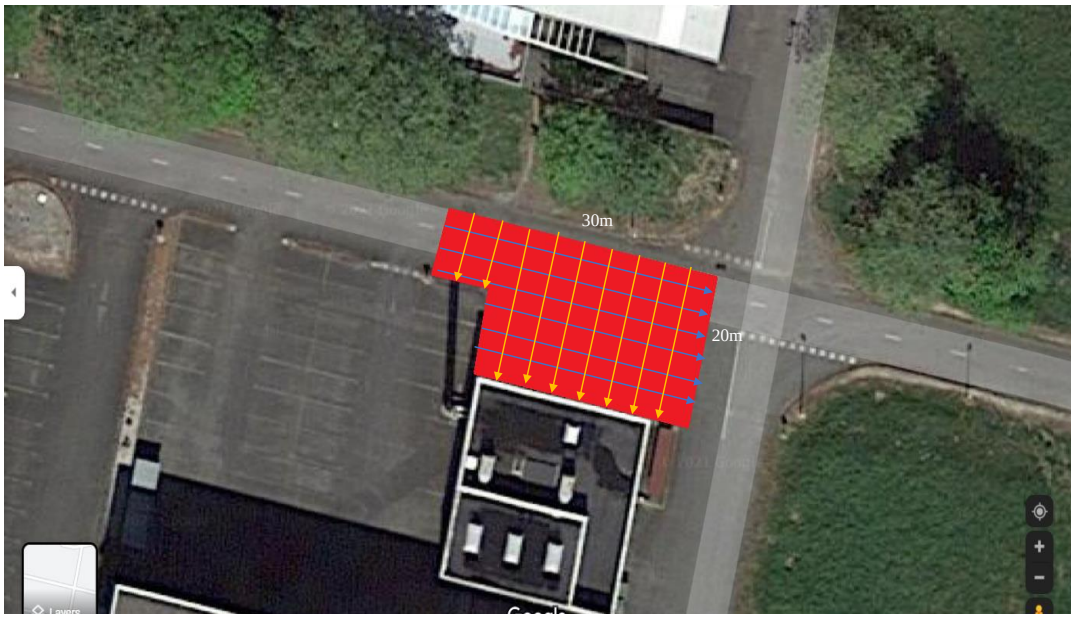

Figure 4.1: Aerial view of the test site in University of Gustave Eiffel, Nantes.

The trained Faster R-CNN and YOLOv4 models were evaluated separately on their respective trained models. In this context, the test site GPR survey was carried out in a grid, as seen in Figure 4.1. As a result, the Figure 4.2 is offered as courtesy evidence obtained during the survey. Parallel survey profiles were placed at 0.5 m intervals (blue profiles with an approximate distance of 30 m each) with parallel to the road, whereas perpendicular profiles were spaced at 1 m intervals (yellow profiles with 20 m each). To ensure the datasets' exclusivity, the training data set was gathered from various parts of campus. An example of two training images are presented in Figure 4.3.

Figure 4.2: Ground view of test site in University of Gustave Eiffel, Nantes.

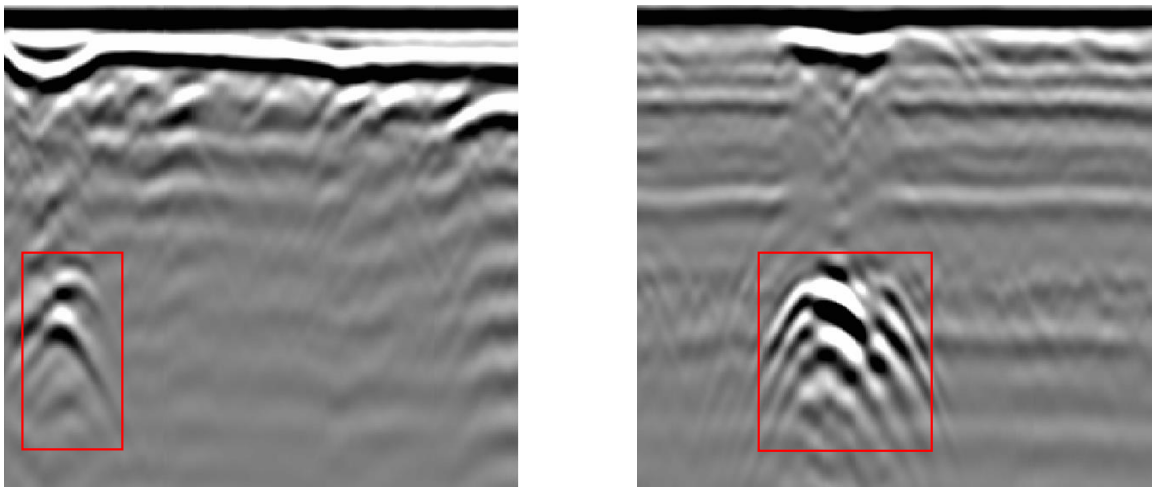

Figure 4.3: Example of GPR B-scan images obtained in University of Gustave Eiffel, Nantes for the training model. Size: 600 x 600 pixels-images, format: png, horizontal spatial length: 5 m, time samples: 1024 (5 m x 1024).

The GPR acquisition rate of both GPRs was set to 70 A-scans/m and 1024-time samples per A-scan across a 35-ns time frame. The spatial step size of the B-scan is set at this level because high resolution can cause artefact hyperbola from aggregate diffractions, and it can also slow down the acquisition speed. In addition, any value between 1 cm - 5 cm spatial resolution is sufficient for the parameter estimation as validated in the numerical study Chapter 3. Hence, 70 A-scans / m is selected. Further, the resolution can be controlled by k proposals in Faster R-CNN as discussed in 2.2.1.a. Despite the fact that the obtained B-scans varied in length, the

whole B-scan was segmented into 5 m spans for each photo. Finally, for YOLOv4, each 5 m B-scan was pre-processed with a specific logarithmic gain setting, time zero offset, and scaled to 600 x 600-pixel images. A total of 84 B-scans with 116 hyperbolas were used, with 67 B-scans used for training and 17 B-scans used for validation. The reason for the selection of training data sets is based on the observation obtained from the numerical study. Whereas, the training size of above 50 B-scans were sufficient to obtain better results in numerical study. Therefore, minimum training database size were decided accordingly. The training database size can be increased in the future to study whether the model performance can be improved further in field data. Regarding the test sets, there were 99 B-scans and 151 hyperbolas in the test zone. The B-scans were subjected to pre-processing techniques such as time zero referencing and exponential gain, conversion which were applied to the full data set as a single setting using Reflexw batch processing. This is because the goal of automated detection is to utilise a robust model to handle huge amounts of GPR data with a single set of global parameters. In this regard, only minimum pre-processing is used at this level to test the model's resilience on near-raw data. Since, the objective of the study is limited to validate the detection model's accuracy, the automation of the pre-processing is not considered at this level. Hence, the Reflexw based manual pre-processing is used. Moreover, the automation is more likely an engineering task than scientific aspect, so it's retained for future prospect. Then, resizing and "B-scan to image conversion" were processed in Matlab according to the method proposed in 2.2.3.b.

The resized images went through annotation process for the training sets. In this respect, the two Annotation approaches were done in this sequence, and two sets of annotated training data sets were created for each Annotation scenario, such as Annotation-1 and Annotation-2. The Annotation methodologies and goals were covered in the subsection 2.2.3.a.

Finally, the four distinct trained models listed above were tested with test site B-scans, and their performance was assessed using the performance matrix. As a reminder, the performance matrix and its interpretation, below here.

1. True positive (TP): True pipe detected as a pipe
2. False Negative (FN): Pipe is not detected
3. False positive (FP): Non-pipe detected as a pipe
4. True negative (TN): Non-pipe detected as a Non-pipe. It indicates the background and can not be quantified at this application.

Recall: It is the proportion of correctly identified pipes. In other words, Recall defines the percentage of pipes that were correctly identified by the method. It is also called as sensitivity. Further, it describes how far the model can miss detecting a pipe.
Recall can be given as:

$$Recall = \frac{TP}{TP + FN} \tag{4.1}$$

Precision: It is the fraction of the positive data that is actually pipes. In other words, Precision can be defined as the fraction of detected pipes that are actually pipes.

Precision can be given as:

$$Precision = \frac{TP}{TP + FP} \tag{4.2}$$

4.1.1 Experimental validation of Faster R-CNN

The primary goal is to guarantee that the Faster R-CNN model can detect many pipes (in the form of hyperbola) in a single B-scan with acceptable performance for an operational model. Furthermore, this study was accompanied by measurement of detection performance in terms of "Precision" and "Recall," as observed in a numerical analysis. In this context, the models such as "Faster R-CNN + Annotation-1" and "Faster R-CNN + Annotation-2" were trained

in tensor-flow using Google Colab. The above-mentioned annotated field GPR data sets were used to training, validation and testing in the similar manner. The model parameters have been set similar to the one in numerical study that has explained in the subsection in 2.3.3.a namely "model parameters". The manual labelling (annotation) of a single hyperbola using the tool "labelimg" consumes around 1 min per hyperbola. The model training loss converges in around 35,000 - 40,000 learning rate iteration cycles. Hence, one of the least error model was selected for testing. The, loss curve trend is very similar to that of numerical model training. For instance, the Figure 4.4 depicts the training validation M.S.E curves. For training in Google Colab, the entire procedure takes about 6 hours per model (cloud based high performance computing resource). However, in local PCs, the time will be substantially longer depending on the hardware resources. For example, a PC with 8 Gb GPU can take around minimum 24 hours to train a model at this size. The models considered in this study are,

- Faster R-CNN + ResNet-50 + Annotation-1 (Grey-scale input)
- Faster R-CNN + ResNet-50 + Annotation-2 (Grey-scale input)

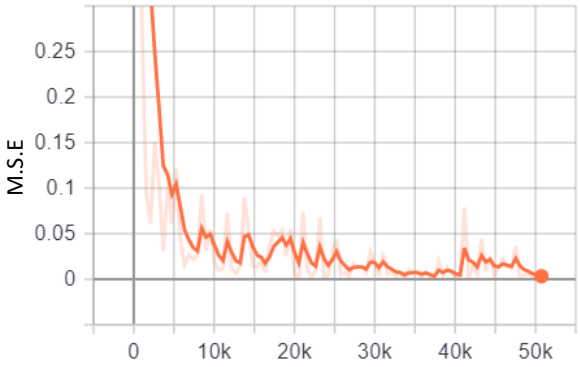

Figure 4.4: Example of model total training loss function of Faster R-CNN with ResNet-50 and Annotation-1. X-axis represents iteration numbers, while Y axis indicates Mean Square Error (M.S.E).

Furthermore, the performance measures like Precision and Recall were determined based on the global assumption that at least one pipe is detected at high density overlapping hyperbola. As a result, several pipes at a single area are regarded as a single target. This hypothesis was considered at the time of labelling. A carefully controlled test site is required to evaluate the model's ability to distinguish individual pipes in a congested environment. However, individual pipe distinction, impact of centre frequency were covered in the numerical study in Chapter 2. Hence, the experimental study of the scope has been kept for future prospect.

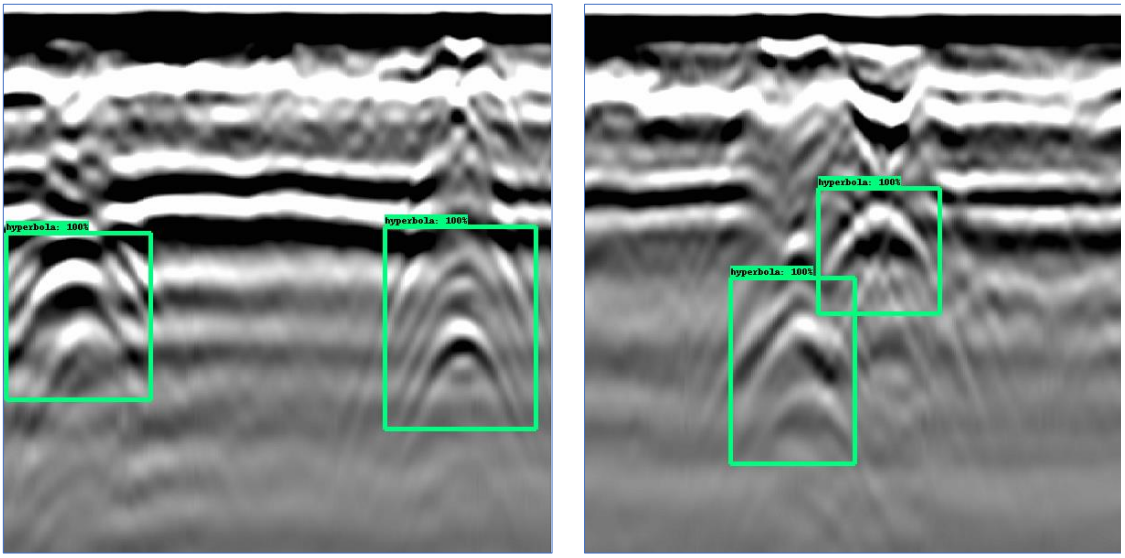

a) b)

Figure 4.5: Example for True-Positive detection with Faster R-CNN + ResNet-50 model using Annotation scenario-1. a) pipes within trenches detected as a single zone, b) two separated pipes detected individually.

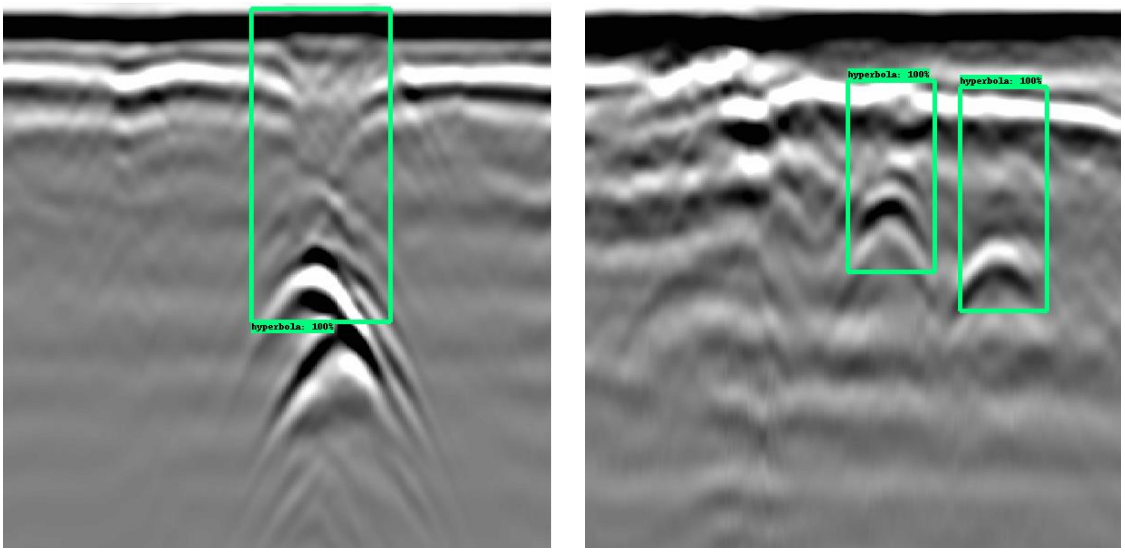

a) b)

Figure 4.6: Example for True-Positive detection with Faster R-CNN + ResNet-50 model using Annotation scenario-2. a) two multiple overlapped pipe within trenches detected as single target, b) two separated pipes detected individually.

Figures 4.5 and 4.6 illustrate some real positive detection results obtained in the models "Faster R-CNN + ResNet-50 + Annotation-1" and "Faster R-CNN + ResNet-50 + Annotation-2", respectively (two separate models). The findings show that the models perform as intended. Specifically, Figure 4.6.a in the illustration, the Annotation-2 model recognizes the two overlapping hyperbola zones as a single target, which is corroborated by subsurface echo.

Meanwhile, Figure 4.5.a shows the model's ability to prevent false positives caused by several reflections below the top pipe. To incorporate some false alarms from the two models, Figures 4.7 and 4.8 show false alarms from the Annotation-1 and Annotation-2 models, respectively. The top of the pipe and bottom reflection are visible in Figure 4.7.b. As a result, the false positive is formed. Because the bounding boxes are symmetrically overlapping, an extra NMS filter can counteract these false positive effects. Meanwhile, as shown in Figure 4.7.b, a multi reflection and a layer interface are recognized as false positives. It's caused by the Faster R-CNN network's perplexity on half-curve hyperbola edges. It implies that the model must also be trained with particular "true negative" classes. However, this approach may create false alarms of true targets of half hyperbola signatures. This can be studied in detail in the future, whether the approach can further improve the model performance.

Furthermore, in the Annotation-2 technique shown in Figures 4.8, false positives are generated by misclassifying the edge effect as real hyperbola. And the Figures 4.8.b are a false positive that may be eliminated by the extra NMS filter stated in the preceding paragraph.

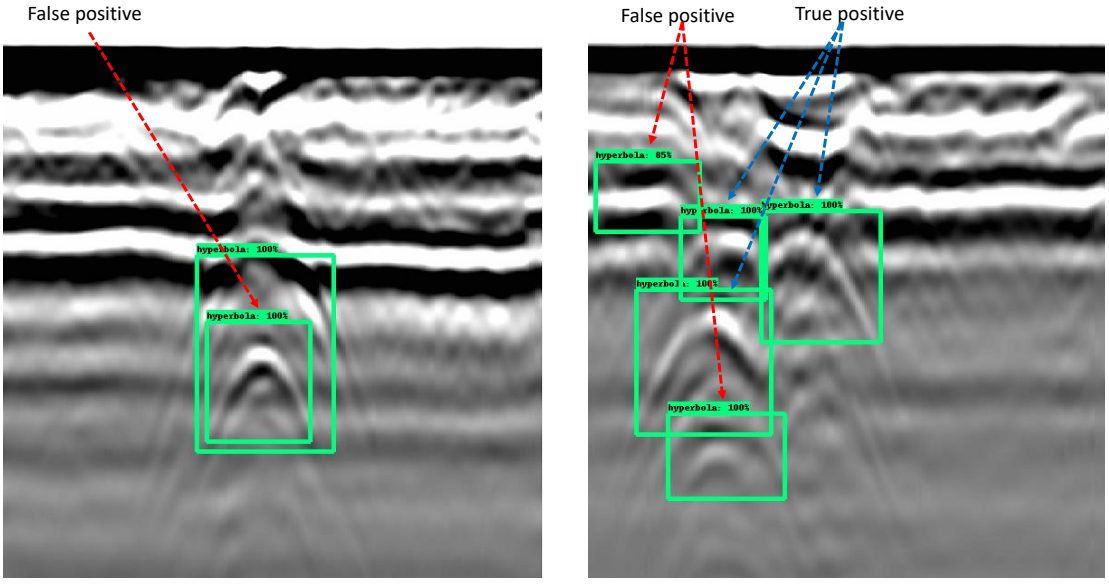

Figure 4.7: Example for False alarms with Faster R-CNN + ResNet-50 model using Annotation scenario-1

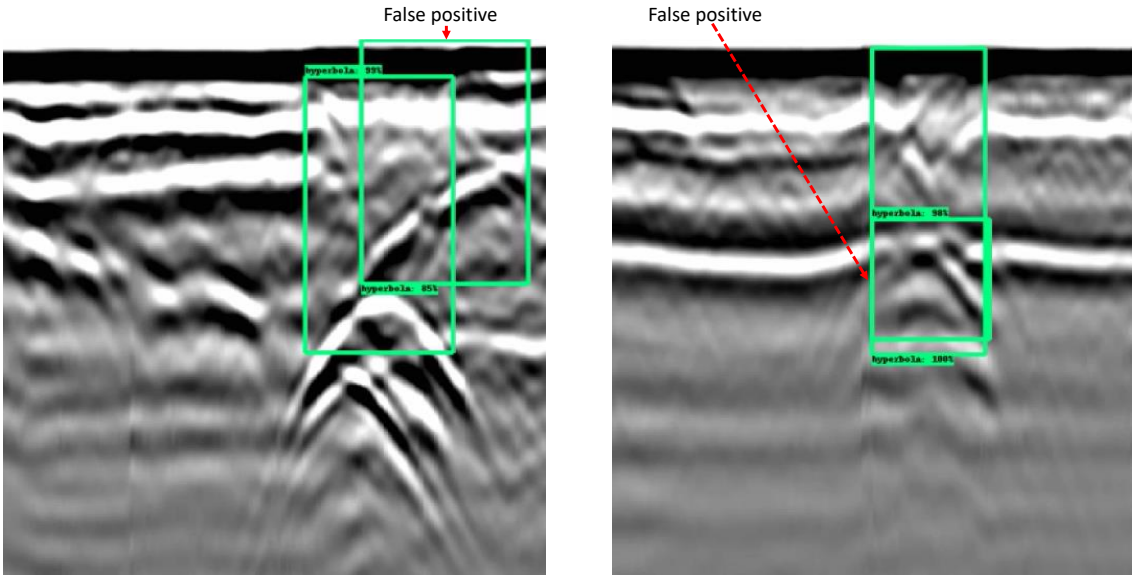

Figure 4.8: Example for False alarms with Faster R-CNN + ResNet-50 model using Annotation scenario-2.

Figure 4.9 shows how the Faster R-CNN + ResNet-50 based detection models react on comparable B-scans using two different Annotation techniques when the two Annotation approaches are compared in terms of pattern of false alarms. The first row of figures corresponds to the results from Annotation scenario-1, while the second row corresponds to Annotation scenario-2. In case of scenario-1, the models generate more false positives, but in scenario-2, the models miss the targets, resulting in false negatives. However, the increased false negative is not appreciated in terms of safety.

The total performance of the two Faster R-CNN models is shown in the Table 4.1. The results show that Annotation-2 has a greater Precision of 91.6%, whereas Annotation-1 has a higher Recall of 92.7%. Meanwhile, the Precision difference between the models is less, while the Recall of the Annotation-2 model has dramatically decreased. Because better Recall is favoured above higher Precision. Annotation-1 models outperform the other models. The possible reason for the lower Recall in annotation-2 can be attributed to the inclusion of layer interface echo and with lower number of training data. Since higher "Recall" lower risk of missing a real pipe during detection, annotation-1 is recommended at this stage.

Faster R-CNN Model	B-scans	Hyperbolas	TP	FN	FP	Precision (%)	Recall(%)
ResNet-50 + Annotation-1	99	151	140	11	19	88.0	92.7
ResNet-50 + Annotation-2	99	151	131	20	12	91.6	86.7

Table 4.1: Experimental test performance results of automatic pipe detection models based on Faster R-CNN + ResNet-50, at IOU of 0.6.

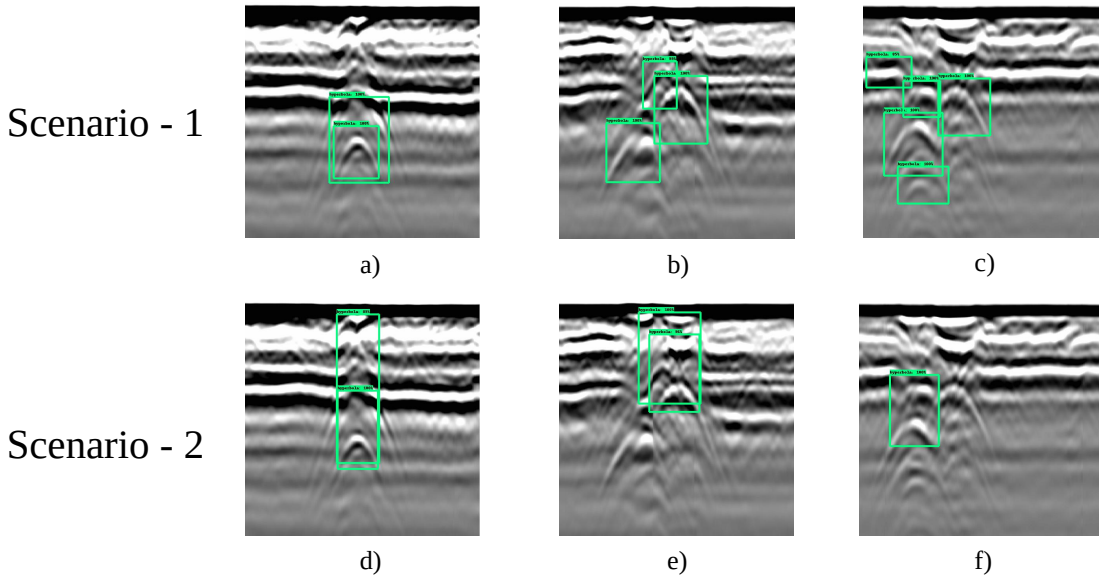

Figure 4.9: Example for comparison of few False alarms with Faster R-CNN + ResNet-50 models with scenario-1 & 2, where a, b, c are the results of the model with annotation-1, while c, d, e are the results with annotation-2 for the corresponding B-scans on the top row.

Conclusion

In conclusion, the aforementioned field validation indicates that the Faster R-CNN model can be deployed to automatically identify numerous hyperbola in a single B-scan. The suggested model is validated using commercial impulse GPR field data. Due to the lack of a substantial data with ground truth, multiple overlapping pipes within a single trench are thought to be a single target, which is sufficient to draw a no-dig safety zone around the target regardless of whether it is a single or several deployments at a place. Furthermore, Annotation-1 has a greater "Recall" (92.7%), although Annotation-2 has a higher "Precision" (91.6%). Higher "Recall" is desired, because it suggests a lower risk of missing a real pipe during detection. As a result, it ensures network security. However, the Precision of the Annotation-1 scenario did not decrease considerably and remains about 88%, which is compelling. Larger training datasets, as well as parametric studies to optimize the Faster R-CNN architecture, can boost model performance even further. Even though the Annotation-1 strategy is somewhat superior, both annotation strategies may be tested for robustness with larger datasets. Certain false positives can be reduced by customizing the Faster R-CNN architecture with an extra NMS (Non Max Suppression) filter, which is not included in this stage. Because, it requires customisation of Faster R-CNN network with extensive engineering development. Therefore, it has retained for future scope. However, at this moment, Annotation-1 is preferable. When parallel B-scans are processed using Faster R-CNN in 3D, the hyperbola derived from real pipe targets will be replicated in adjacent B-scans, while clutter will disappear. As a result, parallel B-scans processing acts as a 3D filter to reduce false positives even further. In conclusion, the current findings indicate that Faster R-CNN may be used as an operational automatic pipe detection model in large GPR data processing, and it suggests the need for additional parametric research in this area.

The next subsection experimentally validates the proposed YOLOv4 model.

4.1.2 Experimental validation of YOLOv4

In addition to Faster R-CNN, the objective of the adoption of YOLOv4 is to study its applicability for the global objective of automatic detection as well as a potential model for real time detection. The reason for separating both studies is that, even though YOLOv4 can be considered as alternative to Faster R-CNN, YOLO's real-time detection ability is unique, which Faster R-CNN can not provide. Therefore, Faster R-CNN and YOLOv4 can be compared for the post-processing detection technique, while YOLOv4 is stand-alone option for real-time pipe detection algorithm. Hence, YOLOv4 experimental results are presented below.

In this context, by using the annotated data sets described in the previous subsection, the following two YOLOv4 models were trained and tested.

- YOLOv4 + Annotation-1 (Grey-scale input)
- YOLOv4 + Annotation-2 (Grey-scale input)

The Table 4.2 presents the performance matrix of both Faster R-CNN and YOLOv4 in the same table. According to the Table 4.2, the Recall of YOLOv4 has reduced drastically to 81% and 76% in Annotation-1 and Annotation-2 models, respectively, when compared with its opponent in Faster-RCNN. The reason for this because both models have a significant number of false negatives. This suggests that the model misidentified more hyperbolas throughout the detection process. This might be owing to tiny training data sets, and the behaviour is identical to that observed in a numerical evaluation of YOLOv4 in a higher noise environment. As a result, it is clear that the YOLOv4 design and principles are less resistant to noise.

Furthermore, the Figures 4.10 and 4.11 show some true positives from both YOLOv4 models (Annotation-1 and Annotation-2).

Model	B-scans	Hyperbolas	TP	FN	FP	Precision (%)	Recall(%)
F-ResNet-50 + Annotation-1	99	151	140	11	19	88.0	92.7
F-ResNet-50 + Annotation-2	99	151	131	20	12	91.6	86.7
YOLOv4 + Annotation-1	99	151	123	28	3	97.6	81.45
YOLOv4 + Annotation-2	99	151	115	36	18	86.46	76.15

Table 4.2: Experimental test performance results of Faster R-CNN and YOLOv4 automatic pipe detection models.

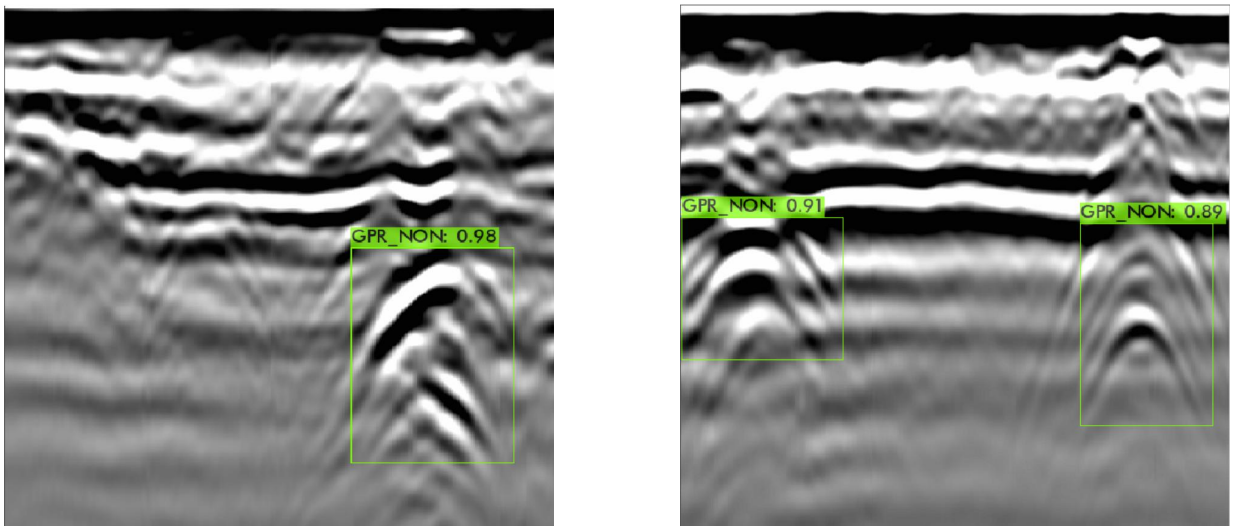

a) b)

Figure 4.10: Example for True-Positive detection of YOLOv4 model using Annotation scenario-1.

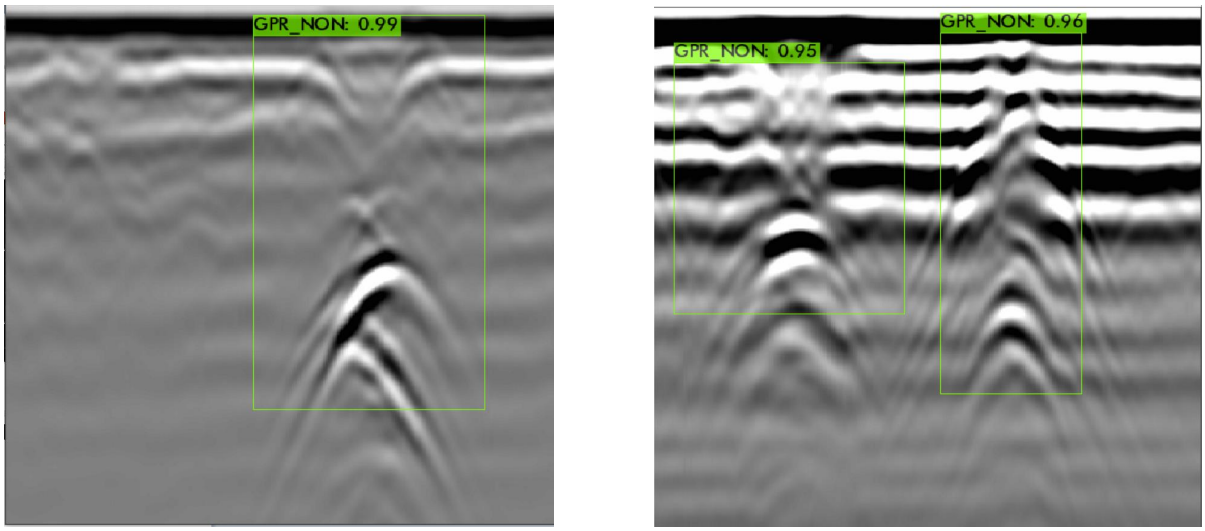

a) b)

Figure 4.11: Example for True-Positive detection of YOLOv4 model using Annotation scenario-2.

In terms of false alarms pattern, like in the Figure 4.12.b, the model failed to detect a single hyperbola in the whole B-scan (false negative). Likewise, in the Annotation scenario-2, the model creates false positives which overlaps the true positive bounding box. This can be eliminated by additional NMS (Non Max Suppression) layer in future. Hence, the Precision can be improved. However, it requires a parametric study in this direction.

In terms of false alarms, as seen in Figure 4.12.b, the model failed to recognize at least a single hyperbola in the whole B-scan (false negative). This due to the YOLOv4's convolution architectural drawback, or mismatch of aspect ratio between the training data and test data. The specific reason can not be spotted due to the complex architectures of YOLOv4. However, the performance can be studied by increasing the training database in the future. At this stage, it is a comparative drawback of YOLOv4 in front of Faster R-CNN for the given dataset and configurations. Similarly, in Annotation scenario-2 as shown in Figure 4.13, the model generates false positives that overlap the true positive bounding box.

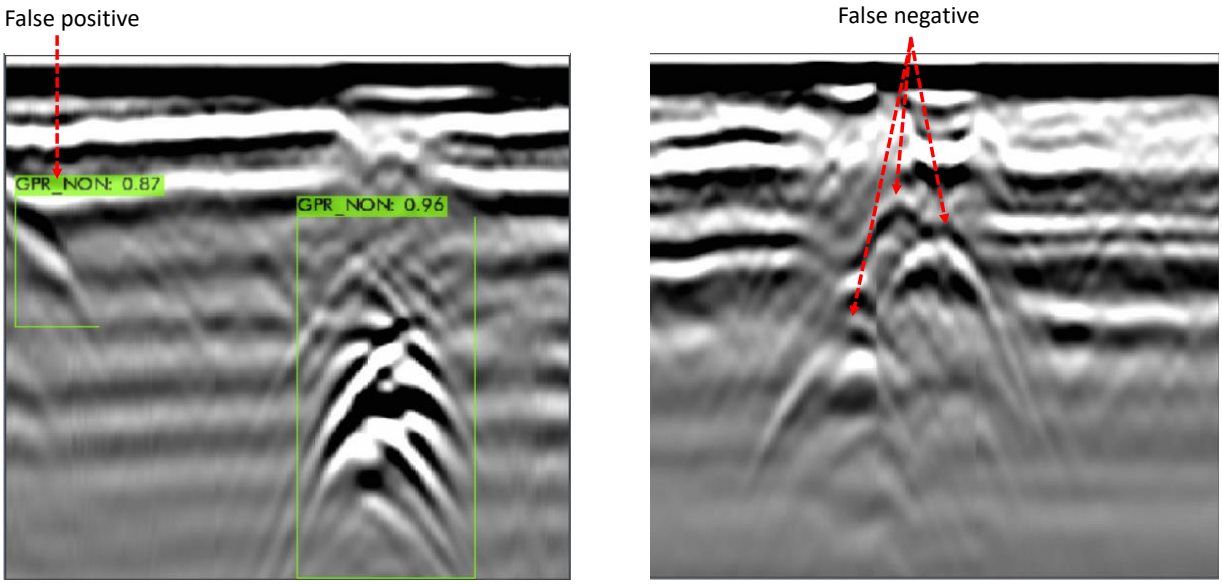

Figure 4.12: Example for false alarms of YOLOv4 model using Annotation scenario-1.

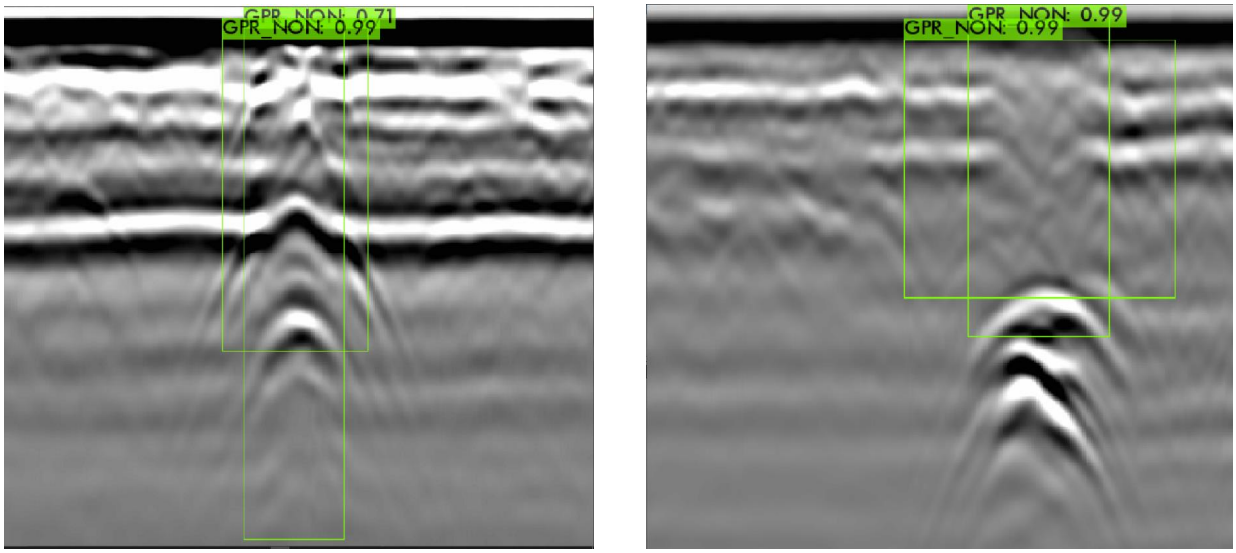

a) b)

Figure 4.13: Example for false alarms of YOLOv4 model using Annotation scenario-2.

Conclusion

The subsection discusses the validation of an automated pipe detecting approach based on YOLOv4. The main goal, on the other hand, was to see if the suggested model can detect several hyperbolas in a single B-scan with acceptable accuracy. Multiple hyperbola detection is validated and confirmed. In this case, 50 B-scans and 99 B-scans containing 151 hyperbolas were employed to train the model. In terms of data preparation for training, the pre-processing in Reflexw required about 15 minutes each B-scan. Then, as long as the conversion script is ready, the Matlab based image conversion will take a few minutes. Finally, labeling with the Labelimg tool takes around 5 minutes for every B-scan. Once the data is ready, the training will take at least 12 - 24 hours in google colab. The cycle is repeated for each minor parameter change. In terms of results, in compared with Faster R-CNN, the "Recall" of the YOLOv4 is quite poor. Precision, on the other hand, stays over 97 percent, while Recall is above 81%. The YOLOv4 convolution design or the bounding box proposal process may be the cause for the performance reduction. As a result, the training data must be increased in order to determine whether the model's performance can be improved. YOLOv4 does, however, have the characteristic of real-time detection, which Faster R-CNN does not have.

4.1.3 Conclusion

The section presents experimental validation of deep learning-based automatic pipe detection models based on GPR data, with an emphasis on large-scale data processing for utility mapping. In this experimental validation, two Faster R-CNN models and two YOLOv4 models from each category were chosen with different Annotation methodologies, as shown in the Table 4.2. Though the Faster R-CNN includes various convolution network options such as ResNet-50, ResNet-101 and Inception-v2, the ResNet-50 was chosen with the idea that the performance does not vary much depending on the convolution network. In reality, the numerical study

findings demonstrated this. However, ResNet-50 has shown relatively better performance, and further considered for experimental validation.

In the experimental study, the main goal, on the other hand, was to see if the suggested model can detect several hyperbolas in a single B-scan with acceptable accuracy, using field data. Hence, all the models confirms its ability to detect multiple hyperbola in a single B-scan.

In addition, the performance of the models in terms of Precision and Recall were measured to ensure whether the model can provide acceptable accuracy to deploy as an operational solution. The performance matrices of four studied models used for this experimental validation are summarized in Table 4.2. Whereas, the "Faster R-CNN + ResNet-50 + Annotation-1" model has the highest Recall, according to the specifc data (92.7%). Such that, it has missed the true targets (pipes) the fewer times when compared with other models. However, the Precision is pretty reasonable at 88.0%, and Precision can potentially be increased by an extra filter (NMS layer) because the majority of false positives are seen in strongly overlapping bounding boxes over real positives. Meanwhile, the "YOLOv4+ Annotation-2" model has demonstrated the greatest Precision (97.6%). However, the Recall values of YOLOv4 are quite low (81.45% and 76.15%). As a result, the YOLOv4 has the higher probability of missing the targets. In fact, 'Recall' is more important than accuracy in this utility application. Because while the detection may tolerate some false positives, false negatives (miss detection) might increase the risk of strikes during the excavation works. As a result, for large-scale GPR post-processing applications, Faster R-CNN-based automatic pipe detection models are recommended based on the outcome of this study. Meanwhile, though the YOLOv4's performance is somewhat poor, its detection speed is extremely fast and may be used for real-time detection during the survey. However, in terms of big scale mapping, real-time detection is an optional capability. On the other hand, performance is tested for the specific data set, one specific GPR equipment and centre frequency, and only 67 B-scans of training sets. Large training data sets, more hyperparameter adjustments, extra NMS layers (customisation of existing architecture), and diverse parametric investigation can all assist to make a more firm conclusion. Nonetheless, the analysed performance raises the prospect of an operational automated pipe detecting program. In conclusion, the feature of multiple hyperbola detection in a single B-scan at acceptable performance is acknowledged in this study. Hence, it promises further investigation to produce a fully operational model for large scale GPR data in utility detection.

4.2 Open-air experimental validation of parameter estimation

A large scale controlled site with varying permittivity, depth, and radius of pipes is required to train the supervised machine learning models in the context of the validation of the suggested parameter estimation methods such as SVM, SVR, and ANN. However, such controlled site facility is currently unavailable. As a result, we decided to perform a controlled experiment in an open-air setting. Even if the open-air permittivity doesn't change ($\epsilon_r = 1$), the depth and radius can be estimated. Because the shape of the hyperbolas differ due to variation in depth (d) and radius (r). As a result, the data and features will change. Therefore, the objective of the open-air experimental validation is to collect data to build SVM, SVR and ANN models and, then to perform estimation of depth (d) and radius (r) of the pipes using such trained models. Hence, the model's performance can be measured as stated in Chapter 3. Both training and test data were collected from the open-air controlled experiment. In terms of the experimental setup, a monostatic Step Frequency Radar (SFR) test bench is employed, which is equipped with controlled motors for horizontal and vertical movement of the antenna and is positioned in around RF absorbers. The test bench was developed for a project called ECODEM and is

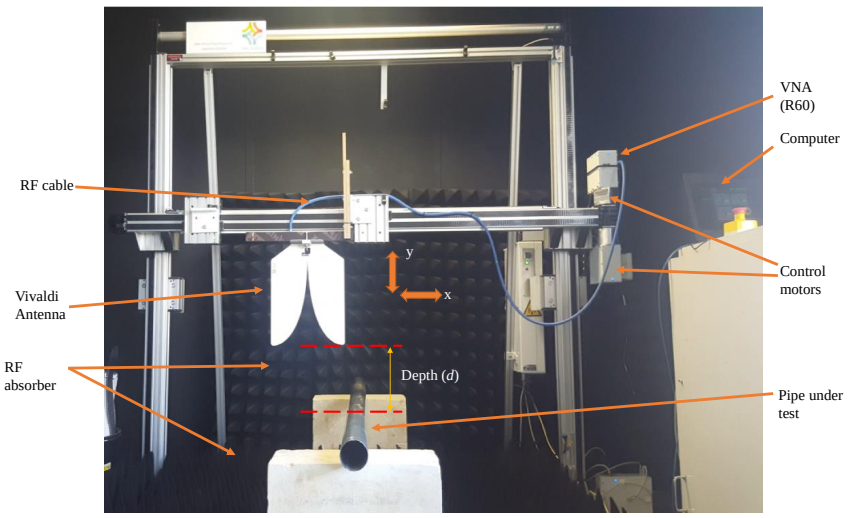

Figure 4.14: Open air depth radius estimation experimental setup in test chamber with step frequency radar test bench, in Cerema, Anger.

now being utilised for various different GPR investigations. The experimental setup is shown in Figure 4.14, and the configuration parameters presented in the Table 4.3.

In this regard, 5 metallic pipes of varying diameters $(20, 43, 80, 100, 161$ mm) were employed in the experiment. All the pipes are seen in Figure 4.15. Then, by adjusting the antenna horizontally and vertically, each pipe had 69 B-scans at varied depths. The step size between two A-scans in a B-scan were 2 cm, and 31 A-scans are in a B-scan. The reason to define 31 traces was that, the effective width of the test bench without significant interference was observed as 60 cm. Therefore, the number of A-scans in a B-scan was limited to 31. Like wise, one B-scan per depth position was acquired. Hence, the depth was changed at the resolution of 1 cm, varying between 20 cm to 88 cm (height between pipe and bottom edge of the antenna). This resulted in around 345 B-scans in total. The obtained B-scans were shuffled in $80:20$ ratios for training and testing. In terms of hardware, to facilitate a monostatic SFR, a high directive Vivaldi antenna is used, with R60 reflectometer. Hence, the acquisition provides complex S_{11} measurements. The configured bandwidth was 435 - 4435 MHz to respect the antenna bandwidth and maintain the centre frequency to be in the range of commercial SFR configurations. Other parameters can also be referred in the Table 4.3.

Figure 4.15: Metallic pipes used for experiment with its diameter size.

Pipes size	Metallic: $20, 43, 80, 100, 161$ mm (diameters)
Depth range	$0.2 : 0.01 : 0.88$ m (69 depth values)
Horizontal step size	$-30 : 2 : 30$ cm (31 A-scans)
Pipe buried medium	Open air
GPR type	Step frequency radar with Reflectometer (R60 - Copper mountain)
Antenna	Vivaldi
Sweep frequency	$435 - 4435$ MHz
Number of frequency points	801
Open Air t0 performed	Without pipe
Database (B-scans)	266 training B-scans (80%), 79 testing B-scans (20%)

Table 4.3: Experimental configuration parameters.

As previously stated, the used SFR setup was monostatic, allowing complex S_{11} (reflection coefficient) parameters to be measured throughout whole sweep frequency points. As a result, S_{11} readings from a single complete sweep comprise the information of a single trace (A-scan). A single trace's log scale S_{11} plot is shown in Figure 4.16. There are 801 sweep points between 435 and 4435 MHz. Furthermore, it indicates that the S_{11} values are less than -10 dB, which respects the antenna bandwidth (-10 dB threshold) in-terms of impedance matching (energy transfer). The time signal (A-scan) was derived by performing an Inverse Fast Fourier Transform (IFFT) on the recorded complex S_{11} sweep, as shown in Figure 4.17. In this case, it is referred to as a raw A-scan (A_r). Whereas, the two strong reflection peaks at the beginning of the signal seen in the Figure 4.17, are formed due to the impedance mismatch at the reflectometer antenna cable connector and due to antenna effect. Therefore, the effective reflection occurrences, however, are not evident in raw A-scan because of the significant influence of connector effects, antenna effects, external noise, and clutters. As a result, a free space A-scan measurement (T_0) was obtained as shown in Figure 4.18, without any pipe to quantify the aforementioned antenna effects and other clutters. Consequently, the free space (T_0) were eliminated from all A-scans as provided in the Equation 4.3. Thus, the effective (filtered) A-scans (A_e) were calculated and the reflected occurrences were seen more clearly. Whereas, The effective A-scan is presented in the Figure 4.19. Whereas,

$$A_e = A_r - T_0 \tag{4.3}$$

The filtered A-scans are then stacked together to construct B-scans, which are then used for hyperbola picking. In Figure 4.20, you can see an example of a B-scan. Although there is still some clutter and noise apparent in the B-scan, the hyperbola is clearly visible with high contrast in the top half of the B-scan. As a consequence, as shown in Figure 4.19, hyperbola picking was performed between peak to peak. Nonetheless, for the travel time calculation in the numerical analysis, we employed the minimum peak of the direct coupling and the highest peak of the pipe reflection. The first echo's minimal peak' and the 'minimum peak of the pipe reflection' are chosen in this experimental validation.

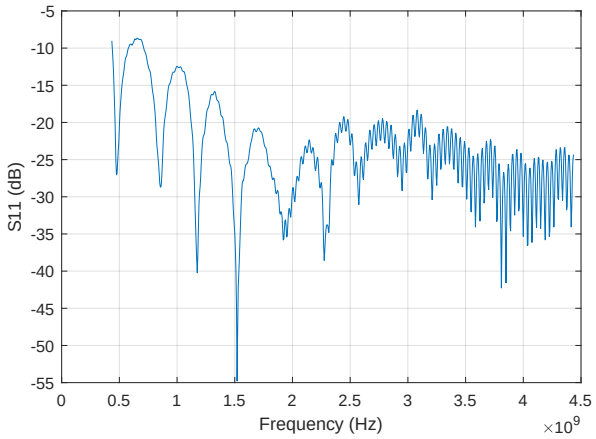

Figure 4.16: Log scale S_{11} (real part) plot of a single trace (A-scan). 801 sweep points between 435 - 4435 MHz.

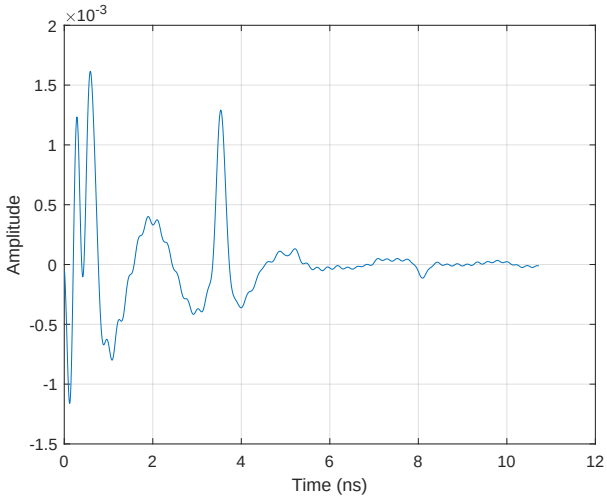

Figure 4.17: Example of a raw A-scan after IFFT.

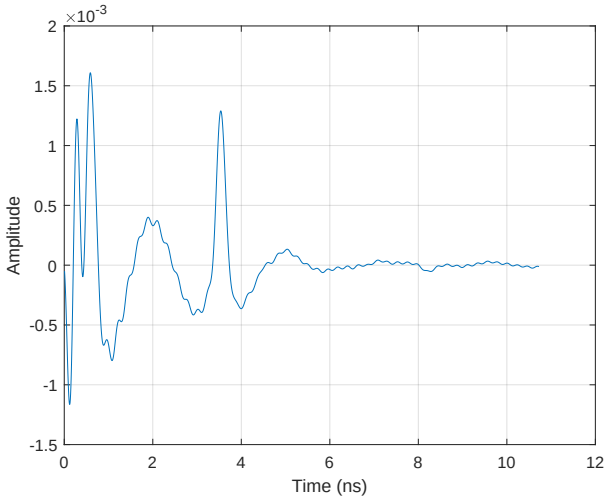

Figure 4.18: Example of an open air A-scan.

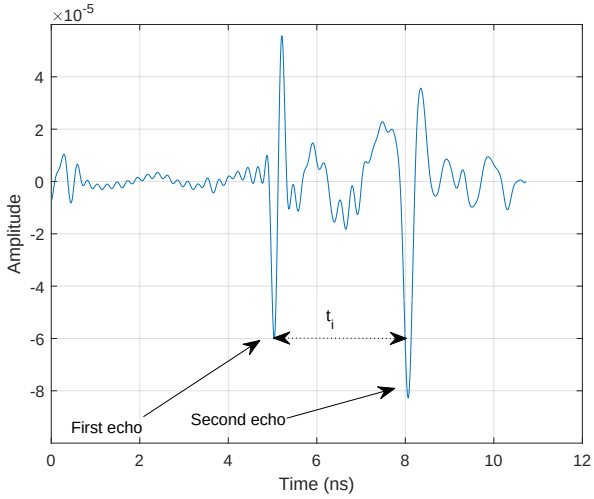

Figure 4.19: Example of an A-scan after free space (T_0) removal.

The initial reflection wavelet (first echo) does not, however, correlate to the radiation centre. Rather, it's near the antenna's bottom edge (but not exactly). Correctly estimating the radiation centre (t_0) in commercial GPRs is a complicated procedure that depends on the antenna's mechanical and electromagnetic characteristics. As a result, the minimum peak of the first echo as seen in the Figure 4.19 was presumed to be the t_0 reference. Furthermore, changing the t_0 reference has no effect on the suggested "supervised" machine learning models' performance. For example, in a numerical investigation, when the point t_0 was varied by 200 ps, the mean absolute relative error of the radius estimation using SVR was 5.2% before and after changing t_0. As a result, it indicated that, any common reference point for t_0 may be utilised for machine learning. Because, when the additional travel time error owing to t_0 is included, the bias in all A-scans remains constant. As a result, it has no bearing on the supervised learning model. Then, assuming that a common reference is maintained globally, the suggested features and machine learning models are independent of the t_0 correction error. As a consequence, the t_0 reference was picked as the first echo. Finally, hyperbolas similar to those shown in the B-scan on the Figure 4.20 were selected, and the features were retrieved as described in Chapter 3. The hyperbolas are presented in the Figure 4.21 in three different depths and for a specific pipe.

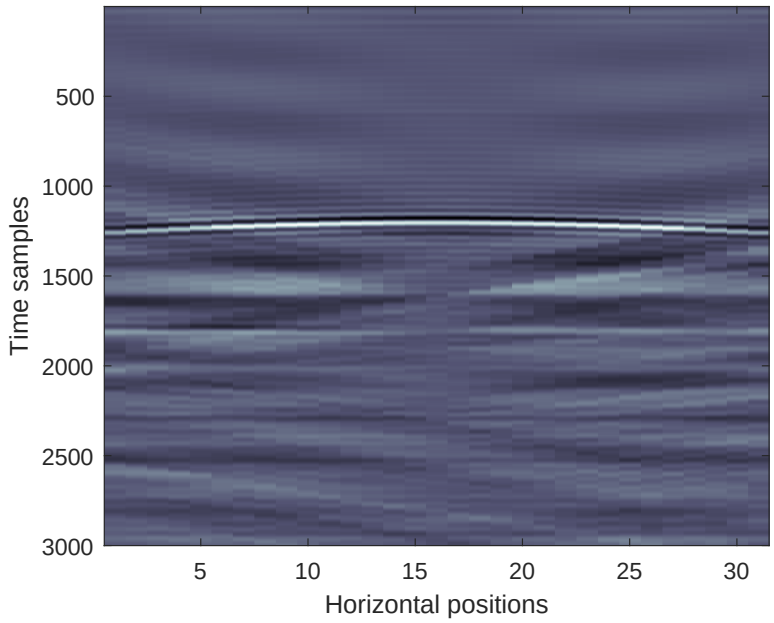

Figure 4.20: Example of a B-scan with hyperbola.

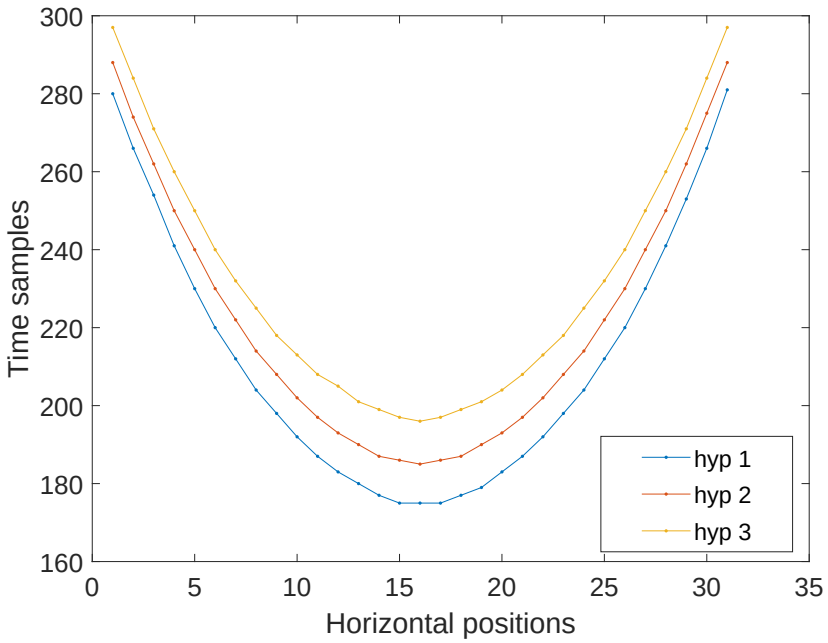

Figure 4.21: Example of 3 hyperbolas extracted from separate B-scans at 3 different depths.

In this context, the data were split into training and test sets as defined in the above table, and respective Multi Class SVM, SVR and ANN models were trained, as described in the Chapter 3. Relevant results and key findings are presented in the below subsection.

4.2.1 Results and discussion

There was a multi-class SVM model (SVM_r) for radius estimation, and two separate ϵ-SVR models (SVR_r, SVR_d) were trained independently with its corresponding labels using the

database described in the Table 4.3 (266 training B-scans (80%), 79 testing B-scans (20%)). Meanwhile, ANN_r, ANN_d also built using the same training set and features. Whereas, the features had been described in the Chapter 3. Moreover, the ANN architecture and activation functions were kept similar to the settings described in the numerical study (Chapter 3). Whereas, separate models enable single parameter inversion at a time by solely depend on the proposed six features. However, the model for velocity estimation was avoided since the study is performed in open air settings, thus the medium velocity doesn't vary and its constant.

Table 4.4 compares the performance results of the mean relative error (mean err) those were computed using the Equation 4.4:

$$err = \left| \frac{(M_{est} - M_{act})}{M_{act}} \right| \times 100 \tag{4.4}$$

where, M_{est} is the estimated value and M_{act} is the actual value.
The relative error (err) of the predicted value with reference to its actual value of every tested hyperbola were estimated. Then, the relative errors (err) are populated for the whole test results in order to obtain the mean relative error (mean err). Like wise, the mean relative error (mean err) of each parameter estimation (for radius (r) and depth (d)) was calculated separately for every proposed model that are presented in the Table 4.4.

	Radius estimation		Depth estimation	
	ANN_r	SVR_r	ANN_d	SVR_d
mean err	10.5 %	18 %	0.18 %	0.31 %
median err	5.1 %	10 %	0.10 %	0.13 %

Table 4.4: Experimental Results.

Based on the findings shown in Table 4.4, the depth estimate model is very accurate, with mean err less than 0.5% in all situations. ANN, on the other hand, delivers 0.18%, whereas SVR provides 0.31% of mean err. Even while ANN performs somewhat better, the difference is minimal. As a result, both ANN and SVR may be employed for depth estimate. The prediction time takes less than one second per hyperbola in Matlab. Hence, it is capable of real-time estimation combined with YOLO based real-time detection. However, the actual time can be quantified upon building the complete data pipeline in the future (from automatic detection, pre-processing, features extraction up to the prediction). Furthermore, the speed depends on the hardware resources and development environment too (for example, Matlab or python or C++). Because, this study uses different tools as standalone for each processing steps in the research stage. The operational model shall be deployed as a data pipeline in a single platform.

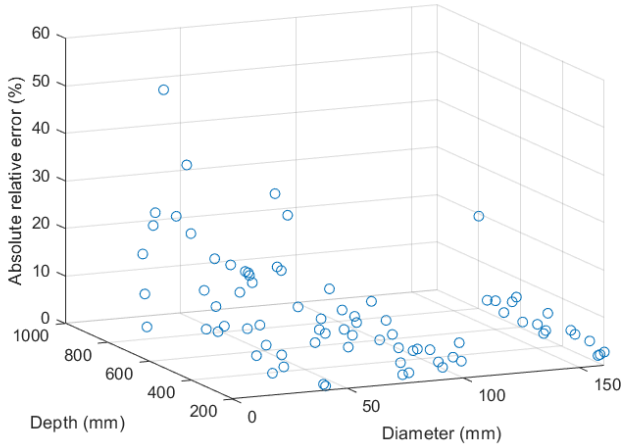

Figure 4.22: 3D scatter plot of absolute relative error in radius estimation using ANN. The 3D error distribution plot visualise the relative radius estimation error at different depth and radius ground truth scenarios.

Similarly, in the radius (r) estimation, the mean err in the ANN and SVR models is 10.5% and 18%, respectively. Meanwhile, the median err in both models is 5.1% and 10%. As a result, ANN-based radius estimate outperforms SVR. Furthermore, as shown in Figure 4.22, the relative absolute error distribution has a relatively large error when the radius is smaller and the depth is greater. The accuracy, on the other hand, improves with lower depth and greater radius classes. Therefore, outliers are more common in areas with a smaller radius and a greater depth. Hence, it impacts the mean err; nevertheless, the median err is substantially lower than the mean err. Furthermore, because the utilised 5 pipes have a fixed radius size, they can be categorized using the Multi-class SVM classification presented in Chapter 3. As a result, it is empirically validated here.

The Figure 4.23 shows the confusion matrix of diameter estimation results obtained using multi class SVM. Whereas, the x-axis refers to the predicted classes of diameter $(20, 43, 80, 100, 161$ mm). While, y-axis is for the actual diameter values $(20, 43, 80, 100, 161$ mm). Based on this confusion matrix, the overall correct prediction is 88% (70/79). False alarms are listed as follows.

- 20 mm class: Total (19), True positive (18), False alarms (1)
- 43 mm class: Total (13), True positive (12), False alarms (1)
- 80 mm class: Total (17), True positive (14), False alarms (3)
- 100 mm class: Total (13), True positive (11), False alarms (2)
- 161 mm class: Total (17), True positive (15), False alarms (2)

As a result, false alarms are increased in the 80 and 100 mm classes. When 80 and 100 mm classes are consolidated into a single group, the total number of false alarms is lowered from 9 to 5. The accuracy should therefore be 94%. Furthermore, when the 20 and 43 mm classes are also merged into a single group, the performance is further enhanced to 96%. As a result, for a global model, the radius classes can be minimized according to industry radius standards. Thus, SVM may obtain greater accuracy for radius categorisation. However, additional examination is a possibility for future work.

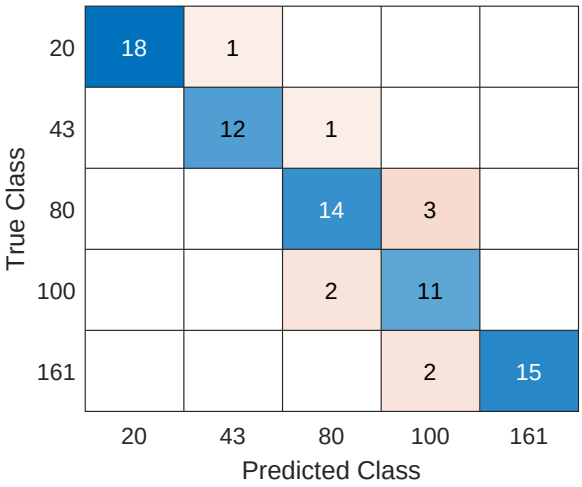

Figure 4.23: Confusion matrix of multi-class SVM classification in radius estimation.

4.2.2 Conclusion

The section experimentally validates the proposed SVM, SVR and ANN based parameter estimation models and analyses the results obtained from such supervised machine learning approaches for estimating the depth (d), radius (r) of the pipe. Hence, with the use of unique feature selection proposed in the Chapter 3. In this regard, due to limited resources, we do not have a controlled location with a sufficient number of pipes of varying depths and diameters to create a supervised machine learning model at this stage. The SVR or ANN, on the other hand, requires hundreds of hyperbolas with ground truth (without overlaps). As a result, the experimental validation is limited to an open air design with a few pipes. In this case, the velocity of the air is constant. Thus, it was not considered for estimation. Furthermore, it is found that, from the open air experimental results, the depth (d) accuracy may be achieved up to 0.5% of mean relative error using both ANN and SVR, which meets the French requirements' Class-A Precision. Whereas, the radius (r) can be estimated with the mean absolute relative error of 10% using ANN and 18% using SVR. Thus, ANN is relatively better than SVR for the radius estimation.

When the radius (r) and depth (d) are well standardized and defined in the classes, the applicability of SVM multi classification is possible. Thus, multi class SVM was applied and observed that, the model can achieve up to 88% mean absolute relative error in open-air settings when classified into 5 classes. Meanwhile, the accuracy can increase up to 96% when the number of classes reduced to 3. However, the depth (d) estimation shows its robustness in noiseless, noisy, random continuous values, metal and PVC pipes configurations (all cases). Then in the open-air settings. These findings promise further acceptability of the methods on 3D localisation of utility network upon validation on more complex experimental data. Nevertheless, the radius (r) estimation performance constitutes 18% of error, and it's not yet regulated by law like depth (d). But the radius information affects the accuracy of the no dig zone boundary. Therefore, ANN based radius estimation model can be used for no-dig zone boundary estimation. Nevertheless, when the radius is standardized into definitive radius classes, multi class SVM also can be deployed for this scope. In the future, more complex controlled experimental study is required in various subsurface mediums and different moisture

levels to vary the permittivity. Thus, large training model can be built, tested and a solid conclusion can be drawn in terms of accuracy and robustness of the proposed models.

4.3 Multi-antenna array step frequency radar development

The important steps of the 3D utility mapping process, such as data acquisition, automatic pipe detection, and geometric parameter estimation, have been identified and explored in Chapter 2, Chapter 3, and prior sections of this chapter. From the literature study and industry analysis, a multi-antenna array step frequency radar technique has been discovered for data collecting, which can fulfil the large scale GPR survey. Because, the multi-antenna array SFR can do concurrent B-scans and create 3D volume data in a single sweep utilizing an array. As a result, the pipe in every direction may be seen in a single pass. Then, the multi-antenna array step frequency radar design has been created to evaluate the concept, and the proof of concept has been confirmed. As a result, the subsections that follow discuss the technology's operational principles, design, implementation, and experimental validation.

4.3.1 SFR Prototyping

To make the SFR prototype development phase easier, we opted to start with a simple design and gradually expand the complexity via consecutive generations. Because a fully fledged big array necessitates complex specialised antenna and RF design, as well as significant resources and expenditures. As a result, the prototype's hardware components, such as VNAs, antennas, multiplexers, and distance encoders, are obtained from the commercial market. The points of trade-off in prototyping were the design need, material availability, cost, and performance. Furthermore, the objective of the prototyping at this stage is, validating the proof of concept of the data acquisition chain. In this regard, two topologies were investigated in this thesis, as seen in Figure 4.24. For real-time data acquisition and B-scan visualisations, integrated hardware as well as the appropriate real-time software and API (Application Programming Interface) were built.

In Figure 4.24.a, the monostatic SFR was created with a single VNA and three antennas, as well as a time division multiplexer. As a result, three channels share a single VNA resource in series. Then, the multiplexer enables switching between antennas in a predefined sequential manner. Three A-scans are measured at a location at a time by switching between antennas. Thus, 03 parallel B-scans are achievable. The PC also powered and controlled the VNA and Multiplexer through the USB port. Several antennas can be added in the future to expand the array's size, necessitating a bigger number of switching ports. However, as shown in the prior subsection, the total SFR speed in this topology decreases as the number of antennas grows.

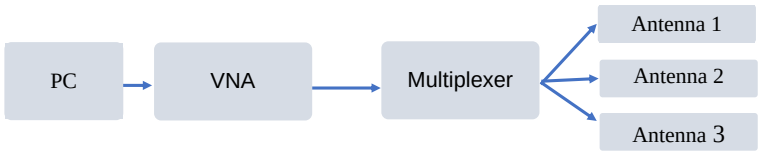

a) Single VNA mono-static three antenna array SFR with multiplexer

b) Two VNA parallel channels mono-static two antenna array SFR.

Figure 4.24: SFR prototyping topologies.

In this regard, when the VNA's speed is insufficient for the architecture shown in Figure 4.24.a, to have multiple channels, parallel VNA's can be built. As shown in Figure 4.24.b, each antenna channel is standalone and executes A-scan acquisition concurrently. As a result, the SFR system's speed is increased. The array size can be increased by adding additional VNAs for every additional channel. Nevertheless, it increases the cost of the system. In this thesis, the two parallel VNA with two antennas prototype, on the other hand, was created with fully operational capabilities, including distance encoder integration, and validated in the field. The detail description and validation of above-mentioned topologies are presented below.

VNA accounts for the majority of system costs because to the trade-off between acquisition speed and cost. The suggested design features single VNA, which significantly reduces the system costs when compared with a multi-VNA system. The system's speed, however, is restricted by the VNA's sweeping speed capacity and array size. Nonetheless, the setup makes it easier to create the parallel profiles necessary for 3D mapping. The mux's function is to transition between antenna channels that share the same VNA resource. As a result, the switching speed of the mux is also an important element in determining total system speed. By increasing the number of VNAs and parallel arrays on a modular basis, we may enhance the system speed. In contrast, it increases the computing resources.

VNA Selection and SFR performance

In this development, the Vector Network Analyzer (VNA) is the central component of the SFR. There are several commercial VNA models on the market. A set of major VNA products was compared in terms of cost, sweep speed, dynamic range, bandwidth, number of ports, computer-based control capabilities, scalability, and so on. The dynamic range of the VNA determines its sensitivity; it specifies the highest difference between the transmitter and receiver signals that the VNA can measure. As a result, a greater dynamic range may result in greater deep penetration capacity in the target medium. The speed of an SFR system is thus mostly determined by the sweeping speed of the VNA.

As a result, in high-speed large-scale utility survey applications, the data acquisition speed of the SFR is a critical element in VNA selection. In most road applications, a towed SFR system is mounted to a vehicle. The measurement should be made while travelling at a reasonable pace alongside other vehicles on the road, so as not to disrupt the flow. Then, the system speed should be measured in tens of kilometres per hour, with the greatest speed always being the goal. Despite the fact that the sweeping speed of the VNA is not the only parameter that determines the SFR system speed, other factors such as the number of sweep frequencies

and the spatial resolution of the measurement (horizontal distance between two A-scan points, refer to Figure B.4) also contribute. The following Equation 4.5 describes the maximum vehicle speed estimation of a multi VNA multi-antenna array monostatic SFR system constructed from a VNA model.

$$V = \frac{3.6 \cdot A_s \cdot p_x \cdot m}{k} \tag{4.5}$$

$$T_s = \frac{1}{A_s} \tag{4.6}$$

$$T_s \propto (n \cdot T_i) \tag{4.7}$$

Whereas,
A_s : Number of A-scans per second.
p_x : Distance between two adjacent A-scan positions.
V : Speed of the vehicle (SFR) (km/h).
T_s : Time for a complete single sweep of n frequency points.
m : Number of parallel VNAs in the SFR.
T_i : Time delay for a single discrete SFR pulse.
n : Number of sweep frequency points.
k: number of antennas in the array which shares same VNA.

In this respect, smaller T_i and smaller n improve SFR acquisition speed, whereas system speed is directly proportional to the horizontal distance d_x between two consecutive A-scans, according to Equations (4.5), (4.6) and (4.7). Therefore, in order to improve speed, the horizontal step size between A-scans (d_x) must be lowered, or the number of frequency points (n) must be reduced, or we may require a high speed VNA (T_i). Hence, multi-antenna array SFR system's speed is highly depended on d_x, m, k, n, T_i. However, T_i (time delay for a single discrete pulse) is the VNA specific parameter for a given "IF Bandwidth". Thus, it's limited by the hardware. The maximum IFBW resolution varies depending on the VNA model, and the T_i slightly varies according to IFBW. Furthermore, reducing the IF receiver bandwidth reduces the effect of random noise on a measurement, it increases the signal-to-noise (SNR).

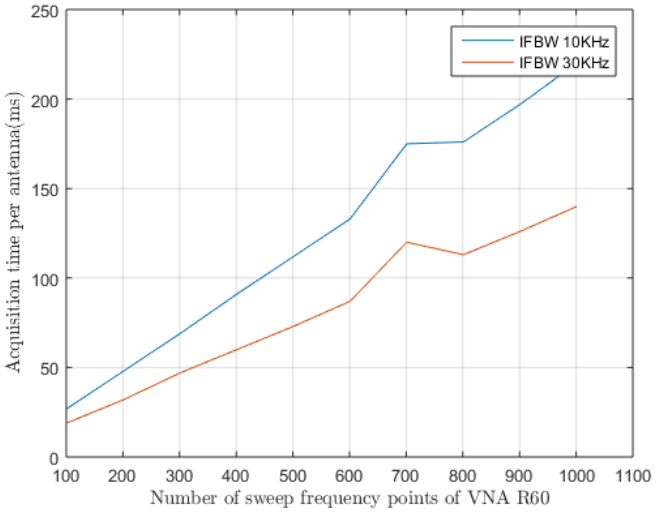

Figure 4.25: R-60 VNA sweep speed empirical analysis.

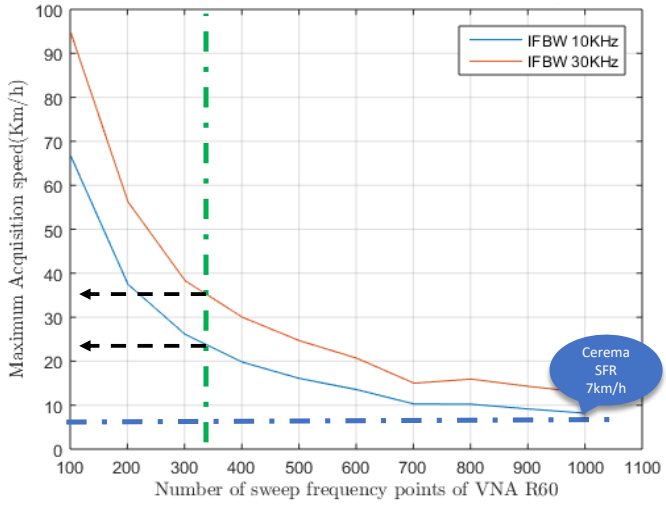

Figure 4.26: R-60 SFR acquisition speed V variation with number of sweep frequencies. Configuration : 450 MHz - 4500 MHz, $p_x = 0.5$ m, $m = 1$, k= 1.

The Figure 4.25 shows how an R-60 copper mountain VNA's T_s value empirically varies across different sweep points (n), and in two different IFBW values. Hence, the single VNA ($m = 1$, and single antenna ($k = 1$) based monostatic SFR system's analytical velocity is then calculated using Equation (4.5), which is plotted in the Figure 4.26. Based on the figure, system velocity v degrading with increasing sweep points. For example, at (p_x) = 0.5 m, and at sweep points $n = 351$, the velocity V is 36 Km/h with 30 KHz IFBW, while the velocity (V) is 24 Km/h at 10 KHz IFBW. However, the minimum p_x required for a better hyperbola visualisation is somewhere $<$ 10 cm. Then, the achievable V using R-60 is, 6 Km/h at IFBW of 30 KHz. This is slower and can be ideal for walking trolley.

As a consequence, system design factors such as speed, horizontal resolution (d_x), cost, integration complexity, computer resources, physical array size, and signal processing approaches are established. After careful analysis of cost, physical size, sweeping speed, and dynamic range, a VNA model of suitable performance has been chosen for the initial prototype development with a cost-performance trade-off. As a result, the concept can be validated. In addition, the antenna selection, which is another critical component of the SFR, is explored more below.

Antenna Selection

In terms of antenna selection requirements, GPR applications for utility scan generally operate at frequencies ranging from 200 MHz to 3 GHz or higher [39, 91]. Antenna properties including as gain, directivity, physical size, and bandwidth are the key parameters to pick antennas for utility application since they are closely connected with SFR performance. Meanwhile, the antenna array width of a multi-antenna array SFR system is restricted by vehicle width or traffic laws. So, antenna size and lower bound (effect on penetration depth) become a trade-off when choosing an antenna. In addition, the radiation pattern, direct coupling noise, and ideal offset between two antennas all influence array size and width. Furthermore, the -10dB bandwidth of the appropriate antenna must fit within the system operating frequency range. Meanwhile, the underground utility network mapping application necessitates a greater penetration depth of up to 3 m. Because of the substantial power dispersion at higher frequencies, utility GPR applications require a considerably lower bound frequency to provide greater penetration performance while keeping the antenna size to a bare minimum. This is due to the fact that the size of the antenna rises with the wavelength of the 'lower bound frequency [113–116], according to (f =c/λ).

Therefore, for the implementation of UWB GPR systems, the performance of various antenna designs, such as bow-tie antenna, spiral antenna, loaded dipole antenna, TEM horn antenna, tapered slot antenna and Vivaldi antenna have been already evaluated by various researchers [115–120]. A variety of ultra-wideband antennas have been widely employed in the industry for GPR applications. 3D radar employs a bowtie antenna for their SFR solution [39], whereas GSSI GPRs employ bowtie and horn antennas [91] in the majority of their product lines. Based on prior research and case studies, it has been determined that bow-tie, Vivaldi, and horn antennas are the best-fit for UWB SFR applications, due to their ultra-wideband properties and directional radiation pattern.

For various GPR applications, each of these three antenna types offers a distinct advantage over the others. The unidirectional antennas listed above, such as the bowtie, Vivaldi, and horn, have stronger directivity and gain. The degree of direct coupling noise varies according to antenna orientation, offset, and airfield proximity. However, signal processing filters can certainly eliminate direct coupling noise to extend. Nevertheless, the problem persists and requires more comparative parametric research. To summarize some of the above antenna type's characteristics,

Bowtie Antenna: A bow-tie UWB antenna is widely used in GPR applications for its ability to reduce ground susceptibility GPR measurements [114]. Figure 4.27 shows an example of a simple bow-tie antenna. Moreover, size reduction of a bowtie antenna is feasible by inserting high permittivity substrate [114]. Furthermore, planer bowties can be installed with ground coupling, which promotes complete energy transfer to the ground while minimizing direct coupling between array antennas and ringing noise between antenna and ground.

Vivaldi Antenna: Example of a Vivaldi antenna, as seen in the Figure 4.28, is used and validated in SFR applications. Hence, its ideal for air coupled configuration according to its

shape, radiation and polarisation. [107,121,122]. However, sufficient clearance between adjacent antenna is required to avoid direct antenna coupling between the array.

Horn Antenna: A horn antenna is one of the greatest alternatives for a GPR system, since it is less subject to ground effects and allows greater transmission of radiated energy into the ground [114]. Figure 4.29 shows a typical horn antenna. However, using size reduction techniques, the horn antenna's features are an ideal match for utility applications.

The horn antenna has wider bandwidth characteristics, and it is attractive to GPR applications. From the works of [115, 116], it's realised that, like bowtie and Vivaldi, the aperture size of the antenna depends on the lower operating frequency. Since the aperture is larger in both dimensions, it can occupy more space in length and width of the array.

Conclusion: Based on the logic presented above, all three antennas are rated appropriate for utility survey applications, with unique advantages and disadvantages. Perhaps more study into performance comparisons will be conducted in the future. However, because of the thesis's time restrictions, the specific design of the antenna and fabrication are the challenges. As a consequence, we used a UWB Vivaldi antenna throughout the first prototype development. Hence, the prototype development and validations are discussed in the following sections.

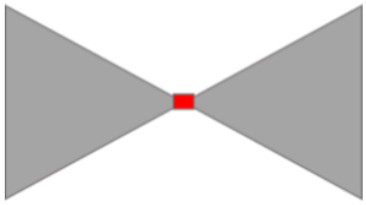

Figure 4.27: A simple bowtie antenna.

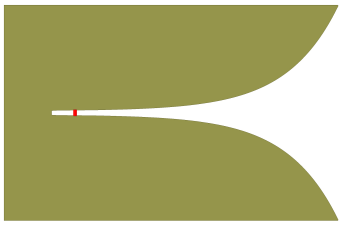

Figure 4.28: A simple Vivaldi antenna.

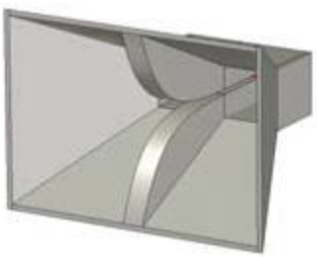

Figure 4.29: A simple horn antenna.

4.3.2 Single VNA + three antenna monostatic UWB SFR with multiplexer

The SFR development was taken place in different phases throughout the last 3 years, and according to available resources. The first generation of the prototype is equipped with single low cost and compact VNA, time division multiplexer and three ultra-wide band Vivaldi antennas. VNA is fully controlled by a computer through python platform, as seen in the Figure 4.30, in accordance with the architecture shown in the Figure 4.24.a.

According to the specification sheet, the selected antenna has an effective operating frequency range of 432 MHz to 6 GHz. The highest bound, on the other hand, is measured to be 8 GHz (-10 dB bandwidth limit). Furthermore, the antenna is dual polarized. As a result, it can work in both H-H and V-V orientations. The SFR is integrated in Figure 4.30 in order to evaluate the acquisition chain with multiplexer and propose the topology in Figure 4.24.a. In this regard, the integrated SFR shown in Figure 4.31, and a real-time acquisition technique based on Python were built. Figure 4.31 shows that,

- PC: It controls VNA and multiplexer, and provides power through USB. Further, the sweep control, S_{11} data retrieval, signal processing and visualisation all performed by PC. Meanwhile, the multiplexer clock and trigger are also controlled by the PC.
- R-60 VNA: It makes S_{11} measurement according to the sweep configuration pushed PC.
- Microcontroller: Controls multiplexer's port switching between antenna.
- Multiplexer: time division multiplexing facilitates connection to a single antenna at a time by switching mechanism.
- Antenna: UWB Vivaldi antenna with 432 MHz - 6 GHz (-10dB) bandwidth, dual polarised.

In this respect, a small experimental setup is conducted as shown in the Figure 4.32 for the validation of the concept. The experiment validates the operational functionality of the multi-antenna array data acquisition with the inclusion of multiplexer. The prospective system to form 3 parallel B-scans, resulting 3D data matrix that visualise B-scan (XY), Cross view (YZ) and C-scan (XZ) respectively. The prototype was initially tested on a single metallic pipe 15 cm below the antenna edge, on a smooth floor, as shown in Figure 4.30. However, the A-scan steps were performed at constant time step instead of distance encoder at this stage of development. The pipe was relatively moved across the array at constant speed to observe a hyperbola in the B-scan. The signal processing follows the step discussed in the subsection 4.2 and Figure B.8. In this scenario, the object of the experiment is to,

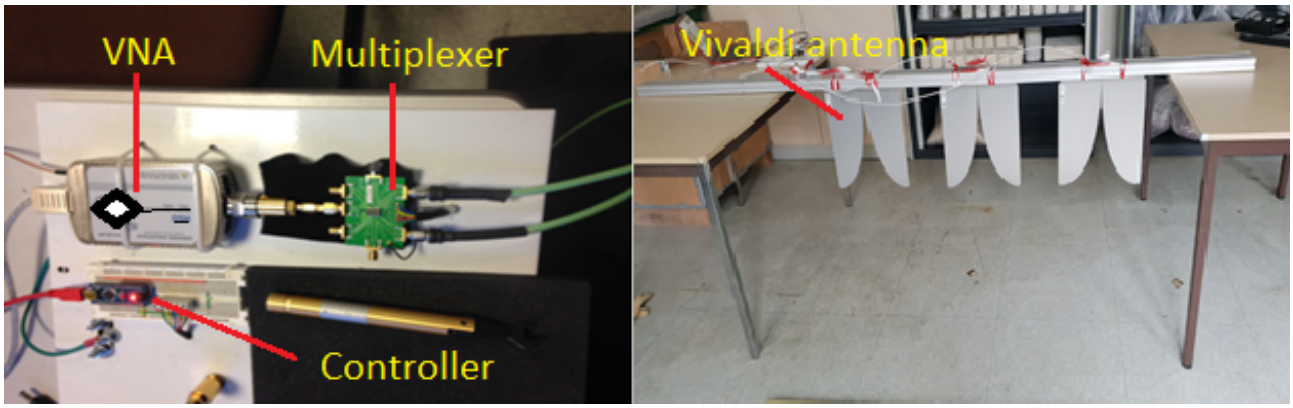

Figure 4.30: 03 Antenna Array SFR Prototype.

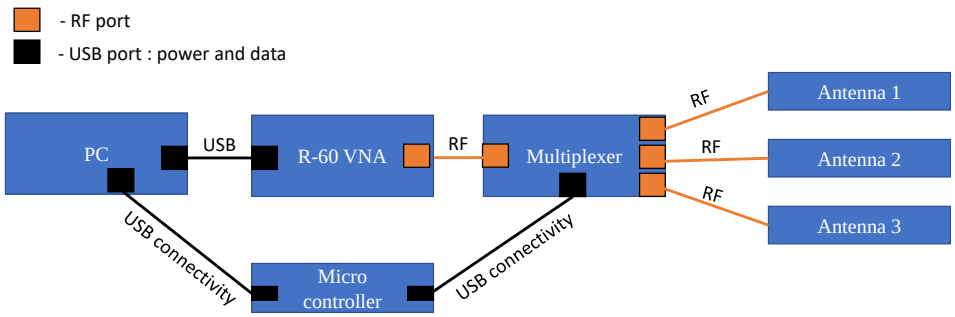

Figure 4.31: 03 Antenna array monostatic single VNA SFR Prototype connectivity schematic.

- Validate the real time acquisition using the topology proposed in Figure 4.24.a.
- Validate the real time acquisition chain using multiplexer and visualise B-scans (S_{11} to B-scan conversion in real time.)
- Form 3D matrix from antenna array as proposed in Figure 4.32.

In terms of sweep configuration, it was defined at 500 MHz - 4GHz, IFBW : 10KHz, frequency points: 801.

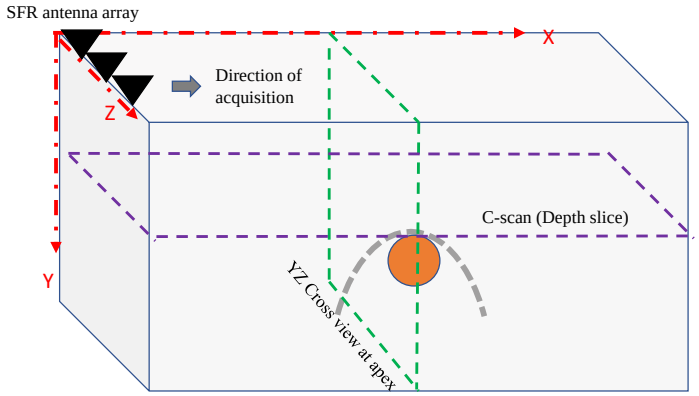

Figure 4.32: 3D matrix formed by B-scan (XY), Cross view (YZ), C-scan (XZ) from multi-antenna array SFR.

Results and discussion: As illustrated in the Figure 4.33, three identical B-scans, a cross view scan at each horizontal position, and a C-scan at each IFFT point were produced from the fused 3D data matrix, as shown in the Figure 4.32. The provided B-scan in the Figure 4.33 validates the pipe's hyperbola also signature, while the C-scan at the apex of the hyperbola displays horizontal black shades, confirming the pipe's orientation. then, the Cross view shows a horizontal shading corresponds to the reflection at top of the pipe

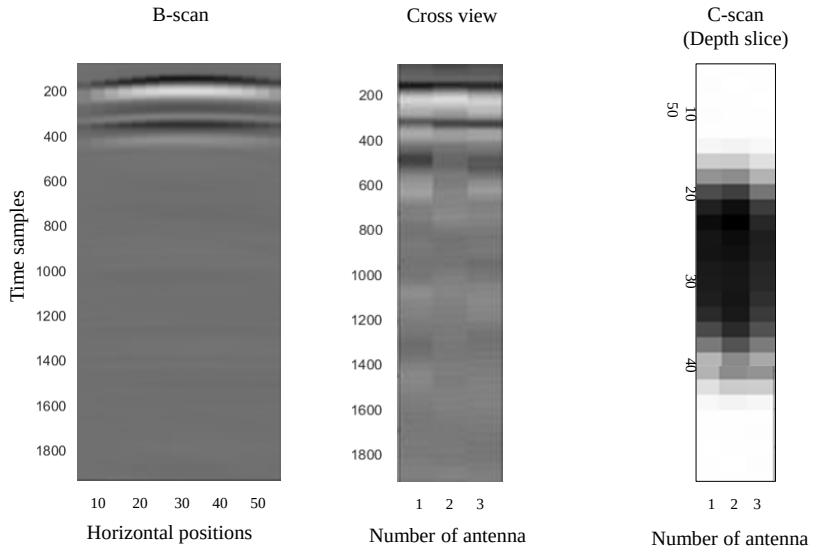

Figure 4.33: Results of B-scan (XY), Cross view (YZ) at apex, C-scan (XZ) at apex from multi-antenna array SFR prototype experiment.

Hence, the reported results confirm the complete acquisition channel from $S11$ through B-scan visualisation, multiplexer operation, communication between the control software and the VNA, and functioning of all topology components. Furthermore, the concept demonstrates that an array-based multi-antenna array step frequency radar could generate a 3D matrix suitable for 3D mapping and localisation of buried pipes. However, for a fully working SFR with this topology, the number of antennas in the array must be increased, with the help of ultra high-speed VNA or comparable RF circuits.

However, due to the existing VNA's sweeping speed constraint, even at walking speed utilizing R-60, it is difficult to adapt this architecture for an array system. Because a reasonable quality of hyperbola demands a minimum horizontal step size resolution of 5 cm in a utility application to observe sufficient number of hyperbola points. Meanwhile, according to the empirical investigation shown in Figures 4.26 and 4.25, the maximum acquisition speed of the R-60 VNA is 3.5 Km/h per VNA at 5 cm step size configuration. As a result, at 5 cm step size and 301 sweep points, the present VNA (R-60) can only handle one channel per VNA. That limits mobile array prototyping with this topology at this stage.

Conclusively, the prototype verifies the suggested SFR structure, which employs a single VNA and many antennas via a multiplexer. As a consequence, the results indicate that the array system may be used to build a 3D matrix of the subsurface. However, due to the present VNA's constraints, the parallel VNA architecture described below is being built at this time for further development and operational validation (to have a mobile array SFR system). The parallel VNA topology may therefore be verified. The second topology (two VNA parallel channels + 02 UWB Antenna Array Monostatic SFR) is implemented and validated as follows.

4.3.3 Two VNA parallel channels + two UWB antenna array monostatic SFR

Due to the limitations in the topology described in the previous section, a second SFR topology with parallel channels was proposed. As shown in Figure 4.34, in this configuration, two VNAs (namely R-60-VNA-1 and R-60-VNA-2) are connected in parallel with the PC that control

their respective independent antennas (namely Antenna-1 and Antenna-2). Additionally, as in case of the previous topology, both the antennas operate in monostatic configuration. Each component from Figure 4.34 as described as follows:

- PC: It controls VNA and the distance encoder, and provides power through USB. Further, the sweep control, S_{11} data retrieval, signal processing and visualisation all performed by PC. Meanwhile, the encoder clock and trigger are also handled by the PC.
- R-60 VNA: Measures S_{11} according to the sweep configuration pushed by the PC.
- Antenna: UWB Vivaldi antenna with 432 MHz - 6 GHz (-10dB) bandwidth, dual polarised.
- Distance encoder: Used to accurately space the acquisition distance between subsequent A-scans.

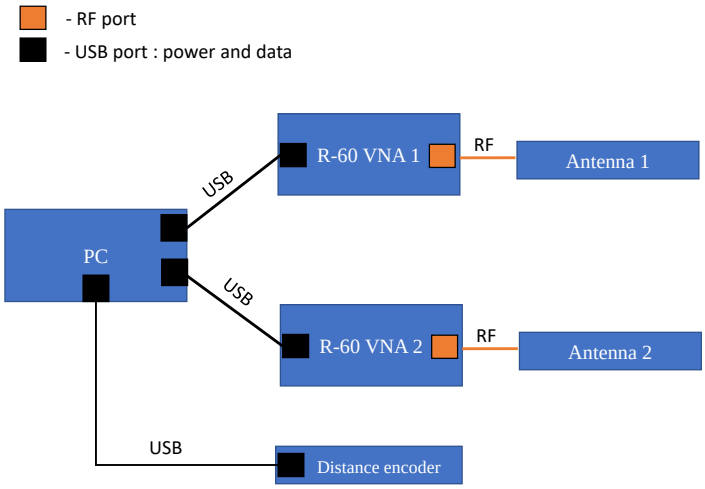

Figure 4.34: 02 Antenna array monostatic two parallel VNA SFR Prototype with distance encoder connectivity schematic.

As mentioned in [123], the distance encoder sends a specific number of pulses per revolution of the wheel to which it is attached. The PC transforms these pulses such that the antenna is triggered at equal distance intervals. Therefore, all GPR scans are indexed by wheel encoder pulses and the data are synchronized with the distance.

An array of two-parallel antenna experimental setup was then created using this topology. This prototype was mounted on a three-wheeled cart that can be used to acquire data at walking speed with integration of distance encoder as shown in Figure 4.35. Finally, as mentioned below, the prototype's proof of concept was validated in the field.

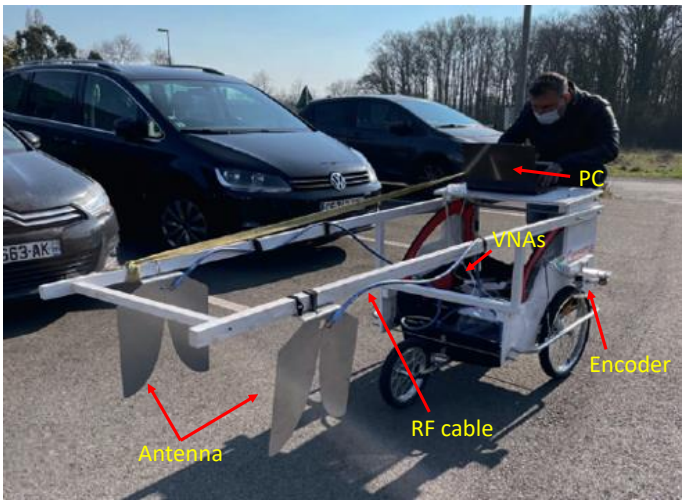

Figure 4.35: Two parallel Vivaldi antenna array SFR with distance encoder.

Experimental site

To validate the SFR setup for the second topology, an experimental Geosite was selected from the Nantes campus of Université Gustave Eiffel. The Geosite for data acquisition is as shown in Figure 4.36.

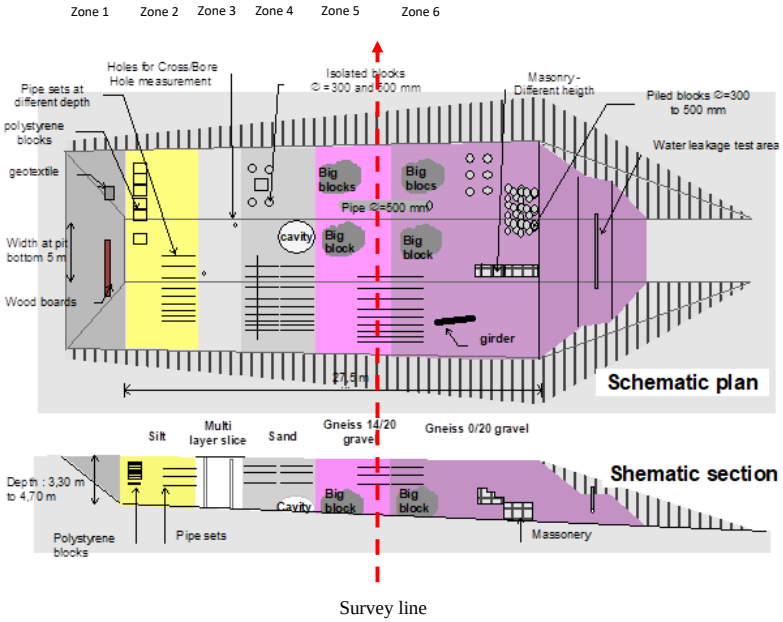

Figure 4.36: Geosite in UGE.

The Geosite is divided into 6 zones (marked in various colours, see Figure 4.36) with each

zone having different subsurface material characteristics (such as permittivity, *etc.*). Each zone had multiple pipes of different radii and materials buried at various depths.

In zone 5, there are 10 pipes of which one is a concrete pipe and the remaining nine are made of various materials (metal, PVC and PVC with water *etc.*). Each pipe is at a different depth, ranging between 1 m to 2 m. Since this zone has lower subsurface permittivity ($\varepsilon_r = 4$ - 5), it allows for higher penetration depth. Therefore, it was used for data acquisition to validate the results. The red line in Figure 4.36 shows the data acquisition trajectory for the B-scan which is presented in the results below. The SFR parameter configuration is as described in Table 4.5.

Parameter	**Value**
Horizontal step size	5 cm
GPR type	Two parallel channels step frequency radar with VNA (R60 - Copper mountain)
Antenna	Vivaldi (02) - Air coupled
Sweep frequency	$435 - 4435$ MHz
Number of frequency points	301
Open Air T_0 performed	Yes

Table 4.5: SFR and test site configuration parameters.

Results and discussion: With the help of real-time acquisition chain, as shown in Figure 4.37, a quick preprocessed B-scan is available for the operator to visualise in real time. The S_{11} parameters are measured and sent to the PC. An inverse FFT is then performed to obtain the raw time-domain signal of the instance (*i.e*, the A-scan). As multiple raw A-scans are stacked, the preprocessing steps of time windowing, T_0 removal and exponential gain are applied. This final preprocessed B-scan image is then visualised by the operator on his screen.

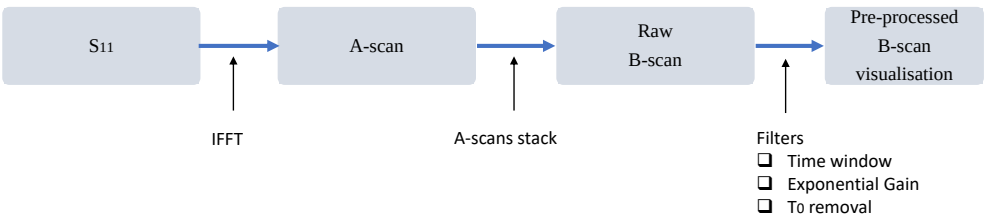

Figure 4.37: Realtime acquisition chain.

In Figure 4.38, we show an example of how a raw A-scan is prepared. Figure 4.38(a) shows the raw unprocessed A-scan, Figure 4.38(b) shows the A-scan after T_0 removal and Figure 4.38(c) is the final preprocessed A-scan after the exponential gain is applied.

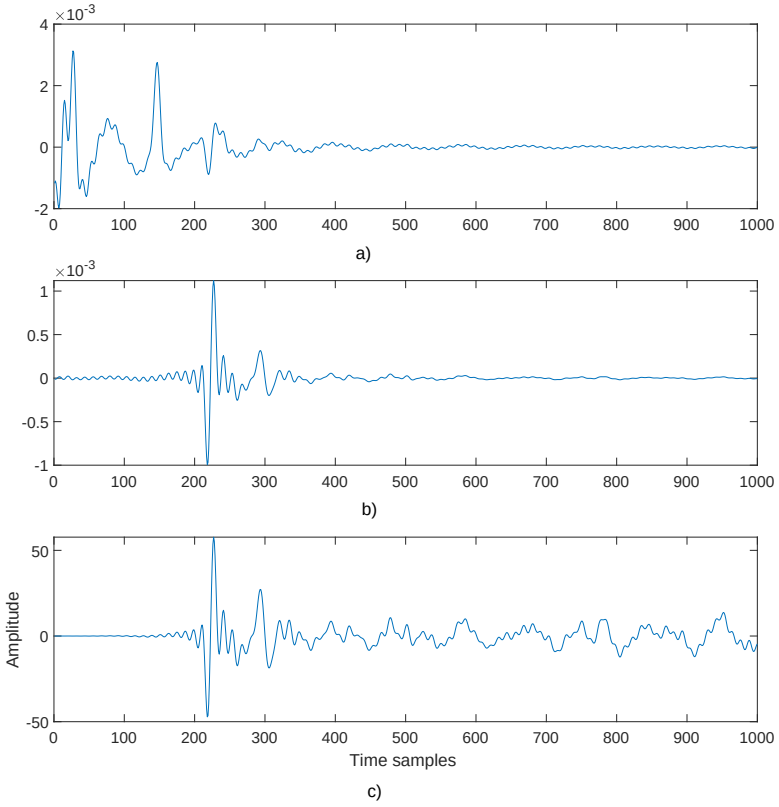

Figure 4.38: A-scan comparison of SFR.

From the Geosite zone-5, two parallel B-scans were obtained using the proposed topology. Figure 4.39 shows these preprocessed parallel GPR B-scan profiles acquired using the two parallel channels. Therefore, we infer that the second proposed topology with two VNA-channels are capable of efficient data acquisition, which can be further scaled up for multi-antenna arrays to construct 3D volume data.

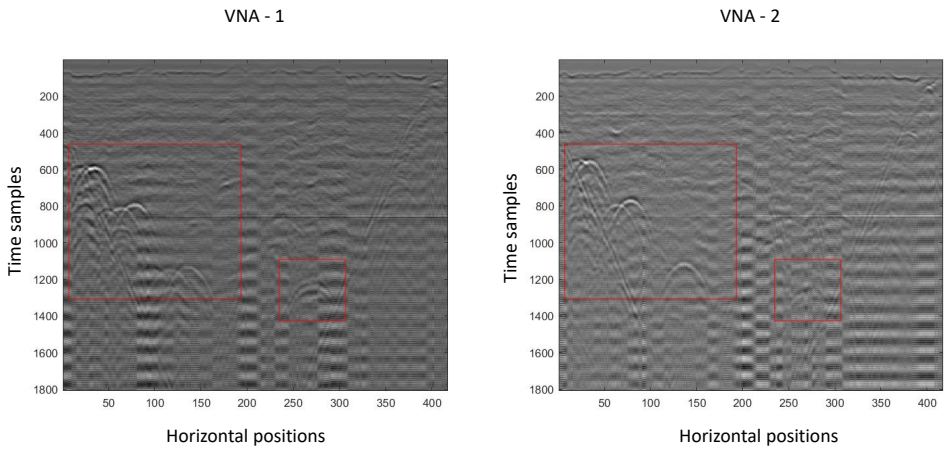

Figure 4.39: Two parallel channel B-scans of SFR survey in Geosite.

In Figure 4.40, we show one of the two parallel profiles from zone 5. After the real-time preprocessing steps from the acquisition chain, it can be observed that, 8 out of 9 pipes and the concrete pipe were visible. Thus, with reference to the ground truth of 10 pipes, 9 pipes were visualised here. We may also deduce that the prototype can penetrate up to 2 meters with this design and subsurface material. Furthermore, the survey span of 22.5 m includes 451 A-scans (22.5 m = 450 · 5 cm). As a result, the distance encoder integration functions are confirmed as predicted intervals with no substantial error. It's also clear from the B-scan, which shows a consistent shape the hyperbola. It is, however, acknowledged by the process of encoder calibration at the start of the survey. On average, the encoder's distance inaccuracy at a distance of 10 m is +-3 mm/m on average.

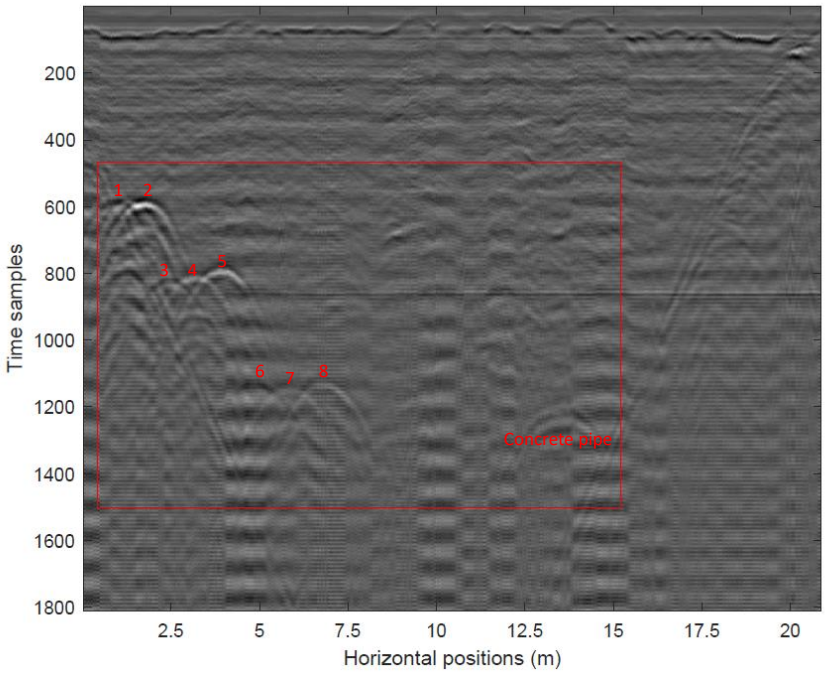

Figure 4.40: SFR Prototype B-scan of geosite.

However, with the increase in depth by adding exponential gain, the ringing effects are also amplified (see Figure 4.38(c) and Figure 4.41). One possible solution to suppress the low frequency ringing effect is the use of high-pass filter. Figure 4.41 shows the B-scan after the implementation of high-pass filter on Figure 4.40.

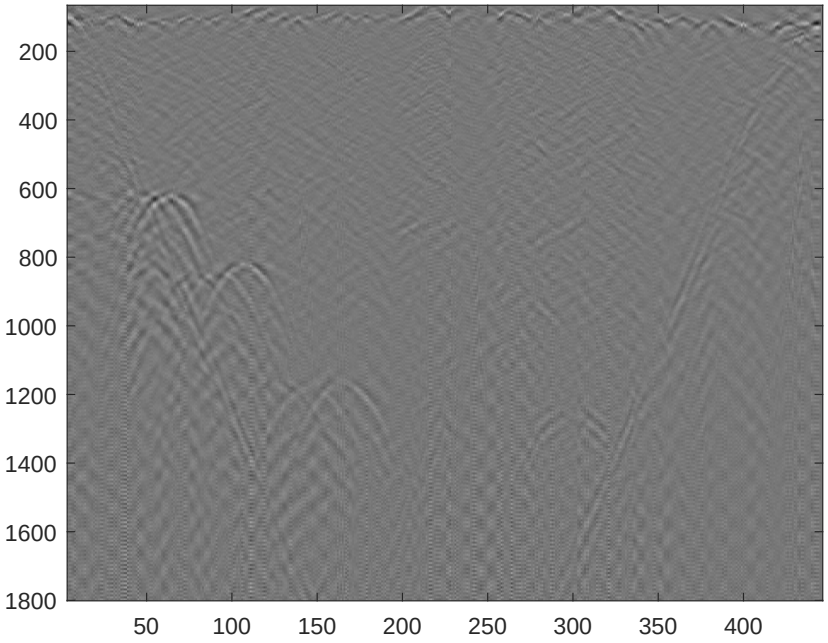

Figure 4.41: B-scan after high-pass filter.

By comparing Figures 4.40 and 4.41, it can be observed that although high-pass filtering reduces the ringing effect, there is an observable loss in hyperbola information. Therefore, it is necessary to find a trade-off between the loss of information and the suppression of ringing effects, without which, the parametric study would be incomplete. The problem could be overcome by implementing the GPR in ground-coupled configuration. The ground-coupled configuration can be useful to provide even higher penetration depth, avoid coupling effects and, possibly, eliminate the ringing effects without the use of high-pass filtering. In addition, the study was conducted only on zone 5 where the subsurface permittivity was low and lossless. Using ground-coupled antenna, it would be possible to observe hyperbola information from other zones as well, where the permittivity and dispersion is higher. However, this subject is open to parametric study of ground-coupled SFR as a perspective. Then, the array size can be scaled up upon validation of penetration performance.

In summary, a parallel VNA-based two antenna SFR array system produced two real-time B-scan profiles of underground pipelines with sufficient penetration depth and hyperbola signatures. As a result, it confirms a possible approach for forming a volume matrix for 3D mapping of utility networks. However, in order to provide a comprehensive solution in the future, the array size must be increased. Furthermore, the distance encoder helps in acquisition by providing a uniform step size. Overall, the experiment confirms the suggested parallel channel design, acquisition chain, software, and signal processes. As a consequence, with the use of a customized ground coupled antenna, a high power VNA, and a scaled up array, performance may be increased, and further study can be conducted. Walking speed is currently limited by the capacity of VNA. A high speed VNA or equivalent RF system can be used to make the high speed vehicle mounted system possible. Furthermore, parallel design improves acquisition speed while increasing material and processing costs, whereas multiplex architecture is less expensive

but slower. The next part provides a high-level description of the GUI program designed for real-time capture.

SFR Control Software and protocol

The above-mentioned prototypes are based on computer-controlled software that interfaces with a VNA and conducts real time data acquisition, signal processing, and B-scan visualisation. The Vector Network Analyzer (VNA) used in prototyping is enabled to be controlled by the Python platform through a personal Computer in this context. As a result, the VNA's control, as well as all real-time and post-processing stages, are best accomplished using an open source programming language such as Python. It's appealing since the project aims for a low-cost solution, and it has free development and license costs, as well as excellent libraries for high-speed scientific plots and multiprocessing capabilities. As a result, for the prototypes shown above, we've been developing an automated data collecting platform with a graphical user interface (GUI). Python's multiprocess techniques are utilised to reduce delays and optimize the VNA's data acquisition speed during the real-time acquisition and visualisation stage. For two reasons, multiprocessing is a critical software architecture for parallel channel processing. First, in real-time visualisation, the period between S_{11} acquisition and B-scan must be as short as possible. Second, because the prototype works with parallel channels, the system must process both channels independently and concurrently. Therefore, the multiprocess architecture is followed for every process.

We have developed a GUI based real-time data acquisition platform for single antenna and multi-antenna array configurations as seen in the Appendix A. The GUI features VNA sweep configuration, encoder calibration, metallic plat / T_0 measurement, plot configurations, A-scan and B-scan visualisations and acquisition control. The software development phases adhere to a real-time single antenna system and a real-time multi-antenna system. In the multi-antenna array configuration, a single B-scan can be visualised for a selective antenna or two B-scans can be visible. As demonstrated in, we created a GUI-based real-time data collecting platform for single antenna and multi-antenna array setups. VNA sweep setup, encoder calibration, metallic plat / T_0 measurement, plot configurations, A-scan and B-scan visualisations, and acquisition control are all available through the GUI. The software development phases conform to a real-time single antenna system, and a real-time multi-antenna system. In the multi-antenna array design, a single B-scan for a specific antenna or two B-scans can be seen. Appendix A describes the essential aspects of the developed control software in the sequence of a survey protocol.

In summary, the aforementioned GUI is designed for real-time control, acquisition, and visualisation of prototype B-scans. The software was written in Python and includes libraries given by VNA vendors for communicating with VNAs from a PC. The designed software architecture is partially dependent on the type of VNA and its operating principle. As a result, the software design must be updated to accommodate varied topologies, VNA types, encoders, and multiplexers. However, at this point, the software provides enough functionality for a functioning two antenna array SFR. Furthermore, additional signal processing characteristics might be introduced based on comprehensive parametric investigations. In the future, there will also be the development of post-processing software that can handle large scale collection data using physical and machine learning approaches, and eventually produce a 3D geometric mapping of subsurface utility pipelines.

4.3.4 Conclusion

GPR was discovered as a viable Non-destructive sensor for the identification and localisation of buried pipes in an underground utility 3D mapping application. SFR is a type of ground penetrating radar that operates in the frequency domain rather than the time domain, like impulse

GPR does. A simple monostatic / bistatic SFR's design can include Vector Network Analyzers (VNA) or an equivalent RF circuit, as well as antennas. The VNA measures the complex reflection coefficient (S_{11} parameters) between the VNA and the coupled target medium through the connected single antenna in monostatic mode, and (S_{12}) in bistatic mode at each frequency point. We created monostatic setups in this thesis. The monostatic design was chosen to reduce the amount of hardware resources and costs (VNA and antenna). However, a bistatic setup can also reduce direct coupling and ringing effects. As a result, the bistatic setup can be tested in the future.

A multi-antenna array SFR system with a large array size, high speed, deep penetration, wide bandwidth, and greater spatial resolution is desirable. Nonetheless, the capacity of such a system varies due to VNA characteristics, antenna type, and features. We presented two distinct SFR designs for future multi-antenna array configurations based on a literature research and commercial product analysis. Both approaches have advantages and downsides. The first design, on the other hand, proposes a single VNA-based SFR with a multi-antenna array employing a time division multiplexer switch. As a result, in time sequence, a single VNA resource can be shared. The method, however, restricts overall SFR speed performance to the sweep speed of a single VNA. The second architecture, on the other hand, offered a full parallel channels multi array employing multiple VNAs (one VNA per antenna element) to boost the SFR speed. The specified topology, on the other hand, raises the cost by increasing the number of VNAs, as well as the processing resources. Regardless, both approaches can generate multiple B-scan slices required for 3D matrix generation, which is required for 3D mapping of utility networks. The primary performance indication in hardware selection is the VNA's sweep speed and bandwidth, which determines the topology and SFR speed.

Meanwhile, for the specific application, an ultra-wide band directional antenna is required. As a result, the Vivaldi, horn, and bowtie antenna types were recognized as suitable types for utility applications, each with its own set of advantages and limitations. To avoid costly VNAs and a time-consuming antenna design procedure at this level, the materials for prototyping were chosen based on market availability. Because the prototype's aim is to validate the proof of concept in terms of the acquisition chain and topology. In this context, the first prototype (VNA + multiplexer switch) was experimentally tested in a static location to check the function of operating principles, acquisition chain, multiplexer, and 3D matrix generation. The findings support the experiment's objectives by observing B-scan, C-scan and cross view radagram as expected. Meanwhile, a second prototype with a completely working aspect was created employing two VNA, two antennas, and a distance encoder. As a result, the prototype was placed on a three-wheel cart. The geosite was then successfully evaluated in the field at the UGE Nantes campus. In contrast, two parallel B-scan profiles with hyperbolas were acquired to evaluate the idea, architecture, hardware and software function as a system, as well as the signal processing procedures used. The results support the objectives using two B-scans with various hyperbola representing the survey site's ground truth. The measurements in the high permittivty zones, on the other hand, did not yield adequate results due to strong coupling noise and poor pentration performance due to the emitting power constrain of the VNA. In this situation, a ground coupled bowtie antenna and a high power VNA are proposed for future development.

Furthermore, the Python API, control, and acquisition software is operational for a two antenna array SFR at this time. However, it still has to be improved in terms of scaling up to bigger array sizes and post-processing capabilities. Since, the large array requires several parallel processing services, computer hardware needs upgrade with multiprocessing capacity to minimise delay between acquisition and visualisation. In terms of acquisition speed, we reach up to 3 km/h using a single antenna in monostatic mode with a VNA sweep configuration of 0.5 - 4.5 GHz, 301 points, 10 KHz IFBW, and 5 cm spatial resolution at the x-axis. With

a high-speed VNA, the speed may be boosted in the future. However, installing a ground coupled bowtie antenna with a high power high speed VNA is a critical next step to confirm the penetration depth and signal quality under higher permittivity subsurface conditions. Future research will focus on the best operating frequency configurations, antenna configuration, antenna offset, feasible maximum array size, different SFR architectures, and their complex performance matrices, which will be heavily influenced by signal processing techniques and antenna characteristics. The next prototype version will have two parallel VNAs with ground coupled antennas.

Throughout the investigation, the suggested two architectures were theoretically validated. Hence, establishing the promise to continue in this direction.

4.4 Conclusion

The content of the Chapter discusses experimental validation of the models and SFR prototype studied in this thesis. The first section of the chapter comprises the experimental validation of automated pipe detection models based on Faster R-CNN and YOLOv4. Second, open-air experimental validation of SVR and ANN-based depth and radius estimation models is covered in the chapter. Finally, the chapter is followed by the development and field validation of a multi-antenna array step frequency radar prototype.

The first section presented experimental validation of deep learning-based automatic pipe detection models based on GPR data, with an emphasis on large-scale data processing for utility mapping. In this experimental validation, two Faster R-CNN models and two YOLOv4 models with different Annotation methodologies have been studied. In the experimental study, the main goal, was to see if the suggested model can detect several hyperbolas in a single B-scan with acceptable accuracy, using field data. Hence, all the models confirms its ability to detect multiple hyperbola in a single B-scan. In addition, the performance of the models in terms of Precision and Recall were measured to ensure whether the model can provide acceptable accuracy to deploy as an operational solution. The performance matrices of four studied models used for this experimental validation are summarized in Table 4.2. Whereas, the "Faster R-CNN + ResNet-50 + Annotation-1" model has the highest Recall, according to the specifc data (92.7%). Such that, it has missed the true targets (pipes) fewer times when compared with other models. However, the Precision is pretty reasonable at 88.0%, and Precision can potentially be increased by an extra filter (NMS layer) because the majority of false positives are seen in strongly overlapping bounding boxes over real positives. Meanwhile, the "YOLOv4+ Annotation-2" model has demonstrated the greatest Precision (97.6%). However, the Recall values of YOLOv4 are quite low (81.45% and 76.15%). As a result, the YOLOv4 has the higher probability of missing the targets. In fact, 'Recall' is more important than accuracy in this utility application. Because while the detection may tolerate some false positives, false negatives (miss detection) might increase the risk of strikes during the excavation works. As a result, for large-scale GPR post-processing applications, Faster R-CNN-based automatic pipe detection models are recommended based on the outcome of this study. Meanwhile, though the YOLOv4's performance is somewhat poor, its detection speed is extremely fast and may be used for real-time detection during the survey. However, in terms of big scale mapping, real-time detection is an optional capability.

The second section experimentally validates the proposed SVM, SVR and ANN based parameter estimation models and analyses the results obtained from such supervised machine learning approaches for estimating the depth (d), radius (r) of the pipe. Hence, with the use of unique feature selection proposed in the Chapter 3. In this regard, due to limited resources, we do not have a controlled location with a sufficient number of pipes of varying depths and

diameters to create a supervised machine learning model at this stage. The SVR or ANN, on the other hand, requires hundreds of hyperbolas with ground truth (without overlaps). As a result, the experimental validation is limited to an open air design with a few pipes. In this case, the velocity of the air is constant. Thus, it was not considered for estimation. Furthermore, it is found that, from the open air experimental results, the depth (d) accuracy may be achieved up to 0.5% of mean relative error using both ANN and SVR, which meets Class-A precision. Whereas, the radius (r) can be estimated with the mean absolute relative error of 10% using ANN and 18% using SVR. Thus, ANN is relatively better than SVR for the radius estimation.

When the radius (r) and depth (d) are well standardized and defined in the classes, the applicability of SVM multi classification is possible. Thus, multi class SVM was applied and observed that, the model can achieve up to 88% of correct predictions in open-air settings when classified into 5 classes. Meanwhile, the accuracy can increase up to 96% when the number of classes reduced to 3. However, the depth (d) estimation shows its robustness in noiseless, noisy, random continuous values, metal and PVC pipes configurations (all cases). Then in the open-air settings. These findings promise further acceptability of the methods on 3D localisation of utility network upon validation on more complex experimental data. Nevertheless, the radius (r) estimation performance constitutes 18% of error, and it's not yet regulated by law like depth (d). But it affects the accuracy of the no dig zone boundary. Therefore, ANN based radius estimation model can be used for no-dig zone boundary estimation. Nevertheless, when the radius is standardized into definitive radius classes, multi class SVM also can be deployed for this scope. In the future, more complex controlled experimental study is required in various subsurface mediums and different moisture levels to vary the permittivity. Thus, large training model can be built, tested and a solid conclusion can be drawn in terms of accuracy and robustness of the proposed models.

In the third section, the multi-antenna array step frequency radar prototyping and field validation results were presented. In this respect, two different SFR array topologies were proposed. The first design offers a single VNA-based SFR with a multi-antenna array and a time division multiplexer switch. The second architecture, on the other hand, provided a complete parallel channels multi array with multiple VNAs to increase SFR speed. The stated second topology, on the other hand, increases the cost by increasing the number of VNAs and processing resources. However, in the prototyping, the number of array channels were limited to three in first topology. Then, the number of channels were two in the second topology due to lack of resources at this stage. The scale up of the array size can be retained for future scope.

The first prototype (VNA + multiplexer switch) was experimentally tested in a static location to check the function of operating principles, acquisition chain, multiplexer, and 3D matrix generation. The findings support the experiment's objectives by observing B-scan, C-scan and cross view radagram as expected. Meanwhile, a second prototype with a completely working aspect was created employing two VNA, two antennas, and a distance encoder. As a result, the prototype was placed on a three-wheel cart. The geosite was then successfully evaluated in the field at the UGE Nantes campus. In contrast, two parallel B-scan profiles with hyperbolas were acquired to evaluate the idea, architecture, hardware and software function as a system, as well as the signal processing procedures used. The results support the objectives using two B-scans with various hyperbolas that confirms ground truth of the site. The measurements in the high permittivity zones, did not yield adequate results due to strong coupling noise and poor penetration performance due to the emitting power constrain of the VNA. In this situation, a ground coupled bowtie antenna and a high power VNA are proposed for future development.

Furthermore, the Python API, control, and acquisition software is operational for a two antenna array SFR at this time. However, it still has to be improved in terms of scaling up to bigger array sizes and post-processing capabilities. Since, the large array requires several parallel processing services, computer hardware needs upgrade with multiprocessing capacity to

minimise delay between acquisition and visualisation. In terms of acquisition speed, we reach up to 3 km/h using a single antenna in monostatic mode with a VNA sweep configuration of 0.5 - 4.5 GHz, 301 points, 10 KHz IFBW, and 5 cm spatial resolution at the x-axis. With a high-speed VNA, the speed may be boosted in the future. However, installing a ground coupled bowtie antenna with a high power high speed VNA is a critical next step to confirm the penetration depth and signal quality under higher permittivity subsurface conditions. Future research will focus on the best operating frequency configurations, antenna configuration, antenna offset, feasible maximum array size, different SFR architectures, and their complex performance matrices, which will be heavily influenced by signal processing techniques and antenna characteristics. The next prototype version will have two parallel VNAs with ground coupled antennas.

The next Chapter draws the global conclusion and future work of the thesis.

Chapter 5

Conclusion and future works

5.1 Conclusion

The thesis study focuses on the research and development of the essential solution for automated and large-scale 3D mapping of underground utility networks. As a result, this study investigates necessary signal processing methods for 3D subsurface utility mapping. The objective is prioritised on practical solution with high Precision, and robustness to conform with existing standards and laws. In this regard, it has been noted that there are legislation and various initiatives being implemented all over the world to manage subsurface assets with 3D localisation Precision. However, legislation, accuracy expectations, and practices vary from one country to another. In France, for example, three classes of subsurface asset mapping are governed by law. In this regard, all critical networks require Class A precision with 40 cm accuracy, Class B precision with 1.5 m accuracy, and Class C precision with more than 1.5 m accuracy. According to the literature, the high level process steps in utility mapping were identified as data acquisition, automatic pipe detection, physical and geometrical parameter estimation, and 2D/3D mapping. Among the identified utility mapping process steps, this research is highly focused on development of automatic pipe detection algorithms and parameter estimation models combined with physical signal processing techniques. It's assumed that the models can be implemented on commercial multi-antenna array SFR data. Moreover, the key contribution of the research was shown towards depth and radius estimation models.

In the data acquisition, GPR was identified as a viable Non-destructive instrument for the purpose. Whereas, SFR is a form of GPR that, unlike impulse GPR, works in the frequency domain rather than the time domain. The SFR calculates the complex reflection coefficient (S_{11} parameters) and transforms it to A-scan using IFFT. In this respect, a multi-antenna array system was considered for data acquisition in this thesis, that can generate parallel B-scans at the same time, saving time and avoiding grid survey.

In this context, with regard to the automatic pipe detection algorithms, whereas hyperbolas in the B-scans were identified as the signature that represents a pipe (but not always). Hence, the work evaluates two deep learning object detection algorithms such as Faster R-CNN and YOLOv4 for automatic pipe detection. Both models use automatic features extractions using convolutional network and different sliding window technique that facilitates multiple target detection within an image. In addition, B-scans were subjected to very minimal pre-processing techniques such as time zero referencing and exponential gain, conversion which were applied to the full data set as a single setting. This is because the goal of automated detection is to utilise a robust model to handle large GPR data with a single set of global parameters.

First, from the numerical study conducted using data from gprMax 2D simulations. Whereas, B-scan databases were generated at different centre frequency, pipe depth, and multiple pipes configurations. Then, the proposed models were, trained, validated and tested. Based on the study outcome, it confirms that both Faster R-CNN models and YOLOv4-based automatic pipe

detection models were able to detect non-overlapped multiple hyperbolas in a single B-scan. Hence, the model's performance matrices were evaluated for its ability to distinguish individual pipes. The models detected individual multiple pipes in a single B-scan with an overall Precision or Recall in the range of 85 - 98%. The performance gap between Faster R-CNN and YOLOv4 was very narrow. Moreover, the influence of different convolution networks (ResNet and Inception) in the Faster R-CNN's performance is visible, and small. In addition, annotation and pre-processing (greyscale or binary image) techniques, also have a significant impact on model performance. Whereas, two annotation techniques were adopted. Firstly, the bounding box was drawn from the apex of the hyperbola until the bottom (Annotation - 1). Secondly, the bounding box was drawn from any nearest top horizontal layer interface until the apex (Annotation - 2). Both annotation techniques fulfil its objectives. Indeed, the Annotation-2 removes false positives caused by the multiple reflection effects, that validates the objective of the specific annotation strategy. However, the overall performance of annotation - 1 is comparatively higher than annotation - 2 models in terms of Recall value. Moreover, the proposed models also detect hyperbola at varied GPR centre frequencies. The detection Precision and Recall doesn't vary much between centre frequencies and noise differences in Faster R-CNN (as long as the training and test data are from the same GPR centre frequency). That, indicates the robustness of Faster R-CNN. However, when the centre frequency between the training and test data was different (400 and 900 MHz), the Precision value dropped from 98% from 88%.

In the experimental study, field validation of automatic pipe detection was done using impulse GPR data obtained from GSSI SIR 4000 + 350 MHz antenna system, in Gustave Eiffel University campus of Nantes. Whereas, the "Faster R-CNN + ResNet-50 + Annotation-1" model shows the highest Recall, according to the results (92.7%). Such that, it has missed the true targets (pipes) the fewer times when compared with other models. However, the Precision is reasonable at 88.0%, and Precision can potentially be reduced by an extra NMS (Non Max Suppression) layer, because the majority of false positives are seen in strongly overlapping bounding boxes over real positives. Meanwhile, the "YOLOv4+ Annotation-2" model has demonstrated the greatest Precision (97.6%). However, the Recall values of YOLOv4 are quite low (81.45% and 76.15%). As a result, the YOLOv4 has the high chance of missing the targets. In fact, 'Recall' is more important than accuracy in this utility application. Because, while the detection may tolerate some false positives, false negatives (miss detection) increase the risk of strikes during the excavation works. As a result, for large-scale GPR post-processing applications, Faster R-CNN-based automatic pipe detection models are recommended at this stage. Meanwhile, though the YOLOv4's performance is somewhat poor, it can be used for real-time detection. In overall, automatic multiple hyperbola detection in a single B-scan is acknowledged in this study. Hence, it promises further validation on field data to produce a fully operational model for large scale GPR data based utility mapping with further higher performance. In the context of 3D localisation of pipes, several parameter (velocity (v), depth (d) and radius (r)) estimation methods were studied. In all cases, the hypothesis is taken as the pipes were already detected automatically. Hence, the pipes within the detected bounding box have been utilised for the parameter estimation. The work evaluates several methods like Ray-based method and machine learning approaches (SVM, SVR, ANN) for estimating the depth (d), radius (r) of the pipe, and velocity (v) of the stratified media. In this respect, the study observed that, the hyperbola shapes that represent pipe in the B-scan, varies according to its ground truth such as depth, radius and permittivity. As the result, six features for the machine learning were extracted from hyperbola shape that can represent the shape statistically (based on hyperbola travel time). Firstly, all models were numerically validated using 2D gprMax data at different centre frequencies, and by approximating infinite subsurface multi layers medium to a single homogenous layer with its average velocity and conductivity. In overall, the numerical analysis predicts that the proposed machine learning models would outperform Ray-based approaches

in all scenarios (with or without noise). Furthermore, numerical study outcome indicates that, the depth (d) accuracy may be achieved to meet the French requirements' Class-A precision (40 cm of accuracy). When the radius (r) and depth (d) are well standardised, the applicability of SVM multi classification is also viable as alternative to SVR or ANN regression. Because, standardisation of the depth (d) and radius (r) is becoming more common for new installations. In the meanwhile, the numerical study reveals that SVR or ANN could be implemented in any environment that can perform, with mean relative errors ranging from 5% to 35% for radius (r) and 2% to 3.5% for depth (d) estimate, respectively. ANN, on the other hand, performs somewhat better than SVR. Furthermore, SVR and ANN performance declines with the increase in noise levels. The depth (d) estimation shows its robustness in noiseless, noisy, random continuous values, metal and PVC pipes configurations (The relative error ranging 2% to 3.5% for the studied depth from 30 cm - 1.2 cm). This promise further acceptability of the machine learning methods on depth estimation upon validation on experimental data. Nevertheless, the radius (r) estimation performance of SVR and ANN is not convincing for the random value configurations data. However, the relative mean error remains below 50%, and it's not yet regulated by law like depth (d). Thus, the proposed approach for radius (r) estimation can be utilised for radius (r) standardised applications or any applications that require approximate estimations. In a separate study, the content covered depth (d) and radius (r) estimation using DCNN with automatic feature extraction on raw B-scan. Because, all the above-mentioned models make use of a set of characteristics carefully retrieved from the hyperbola. The goal was to employ a DCNN that can automatically extract features and the methods to determine if the raw signal B-scan can be utilised instead of the B-scan image. The methods show very encouraging results for depth estimation with error similar to the SVR and ANN. However, the study must be extended for further complex data. Moreover, a study on 3D modelling at various pipe orientation is essential to observe the hyperbola shape variation with the azimuth and elevation angle of the pipe, and to include orientation angle into the features. Because current study is limited the acquisition perpendicular to the pipe orientation.

In order to validate the proposed estimation models on experimental data, due to limited resources, we do not have a controlled location with a sufficient number of pipes with varying depths and diameters to create a supervised machine learning model at this stage. As a result, the experimental validation is limited to an open air setting with a few number of pipes. In this case, the velocity of the air is constant. Thus, velocity was not considered for estimation. Furthermore, it is found that, from the open air experimental results, the depth (d) accuracy may be achieved up to 0.5% of mean relative error using both ANN and SVR, which meets the French requirements' Class-A precision. Whereas, the radius (r) can be estimated with the mean absolute relative error of 10% using ANN and 18% using SVR. Thus, ANN is relatively better than SVR for the radius estimation. When the radius (r) and depth (d) are well standardized and defined in the classes, the applicability of SVM multi classification is possible. Thus, multi class SVM was applied and observed that, the model can achieve up to 88% of accuracy in open-air settings when classified into 5 classes. Meanwhile, the accuracy can increase up to 96% when the number of classes reduced to 3. Globally, the depth (d) estimation shows its robustness in noiseless, noisy, random continuous values, metal and PVC pipes configurations (all cases). Then in the open-air settings. These findings promise further acceptability of the methods on 3D localisation of utility network upon validation on more complex experimental data. Nevertheless, the radius (r) estimation performance is still convincing as it constitute only 18% of error, and it's not yet regulated by law like depth (d). But it affects the accuracy of the no dig zone boundary. Therefore, ANN based radius estimation model can be used for no-dig zone boundary estimation. Nevertheless, when the radius is standardized into definitive radius classes, multi class SVM also can be deployed for this scope. In global scope, the obtained depth and radius values can be combined with GNSS + RTK 2D geo coordinates to

plot the 3D geometry of the pipe and the safe zone boundary. Furthermore, another study describes a preliminary study about pipe type classification method that can differentiate between metal and PVC pipes. According to the results, supervised machine learning such as BSVM or KNN can be used to classify the objective with the accuracy more than 85%. In addition, the proposed model classify metallic pipes 100% accurately. That's a promising indication to ensure the critical pipes like gas and power are identified in terms of network and human safety.

In general, for the experimental validation of all proposed models in this thesis, at this stage, due to lack of sufficient field data with ground truth information, all models has been numerically validated, and with an open air experiment settings. Moreover, since the proposed model is highly sensitive to the shape the hyperbola, the model can work for a specific GPR equipment. Because, the shape the hyperbola varies according to the antenna offset size, height. Therefore, the database for the experimental validation must be built by single equipment.

With regard to multi-antenna array SFR prototyping, the objective is to develop an array system that can be used for parametric studies. Then, the prototype can scaledup in the future as a low cost highdense array system with gradual imrovements. In this context, array architecture and proof of concept were validated in this thesis. This development can help the scientific community for further imrpvoement of the existing commercial systems, and on parametric studies. The scope of ultra-wideband is adopted for the reason that, ultrawide band signal narrow down the pulse width. As a consequence, it produces high resolution B-scan. Thus, precision of depth localisation, and ability of distinguishing overlapped hyperbolas can be increased. Hence, for multi-antenna array configurations, we offered two alternative SFR designs. The first design offers a single VNA-based SFR with a multi-antenna array and a time division multiplexer switch. The second architecture, on the other hand, provided a complete parallel channels multi array with multiple VNAs to increase SFR speed. The stated second topology, on the other hand, increases the cost by increasing the number of VNAs and processing resources.

Regardless of the design differences, both architecture can create multiple B-scan slices, which are necessary for 3D matrix formation for 3D mapping of utility networks. The VNA's sweep speed and bandwidth, which influence the topology and SFR speed, are the major performance indicators in hardware selection. Meanwhile, an ultra-wide band directional antenna is required for the specific application. Hence, the Vivaldi, horn, and bowtie antenna types were identified as appropriate. However, because of its availability, vivaldi is employed at this point. Because the goal of the prototype is to validate the proof of concept in terms of the acquisition chain and topology. In this context, the frist prototype (VNA + multiplexer) was tested experimentally in a static position to ensure that the operating principles, acquisition chain, multiplexer, 3D matrix formation all functioned well. By seeing B-scan, C-scan, and cross view B-scan as predicted, the findings confirm the experiment's objectives. Meanwhile, a second prototype with a fully functional aspect was developed using two VNAs, two antennae, and a distance encoder. As a basis, the prototype was mounted to a three-wheel cart and then tested in the field at the UGE Nantes campus. As a result, two parallel B-scan profiles with hyperbolas were acquired to verify the concept, architecture, hardware, and software system function, as well as the signal processing employed. The findings of two B-scans with various hyperbolas are reflecting the survey site's ground truth. The measurements in the high permittivity zones, on the other hand, did not produce satisfactory results due to excessive coupling noise and poor penetration performance due to the VNA's emitting power constraint. A ground coupled bow-tie antenna with a high power VNA are recommended for future development in this circumstance. Furthermore, the Python API, control, and acquisition software for a two antenna array SFR that has all necessary real time signal processing and visualisation from S parameters to B-scan conversion is currently operational. We achieved up to 3 km/h acquisi-

tion speed using a single antenna in monostatic mode, a VNA sweep configuration of 0.5 - 4.5 GHz, 301 points, 10 KHz IFBW, and 5 cm spatial resolution at the x-axis. The proposed two architectures were validated throughout the experiment. Hence, its validations are sufficient for a walking SFR system at this moment. However, more advancements are required for a larger array system and to operate at traffic speeds when mounted in a vehicle.

Overall, the thesis efforts and findings provide the basis for a global framework to handle all elements of autonomous 3D utility mapping challenges and present practical solutions for acquisition and data processing in a large scale 3D mapping context utilizing physical and machine learning techniques. Despite the fact that the global solution includes automated 3D mapping, each step was scientifically evaluated as a separate scope, and the fully automated pipeline development was retained for future work. Because a completely functional solution needs additional experimental validation and complex engineering development.

5.2 Future work

Automatic pipe detection: The numerical analysis may be expanded in the future by modifying the k proposals of Faster R-CNN, convolution kernel's type and size, and other hyperparameters, as well as on more complex 3D models. Because of the unavailability of high-performance computer resources at this moment, this has been limited. Furthermore, large training data sets, additional Non Max Suppression layers, half hyperbola scenario (deformed hyperbola detection) and various parameter analysis can all help to improve the model's performance and reach a more definite conclusion. Furthermore, the experimental validation recommended on larger datasets and hyperparameter customisation be included in the future study. Moreover, multiple models may be constructed concurrently using various GPR equipments. Finally, in order to develop a full solution, a detection model based on the data from SFR prototypes (final version) is required. Automatic pipe detection models, on the other hand, may be used as stand-alone approaches for any commercial GPR data. The detection model based on Mask R-CNN is also a prospective study to directly locate the segment of the apex of the hyperbola.

Parameters estimation: The suggested machine learning models were evaluated numerically and in open-air scenarios. However, it requires experimental validation utilizing a field database gathered by a single GPR model, in a controlled site with ground truth. In order to vary the permittivity, a more sophisticated controlled experimental research in diverse subsurface media and moisture levels is necessary. As a result, a big training model can be developed, tested, and a solid conclusion can be drawn in terms of the accuracy and robustness of the proposed models. Despite this, it may be further confirmed numerically utilizing 3D gprMax data and more sophisticated multi layer configurations, with including hyperbola deformation situations. Because the current study focuses on full symmetrical hyperbola, a half hyperbola scenario would be investigated in the future. Moreover, a study on 3D modelling at various pipe orientation is essential to observe the hyperbola shape variation with the azimuth and elevation angle of the pipe, and to include orientation angle into the features. Because the current study is limited to the acquisition perpendicular to the pipe orientation. GAN or similar deep learning algorithm can be implemented to increase the training database that has been addressed in the scope of another research project namely "Prometheus".

Furthermore, antenna impacts may be minimized by utilizing an antenna calibration (estimating the antenna transfer function and radiation centre), and the Green function can be assessed instead of the B-scan during the parameter estimation step, that has been addressed in the scope of "Prometheus". As a consequence, more noise-filtered data for machine learning

models might be acquired. Because, Green function removes any noise and clutter generated by the antenna radiation pattern. As a result, this method has the potential to improve performance. Furthermore, numerical validation in 3D simulation and pipes at an angle are also necessary. In addition, the classification of pipe types was conducted as a preliminary research. In fact, there is a need for a multi-classification study that can identify between all types of pipes other than metal and PVC. Then, several feature selection methods also may be investigated to improve the performance of pipe type classification models.

Multi-antenna array step frequency radar prototyping: Installing a ground coupled bow-tie antenna with a higher power VNA is the next crucial step in confirming the penetration depth and signal quality under higher permittivity subsurface circumstances. Further, a bistatic configuration can help lessen direct coupling and ringing effects. Moreover, in addition to time zero removal, a calibration step also can be incorporated to remove antenna effects and improve B-scan clarity. Furthermore, accurate radiation centre estimate can help the SFR for FWI-related signal processing algorithms, that can be investigated for parameter estimation. Further, a size reduced antenna array can potentially increase the array density and subsequently increase the B-scan resolution of cross-view. Because, current, commercial SFR array systems have maximum 40 channels within 2 m. Thus, it limits the cross-view B-scans horizontal resolution to maximum 40 points per hyperbola. In this case, it requires more size reduced higher number of antennas to increase this resolution.

3D mapping: Towards the solution of 3D mapping, when the automatic pipe detection method recognizes a pipe with a bounding box, the apex of the hyperbola and its relative location can be determined. The coordinates of the hyperbola apex between two parallel B-scans can then be joined using an interpolation method and translated to 3D geometry of the cylindrical pipe. This algorithm must be created in the future as a key step towards 3D mapping.

Over all solution: Every phase in the thesis work is addressed as a separate scope and evaluated in scientific aspect. Thus, once all models have been validated experimentally and at acceptable performance levels, the complete data flow pipeline may be established, which will need substantial engineering development.

Appendix A

Real time acquisition GUI and protocol

In this appendix, we demonstrate the protocols using the Graphical User Interface (GUI) for real-time acquisition. The protocol is carried out in two steps: (a) VNA setup and calibration, and (b) SFR setting and acquisition.

We clarify the procedure steps used during every survey for sample data that is irrelevant to the experimental data reported in the chapters. This protocol, however, applies to any data acquisition utilizing this prototype configuration. As a result, the demonstration is meant to be a snapshot of the software and does not include realistic signal. Furthermore, the example is for the construction of two VNA parallel channels.

VNA setup and calibration

The VNA is connected to the PC using the USB cable and the VNA setup software is launched. This calibration software is provided by the VNA manufacturer. After launching the software, the parametric initialisation is done.

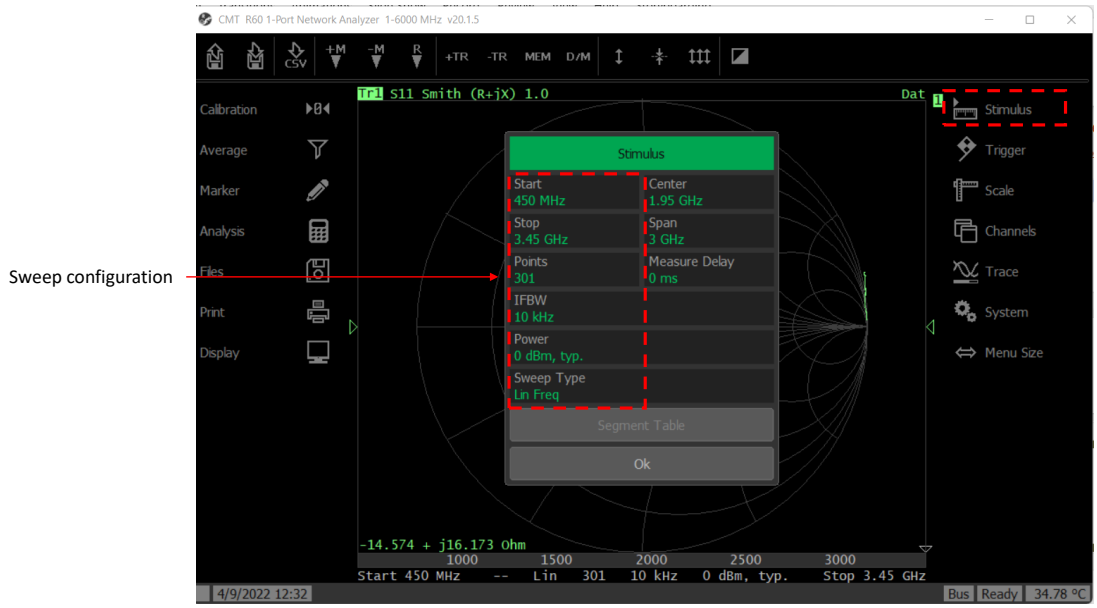

Figure A.1: Sweep configuration for VNA calibration.

As shown in Figure A.1, the sweep configurations are described as follows:

- **Start**: The start frequency (f_{min})

- **Stop**: The stop frequency (f_{max})
- **Points**: Number of frequency points
- **IFBW**: Inter-frequency Bandwidth , typically set to 10 kHz
- **Power**: VNA power value in dBm
- **Sweep type**: Increment step in sweep points from f_{min} to f_{max}, set to linear.

After initializing the parameters, the VNA is now connected to the calibration kit. Once the calibration kit is ready, the "Auto-calibration" option is chosen under the "Calibration" menu as shown in Figure A.2. The settings are then accepted by clicking on the "Apply" button.

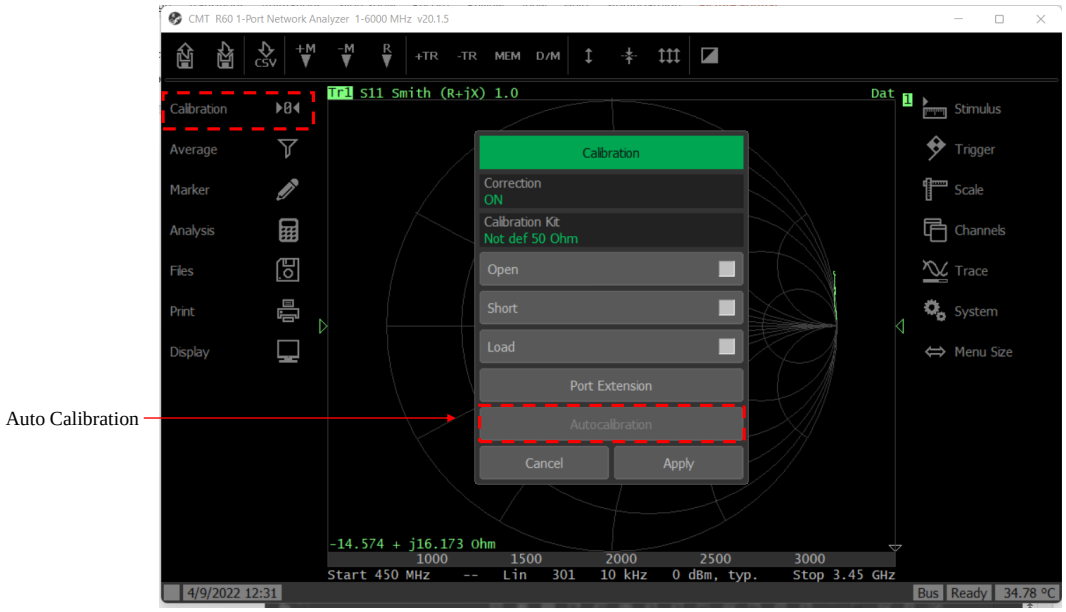

Figure A.2: Automatic VNA calibration.

Since our prototype SFR is made up of two VNA-antennas, the calibration procedure will be repeated for the second VNA as well.

SFR GUI settings and data acquisition

Once the VNA are calibrated as mentioned in the previous section, the antennas are connected and the SFR GUI is launched. In the VNA settings window of the GUI (shown in Figure A.3), the parameters are set for the Start frequency, stop frequency, Number of frequency points and IFBW. These parameters should be the same that were initialised during the VNA calibration stage (as described in the previous section).

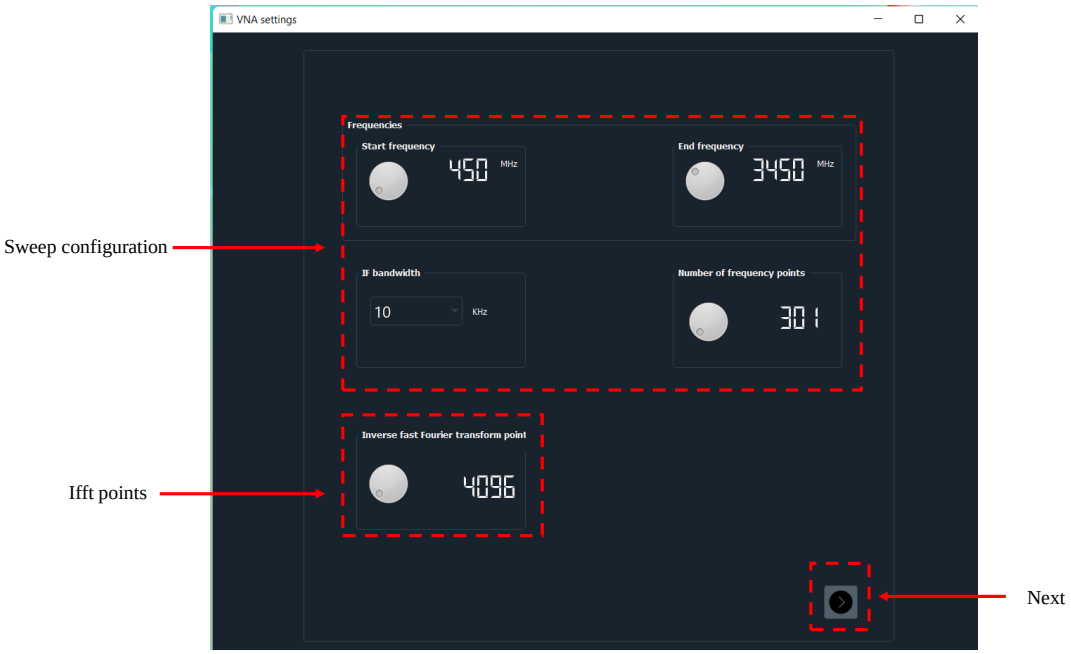

Figure A.3: Example of sweep configuration features for SFR survey in developed software prototype.

An additional parameter 'IFFT points' is also set. This parameter refers to the transformation of S11 parameters to the time domain.

After the VNA setup, the antenna calibration are done. The calibration can be done in either one of the three following ways: (a) Air-shot calibration, (b) Metallic plate calibration, or (c) Calibration using a known section of site. The reference signal obtained during this calibration is subtracted from the data during acquisition.

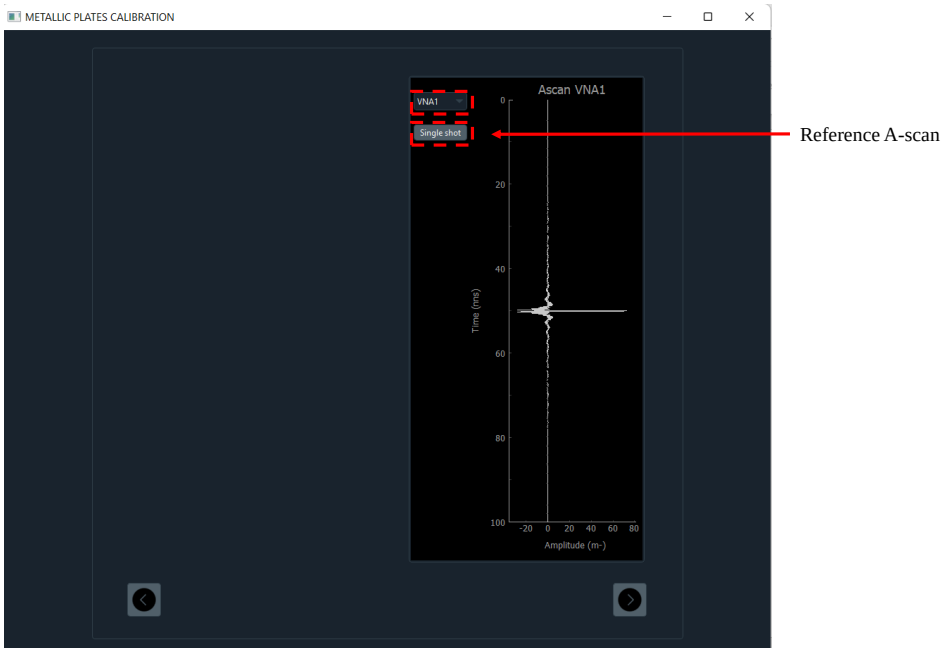

Figure A.4: Open-air / Metallic plate / reference A-scan measurement.

As shown in Figure A.4, each VNA individually is chosen from the menu and the 'Snapshot'

button is clicked to obtain the reference signals for both antennas.

The next window performs the 'Encoder settings' shown in Figure A.5. In order to precisely calibrate the data acquisition, the distance encoder is used. In this step, a calibration distance in cm is fixed and the 'Confirm' button is clicked. The calibration begins, and the prototype cart is moved for this fixed distance in the forward direction. Once the distance is covered, the GUI automatically computes the 'Tick parameter'.

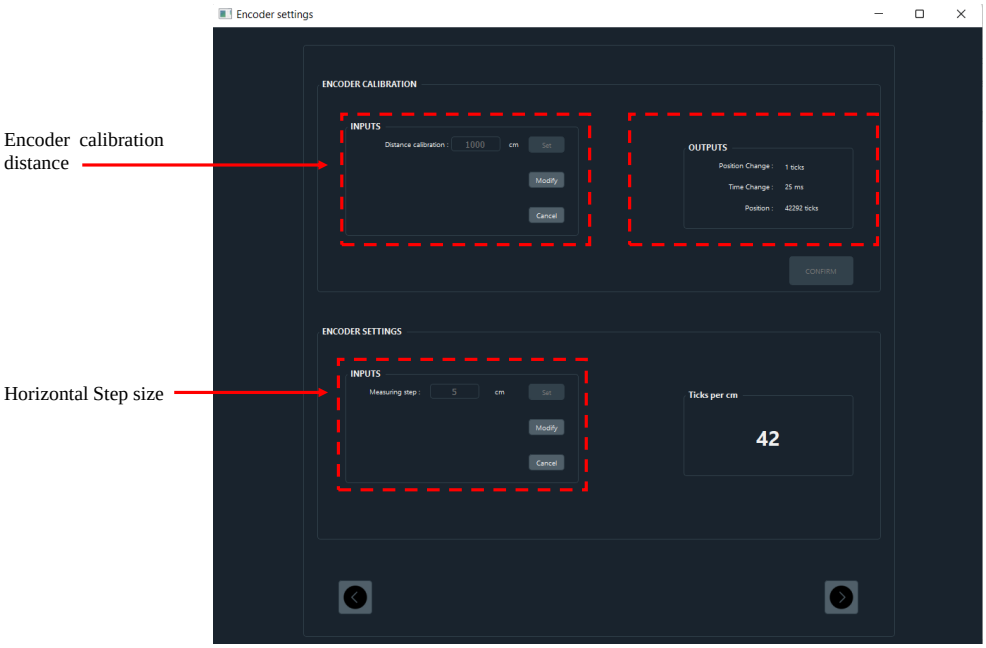

Figure A.5: Distance encoder calibration settings.

The 'Horizontal step size' value refers to the spatial distance between two adjacently acquired A-scans. The tick parameter obtained will correlate to the horizontal step size such that when the tick is triggered, it indicates that the step-size distance is covered and the next A-scan should be measured.

In the 'Plotting Parameters' window, the time filtering and visualisation parameters are specified. As shown in Figure A.6, the time filtering is done by fixing the upper and lower bound limit of the time window in terms of the sample number. The filtering results are shown on the right side of the window for confirmation. The 'Gain' parameter is set in case the user wishes to add gain to the A-scan data.

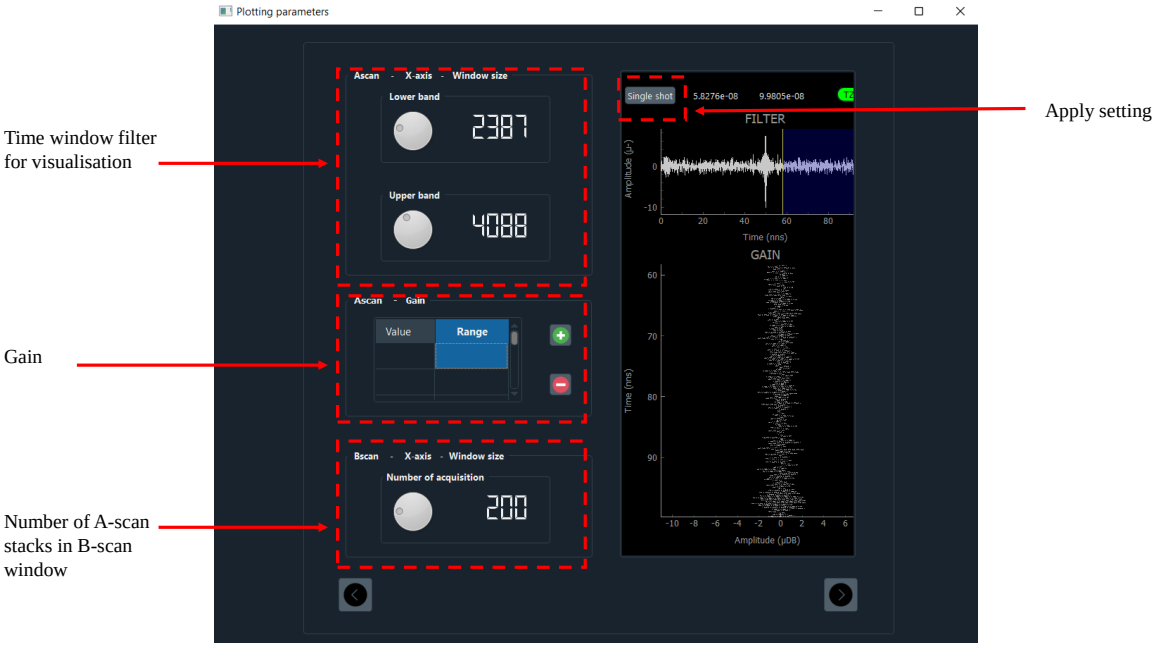

Figure A.6: [Filters settings and pre-visual.

Lastly, the value for the number of A-scans to be stacked is specified. This value refers to the maximum horizontal window size of the B-scan that can be visualised in the GUI during data acquisition.

The user can go back and forth to modify the parameters set up to this stage, after which the data acquisition step begins and the modification is no longer allowed.

After all the parameters are set, the real-time data acquisition and visualisation is done. In this window, the user can choose to view the acquisition of either or both antennas at the same time by choosing the option from 'VNA choose' as seen in Figure A.7. The T_0 removal option can be activated or deactivated. When activated, the reference A-scan signal is subtracted from the acquired A-scan at that instant and the calibrated signals are viewed.

The 'Speed indicator' refers to the data collected rate and is used to warn the user in case the acquisition rate is very high. The collection controls allow the user to 'Start', 'Pause' and 'Stop' data collection at any time. Finally, when the data collection is complete, the 'Save' button is clicked. For every B-scan acquired, the GUI saves three files as follows:

- File 1: Raw S_{11} data for the B-scan.
- File 2: Raw time domain B-scan data.
- File 3: Calibrated and filtered time domain B-scan data.

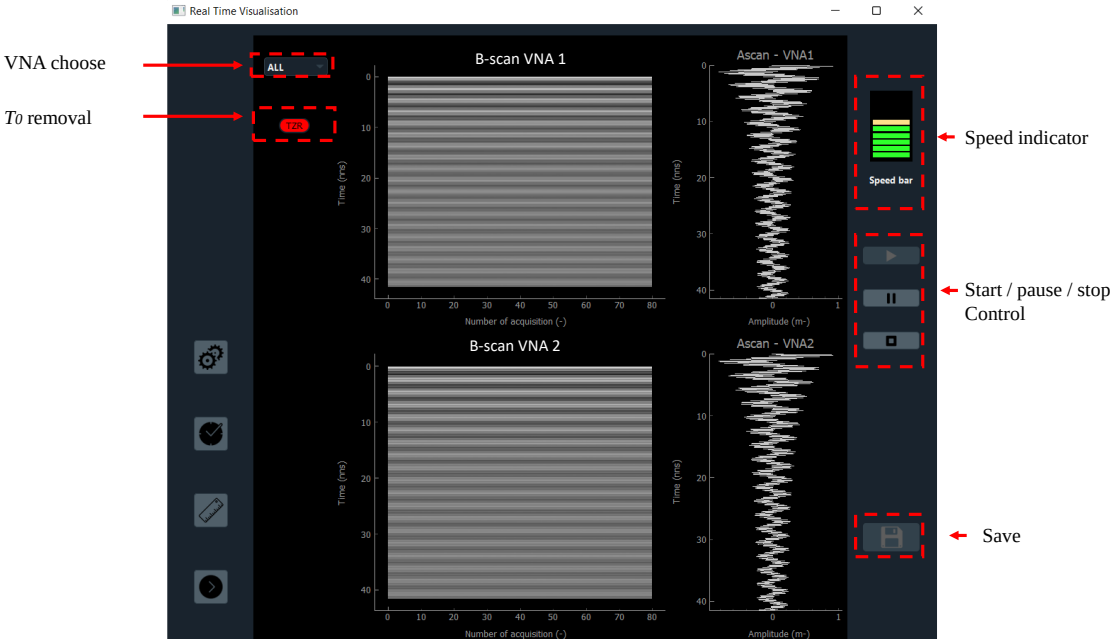

Figure A.7: Real time Multi B-scan visualisation and acquisition control.

Appendix B

State of Art

B.1 French regulations and practice in utility mapping

In the framework of utility mapping, France has created a nationwide damage prevention system since 2013, requiring 40 cm precision for the location of all critical underground network infrastructure prior to installation. Since 2013, annual statistics show a decrease in the quantity of underground utility damage.

The DT-DICT system in France resembles a North American one-call system on the appearance, but it is fundamentally different in that the DT-DICT mechanism actively enhances the quality of underground location data as their functions. The Guichet Unique (*Téléservice réseaux et canalisations*) offers a list of all utility and telecom providers in France, as well as maps of their service regions and contact information. The project manager must create a DT (*Déclaration de projet de Travaux*) at the start of each construction project, which is a notice of anticipated construction activity. The DT is delivered to each network operator with assets at or around the planned construction site using the information supplied by the Guichet Unique. The DT must be responded to within 9 working days by all network providers. Operators must give any information they have on the location of their current networks at the proposed site. There are two methods for network operators to respond. They may supply maps of their Class A underground infrastructure (accurate to 40 cm). However, if they are unable to submit compatible maps, they may request that the project manager conduct one or more *Investigations Complémentaires* (IC), or additional complementary investigations.

In this situation, the project manager will hire a utility surveyor to undertake locating operations with the goal of achieving relevant Class compliance for all non-compliant underground utility facilities. The network operator or operators bear the IC costs. The important result of this approach is that when the project manager is ready to begin excavation, he or she knows the exact position of all subsurface infrastructure at the project site. Because the laws demand that the results of the additional survey be communicated to the relevant network operators within 15 days, the IC process also results in changes to network operator records. The network operators must update their network records with the information from the investigations. The DT-DICT regulations make reporting incidents of underground damage during construction mandatory for network operators. The National Observatory DT-DICT compiles these reports annually and issues a network operator dashboard summarizing the damage statistics for the year. On February 15, 2012, the national rule mandating subsurface infrastructure mapping in different classes, titled decree related to excavations near underground, overhead, or underwater transmission or distribution networks, was promulgated. The "anti-network damage" reform, named "DT-DICT," went into force on July 1, 2012. The decree's implementation is the duty of a "competent municipal authority." Various departmental entities across France have assumed responsibility for enforcing the directive. According to the regulation, critical infrastructure includes subsurface electric power cables, pipelines, and public transportation infrastructure,

but not buried water and telecommunications equipment. The deadline for enforcement of the law for cities was January, 1, 2019, and for non-cities was January, 1, 2026.

The location accuracy classes apply to planimetry (x, y) and depth (z). They are defined as follows:

Class A: Structure with a maximum location uncertainty of less than or equal to 40 cm if rigid, or 50 cm if flexible; the maximum uncertainty is increased to 80 cm for underground civil engineering structures attached to installations intended for the circulation of rail transport vehicles built prior to January, 1, 2011. For example: Gas, Public lighting, Electricity cables.

Class B: Structure of which the maximum location uncertainty is greater than Class A and less than or equal to 1.5 m; the maximum uncertainty is lowered to 1 m for connections to critical underground structures for safety purposes and from January, 1, 2021, for connections to non-critical underground structures. For example: Water and Telecommunications cables.

Class C: Structure for which the maximum location uncertainty is greater than 1.5 m, or 1 m for connections to critical underground structures for safety purposes and from January, 1, 2021, for connections to non-critical underground structures, or for which the operator is unable to provide accuracy information. For example: other non-critical cables.

B.1.1 GPR based 3D utility network mapping global case studies

GPR has been successfully used coupled with other NDT technologies to identify and locate utilities. However, it has not been utilised with its full potential for large scale mapping. Non-destructive utility survey pilot projects have been widely undertaken across the world as a result of the importance of utility network information and the laws that govern it. In France, a multibillion-euro effort is ongoing to enhance the accuracy of geolocation information regarding the country's subterranean utility infrastructure. It is backed up by the legal framework, as explained in the preceding section. The 500 MHz GPR device was used to discover a main water supply pipe [124] in Stockholm in 2001. They created a 3D visualisation by producing 16 parallel short GPR profiles perpendicular to the pipe orientation.

Finally, the data were fed into a signal processing program for human interpretation and estimation of the pipe's position. Then, in recent years, pilot projects in Milan, New York, and Las Vegas have proved the benefits of correctly Geo-locating subsurface infrastructure. In the year 2000, Edison-Co of New York undertook a project to map the underground utility network, measuring an area of 12,000 square meters in four days at a speed of 1 km/h with the assistance of a GPR array system known as the CART system. In addition, another research was conducted by the University Sains Malaysia. The project's goal was to find and map underground utility pipes in the studied region [125]. In this investigation, they employed a 250 MHz Impulse GPR to measure 8 parallel profiles with 2 m line spacing. They discovered several pipelines at a depth of 2.5 m. In another case, an impulse GPR-based utility survey was carried out in Hong Kong in three separate locations with three different pipe types [126]. Drains, water mains, and power lines were among the pipes put to the test. Three distinct impulse GPR at operating centre frequencies of 100 MHz, 270 MHz, and 400 MHz were employed for this investigation. The findings for depths less than 2 m were differentiated by 400 MHz, whereas depths more than 2 m were better by 270 MHz. Furthermore, 100 MHz was deleted owing to a difficulty with horizontal alignment accuracy.

As previously stated, typical single antenna impulse GPR is time-consuming in wide area

survey circumstances. The delay is mostly due to the poor acquisition speed and inability of producing parallel profiles to build 3D mapping. Among all known NDT methods, it has been shown to be the fastest non-destructive testing procedure. As a result, data acquisition may be done very efficiently employing arrays of antennas to reduce parallel profile acquisition. Thus, for the first time, the Norwegian University of Science and Technology created a multi-antenna array ultra-wide band GPR type that operates in the frequency domain, known as "Step Frequency Radar (SFR)" [127]. The designed SFR has a customizable operational frequency range of 10 MHz to 3.4 GHz. The array is made up of 31 pairs of monostatic bow-tie mono-pole antennas installed on a shared ground plane that spans 1 m in width. They were able to collect data on a 3.2 cm $\times$ 3.2 cm grid at a pace of 1-2 m/s using this method. This SFR approach resulted in successful mapping of the pipes, cables and old tramlines in Trondheim in 2001. Later, the approach was introduced as a commercial SFR type 3D GPR in the trade name of "3D-Radar" [39]. However, the developed platform is highly expensive and still it doesn't include any automated signal processing features for large scale utility mapping. Nevertheless, this solution is highly a primary reference for the motivation of the solution development of this thesis. Whereas, array GPR was considered as the prospective data acquisition system. As a result, a rapid, robust, and feasible signal processing methods must be developed, inorder to automate 3D mapping of underground utility mapping of large scale data, on the basis of current challenges, available resources and methodologies.

B.1.2 Introduction to Ground Penetrating Radar

Ground Penetrating Radar Principles (GPR)

GPR-based approaches have been shown to have various benefits over other non-destructive techniques, making them of special relevance as a potential solution to the utility network detection, localisation, and classification problem mentioned in this thesis. GPR [38] is a non-destructive technology for locating objects or interfaces buried under the earth's surface or within any electromagnetic wave penetrable structure. GPR is capable of detecting both metallic and non-metallic objects. The parameters of GPR measurement and associated radar-gram (known as "B-scan" in the GPR community) change depending on the complicated dielectric permittivity and conductivity of the target host medium. As a result, the prospective depth and diameter can be calculated as a function of dielectric characteristics and impulse travel time that has been validated in above section. The key operational benefit of the GPR is that the radar antennae do not need to be in touch with the ground, allowing for quick surveying capability, subject to acquisition hardware speed constraints.

When we look at the GPR's operating principles, we can see that it uses single or multiple antennas to transmit controlled electromagnetic pulses to the subsurface at frequencies ranging from 20 MHz to 3 GHz or higher depending on the type of GPR [38, 39, 91], and the pulses penetrate the ground and are reflected back to a receiver by the various subsurface layers and any objects or features within the antenna's radiation visibility, as shown in Figure B.1. The impulse GPR pulse, for instance a ricker wavelet, is emitted. The reflected pulse response is then recorded as a function of time, as seen in the Figure B.2.

The Figure B.1 shows how a hyperbola signature is created on a B-scan (Radar-gram) when a GPR is run over a pipe. The scattered echoes record a peak signal amplitude that changes with the distance between the GPR and the target at the reflection point on the pipe in each trace location. The traces are then piled together to generate a B-scan picture, which consists of the shape of a hyperbola formed by multiple traces (A-scans), as seen in Figure B.1.

However, the electrical characteristics of the soil, particularly the complex permittivity and conductivity, as well as antenna parameters like as gain, bandwidth, and radiation pattern, have a considerable influence on the scattered echo's characteristics. Depending on the kind

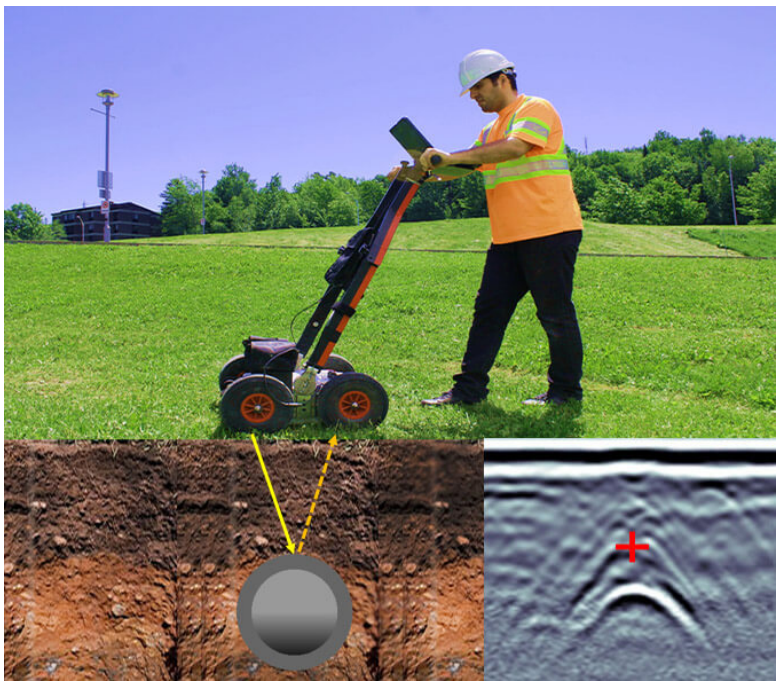

Figure B.1: GPR operating principle and an example of B-scan in the presence of a pipe.

of GPR, the radar system receives the impulse response of the emitted pulse as a function of time or frequency. The amplitude and phase response of a standard impulse GPR are recorded as a function of time, whereas SFR (Step Frequency Radar) works on the complex reflection coefficient as a function of frequency. The amplitude and phase of the "echoes" can provide information regarding the target's scattering properties, and the timing of arrival of different pulses provides indirect distance indications.

The paragraph that follows discusses the detailed fundamental data processing and interpretation methods. As a result, the operational fundamentals of the GPR inspire and pave the way to achieve the scope of this thesis. However, owing to different technological restrictions of

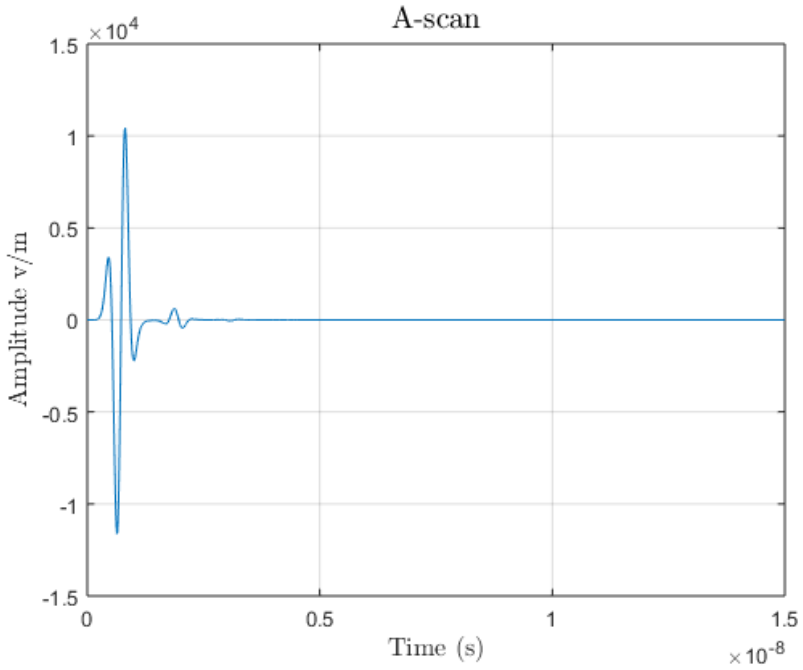

Figure B.2: Example of an A-scan (single temporal response) of a GPR.

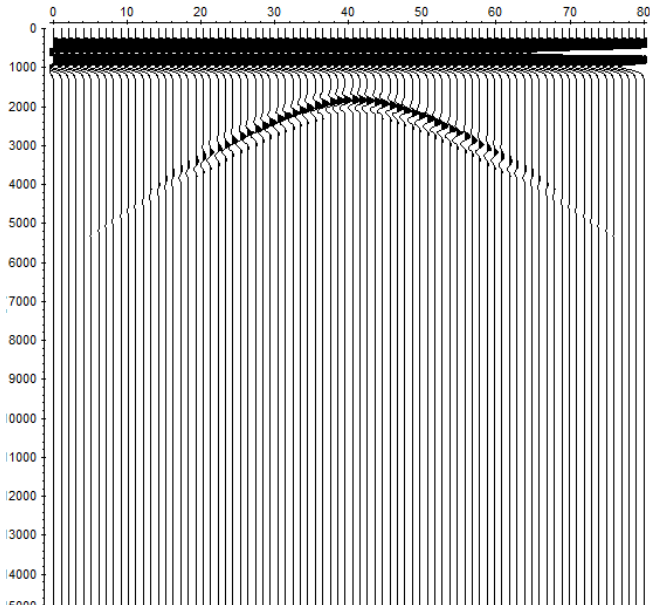

Figure B.3: Stacks of several A-scans over a buried pipe.

impulse GPR for application on a large scale of 3D utility mapping scope, it has led in focusing on SFR type GPR technology, which is a form of GPR that operates on frequency domain rather than direct time domain signal acquisition.

GPR Data Processing

A commercial GPR display typically consists of a collection of reflected time signals known as A-scans viewed side-by-side as seen in the Figure B.3 giving scattered travel time profiles of the subsurface, where stacks result in an image known as B-scan (refer to Figure B.4) where the pixel resolution is scaled against the reflected signal amplitude. The Figure B.4 depicts the comparable B-scan image of the A-scan stacks shown in the Figure B.3. These B-scans are complicated, need skilled interpretation and post-processing to obtain depth and other subsurface characteristics. Much of the effective direct interpretation stemmed from combining the operator's skills, such as interpreting the features such as hyperbola in the B-scan, with knowledge of the host materials' structure and target properties. In most cases, such data is post-processed using a combination of manual and automated signal processes.

Then, as seen in the Figure B.5, many parallel B-scans are layered together to create a 3D volumetric matrix. The purpose of the multi-antenna array system was to generate such 3D matrix using numerous B-scan profiles for subsurface mapping and utility network identification, positioning, and localisation. The number of parallel B-scan profiles depends on the number of channels in the array. In a monostatic design, n channels have n antennas, whereas bistatic arrangements have $2n$ antennas. In the case of an SFR, the echoes are also logged in frequency domain as complex reflection coefficients (S_{11}). As a result, the Inverse Fast Fourier Transform (IFFT) is used to generate the A-scan, which is a frequency domain to time domain transformation, as shown in Figure B.8 bscan.png and in the subsection 4.2; and then the interpretation and post signal processing steps are carried out as with impulse GPR. In this regard, a quick overview of SFR is provided below.

Step Frequency Radar

SFR is a form of ground penetrating radar that operates in the frequency domain rather than the time domain like impulse GPR. In its architecture, a basic monostatic SFR can consist

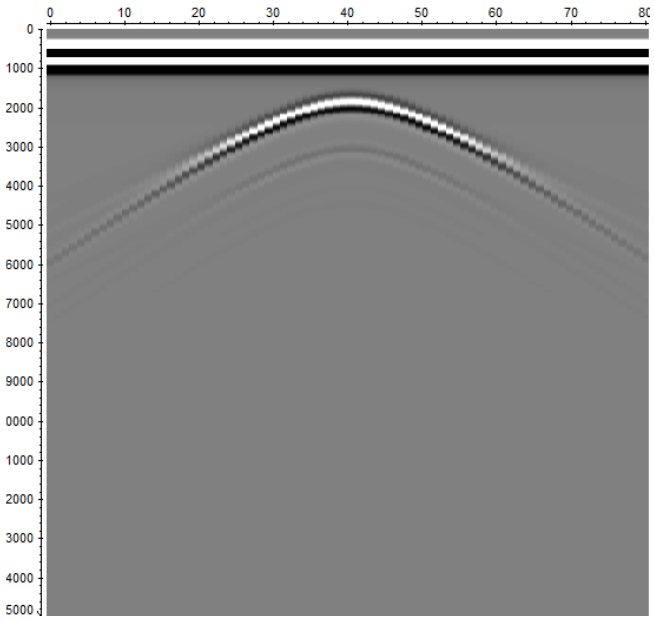

Figure B.4: B-scan of GPR signal over a single buried pipe.

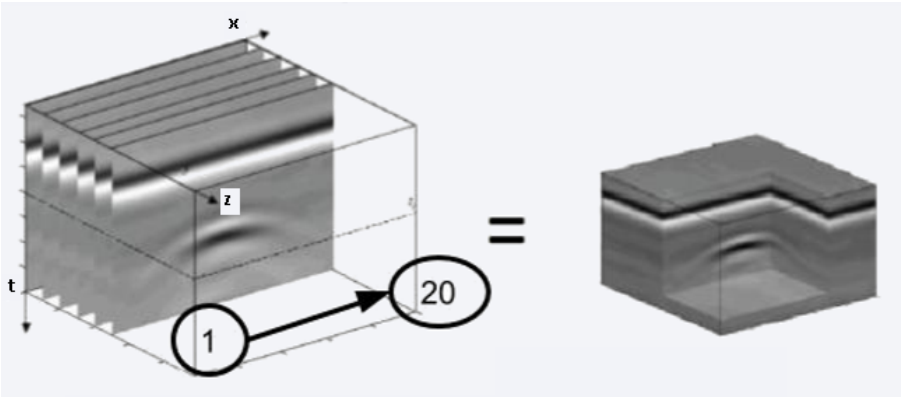

Figure B.5: Formation of C-scan from Multiple Parallel B-scans

of a Vector Network Analyzer (VNA) or an equivalent RF circuit, and an antenna (see to Figure B.6). At each frequency point, the VNA measures the complex reflection coefficient ($S11$) between the VNA and the coupled target medium through the attached single antenna in the monostatic mode. Nevertheless, in the bistatic configuration, two ports VNA is attached to two antennas and measures S_{12}. The operating principle of a VNA is to produce very narrow electromagnetic pulses (almost a discrete pulse) at given frequency intervals, as shown in Figure B.7. The discrete pulses form an ultra-wideband electromagnetic pulse in time domain, resulting in high resolution B-scans. Whereas the total bandwidth can vary from 1 MHz to 20 GHz or higher depending on the application, type of VNA, and antenna. However, in commercial SFRs, the upper frequency limit is observed between 1 and 3 GHz in utility applications. The maximum operating bandwidth, as well as its upper and lower bounds, are determined by the sweep speed of the VNA, the necessary time window, and the maximum 10 dB bandwidth of the antenna. Hence, the frequency sweep configuration can be dynamically adjusted according to application and hardware resources as an added advantage of SFR.

In this regard, ultra-wide bandwidth, dynamic bandwidth control, and high speed measurement are the key attractions for using SFR in GPR applications such as utility surveying. Because the pulse width narrows as the bandwidth increases. As a result, high-resolution B-scans may be obtained. Subsurface medium, on the other hand, works as a frequency filter

Figure B.6: (*left*) Single antenna SFR architecture, (*right*) example of a VNA based SFR test bench in Cerema, Angers.

attributable to depth and permittivity. As a result, SFR enables better resolution on top and gradually reduces resolution while maintaining penetration via its low frequency components. Thus, the resolution and penetration are well-balanced when utilizing an ultra-wide band pulse. In the process of forming a B-scan in a monostatic setup, for example, the measured (S_{11}) is used to perform IFFT to build an A-scan and then a B-scan by stacks, as shown in Figure B.8 and detailed in the subsection 4.2. Certain signal processing methods, such as full wave inversion (FWI), allow the signal to be treated in the frequency domain without requiring IFFT [121, 122]. As a result, in this scenario, an SFR raw signal is beneficial over an impulse GPR.

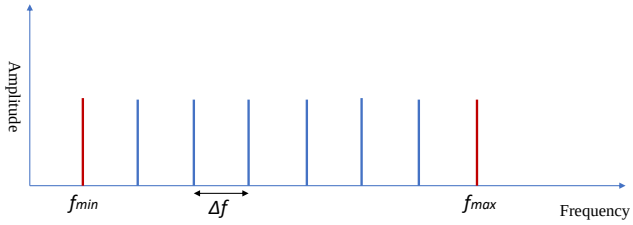

Figure B.7: Discrete pulse sweep of SFR in the frequency domain.

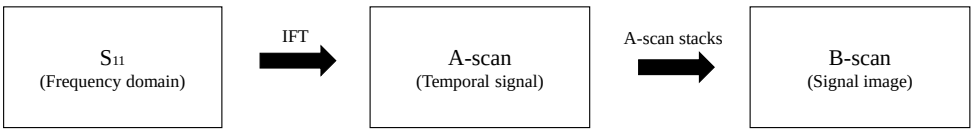

Figure B.8: S_{11} to B-scan conversion in SFR.

VNA configurations are carefully chosen in high speed mobility applications such as utility network survey applications to maximize measurement speed and penetration depth. As a result, these performance parameter matrices are extremely dependent on bandwidth, the number of sweep frequency points, the IF-Bandwidth of the discrete pulse, the maximum needed A-scan resolution range, and so on. Also, it's highly limited by the sweeping speed of the VNA.

The following correlations may be used to relate the SFR sweep planning. Whereas, the Equation B.1 provides how the frequency boundaries and number of sweep points are defined. Accordingly, depending on the required bandwidth and the maximum 10 dB bandwidth of the antenna, the lower and upper bound frequencies are set.

$$f_n = f_0 + n \cdot \Delta f \tag{B.1}$$

Whereas, f_n is the maximum frequency (Hz); f_0 is the minimum frequency (Hz); n is the number of frequency points ; Δf is the frequency step size between two adjacent discrete frequency pulses. Thus, the total bandwidth, $BW = f_n$ - f_0. However, the selection of the Δf is estimated based on the required time window of the A-scan as shown in the Equation B.2. Hence, the time window (T_a) is defined by probable maximum depth (D_s) and the maximum relative permittivity (ε_r) of the subsurface, according to the Equation B.3.

$$T_a = \frac{1}{\Delta f} \tag{B.2}$$

T_a is the time window range of A-scan (s) (time signal like seen in Figure B.2)

$$D_s = \frac{T_a \cdot C}{2 \cdot \sqrt{(\varepsilon_\tau \cdot \mu_r)}} \tag{B.3}$$

D_s is the required maximum survey depth (m), C is velocity of electromagnetic waves in the free space (m/s), ε_r is relative permittivity of the target medium, μ_r is relative permeability of the target medium.

To summarize, the overall bandwidth value is specified within the bandwidth capacity range of the VNA and Antenna. The maximum time range resolution of the A-scan is then determined based on the needed maximum depth range. The value of n (number of sweep frequency points) is determined by these two factors. It then calculates the speed of a single full sweep cycle (n $\cdot$ Δf) as well as the SFR data acquisition speed. As a result, speed performance and related metrics are covered in the subsections that follow.

Based on the mentioned technological attributes and benefits of the SFR, the development of multi-antenna Array step frequency radar became the focus of this thesis study. As a result, the multi-antenna array enables high resolution, faster and many parallel B-scans to build a three-dimensional mapping of the huge subsurface region prospected in underground utility network detection. The difficulties originate from the design of an appropriate SFR architecture, the identification of hardware components, the selection of an appropriate UWB antenna type suited for a wide antenna array, and the switching mechanism. Finally, trade-offs between hardware capacity, necessary optimal resolution, accuracy, and SFR speed must be investigated.

Bibliography

[1] Gouv.fr, "Arrêté du 15 février 2012 pris en application du chapitre iv du titre v du livre v du code de l'environnement relatif à l'exécution de travaux à proximité de certains ouvrages souterrains, aériens ou subaquatiques de transport ou de distribution," Gouv.fr, 2022. [Online]. Available: https://www.legifrance.gouv.fr/loda/id/JORFTEXT000025391351/.

[2] G. ZEISS, "France's national project to map underground utilities," Between the Poles, 05 2014. [Online]. Available: https://geospatial.blogs.com/geospatial/2014/05/frances-national-project-to-map-underground-utilities.html.

[3] L. e. G. C. POLIDORI, "Réseaux enterrés, sécurité, fiabilité, géomètre géomètre, n°2087, p.31–42." 2011.

[4] PIARC, "Gestion des ponts en service. rapport technique/management of the inservice bridges. technical report," *World Road Association 2012*, 2012.

[5] SETRA, "Valorisation du patrimoine routier national - cout de remise en etat des ouvrages d'art/valorization of the national road patrimony - maintenance cost of structures," 2013.

[6] . ., "Call811 | know what's below. call before you dig. unites states," Call 811. [Online]. Available: https://call811.com/

[7] G. Terrasse, J.-M. Nicolas, E. Trouvé, and É. Drouet, "Automatic Localization of Gas Pipes from GPR Imagery," in *EUSIPCO*, Budapest, Hungary, Aug. 2016. [Online]. Available: https://hal.archives-ouvertes.fr/hal-01351239

[8] W. Lai, X. Dérobert, and P. Annan, "A review of ground penetrating radar application in civil engineering: A 30-year journey from locating and testing to imaging and diagnosis," *NDT & E International*, 05 2017.

[9] H. Harkat, Y. Elfakir, S. Bennani, G. Khaissidi, and M. Mrabti, "Ground penetrating radar hyperbola detection using scale-invariant feature transform," *2016 International Conference on Electrical and Information Technologies (ICEIT)*, pp. 392–397, 2016.

[10] W. Shao, A. Bouzerdoum, and S. L. Phung, "Sparse representation of gpr traces with application to signal classification," *IEEE Transactions on Geoscience and Remote Sensing*, vol. 51, no. 7, pp. 3922–3930, 2013.

[11] C. Maas and J. Schmalzl, "Using pattern recognition to automatically localize reflection hyperbolas in data from ground penetrating radar," *Computers and Geosciences*, vol. 58, 2013.

[12] A. Krizhevsky, I. Sutskever, and G. E. Hinton, "Imagenet classification with deep convolutional neural networks," in *Advances in Neural Information Processing Systems*, F. Pereira, C. J. C. Burges, L. Bottou, and K. Q. Weinberger, Eds., vol. 25. Curran Associates, Inc., 2012. [Online]. Available: https://proceedings.neurips.cc/paper/2012/file/c399862d3b9d6b76c8436e924a68c45b-Paper.pdf.

[13] M. Pham and S. Lefèvre, "Buried object detection from b-scan ground penetrating radar data using faster-rcnn," *CoRR*, vol. abs/1803.08414, 2018. [Online]. Available: http://arxiv.org/abs/1803.08414

[14] D. Reichman, L. M. Collins, and J. M. Malof, "Some good practices for applying convolutional neural networks to buried threat detection in ground penetrating radar," in *2017 9th International Workshop on Advanced Ground Penetrating Radar (IWAGPR)*, 2017, pp. 1–5.

[15] S. Ren, K. He, R. Girshick, and J. Sun, "Faster r-cnn: Towards real-time object detection with region proposal networks," in *Advances in Neural Information Processing Systems*, C. Cortes, N. Lawrence, D. Lee, M. Sugiyama, and R. Garnett, Eds., vol. 28. Curran Associates, Inc., 2015. [Online]. Available: https://proceedings.neurips.cc/paper/2015/file/14bfa6bb14875e45bba028a21ed38046-Paper.pdf.

[16] J. Redmon, S. K. Divvala, R. B. Girshick, and A. Farhadi, "You only look once: Unified, real-time object detection," *2016 IEEE Conference on Computer Vision and Pattern Recognition (CVPR)*, pp. 779–788, 2016.

[17] J. Feng, L. Yang, H. Wang, Y. Song, and J. Xiao, "Gpr-based subsurface object detection and reconstruction using random motion and depthnet," 2020.

[18] Y. Li, Z. Zhao, Y. Luo, and Z. Qiu, "Real-time pattern-recognition of gpr images with yolo v3 implemented by tensorflow," *Sensors (Basel, Switzerland)*, vol. 20, 2020.

[19] Z. Mechbal and A. Khamlichi, "Sensitivity of the inverse problem solution related to detection of rebars buried in concrete by using gpr scanning," *MATEC Web of Conferences*, vol. 191, p. 00010, 01 2018.

[20] T. Liu, A. Klotzsche, M. Pondkule, H. Vereecken, Y. Su, and J. van der Kruk, "Radius estimation of subsurface cylindrical objects from ground-penetrating-radar data using full-waveform inversion," *Geophysics*, vol. 83, no. 6, pp. H43–H54, 2018.

[21] C. Windsor, L. Capineri, and P. Falorni, "The estimation of buried pipe diameters by generalized hough transform of radar data," *Piers Online*, vol. 1, pp. 345–349, 2005.

[22] N. Muniappan, E. P. Rao, A. V. Hebsur, and G. Venkatachalam, "Radius estimation of buried cylindrical objects using GPR — a case study," in *2012 14th International Conference on Ground Penetrating Radar (GPR)*, 06 2012, pp. 789–794.

[23] Li Ting-jun and Z. Zheng-ou, "Fast extraction of hyperbolic signatures in gpr," in *2007 International Conference on Microwave and Millimeter Wave Technology*, 04 2007, pp. 1–3.

[24] A. Dolgiy and V. Zolotarev, "GPR estimation for diameter of buried pipes," *Conference Proceedings, Near Surface 2005 - 11th European Meeting of Environmental and Engineering Geophysics*, vol. cp-13-00175, Sep 2005.

[25] J. F. Sham and W. W. Lai, "Development of a new algorithm for accurate estimation of GPR's wave propagation velocity by common-offset survey method," *NDT E International*, vol. 83, pp. 104–113, 2016. [Online]. Available: https://www.sciencedirect.com/science/article/pii/S0963869516300391.

[26] A. V. Ristic, D. Petrovacki, and M. Govedarica, "A new method to simultaneously estimate the radius of a cylindrical object and the wave propagation velocity from GPR data," *Computers & Geosciences*, vol. 35, no. 8, pp. 1620–1630, 2009.

[27] G. Borgioli, L. Capineri, P. Falorni, S. Matucci, and C. G. Windsor, "The detection of buried pipes from time-of-flight radar data," *IEEE Transactions on Geoscience and Remote Sensing*, vol. 46, no. 8, pp. 2254–2266, 08 2008.

[28] G. Terrasse, J. Nicolas, E. Trouvé, and É. Drouet, "Application of the curvelet transform for clutter and noise removal in GPR data," *IEEE Journal of Selected Topics in Applied Earth Observations and Remote Sensing*, vol. 10, no. 10, pp. 4280–4294, 10 2017.

[29] G. Terrasse, J.-M. Nicolas, E. Trouvé, and É. Drouet, "Automatic localization of gas pipes from GPR imagery," in *2016 24th European Signal Processing Conference (EUSIPCO)*. IEEE, pp. 2395–2399.

[30] P. Kaur, K. J. Dana, F. A. Romero, and N. Gucunski, "Automated GPR rebar analysis for robotic bridge deck evaluation," *IEEE Transactions on Cybernetics*, vol. 46, no. 10, pp. 2265–2276, 10 2016.

[31] R. Jaufer, S. S. Todkar, A. Ihamouten, Y. Goyat, D. Guilbert, A. Caucheteux, V. Baltazart, C. Heinkele, and X. Dérobert, *Ray-based method vs. SVM for the inversion of embedded cylindrical pipe's parameters from GPR data: Numerical comparative study*, 2020, pp. 356–359. [Online]. Available: https://library.seg.org/doi/abs/10.1190/gpr2020-093.1

[32] I. Giannakis, A. Giannopoulos, and C. Warren, "A machine learning scheme for estimating the diameter of reinforcing bars using ground penetrating radar," *IEEE Geoscience and Remote Sensing Letters*, vol. 18, no. 3, pp. 461–465, 2021.

[33] H. Liu, C. Lin, J. Cui, L. Fan, X. Xie, and B. F. Spencer, "Detection and localization of rebar in concrete by deep learning using ground penetrating radar," *Automation in Construction*, vol. 118, p. 103279, 2020. [Online]. Available: https://www.sciencedirect.com/science/article/pii/S0926580519315882.

[34] B. Park, J. Kim, J. Lee, M.-S. Kang, and Y.-K. An, "Underground object classification for urban roads using instantaneous phase analysis of ground-penetrating radar (GPR) data," *Remote Sensing*, vol. 10, no. 9, 2018. [Online]. Available: https://www.mdpi.com/2072-4292/10/9/1417.

[35] Q. Lu, J. Pu, and Z. Liu, "Feature extraction and automatic material classification of underground objects from ground penetrating radar data," *Journal of Electrical and Computer Engineering*, vol. 2014, 11 2014.

[36] S. Khudoyarov, N. Kim, and J.-J. Lee, "Three-dimensional convolutional neural network–based underground object classification using three-dimensional ground penetrating radar data," *Structural Health Monitoring*, vol. 19, no. 6, pp. 1884–1893, 2020. [Online]. Available: https://doi.org/10.1177/1475921720902700.

[37] M. El-Mahallawy and M. Hashim, "Material classification of underground utilities from gpr images using dct-based svm approach," *IEEE Geoscience and Remote Sensing Letters*, 04 2013.

[38] S. Seren, A. Eder-Hinterleitner, W. Neubauer, and P. Melichar, "Extended comparison of different gpr systems and antenna configurations at the roman site of carnuntum," *Near Surface Geophysics*, vol. 5, 12 2007.

[39] 3D-Radar, "3d radar sfr solution product brochure," http://3d-radar.com/technology/, accessed: 2019-10-30.

[40] G. A. Manual, "Geophysical survey systems, inc," *Salem, NH, MN30-903 Rev. E, 99ápp*, 2014.

[41] E. Eide, P. A. Våland, and J. Sala, "Ground-coupled antenna array for step-frequency gpr," in *Proceedings of the 15th International Conference on Ground Penetrating Radar*, 2014, pp. 756–761.

[42] A. Ristić, Željko Bugarinović, M. Vrtunski, and M. Govedarica, "Point coordinates extraction from localized hyperbolic reflections in gpr data," *Journal of Applied Geophysics*, vol. 144, pp. 1–17, 2017. [Online]. Available: https://www.sciencedirect.com/science/article/pii/S0926985117305670

[43] D. Dimitrov and D. Atanasov, "Implemention of the hough transform in detection of target trajectory." 2017 Defense technology forum Shumen, 01 2017.

[44] H.-S. Youn and C.-C. Chen, "Automatic GPR target detection and clutter reduction using neural network," in *Ninth International Conference on Ground Penetrating Radar*, S. Koppenjan and H. Lee, Eds., vol. 4758, International Society for Optics and Photonics. SPIE, 2002, pp. 579 – 582. [Online]. Available: https://doi.org/10.1117/12.462229.

[45] C. Maas and J. Schmalzl, "Using pattern recognition to automatically localize reflection hyperbolas in data from ground penetrating radar," *Computers & Geosciences*, vol. 58, pp. 116–125, 2013. [Online]. Available: https://www.sciencedirect.com/science/article/pii/S009830041300112X.

[46] L. E. Besaw, "Detecting buried explosive hazards with handheld GPR and deep learning," in *Detection and Sensing of Mines, Explosive Objects, and Obscured Targets XXI*, ser. Society of Photo-Optical Instrumentation Engineers (SPIE) Conference Series, S. S. Bishop and J. C. Isaacs, Eds., vol. 9823, May 2016, p. 98230N.

[47] E. Pasolli, F. Melgani, and M. Donelli, "Automatic analysis of gpr images: A pattern-recognition approach," *IEEE Transactions on Geoscience and Remote Sensing*, vol. 47, no. 7, pp. 2206–2217, 2009.

[48] T. Rahkar-Farshi, O. Kesemen, and S. Behjat-Jamal, "Multi hyperbole detection on images using modified artificial bee colony (ABC) for multimodal function optimization," in *2014 22nd Signal Processing and Communications Applications Conference (SIU)*. IEEE, Apr. 2014, pp. 894–898.

[49] H. Harkat, Y. Elfakir, S. D. Bennani, G. Khaissidi, and M. Mrabti, "Ground penetrating radar hyperbola detection using scale-invariant feature transform," in *2016 International Conference on Electrical and Information Technologies (ICEIT)*, 2016, pp. 392–397.

[50] Q. Hoarau, G. Ginolhac, A. M. Atto, and J.-M. Nicolas, "Robust Adaptive Detection of Buried Pipes using GPR," *Signal Processing*, vol. 132, pp. 293–305, Mar. 2017. [Online]. Available: https://hal.archives-ouvertes.fr/hal-01375659.

[51] G. R. Chandra, K. Rajiv, and B. B. Rao, "A distinctive similarity rendering approach to reconstitute hyperbola apices in GPR images," in *TENCON 2017 - 2017 IEEE Region 10 Conference*, 2017, pp. 350–353.

[52] Q. Dou, L. Wei, D. R. Magee, and A. G. Cohn, "Real-time hyperbola recognition and fitting in GPR data," *IEEE Transactions on Geoscience and Remote Sensing*, vol. 55, no. 1, pp. 51–62, 2017.

[53] K. Ishitsuka, S. Iso, K. Onishi, and T. Matsuoka, "Object detection in ground-penetrating radar images using a deep convolutional neural network and image set preparation by migration," *International Journal of Geophysics*, vol. 2018, pp. 1–8, 11 2018.

[54] M.-T. Pham and S. Lefèvre, "Buried Object Detection from B-Scan Ground Penetrating Radar Data Using Faster-RCNN," in *IGARSS 2018 - 2018 IEEE International Geoscience and Remote Sensing Symposium*, Valencia, Spain, 2018. [Online]. Available: https://hal.archives-ouvertes.fr/hal-01969029.

[55] W. Lei, F. Hou, J. Xi, Q. Tan, M. Xu, X. Jiang, G. Liu, and Q. Gu, "Automatic hyperbola detection and fitting in GPR B-scan image," *Automation in Construction*, vol. 106, p. 102839, 2019. [Online]. Available: https://www.sciencedirect.com/science/article/pii/S0926580519301347.

[56] Z. Liu, W. Wu, X. Gu, S. Li, L. Wang, and T. Zhang, "Application of combining yolo models and 3D GPR images in road detection and maintenance," *Remote Sensing*, vol. 13, no. 6, 2021. [Online]. Available: https://www.mdpi.com/2072-4292/13/6/1081.

[57] S. Li, X. Gu, X. Xu, D. Xu, T. Zhang, Z. Liu, and Q. Dong, "Detection of concealed cracks from ground penetrating radar images based on deep learning algorithm," *Construction and Building Materials*, vol. 273, p. 121949, 2021. [Online]. Available: https://www.sciencedirect.com/science/article/pii/S0950061820339532.

[58] K. He, X. Zhang, S. Ren, and J. Sun, "Deep residual learning for image recognition," 2016 IEEE Conference on Computer Vision and Pattern Recognition (CVPR), 2015.

[59] L. Weng, "Object detection for dummies part 3: R-cnn family," Dec 2017. [Online]. Available: https://lilianweng.github.io/posts/2017-12-31-object-recognition-part-3/

[60] R. Girshick, "Fast r-cnn," in *Proceedings of the 2015 IEEE International Conference on Computer Vision (ICCV)*, ser. ICCV '15. USA: IEEE Computer Society, 2015, p. 1440–1448. [Online]. Available: https://doi.org/10.1109/ICCV.2015.169

[61] L. Alzubaidi, J. Zhang, A. J. Humaidi, A. Al-Dujaili, Y. Duan, O. Al-Shamma, J. Santamaría, M. A. Fadhel, M. Al-Amidie, and L. Farhan, "Review of deep learning: concepts, cnn architectures, challenges, applications, future directions," *Journal of Big Data*, vol. 8, no. 1, p. 53, Mar 2021. [Online]. Available: https://doi.org/10.1186/s40537-021-00444-8.

[62] A. Krizhevsky, I. Sutskever, and G. E. Hinton, "Imagenet classification with deep convolutional neural networks," *Commun. ACM*, vol. 60, no. 6, p. 84–90, May 2017. [Online]. Available: https://doi.org/10.1145/3065386.

[63] J. Gu, Z. Wang, J. Kuen, L. Ma, A. Shahroudy, B. Shuai, T. Liu, X. Wang, G. Wang, J. Cai, and T. Chen, "Recent advances in convolutional neural networks," *Pattern Recognition*, vol. 77, pp. 354–377, 2018. [Online]. Available: https://www.sciencedirect.com/science/article/pii/S0031320317304120.

[64] I. Goodfellow, Y. Bengio, and A. Courville, *Deep Learning*. MIT Press, 2016, http://www.deeplearningbook.org.

[65] K. He, X. Zhang, S. Ren, and J. Sun, "Deep residual learning for image recognition," *2016 IEEE Conference on Computer Vision and Pattern Recognition (CVPR)*, pp. 770–778, 2016.

[66] S. Ren, K. He, R. B. Girshick, and J. Sun, "Faster R-CNN: towards real-time object detection with region proposal networks," *CoRR*, vol. abs/1506.01497, 2015. [Online]. Available: http://arxiv.org/abs/1506.01497

[67] C. Szegedy, V. Vanhoucke, S. Ioffe, J. Shlens, and Z. Wojna, "Rethinking the inception architecture for computer vision," in *2016 IEEE Conference on Computer Vision and Pattern Recognition (CVPR)*. Los Alamitos, CA, USA: IEEE Computer Society, jun 2016, pp. 2818–2826. [Online]. Available: https://doi.ieeecomputersociety.org/10.1109/CVPR.2016.308.

[68] J. Kim and J. Cho, "Exploring a multimodal mixture-of-yolos framework for advanced real-time object detection," *Applied Sciences*, vol. 10, no. 2, 2020. [Online]. Available: https://www.mdpi.com/2076-3417/10/2/612

[69] X. Huang, X. Wang, W. Lv, X. Bai, X. Long, K. Deng, Q. Dang, S. Han, Q. Liu, X. Hu, D. Yu, Y. Ma, and O. Yoshie, "PP-YOLOv2: A practical object detector," 2021.

[70] J. Redmon and A. Farhadi, "Yolov3: An incremental improvement," *CoRR*, vol. abs/1804.02767, 2018. [Online]. Available: http://arxiv.org/abs/1804.02767.

[71] A. Bochkovskiy, C.-Y. Wang, and H.-Y. M. Liao, "Yolov4: Optimal speed and accuracy of object detection," 2020.

[72] X. Zhu, S. Lyu, X. Wang, and Q. Zhao, "TPH-YOLOv5: Improved yolov5 based on transformer prediction head for object detection on drone-captured scenarios," *CoRR*, vol. abs/2108.11539, 2021. [Online]. Available: https://arxiv.org/abs/2108.11539

[73] Y. Du, N. Pan, Z. Xu, F. Deng, Y. Shen, and H. Kang, "Pavement distress detection and classification based on YOLO network," *International Journal of Pavement Engineering*, vol. 22, no. 13, pp. 1659–1672, 2021. [Online]. Available: https://doi.org/10.1080/10298436.2020.1714047.

[74] E. N. Ukhwah, E. M. Yuniarno, and Y. K. Suprapto, "Asphalt pavement pothole detection using deep learning method based on yolo neural network," *2019 International Seminar on Intelligent Technology and Its Applications (ISITIA)*, pp. 35–40, 2019.

[75] H. Zhang, L. Qin, J. Li, Y. Guo, Y. Zhou, J. Zhang, and Z. Xu, "Real-time detection method for small traffic signs based on yolov3," *IEEE Access*, vol. 8, pp. 64 145–64 156, 2020.

[76] Y.-Q. Huang, J.-C. Zheng, S.-D. Sun, C.-F. Yang, and J. Liu, "Optimized yolov3 algorithm and its application in traffic flow detections," *Applied Sciences*, vol. 10, no. 9, 2020. [Online]. Available: https://www.mdpi.com/2076-3417/10/9/3079.

[77] V. Taran, Y. G. Gordienko, A. Rokovyi, O. Alienin, and S. G. Stirenko, "Impact of ground truth annotation quality on performance of semantic image segmentation of traffic conditions," *CoRR*, vol. abs/1901.00001, 2019. [Online]. Available: http://arxiv.org/abs/1901.00001.

[78] G. Terrasse, "Géodétection des réseaux enterrés par imagerie radar traitement du signal et de l'image," Ph.D. dissertation, Télécom ParisTech, Français, 2017.

[79] D. Daniels, *Ground Penetrating Radar IEE, 2nd ed.*, 07 2004.

[80] P. Monasse, "Extraction of the Level Lines of a Bilinear Image," *Image Processing On Line*, vol. 9, pp. 205–219, 2019, https://doi.org/10.5201/ipol.2019.269.

[81] T. Araújo, P. Chagas, J. Alves, C. Santos, B. Sousa Santos, and B. Serique Meiguins, "A real-world approach on the problem of chart recognition using classification, detection and perspective correction," *Sensors*, vol. 20, no. 16, 2020. [Online]. Available: https://www.mdpi.com/1424-8220/20/16/4370.

[82] J. Hanley and B. Mcneil, "The meaning and use of the area under a receiver operating characteristic (roc) curve," *Radiology*, vol. 143, pp. 29–36, 05 1982.

[83] C. Warren, A. Giannopoulos, and I. Giannakis, "gprmax: Open source software to simulate electromagnetic wave propagation for ground penetrating radar," *Computer Physics Communications*, vol. 209, pp. 163 – 170, 2016. [Online]. Available: http://www.sciencedirect.com/science/article/pii/S0010465516302533.

[84] K. S. Kunz and R. J. Luebbers, *The finite difference time domain method for electromagnetics*. CRC press, 1993.

[85] A. Taflove and S. C. Hagness, *Computational electrodynamics: the finite-difference time-domain method*. Artech house, 2005.

[86] A. Giannopoulos, "Modelling ground penetrating radar by gprmax," *Construction and Building Materials*, vol. 19, no. 10, pp. 755–762, 2005.

[87] ——, "The investigation of transmission-line matrix and finite-difference time-domain methods for the forward problem of ground probing radar," 1998.

[88] C. Warren and A. Giannopoulos, "gprmax user guide."

[89] A. Giannopoulos and N. Diamanti, "Numerical modeling of ground penetrating radar response from rough subsurface interfaces," *Near surface geophysics*, vol. 6, pp. 357–369, 12 2008.

[90] I. Giannakis, A. Giannopoulos, and C. Warren, "A realistic fdtd numerical modeling framework of ground penetrating radar for landmine detection," *IEEE Journal of Selected Topics in Applied Earth Observations and Remote Sensing*, vol. 9, no. 1, pp. 37–51, Jan 2016.

[91] "GSSI Solutions product brochure," https://www.geophysical.com/products/roadscan, accessed: 2019-10-30.

[92] Y. Wang, "Frequencies of the ricker wavelet," *Geophysics*, vol. 80, pp. A31–A37, 02 2015.

[93] B. Poluha, J. L. Porsani, E. R. Almeida, V. R. N. D. Santos, and S. J. Allen, "Depth estimates of buried utility systems using the gpr method: Studies at the iag/usp geophysics test site," *International Journal of Geosciences*, vol. 08, no. 05, p. 726–742, 2017.

[94] C. Warren, A. Giannopoulos, and I. Giannakis, "gprmax: Open source software to simulate electromagnetic wave propagation for ground penetrating radar," *Computer Physics Communications*, vol. 209, 09 2016.

[95] L. Pajewski, A. Benedetto, X. Derobert, A. Giannopoulos, A. Loizos, G. Manacorda, M. Marciniak, C. Plati, G. Schettini, and I. Trinks, "Applications of ground penetrating radar in civil engineering—cost action tu1208," in *2013 7th International Workshop on Advanced Ground Penetrating Radar*. IEEE, 2013, pp. 1–6.

[96] N. Muniappan, A. Hebsur, E. Rao, and G. Venkatachalam, "Radius estimation of buried cylindrical objects using GPR — a case study," 06 2012, pp. 789–794.

[97] A. Subasi and M. Ismail Gursoy, "Eeg signal classification using pca, ica, lda and support vector machines," *Expert Syst. Appl.*, vol. 37, no. 12, pp. 8659–8666, Dec. 2010. [Online]. Available: http://dx.doi.org/10.1016/j.eswa.2010.06.065

[98] F. Melgani and Y. Bazi, "Classification of electrocardiogram signals with support vector machines and particle swarm optimization," *IEEE Transactions on Information Technology in Biomedicine*, vol. 12, no. 5, pp. 667–677, Sep. 2008.

[99] T.-K. Lin, "Pca/svm-based method for pattern detection in a multisensor system," *Mathematical Problems in Engineering*, vol. 2018, pp. 1–11, 02 2018.

[100] F. Samadzadegan, H. Hasani, and T. Partovi, "Sensitivity analysis of support vector machine in classification of hyperspectral imagery," in *Proceedings of the Canadian Geomatics Conference, Calgary, Canada*, 2010.

[101] N. Ahmad, H. Lorenzl, and M. P. Wistuba, "Crack detection in asphalt pavements - how useful is the gpr?" in *2011 6th International Workshop on Advanced Ground Penetrating Radar (IWAGPR)*, June 2011, pp. 1–6.

[102] M. Andrzej and M. Marta, "Modern ndt systems for structural integrity examination of concrete bridge structures," *Procedia Engineering*, vol. 91, pp. 418 – 423, 2014, xXIII R-S-P Seminar, Theoretical Foundation of Civil Engineering (23RSP) (TFoCE 2014). [Online]. Available: http://www.sciencedirect.com/science/article/pii/S187770581403104X

[103] M. S. El-Mahallawy and M. Hashim, "Material classification of underground utilities from gpr images using dct-based svm approach," *IEEE Geoscience and Remote Sensing Letters*, vol. 10, no. 6, pp. 1542–1546, Nov 2013.

[104] X. Xie, H. Qin, C. Yu, and L. Liu, "An automatic recognition algorithm for gpr images of rc structure voids," *Journal of Applied Geophysics*, vol. 99, pp. 125 – 134, 2013.

[105] A. Ihamouten, C. Le Bastard, D. Xavier, F. Bosc, and G. Villain, "Using machine learning algorithms to link volumetric water content to complex dielectric permittivity in a wide (33–2000 mhz) frequency band for hydraulic concretes," *Near Surface Geophysics*, vol. 14, no. 6, pp. 527–536, 2016. [Online]. Available: https://www.earthdoc.org/content/journals/10.3997/1873-0604.2016045.

[106] C. Le Bastard, V. Baltazart, X. Dérobert, and Y. Wang, "Support vector regression method applied to thin pavement thickness estimation by gpr," in *2012 14th International Conference on Ground Penetrating Radar (GPR)*, 06 2012, pp. 349–353.

[107] S. S. Todkar, C. Le Bastard, A. Ihamouten, V. Baltazart, X. Dérobert, C. Fauchard, D. Guilbert, and F. Bosc, "Detection of debondings with ground penetrating radar using a machine learning method," in *2017 9th International Workshop on Advanced Ground Penetrating Radar (IWAGPR)*, June 2017, pp. 1–6.

[108] C. Warren, A. Giannopoulos, and I. Giannakis, "gprmax: Open source software to simulate electromagnetic wave propagation for ground penetrating radar," *Computer Physics Communications*, vol. 209, pp. 163–170, 2016.

[109] A. J. Smola and B. Schölkopf, "A tutorial on support vector regression," *Statistics and Computing*, vol. 14, pp. 199–222, 2004.

[110] S. S. Todkar, V. Baltazart, A. Ihamouten, X. Dérobert, and D. Guilbert, "One-class svm based outlier detection strategy to detect thin interlayer debondings within pavement structures using ground penetrating radar data," *Journal of Applied Geophysics*, vol. 192, p. 104392, 2021. [Online]. Available: https://www.sciencedirect.com/science/article/pii/S0926985121001397.

[111] AFNOR, "Chaussées et dépendances; tranchées ; ouverture, remblayage, réflection," Février 2005, norme française NP P98-331.

[112] P. Cunningham and S. J. Delany, "k-nearest neighbour classifiers - a tutorial," *ACM Computing Surveys*, vol. 54, no. 6, p. 1–25, Jul 2022. [Online]. Available: http://dx.doi.org/10.1145/3459665.

[113] J. Shan, A. Xu, and J. Lin, "A parametric study of microstrip-fed vivaldi antenna," in *2017 3rd IEEE International Conference on Computer and Communications (ICCC)*, 2017, pp. 1099–1103.

[114] F. B. Gross, *Frontiers in antennas: Next generation design engineering.* New York: McGraw-Hill Professional, 2011.

[115] A. Ahmed, Y. Zhang, D. Burns, D. Huston, and T. Xia, "Design of UWB antenna for air-coupled impulse ground-penetrating radar, "IEEE geoscience and remote sensing letters," vol. 13, pp. 92–96, 2016.

[116] A. A. Jamali and R. Marklein, *"Design and optimization of ultrawideband TEM horn antennas for GPR applications, " XXXth URSI General Assembly and Scientific Symposium, Istanbul*, 2011.

[117] C. Ozdemir, B. Yilmaz, S. I. Keceli, H. Lezki, and O. Sutcuoglu, *Ultra Wide Band horn antenna design for Ground Penetrating Radar: A feeder practice.* 15th Int, 2014.

[118] I. Hertl and M. Strycek, in *UWB antennas for ground penetrating radar application.* 2007 19th International Conference on Applied Electromagnetics and Communications, 2007, pp. 1–4.

[119] K. K. Ajith and A. Bhattacharya, *Improved ultra-wide bandwidth bowtie antenna with metamaterial lens for GPR applications.* Proceeding of the 15th Int, 2014.

[120] D. M. Elsheakh and E. A. Abdallah, *"Novel shapes of Vivaldi antenna for ground penetrating radar (GPR), " 7th European Conference on Antenna and Propagation (EuCAP), Gothenburg*, 2013.

[121] A. Ihamouten, C. Le Bastard, X. Derobert, F. Bosc, and G. Villain, "Using machine learning algorithms to link volumetric water content to complex dielectric permittivity in a wide (33–2000 MHz) frequency band for hydraulic concretes," *Near Surface Geophysics*, vol. 14, no. 2144, 2016. [Online]. Available: https://hal.archives-ouvertes.fr/hal-01708048

[122] B. GUAN, "Characterization of building materials by electromagnetic non-destructive methods application to limestone," Ph.D. dissertation, 'École doctorale : Sciences et technologies de l'information, et mathématiques, Université de Nantes sous le sceau de l'Université Bretagne Loire, France, 2018.

[123] C. Chou, H. Li, and D. Song, "Encoder-camera-ground penetrating radar sensor fusion: Bimodal calibration and subsurface mapping," *IEEE Transactions on Robotics*, vol. PP, pp. 1–15, 08 2020.

[124] J. Nissen, B. Johansson, M. Wolf, and L. Skoog, "Ground penetrating radar - a ground investigation method applied to utility locating in no-dig technologies, pp, 1-6, mala geoscience raycon, stockholm," 2001.

[125] M. N. Ismail N.A, Saad R. and N. Ali, "Predictive mapping of underground utilities using ground penetrating radar (GPR)," pp. pp. 104–108. ISSN: 2251–9114., 2013.

[126] N. Cheng, H. C. Tang, and C. Chan, "Identification and positioning of underground utilities using ground penetrating radar (GPR)," p. 12, 2013.

[127] E. S. Eide and J. F. Hjelmstad, "3D utility mapping using electronically scanned antenna array," Santa Barbara, CA. [Online]. Available: http://proceedings.spiedigitallibrary.org/proceeding.aspx?articleid=890959

Titre : Cartographie 3D des réseaux de distribution souterrains à l'aide de radar à fréquence pas à pas à réseau multi-antennes ultra-large bande

Mots clés : GPR, Cartographie des services publics, détection des services publics, radar à pas de fréquence, intelligence artificielle.

Résumé : Cette thèse s'inscrit dans le cadre d'une collaboration entre le Cerema, Logiroad et l'Université Gustave Eiffel, financée par Logiroad. L'objectif de cette thèse est de fournir les étapes de traitement du signal nécessaires à l'identification, la localisation et la classification automatique des réseaux enterrés. L'acquisition des données est réalisée par un radar à sauts de fréquence (RSF) à ultra-large bande (ULB) et à réseaux d'antennes. Le système doit être équipé d'un réseau linéaire d'antennes capable de couvrir toute la largeur de la route à grande vitesse, ce qui le rend adapté à l'auscultation des autoroutes et voies urbaines. Par conséquent, il peut faciliter la réalisation de cartographies 3D à grande échelle. Cette thèse a été motivée en réponse aux réglementations gouvernementales récemment mises en place pour conserver une base de données géomatiques des réseaux enterrés et des normes de positionnement comme mesures de prévention des dommages pendant les excavations. Par exemple, la précision de la localisation tridimensionnelle des réseaux rigides est de 40 cm en classe A, comme spécifié dans la norme française NF-S70-003-2.

En outre, la démarche potentielle doit être hautement résiliente dans un environnement souterrain hautement dynamique, complexe, inattendu et chahuté lié à la nature de cette application. Nous avons divisé l'objectif global de la recherche en trois sous-tâches distinctes, telles que la détection automatisée des canalisations, l'estimation de leur profondeur et de leur diamètre, sachant que la précision en terme de localisation satisfait à l'attente de précision en classe A. Pour cela, un radar à sauts de fréquence à réseau d'antennes a été construit pour fournir la preuve du concept. Cela pourrait aider à la création de réseaux RSF personnalisés, à haute densité et à faible coût. Enfin, toutes les méthodes de traitement du signal étudiées sont fortement basées sur des approches physiques et méthodes d'apprentissage automatique telles que Ray-based, SVM, SVR, ANN, KNN, CNN, Faster RCNN et YOLOv4, en lien avec d'autres techniques physiques de prétraitements de signaux et d'images GPR. Dans ce contexte, tous les modèles ont été validés numériquement et validés à l'aide de données expérimentales.

Title: 3D mapping of underground utility networks using ultra-wideband multi antenna array step frequency radar

Keywords: GPR, Utility mapping, utility detection, Step frequency radar, artificial intelligence

Abstract : The thesis study is part of a collaboration between Cerema, Logiroad, and the Universite Gustave Eiffel. Further, the research fully funded by Logiroad. The goal of this thesis study is to provide the signal processing steps required for automatic identification, localization, and classification of underground utility networks. The acquisition of data is focused in Ultrawide Band (UWB) multi antenna array Step Frequency Radar (SFR). The system must be equipped with a linear antenna array that can cover the whole width of the road or survey channel at ideal high speed, making it suited for highways and local urban roads.

As a result, it may make large-scale 3D mapping easier. The thesis was motivated as a response to recently implemented government regulations in keeping a geomatics database of underground utility networks and positioning standards as damage avoidance measures during excavations. For example, the precision of three-dimensional location of critical underground networks in class A is 40 cm, as specified in the NF-S70-003-2 standard in France.

Furthermore, the potential solution must be highly resilient in the highly dynamic, complex, unexpected, and dispersed subsurface environment indicated by the nature of this application. We have divided the overall goal of the research into three distinct subtasks, such as automated pipe detection, depth and diameter estimate, given that the localisation accuracy satisfies the Class A precision expectation. Finally, a multi antenna array step frequency radar was built to provide the proof of concept. This might aid in the creation of customized, high-density, low-cost array SFR.

As a result, all investigated signal processing methods are highly based on the physical and machine learning approaches such as Ray-based, SVM, SVR, ANN, KNN, CNN, Faster R-CNN, and YOLOv4, in conjunction with other physical GPR signal and image pre-processing techniques. In this context, all models were numerically validated and validated using partial experimental data.